

Quantum Measurement of Mechanical Motion close to the Standard Quantum Limit

Présentée le 11 septembre 2020

à la Faculté des sciences de base
Laboratoire de photonique et mesures quantiques (SB/STI)
Programme doctoral en photonique

pour l'obtention du grade de Docteur ès Sciences

par

Liu QIU

Acceptée sur proposition du jury

Prof. L. Thévenaz, président du jury
Prof. T. Kippenberg, directeur de thèse
Dr P. Seidler, rapporteur
Prof. A. Cleland, rapporteur
Prof. C. Galland, rapporteur

To my family...

Acknowledgements

First of all, I would like to thank Tobias for giving me the opportunity to work on this challenging project, despite the very little experience I had with real experiments before. His passion and dedication to science establish the research environment where we can focus on science itself. His continuous inspiration, patience, persistence and optimism have been boosterish during the hard times, in the experiments or in the tedious review processes. What's more, thank him for the broad spectrum of scientific research that I am luckily exposed to.

Thank Chris for the guidance and support when I started, and also the continuous help over the last years. Thank Wolfgang for the help in fabrication and the time together in the cleanroom in the beginning of my PhD. Thank Nico for kindly teaching me all the experimental basics, from searching for an optical resonance, stabilizing a lock, to setting up the cryostat, and also for his delightful sarcasm. Thank Itay for the endless hours in the lab in the last five years together, especially the quiet nights and weekends when all the best data are taken. From him, I learned how to look at questions from completely different perspectives. I'd like to thank Paul for the collaboration over the years. I've been always impressed by his passion towards science and the carefulness into the details. Without him, some of the results and findings in this thesis will be never possible. Thank Daniel and Andreas for the endless discussions and help on the theory side. Thank Alexey for teaching me all the basics in microwave and cryogenics, and what's more, for answering my endless phone calls whenever the cryostat emergency arises. Thank Cyrille, Zdenek, Patrick, Joffrey, Rémy and Michael for the help with fabrication at CMI. Thank Gilles, Claude and Florence for all the help in the PhLab. Thank Katharina and Simon from IBM Zurich over the years with collaborations on different projects. The field of cavity optomechanics has witnessed an extraordinary advancement during my PhD. I'd like to thank other colleagues in the field who continuously push us forward, especially the Vienna and Delft group. Thank Vivishek, Ewold, Albert, Mika, Klemens, John, and Michael for joyful discussions and their deep physical intuition.

Thank all the other colleagues of different generations from the lab over the last years for all the help, my officemates, Clement, Niels, Sergey, Terence and Alberto, my Ph labmates,

Acknowledgements

Philippe, Maxim and Anton, and Daniel, Nathan, Dal, Amir, Victor, Arne, Ryan, Hendrik, Mohammad, John, Martin, Anshuman, Arslan, Marie and Dennis. And Hairun, Junqiu, Wenle and Guanhao, for all the fun together and best wish to Jiahe on the future experiments. Thank H  l  ne, Antonella and Kathleen for all the administrative help.

Life has become much more pleasant with lots of friends in Lausanne. I appreciate Meng, Jiangman, Wei, Xiaoqin, Shiwei, Shenghan, Yang, Min, Xiaoming and the *petite* Lilian, for all the hikes, ski trips, travelling and vacations together. Thank Ping, Quansheng, Yifei, Shengnan, Tianqi and Chongqi for relaxed lunch and coffee discussions. Thank Fengyun, Yinai, Qingwen, Wanze, Xudong and lot of others for the get-togethers.

In the end, I want to thank my parents for the unconditional love and support over the years. 感谢我的父亲给我最初的科学的教导，以及我的母亲的无尽的牺牲。

Thank Cuiyun and *petit* Shaoran, for everything.

Lausanne, 02,02,2020

L. Q.

Abstract

In quantum mechanics, the Heisenberg's uncertainty principle places a fundamental limit in the measurement precision for certain pairs of physical quantities, such as position and momentum, time and energy or amplitude and phase. Due to the Heisenberg uncertainty principle, any attempt to extract certain information from a quantum object would inevitably perturb it in an unpredictable way. This raises one question, "What is the precision limit in such quantum measurements?" The answer, *standard quantum limit* (SQL), has been obtained by Braginsky to figure out the fundamental quantum limits of displacement measurement in the context of gravitational wave detection. To circumvent the unavoidable quantum back-action from the priori measurement, *quantum non-demolition measurement* (QND) methods were introduced by Braginsky and Thorne. To surpass the SQL of the displacement measurement in an interferometer, one can measure only one quadrature of the mechanical motion while giving up the information about the other canonically conjugated quadrature. Such measurements can be performed by periodic driving the mechanical oscillator, i.e. the *back-action evading* (BAE) measurement.

Cavity optomechanics provides an ideal table-top platform for the testing of the quantum measurement theory. The mechanical oscillator is coupled to electromagnetic field via radiation pressure, which is enhanced by an optical micro-cavity. Over the last decade, laser cooling has enabled the preparation of mechanical oscillator in the ground state in both optical and microwave systems. BAE measurements of mechanical motion have been allowed in the microwave electromechanical systems, which led to the observations of mechanical squeezing and entanglement. However, despite the theoretical proposal almost 40 years ago, the sub-SQL measurements still remain elusive. This thesis reports our efforts on the quantum measurements with a highly sideband-resolved silicon optomechanical crystal (OMC) close to the SQL, in a ^3He buffer gas environment at $\sim 2\text{K}$. The OMC couples an optical mode at telecommunication wavelength and a colocalized mechanical mode at GHz frequency. The ^3He buffer gas environment allows sufficient thermalization of the OMC, despite the drastically decreased silicon thermal conductivity at cryogenic temperatures. We observe Floquet dynamics in motional sideband asymmetry measurement when employing multiple probing

Abstract

tones. The Floquet dynamics arises due to presence of Kerr-type nonlinearities and gives rise to an artificially modified motional sideband asymmetry, resulting from a synthetic gauge field among the Fourier modes. We demonstrate the first optical continuous two-tone backaction-evading measurement of a localized GHz frequency mechanical mode of silicon OMC close to the ground state by showing the transition from conventional sideband asymmetry to backaction-evading measurement. We discover a fundamental two-tone optomechanical instability and demonstrate its implications on the back-action evading measurement. Such instability imposes a fundamental limitation on other two-tone schemes, such as dissipative quantum mechanical squeezing. We demonstrate state-of-art laser sideband cooling of the mechanical motion to a mean thermal occupancy of 0.09 quantum, which is -7.4dB of the oscillator's zero-point energy and corresponds to 92% ground state probability. This also enables us to observe the dissipative mechanical squeezing below the zero-point motion for the first time with laser light.

Keywords: quantum measurement, cavity optomechanics, standard quantum limit, quantum non-demolition measurement, back-action evading measurement, sideband asymmetry, quantum mechanical squeezing.

Résumé

En mécanique quantique, le principe d'incertitude de Heisenberg pose une limite fondamentale à la précision de mesure pour certaines paires de quantités physiques, telles que la position et la quantité de mouvement, le temps et l'énergie ou l'amplitude et la phase. En raison du principe d'incertitude de Heisenberg, toute tentative d'extraire certaines informations d'un objet quantique le perturberait inévitablement de manière imprévisible. Cela soulève une question : "Quelle est la limite de précision pour de telles mesures quantiques?" Braginsky a découvert la réponse à cette question, la *limite quantique standard* (SQL), en étudiant les méthodes de détections d'ondes gravitationnelles. Pour contourner la rétro-action quantique inévitable a priori lors d'une mesure, Braginsky et Thorne ont introduit des méthodes de *mesure quantique non-destructive* (QND). Pour dépasser la SQL la mesure de déplacement dans un interféromètre, il est possible de mesurer une seule quadrature du mouvement mécanique tout en renonçant aux informations sur l'autre quadrature canoniquement conjuguée. Ces mesures peuvent être effectuées en entraînant périodiquement l'oscillateur mécanique afin de réaliser une mesure dite *d'évasion de rétro-action* (BAE). L'optomécanique de cavité fournit une plate-forme idéale pour tester la théorie de la mesure quantique. L'oscillateur mécanique est couplé à la lumière via la pression de rayonnement, qui est renforcée par une micro-cavité optique. Au cours de la dernière décennie, le refroidissement laser a permis la préparation d'oscillateurs mécaniques à l'état fondamental dans les systèmes optiques et micro-ondes. Des mesures BAE du mouvement mécanique ont été permises dans les systèmes électromécaniques micro-ondes, ce qui a conduit à des observations de squeezing mécanique et d'intrication. Bien que la proposition théorique ait été soumise il y a près de quarante ans, aucune mesure sub-SQL n'a encore été réalisée à ce jour.

Cette thèse rapporte nos efforts pour tenter de réaliser des mesures sub-SQL avec un cristal optomécanique de silicium (OMC) à résolution latérale élevée dans un environnement de gaz tampon ^3He à $\sim 2\text{K}$. L'OMC couple un mode optique aux longueurs d'onde de télécommunication et un mode mécanique colocalisé aux fréquences GHz. L'environnement de gaz tampon ^3He permet une thermalisation suffisante de l'OMC malgré la conductivité thermique du silicium considérablement réduite. Nous observons la dynamique de Floquet dans la mesure

Résumé

asymétrique de la bande latérale motrice lors de l'utilisation de plusieurs sondes lasers. La dynamique de Floquet résulte de la présence de non-linéarités de type Kerr et donne lieu à une asymétrie de bande latérale de mouvement artificiellement modifiée, trouvant son origine dans le champ de jauge synthétique parmi les modes de Fourier. Nous démontrons la première mesure optique continue à deux tons évitant la rétroaction d'un mode mécanique de fréquence GHz localisé de silicium OMC proche de l'état fondamental en montrant la transition de l'asymétrie de bande latérale conventionnelle à la mesure de contournement. Nous découvrons une instabilité optomécanique bicolore fondamentale et démontrons ses implications sur la mesure de rétro-action. Une telle instabilité impose une limite fondamentale propre aux schémas à deux tons, tels que la squeezing mécanique quantique dissipatif. Nous démontrons le refroidissement par bande latérale laser du mouvement mécanique jusqu'à une occupation thermique moyenne de 0.09 quanta, ce qui représente -7.4dB de l'énergie du point zéro de l'oscillateur et correspond à une probabilité de 92 % de l'état fondamental. Cela nous permet d'observer un squeezing dissipatif mécanique en dessous du mouvement du point zéro.

Keywords : mesure quantique, optomécanique des cavités, limite quantique standard, mesure quantique de non-démolition, d'évasion de rétro-action, d'asymétrie des bandes latérales, squeezing mécanique quantique.

List of Publications

1. **Liu Qiu**[†], Itay Shomroni[†], Jiahe Pan, Paul Seidler, Tobias Kippenberg, “Quantum squeezing of mechanical motion with light” , In preparation.
2. **Liu Qiu**, Itay Shomroni, Paul Seidler, Tobias Kippenberg, “Optical micro-cavity spectroscopy with dissipation” , In preparation.
3. **Liu Qiu**[†], Itay Shomroni[†], Paul Seidler, Tobias Kippenberg, “Laser cooling of a nanomechanical oscillator to its zero-point energy” , Phys. Rev. Lett. 124, 173601 (2020).
4. Itay Shomroni[†], Amir Youssefi[†], Nick Sauerwein[†], **Liu Qiu**[†], Daniel Malz, Andreas Nunnenkamp, Paul Seidler, Tobias J. Kippenberg, “Two-Tone Optomechanical Instability and Its Fundamental Implications for Backaction-Evading Measurements” , Phys. Rev. X 9, 041022 (2019)
5. Itay Shomroni[†], **Liu Qiu**[†], Daniel Malz, Andreas Nunnenkamp, Tobias J. Kippenberg, “Optical Backaction-Evading Measurement of a Mechanical Oscillator” , Nature Communications 10, 2086 (2019).
6. **Liu Qiu**[†], Itay Shomroni[†], Marie Adrienne Ioannou, Daniel Malz, Andreas Nunnenkamp, Tobias Kippenberg, “Floquet dynamics in the quantum measurement of mechanical motion” , Phys. Rev. A 100, 053852 (2019).
7. Itay Shomroni, **Liu Qiu**, Tobias Kippenberg, “Optomechanical generation of a mechanical catlike state by phonon subtraction” , Phys. Rev. A 101, 033812 (2020)
8. Amir Youssefi, Itay Shomroni, Nathan Bernier, Yash J. Joshi, Anton Lukashchuk, **Liu Qiu**, Tobias Kippenberg, “Cryogenic electro-optical interconnect for superconducting circuits” , arXiv:2004.04705 (2020)

Contents

Acknowledgements	v
List of Publications	xi
List of figures	xv
1 Introduction	1
1.1 Quantum Measurement	1
1.1.1 Heisenberg Uncertainty Principle	1
1.1.2 Standard Quantum Limit	3
1.1.3 Quantum Non-Demolition Measurement	6
1.2 Cavity Optomechanics	8
1.3 Overview of the Thesis	11
2 Theory	13
2.1 Input-output theory	13
2.2 The Quantum Harmonic Oscillator	15
2.3 Optical Cavity	18
2.4 Quantum Optomechanics	19
2.5 Bichromatic Optomechanics	25
3 Experimental System	39
3.1 Optomechanical Crystal	39
3.2 Taper Coupling	43
3.3 Fabrication	46
3.4 Experimental System Details	48
3.4.1 Room Temperature Measurement	48
3.4.2 Cryogenic Measurement	57

4	Floquet Dynamics in Quantum Measurements of Mechanical Motion	67
4.1	Floquet dynamics	67
4.2	Experimental Results	69
4.3	Theory	76
4.4	Frequency Response Measurement	81
4.5	Excess Laser Noise	82
4.6	Conclusion	83
5	Optical Back-action Evading Measurement of a Mechanical Oscillator	85
5.1	Introduction	85
5.2	Theory	88
5.3	Experimental Results	89
5.4	Conclusion	92
6	Two-tone Optomechanical Instability	93
6.1	Introduction	93
6.2	Observation of instability in two-tone pumping	94
6.3	Theory	97
6.4	Microwave Experiment	102
6.5	Conclusion	105
7	Laser cooling of a nanomechanical oscillator to the zero-point energy	107
7.1	Introduction	107
7.2	Experimental System Details	109
7.3	Experimental Results	113
7.3.1	Coherent optomechanical spectroscopy	114
7.3.2	Calibration using sideband asymmetry	114
7.3.3	Mechanical Noise Thermometry	117
7.3.4	Results of Sideband Cooling	117
7.3.5	Excess laser noise	123
7.3.6	Conclusion	124
8	Quantum squeezing of mechanical motion with light	127
8.1	Reservoir engineering	127
8.2	Experimental Results	130
8.3	Parametric effects	133
8.4	Conclusion	134

9 Summary and Outlook	135
9.1 Summary	135
9.2 Outlook	136
A List of Symbols	137
B Nano Fabrication	139
B.1 Fabrication Runcard	139
B.2 Etching Test	142
B.2.1 Fluorine Based Etching - Pseudo-Bosch Etching	143
B.2.2 Hydrogen Bromide Based Etching	143
B.2.3 Etching Results	143
B.3 Image Processing	148
C Optical Measurement	151
C.0.1 Coherent Response Measurement	151
C.0.2 Balanced Heterodyne Detection	153
D Laser Noise	157
E Dissipation in optical micro-cavity spectroscopy	165
Curriculum Vitae	189

List of Figures

1.1	Scheme of the Heisenberg microscope	2
1.2	Scheme of a continuous linear measurement	4
1.3	LIGO near Hanford, Washington, U.S	6
1.4	Displacement measurement sensitivity vs. the probing strength	10
2.1	Schematic of a generic optomechanical system	19
3.1	Design of the OMC	42
3.2	Optical Coupling between the waveguide and optical tapered fiber	44
3.3	Effective index of the waveguide TE mode	44
3.4	Optimal coupling length versus the gap between the taper and the waveguide .	45
3.5	Device design	45
3.6	Fabrication Process Flow	46
3.7	Scanning Electron Microscope Image of the fabricated sample	48
3.8	Image processing of the SEM picture of the silicon OMC	49
3.9	Room temperature characterization setup	50
3.10	Optical characterization of the OMC	50
3.11	OMCs of different external coupling rates	51
3.12	Coherent Response Measurement	52
3.13	Optomechanical Induced Transparency of different pumping powers	52
3.14	Incoherent noise spectrum from heterodyne detection	53
3.15	Noise spectrum of balanced heterodyne detection in room temperature side- band cooling at different pumping powers	54
3.16	Effective mechanical damping rate at different intracavity photon number for sideband cooling at room temperature	55
3.17	Final phonon occupancy at different intracavity photon numbers for sideband cooling at room temperature	56
3.18	Design of Heliox TL Cryostat	57

List of Figures

3.19 Preparation of the Cryohead	58
3.20 Optical resonant wavelength of OMC versus the cryostat temperature	60
3.21 Laser power induced heating of the mechanical mode	61
3.22 Sideband cooling of the nanomechanical oscillator	62
3.23 Signal-to-noise ratio (SNR) vs. the cooperativity C	62
3.24 Effect of the buffer ^3He gas on sideband cooling performance	63
3.25 Optical resonant wavelength and mechanical frequency below 4K	64
3.26 Mechanical damping rate below 4K	66
4.1 Optomechanical crystal and experimental setup	69
4.2 Artificial and quantum sideband asymmetry in optomechanical sideband cooling	71
4.3 Observation of asymmetric noise spectra due to Kerr-type nonlinearity	74
4.4 An illustration of the infinite array of coupled Fourier modes	78
4.5 Cavity frequency response measurement	81
4.6 Cavity frequency response at different pressures	82
5.1 Scheme for Backaction-evading measurement	87
5.2 Experimental observation of backaction-evasion	90
5.3 Effect of probe power on quantum backaction and optical absorption heating .	91
6.1 Pumping scheme leading to two-tone instability	95
6.2 Experimental observation of two-tone instability	96
6.3 Two-tone instability in the optical domain	97
6.4 Domains of two-tone instability	100
6.5 Instability domains from eigenvalue analysis	101
6.6 Experimental observation of two-tone instability in microwave domain	103
6.7 Investigation of the two-tone instability in a circuit-electromechanical system .	104
6.8 Vanishing of the effective mechanical frequency	105
7.1 Optomechanical crystal and experimental scheme	109
7.2 Experimental setup	110
7.3 Coherent optomechanical spectroscopy	112
7.4 Incoherent noise spectrum from heterodyne detection	113
7.5 Fitting of the incoherent noise spectrum	114
7.6 Ancillary Quantum Thermometry for power-sweep and detuning-sweep mea- surements	115

7.7	Detuning dependence of quantum back-action in the two-tone ancillary quantum thermometry	116
7.8	Power dependence of sideband cooling	117
7.9	Mechanical Linewidth in the single-tone power-sweep measurements	118
7.10	Final occupancy versus the cooling tone intracavity photon number	119
7.11	Detuning dependence of the sideband cooling	120
7.12	Final occupancy versus the cooling tone detuning in single-tone measurements	121
7.13	Noise floor vs. reflected power in single-tone power-sweep measurements . . .	123
7.14	Recent advancement in laser cooling of mechanical resonators in various platforms	124
8.1	Experimental observation of mechanical squeezing	131
B.1	Pattern for the etching test	144
B.2	Etching Test Result	147
B.3	Graphical user interface for the image processing	149
C.1	Simplified setup for optical coherent response measurements	152
C.2	Coherent response determination of detuning and linewidth	153
C.3	Simplified setup for Balanced Heterodyne Detection	155
D.1	Measurement Setup for the phase noise measurement with a filter cavity	159
D.2	Noise spectrum of the transduced phase noise around 5.3GHz	160
D.3	Calibrated frequency noise spectral density of ECDL	161
D.4	Sideband cooling of OMC with two different lasers with and without a filter cavity	162
D.5	Simplified setup for noise analysis with balanced heterodyne detection	163
D.6	Observed excess noise in the balanced heterodyne detection with different local oscillators	164
E.1	Optical cavity linewidth vs. the intracavity photon number from the coherent response measurement	167
E.2	Final phonon occupancy vs. the intracavity photon number	168

1 Introduction

"No elementary quantum phenomenon is a phenomenon until it is a recorded phenomenon."

John Archibald Wheeler

1.1 Quantum Measurement

1.1.1 Heisenberg Uncertainty Principle

The field of quantum physics starts from Max Planck's solution to the black-body radiation problem in 1900 and Einstein's explanation on the photoelectric effect in 1905 [1]. Over the last century, quantum mechanics has witnessed great success in explanation of the behaviors and interactions of particles at atomic and sub-atomic scales, establishing the foundation of atomic physics, condensed matter physics, nuclear physics and particle physics, and has also revolutionized the modern science and technology, such as the laser, semiconductors, quantum information and etc. Despite the empirical success of quantum physics, the question how the measurement is affecting the quantum system remains extensive discussions [2–7], including debates on philosophical level and the interpretations of quantum mechanics.

In the early days of quantum physics, lots of gedanken experiments were proposed to understand the measurements on single quantum object, such as Heisenberg's microscope and von Neumann's Doppler speed meter. To give an example, we show the original thought experiment proposed by Heisenberg drafted in his lecture, "The physical principles of the

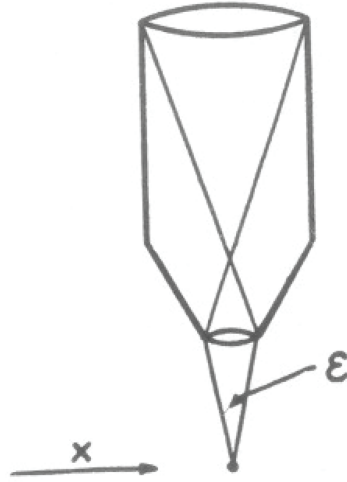


Figure 1.1 – **Scheme of the Heisenberg microscope.**

quantum theory", in 1929 at Chicago. The example shows the destruction of the knowledge of a particle's momentum by an apparatus determining its position using a microscope. As shown in Fig. 1.1, a particle, such as an electron, moves at a distance x from the microscope. The cone of rays of wavelength λ scatter from it through the objective with angular opening ϵ . According to the optical diffraction limit, the resolution for the position is given by,

$$\Delta x = \frac{\lambda}{\sin \epsilon}. \quad (1.1)$$

During the measurement, photons are scattered from the electron and pass through the microscope. The electron receives a Compton recoil from the photon of a magnitude h/λ . The recoil cannot be exactly known, as the direction of the scattered photon is undetermined within the bundle of rays entering the microscope. The uncertainty of the recoil in the x -direction is given by,

$$\Delta p_x \sim \frac{h}{\lambda} \sin \epsilon. \quad (1.2)$$

Thus the particle motion after the measurement is $\Delta x \cdot \Delta p_x \sim h$.

This simple gedanken experiment shows the fundamental property of the process of measurement, even in a completely classical system. The position uncertainty is due to the measurement error when extracting information from the measurement quantity. An inevitable perturbation of the momentum arises due to the measurement process. This is however different from the mathematical formulation of the Heisenberg inequality relating

the standard deviation of position Δx and the standard deviation of momentum Δp ,

$$\Delta x \cdot \Delta p \geq \frac{\hbar}{2}, \quad (1.3)$$

which demonstrates the fundamental property of the quantum system, with position and momentum as two interchangeable observable [2, 8]. This demonstrates the intrinsic inability of measuring position and momentum simultaneously with ultra-precision of a quantum object, independent of how the quantum state of the object is prepared.

1.1.2 Standard Quantum Limit

Due to the Heisenberg uncertainty principle, any attempt to extract information from a quantum object would inevitably perturb it in an unpredictable way, such as the position measurement in the Heisenberg's microscope. The prompt consequence of this unavoidable stochastic perturbation is that the outcomes of the subsequent measurement can be affected by the measurement process. However, in the early days, experiments were focused on interactions of ensembles of photons with ensembles of atoms, and electrons. Little attention was paid from the theory side to the features of quantum mechanics beyond the ensembles of experiments, especially the phenomena associated with measurements of single objects.

"Fundamentally, the reason for this irrelevance of the quantum theory of measurement was technological. The technology of 1940-1980 was not capable of making repetitive measurements on a single quantum mechanical system and thereby discovering in a second measurement how a first measurement had affected the system.", Kip Thorne [9].

In the 1960s, spatial and temporal coherent electromagnetic waves through amplification by stimulated emission in microwave frequency (Maser) [10] and optical frequency (Laser) [11] were demonstrated. Meanwhile, the quantum theory can be applied to the electromagnetic field, where light is described in terms of field operators for photon creation and annihilation. Light also shows different statistical properties, such as coherent light and squeezed light [12–18]. The quantum description of light-matter interaction has been developed since then, which results in the explosion of the field of quantum optics. Most importantly, this allows continuous repeated measurements of a single quantum system and stimulates the development of quantum measurement theory [19–23].

According to Heisenberg uncertainty, measurement of a single quantum object depends on one's a priori information about the state of the measured object and leads to unavoidable

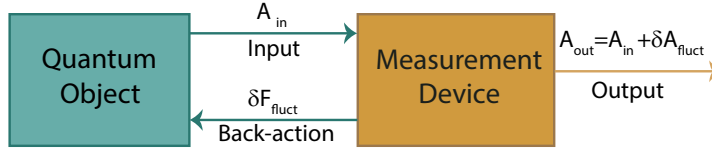


Figure 1.2 – **Scheme of a continuous linear measurement.**

back-action of the measuring device, as shown in Fig. 1.2. The measurement of the quantum object results in an input A_{in} to the measurement device, which imprints back-action "force" δF_{fluct} on the quantum object. For such a continuous linear measurement, the measurement output is given by $A_{\text{out}} = A_{\text{in}} + \delta A_{\text{fluct}}$, where δA_{fluct} is due to the measurement back-action.

This raises one question, what are the accuracy of measurements and the quantum limits in such measurements? Discussions around this range from generalized quantum operators measurements [24], time-energy uncertainty [19], to quantum linear amplifiers [20]. The main impetus for the quantum analysis of single object measurement actually comes from gravitational waves detection [25]. The first people to consider interferometers for gravitational waves detection were M. Gerstenshtein, V. I. Pustovoit [26] and Joseph Weber. The working principle was later analyzed by Weiss [27]. Figure 1.3 shows one gravitational wave detector in Hanford, Washington, from the Laser Interferometer Gravitational-Wave Observatory (LIGO). It has two long ($\sim 4\text{ km}$) perpendicular arms where kilogram-scale mirrors are suspended at each end [28]. Laser light is used to measure the distance of both arms with a target displacement sensitivity $\delta x \sim 10^{-19}$ centimeter for the gravitational wave detection with time intervals between measurements ($\tau < 10^{-3}\text{ s}$).

To observe the gravitational wave, ultra-sensitive displacement of the test mirrors are required. Here we give a simple example on the position measurement of a free test mass. Assuming at time $t = 0$, we measure the particle's position with an error Δx_0 over a duration τ , such as in the Heisenberg microscope. The corresponding perturbation of the momentum is given by,

$$\Delta P_0 = \frac{\hbar}{2\Delta x_0}. \quad (1.4)$$

At the time τ , the momentum perturbation will lead to an additional uncertainty in the position of the particle,

$$\Delta x_{\text{add}} = \frac{\Delta P_0 \tau}{m} = \frac{\hbar \tau}{2m\Delta x_0}, \quad (1.5)$$

where m is the mass. This increases the position measurement error at the second measure-

ment. The inferred momentum from the two measurements is given by

$$P = m \frac{x_\tau - x_0}{\tau}, \quad (1.6)$$

which leads to the momentum error

$$\Delta P = \frac{m}{\tau} \sqrt{[(\Delta x_0)^2 + (\Delta x_\tau)^2 + (\Delta x_{\text{add}})^2]}, \quad (1.7)$$

where Δx_τ is the position measurement error at time τ . To achieve lowest uncertainty for the inferred momentum, Δx_0 can not be made arbitrarily small, as the added noise Δx_{add} will increase accordingly. The optimal position uncertainty is given by $\Delta x_0 = \sqrt{\frac{\hbar \tau}{2m}}$, where $\Delta x_0 = \Delta x_{\text{add}}$. The resulting optimal accuracy for the inferred momentum is obtained at,

$$\Delta P_0 = \Delta P_{\text{SQL}} = \sqrt{\frac{\hbar m}{2\tau}}. \quad (1.8)$$

Similarly, the minimum possible uncertainty for a position measurement is obtained at,

$$\Delta x_0 = \Delta x_{\text{SQL}} = \sqrt{\frac{\hbar \tau}{2m}}. \quad (1.9)$$

For a harmonic oscillator, such as the test mirror in LIGO, the minimum uncertainty for position and momentum for the measurement occurs at,

$$\begin{aligned} \Delta x_0 = \Delta x_{\text{SQL}} &= \sqrt{\frac{\hbar}{2m\Omega_m}} \\ \Delta P_0 = \Delta P_{\text{SQL}} &= \sqrt{\frac{\hbar m \Omega_m}{2}}, \end{aligned} \quad (1.10)$$

where Ω_m is the mechanical frequency. Δx_{SQL} and ΔP_{SQL} are the standard quantum limits (SQL) of a harmonic oscillator.

Quantum effects are known to take place at atomic scales, while they don't seem to appear in the world of large experimental apparatuses like LIGO. One of Braginsky's most important contributions to the gravitational wave detection is to consider the interferometer as a quantum system [25, 29]. Such standard quantum limit has been obtained to figure out the fundamental quantum limits in the context of gravitational wave detection, which arises from the photon-counting statistics against the disturbance of the end mirrors' positions produced by radiation pressure fluctuation. By increasing the laser power, or the mean photon number



Figure 1.3 – **The Laser Interferometer Gravitational-Wave Observatory (LIGO) near Hanford, Washington, U.S.** Credit: Caltech/MIT/LIGO Lab

(N), the resulting uncertainty for the phase is $\sim N^{-1/2}$. However, the fluctuations in the laser power also produce stochastic radiation-pressure forces on the mirror. *If the fluctuations in the two arms are uncorrelated*, the total uncertainty in the displacement measurement given by the SQL occurs at an optimal power [30],

$$P_{\text{opt}} \sim \frac{1}{2} (mc^2/\tau) (1/\omega\tau) (1/b^2), \quad (1.11)$$

where m is the mirror mass, ω is the optical angular frequency and b is the number of reflections at each end mirror.

However, the argument here assumes that the laser-power fluctuations in the two arms are *uncorrelated*. This however implies that the beam splitter in the interferometer splits the incident fluctuations unequally. In 1980, Carlton Caves solved this controversy, where he found that, "*There is a fluctuating radiation pressure force which drives p . However, it has nothing to do with fluctuations in laser power; rather, it is an intrinsic property of a standard interferometer.*" [30]. It is due to the inevitable vacuum fluctuations that enters the interferometric setup, which is superposed on the light from the laser.

1.1.3 Quantum Non-Demolition Measurement

Along with the efforts to construct better detectors for gravitational waves, new methods for ultra-precise interferometric displacement measurements have been explored to approach and even surpass the SQL, such as the quantum non-demolition (QND) methods [31–33].

The earliest proposal of the QND measurement is from Braginsky in 1974 with pioneering idea of performing a nondestructive recording of the *energy state* of an oscillator [25], later analyzed by Unhur [34]. Despite the theoretical possibility, such schemes are rather challenging as they

require direct measurements of the oscillator energy (number of quanta \hat{N}), via quadratic coupling to the displacement of the harmonic oscillator.

Thorne et al. at the same time, proposed an alternative approach to surpass the SQL in the displacement measurement [35], by measuring the quadratures \hat{X}_1 and \hat{X}_2 , which are the canonically conjugate observables of a quantum harmonic oscillator, i.e. $[\hat{X}_1, \hat{X}_2] = i$. In a standard displacement measurement, the two quadratures are typically measured simultaneously with an equal precision. The Heisenberg uncertainty limits the quadrature precision to the zero-point fluctuation. To achieve the quantum non-demolition measurement, one can simply measure \hat{X}_1 , while giving up all the information about the other quadrature \hat{X}_2 and the energy quanta \hat{N} . We can construct a linearly coupled system with interaction Hamiltonian,

$$\hat{H}_I = K \hat{X}_1 \hat{M} = K / \sqrt{2} x_{\text{zpf}} \left(\hat{x} \hat{M} \cos \Omega_m t - \frac{\hat{p}}{m \Omega_m} \hat{M} \sin \Omega_m t \right), \quad (1.12)$$

where \hat{M} is the measurement apparatus and K is a coupling constant between the measurement apparatus and quadrature \hat{X}_1 . In the Heisenberg picture, the dynamical time evolution of \hat{X}_1 and \hat{X}_2 is given by,

$$\begin{aligned} d\hat{X}_1/dt &= 0 \\ d\hat{X}_2/dt &= -K\hat{M}. \end{aligned} \quad (1.13)$$

We see that the measurement only perturbs \hat{X}_2 with \hat{X}_1 unaffected.

Following this idea, different methods are proposed. For example, a "pulsed" measurement of \hat{X}_1 can be implemented by coupling to \hat{x} at times $\Omega_m t = n\pi$. The measurement of the displacement \hat{x} at $\Omega_m t = 0$ produces a random kick to \hat{p} . Despite the unknown perturbation of \hat{p} , \hat{x} returns to the position of the initial value at the time when $\Omega_m t = n\pi$. In this way, the subsequent measurement of \hat{x} can be followed to obtain the arbitrarily high measurement precision. Such measurement strategy is later called *stroboscopic back-action evading measurement*.

Alternatively, one can measure \hat{X}_1 continuously by coupling the displacement \hat{x} to the measurement apparatus with a periodic coupling strength, which results in the Hamiltonian,

$$\begin{aligned} \hat{H}_I &= K \cos \Omega_m t \frac{\hat{x}}{2\sqrt{x_{\text{zpf}}}} \hat{M} \\ &= \frac{K}{2} \hat{M} (\hat{X}_1 + \hat{X}_1 \cos 2\Omega_m t + \hat{X}_2 \sin 2\Omega_m t) \end{aligned} \quad (1.14)$$

In a time-averaged sense, we see that the measurement apparatus \hat{M} is only coupled to the \hat{X}_1 quadrature. In principle, there is still a back-action due to the coupling to \hat{X}_2 . To achieve QND measurement of \hat{X}_1 , the system has to be free from frequency components near $\pm 2\Omega_m$. This results in a *near-nondemolition measurement*. In this method, the periodic coupling strength can be simply realized by driving the mechanical oscillator with two different frequencies separated by twice the mechanical frequency. Such continuous QND measurement is also referred as *two-tone back-action evading measurement*. A full quantum treatment of the scheme is analyzed in detail by Clerk [36] in the context of quantum optomechanics.

QND measurements can be constructed in a way that the interaction results in a system Hamiltonian that commutes with the observable. Such observable is typically called the QND observable, which makes QND measurements one of the most fundamental type of quantum measurements free from measurement back-action. Successful QND measurements have been achieved in a wide range of systems [37, 38], ranging from the photon counting in Kerr media, dispersive readout in cavity and circuit QED systems and etc [39, 40].

Despite the pioneering theoretical quantum analysis of QND displacement measurements, the experimental realization in the optical interferometer still remains elusive. This is primarily due to the emerging technical challenges such as the extraneous noises and instabilities at required high circulating optical powers [41]. That being said, table-top experiments with displacement measurements at the standard quantum limit can be extremely valuable.

1.2 Cavity Optomechanics

Mechanical motion can be measured by coupling to various degrees of freedoms. The radiation pressure from the momentum exchange between the electromagnetic field and the mechanical object can be utilized for such a purpose, such as in LIGO. Originally conceived in the context of gravitational wave detection, such radiation pressure coupling was firstly investigated by Braginsky in 1970 [42]. This leads to an emerging field - cavity quantum optomechanics [43].

Tremendous efforts have made on theory side focusing on the quantum measurement of mechanical motion from different aspects [44], such as ponderomotive squeezing [45], QND measurement [46] and more interestingly non-classical state generation [47]. Quantum measurement of the mechanical motion was precluded in the early days mainly due to the rather weak optomechanical coupling and the large thermal decoherence. Feedback cooling with large-scale mirrors using radiation pressure was firstly demonstrated by Heidman in 1999 [48], which was later pushed to much lower temperatures. The advancement in the nanofabrication

has enabled the quest for systems at micro- and nano scale, where the optomechanical interactions are enhanced significantly. This ranges from optomechanical crystals [49], membranes [50], microdisks [51], to superconducting microwave electromechanical circuits [52], with the mass of the mechanical oscillators ranging from pg to kg [43].

The parametric amplification of the mechanical motion using radiation pressure was discovered in optical micro-toroid in 2005, where the optical modes are coupled to the co-located mechanical modes [53]. On the other hand, laser cooling of the mechanical motion to the quantum ground state was developed theoretically and experimentally [54–57]. Reduction of the thermal noise typically requires precooling the mechanical oscillator under cryogenic environment. The first demonstrated dynamic back-action cooling was in the Doppler regime by Aspelmeyer, Kippenberg and Heidman [54, 58, 59]. The ground state preparation of the mechanical motion with electromagnetic field was demonstrated by Painter and Teufel at 2011 [60, 61].

To approach the quantum limit for displacement measurements, the primary requirement is the strong probing of the mechanical motion, to decrease the measurement imprecision. Measurements with imprecision at and below the SQL were demonstrated in the microwave and optical domain [52, 62].

When the thermal noise and the imprecision noise are eliminated to certain level, the observation of radiation pressure shot noise became possible [63–66]. Motional sideband thermometry, a signature of quantum-mechanical nature of optomechanical coupling, has become feasible. The zero-point motion of mechanical motion was observed from the motional sideband asymmetry in the Painter group [67]. Quantum correlation between the imprecision and the quantum back-action was adopted in a wide range of experiments, from the motional sideband asymmetry to the ponderomotive squeezing of optical light [67–73]. Sensitivities approaching the SQL have been demonstrated [66, 74–76].

In Fig. 1.4, the displacement measurement sensitivity compared to the zero-point fluctuation at the mechanical frequency $\bar{S}_{xx}(\Omega_m)/\bar{S}_{xx}^{zpf}(\Omega_m)$ is shown versus the probing strength $4C$, where C is the optomechanical cooperativity. The dashed blue curve corresponds to the imprecision noise, which is inversely proportional to the pumping power. The dashed green curve corresponds to the quantum back-action, which scales linearly with the pumping power. The black dashed curve corresponds to the standard quantum limit. On top of this is the thermal noise, which is shown in dashed purple curve. This leads to the total noise, as shown in the black curve.

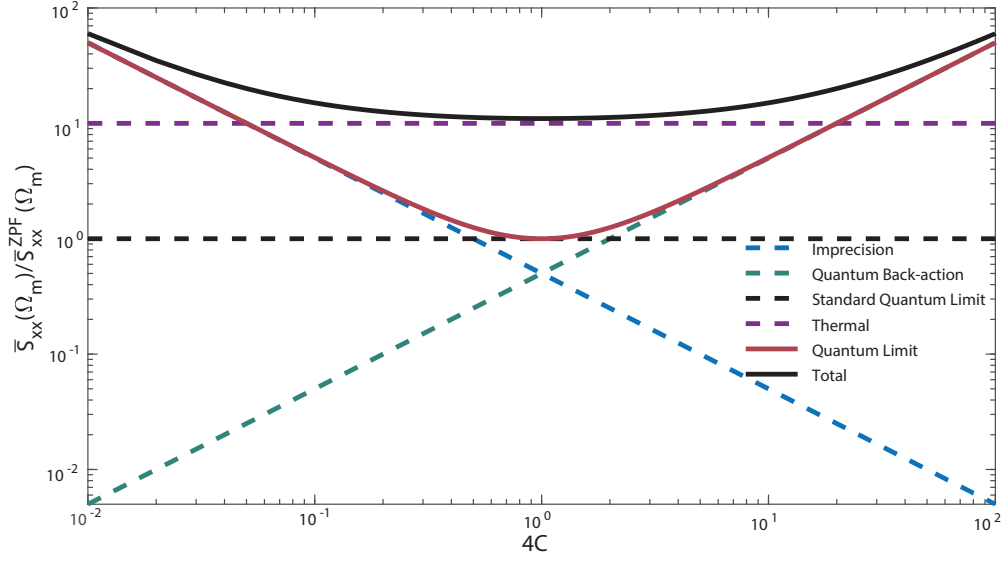


Figure 1.4 – **Displacement measurement sensitivity vs. the probing strength.** The displacement measurement sensitivity is compared to the zero-point fluctuation at the mechanical frequency $\bar{S}_{xx}(\Omega_m)/\bar{S}_{xx}^{zpf}(\Omega_m)$. The probing strength is shown as the $4C$, where C is the optomechanical cooperativity.

Back-action evading measurement of the mechanical motion was attempted by driving the electromechanical microwave circuits with injected excess classical noise in the pumping tones in the Schwab group [77]. In this case, the cancelled back-action comes from the classical noise. The first quantum back-action evading measurement was demonstrated later in the same group in 2015 [78], despite various technical challenges, such as thermal effects and two-level-system defects [79, 80]. Since then, BAE has been established as standard measurement technique in the microwave domain, which immediately enabled the observation of the squeezing of mechanical motion below the zero-point energy using reservoir engineering techniques in the group of Schwab, Teufel and Sillanpää [81–85]. However, due to the use of non-quantum-limited amplifier for the microwave signal, sub-SQL measurements with QND techniques still remain elusive because of the large imprecision noise and excess microwave noise. For this reason, quantum-limited amplifiers, such as Josephson parametric amplifier (JPA) or Travelling wave parametric amplifier (TWPA), need to be used.

On the other hand, continuous displacement measurements approaching the SQL on the optical side remain rather silent, primarily due to the large optical absorption in a wide range of optomechanical platforms. Recent advancements with SiN membranes enable laser cooling to the quantum back-action limit and high fidelity feedback cooling in the Doppler regime, where the residual thermal energy is comparable to the zero-point energy [76, 86]. Varia-

tional measurements techniques [87, 88], have been implemented to perform displacement measurements close to the SQL, utilizing the quantum correlations between the measurement imprecision and quantum back-action [89, 90]. Until now, sub-SQL measurements with two-tone BAE measurements also remain elusive.

Despite the extremely large thermal decoherence at room temperature, several optomechanical experiments have been able to explore the quantum correlation between the measurement imprecision and quantum back-action [91, 92]. The correlations may be used to erase back-action from an interferometric measurement of the mirror's position, using variational measurement techniques [87, 88]. This can also be utilized for a self-calibrated quantum thermometer even at room temperature [91]. More recently, quantum back-action noise comparable to the thermal noise has been observed at audio band of a high-reflectivity single-crystal microresonator [93]. Such platform provides a testbed for studying techniques for quantum back-action mitigation, to improve the sensitivity for future LIGO upgrade. Successful gravitational wave detections in the last years have urged for improved measurement sensitivity for both LIGO and Virgo [41]. For example, the squeezed vacuum are planned in the advanced LIGO upgrade to improve the sensitivity [94].

Cavity optomechanics over the last decade has witnessed significant advances in the quantum measurements of mechanical motion and has made it possible to explore the quantum limits of displacement measurement in table top experiments [43]. On a fundamental level, such studies enable testing quantum mechanics on a macroscopic scale, due to the ability to place the engineered mechanical oscillators into the quantum regime [95]. Non-classical states of mechanical motion have been generated, such as the single phonon Fock state [96] and mechanical entangled states [97]. Beyond offering manipulation and control over mechanical degrees of freedom, quantum optomechanics has also brought new technological advances [98–100]. Mechanical systems are realized as ideal transducers for electrical field, magnetic field, optical signal, and microwave to the optical frequency conversion, in both classical and quantum regime [101–104].

1.3 Overview of the Thesis

This thesis studies the quantum measurements of mechanical motion close to the standard quantum limit. Chapter 2 reviews the theoretical basis concerning the quantum measurements of mechanical motion. Chapter 3 goes through the details of the experimental system, including the design and the fabrication of the Optomechanical Crystal, the cryogenic setup

Chapter 1. Introduction

and the measurement scheme. The experimental results of this thesis are discussed in Chapter 4-8. Chapter 4 discusses about the Floquet dynamics in the motional sideband asymmetry measurements. Chapter 5 discusses about the back-action evading measurement of the mechanical motion in the optical domain. Chapter 6 discusses about the two-tone instability and its fundamental implications for back-action evading measurements. Chapter 7 discusses about the laser sideband cooling of a nanomechanical oscillator to its zero-point energy. Chapter 8 discusses about the quantum mechanical squeezing of mechanical motion with laser light. Finally, Chapter 9 summarizes the results of this thesis and gives an outlook for the potential experiments.

2 Theory

Cavity optomechanics studies the interaction between the mechanical motion and electromagnetic field due to radiation pressure in a micro-cavity. A full quantum treatment of the harmonic oscillator and the optical cavity field and the interaction between them are presented in this chapter. We will present an overall introduction of quantum optomechanical measurement theory, where the dynamics, quantum control and measurement of mechanical motion are discussed.

2.1 Input-output theory

Before we look into the interaction between the mechanical motion and the electromagnetic field, we firstly start with the quantum treatment of the field dissipation where both the mechanical motion and the light field experience energy decay to the environment. Such quantum treatment was developed by Gardiner and Collett, which results in bath-induced dissipation and noise fluctuations [105].

We consider a bosonic harmonic oscillator with frequency ω_A and annihilation operator \hat{A} , such as a mechanical oscillator or an optical cavity. One can start from writing down the total Hamiltonian,

$$\hat{H}_{\text{tot}} = \hat{H}_{\text{sys}} + \hat{H}_{\text{bath}} + \hat{H}_{\text{int}}. \quad (2.1)$$

The system Hamiltonian \hat{H}_{sys} is given by,

$$\hat{H}_{\text{sys}} = \hbar\omega_A \hat{A}^\dagger \hat{A}, \quad (2.2)$$

Chapter 2. Theory

and Hamiltonian of the bosonic continuum bath is given by,

$$\hat{H}_{\text{bath}} = \sum_j \hbar \omega_j \hat{B}_j^\dagger \hat{B}_j, \quad (2.3)$$

where \hat{B}_j and \hat{B}_j^\dagger are the annihilation and the creation operators of the j -th bosonic mode of the bath, which satisfies $[\hat{B}_j, \hat{B}_{j'}^\dagger] = \delta_{j,j'}$.

The linear coupling between the system and the bath takes the form,

$$\hat{H}_{\text{int}} = -i\hbar \sum_j \left[g_j \hat{A}^\dagger \hat{B}_j - g_j^* \hat{A} \hat{B}_j^\dagger \right], \quad (2.4)$$

where g_j corresponds to the linear coupling rate between the j -th bosonic mode and the bosonic harmonic oscillator.

In the Heisenberg picture, the equations of motion for the system and bath operators can be calculated accordingly,

$$\begin{aligned} \frac{d\hat{A}(t)}{dt} &= -i\omega_A \hat{A}(t) - \sum_j g_j \hat{B}_j \\ \frac{d\hat{B}_j(t)}{dt} &= -i\omega_j \hat{B}_j(t) + g_j \hat{A}(t). \end{aligned} \quad (2.5)$$

To eliminate the bath modes, we take the Markovian approximation and assume the coupling is frequency independent for the different bath modes,

$$\sum_j |g_j|^2 e^{-i(\omega_j - \omega_A)(t-t')} = \gamma \delta(t-t'), \quad (2.6)$$

where $\gamma = 2\pi|g|^2\rho$ depends on the density of state of the bath modes ρ .

We thus obtain the quantum Langevin equations for the field of the harmonic oscillator,

$$\dot{\hat{A}} = \frac{i}{\hbar} [\hat{H}_{\text{sys}}, \hat{A}] - \frac{\gamma}{2} \hat{A} + \sqrt{\gamma} \hat{A}_{\text{in}}(t), \quad (2.7)$$

where we introduce the input and output field operators,

$$\begin{aligned} \hat{A}_{\text{in}}(t) &= -\frac{1}{\sqrt{\gamma}} \sum_j \hat{B}_j(t_0) e^{-i\omega_j(t-t_0)} \\ \hat{A}_{\text{out}}(t) &= -\frac{1}{\sqrt{\gamma}} \sum_j \hat{B}_j(t_1) e^{-i\omega_j(t-t_1)}. \end{aligned} \quad (2.8)$$

which depends on the initial condition $\hat{B}_j(t_0)$ and final condition $\hat{B}_j(t_1)$. The input and output fields satisfy the commutation relations,

$$\begin{aligned} [\hat{A}_{\text{in}}(t), \hat{A}_{\text{in}}^\dagger(t')] &= \delta(t - t') \\ [\hat{A}_{\text{out}}(t), \hat{A}_{\text{out}}^\dagger(t')] &= \delta(t - t'). \end{aligned} \quad (2.9)$$

This results in the input-output relation,

$$\hat{A}_{\text{out}}(t) = \hat{A}_{\text{in}}(t) - \sqrt{\gamma} \hat{A}(t). \quad (2.10)$$

When the bath is in thermal equilibrium, there is

$$\langle \hat{A}_{\text{in}}(t) \hat{A}_{\text{in}}^\dagger(t') \rangle = \bar{n}_{\text{th}}^A(\omega_A) \delta(t - t'), \quad (2.11)$$

where

$$\bar{n}_{\text{th}}^A(\omega_A) = \frac{1}{\exp\left(\frac{\hbar\omega_A}{k_B T}\right) - 1}, \quad (2.12)$$

where ω_A is the angular frequency of the specific field, k_B is the Boltzman constant and T is the reservoir temperature. Such dissipation theorem applies to both the mechanical motion and the electromagnetic field. For optical light, the frequency is typically $\sim 10^{14}$ Hz, which means that the light is "cold" in its ground state even at room temperature. For microwave light, the frequency is typically \sim GHz, which has residual thermal occupation even at cryogenic temperatures. For the mechanical oscillator, the thermal occupation is much higher due to the typically lower frequency.

2.2 The Quantum Harmonic Oscillator

We now consider a quantum harmonic oscillator with mass m , spring constant k and angular frequency Ω_m . The Hamiltonian of the harmonic oscillator is given by,

$$\hat{H} = \frac{\hat{p}^2}{2m} + \frac{1}{2} k \hat{x}^2 = \frac{\hat{p}^2}{2m} + \frac{1}{2} m \Omega_m^2 \hat{x}^2. \quad (2.13)$$

The \hat{x} and \hat{p} here are the quantum mechanical operators for the displacement and the momentum, which satisfy the following canonical commutation relation,

$$[\hat{x}, \hat{p}] = i\hbar. \quad (2.14)$$

Chapter 2. Theory

We can define the annihilation and creation operators of the harmonic oscillator,

$$\begin{aligned}\hat{b} &= \sqrt{\frac{m\Omega_m}{2\hbar}} \left(\hat{x} + i \frac{\hat{p}}{m\Omega_m} \right) \\ \hat{b}^\dagger &= \sqrt{\frac{m\Omega_m}{2\hbar}} \left(\hat{x} - i \frac{\hat{p}}{m\Omega_m} \right),\end{aligned}\tag{2.15}$$

where $[\hat{b}, \hat{b}^\dagger] = 1$. Alternatively, the displacement and momentum operators can be expressed in terms of the annihilation and creation operators,

$$\begin{aligned}\hat{x} &= x_{\text{zpf}}(\hat{b}^\dagger + \hat{b}) \\ \hat{p} &= -im\Omega_m x_{\text{zpf}}(\hat{b} - \hat{b}^\dagger),\end{aligned}\tag{2.16}$$

where $x_{\text{zpf}} = \sqrt{\hbar/2m\Omega_m}$ is the zero-point fluctuation. The Hamiltonian can be rewritten as,

$$H = \hbar\Omega_m(\hat{b}^\dagger\hat{b} + \frac{1}{2}),\tag{2.17}$$

which results in quantized energy levels. We see that even in the ground state, the quantum harmonic oscillator still has non-zero energy $E_0 = \frac{\hbar\Omega_m}{2}$.

The equation of motion of the oscillator is given by,

$$m \frac{d^2 \hat{x}}{dt^2} + m\Gamma_m \frac{d\hat{x}}{dt} + m\Omega_m^2 \hat{x} = \delta \hat{F}_{\text{th}}.\tag{2.18}$$

The mechanical damping rate Γ_m characterizes the coupling rate between the mechanical oscillator and the thermal reservoir. We introduce the stochastic thermal force $\delta \hat{F}_{\text{th}}$, whose spectral density is given by $\tilde{S}_{FF}^{\text{th}}[\omega] \sim 2m\Gamma_m k_B T$ at high temperature limit, i.e. $k_B T \gg \hbar\Omega_m$.

We note that, for a mechanical oscillator in equilibrium with the thermal reservoir, the mean phonon occupancy is given by,

$$\bar{n}_{\text{th}} = \frac{1}{\exp\left(\frac{\hbar\Omega_m}{k_B T}\right) - 1}.\tag{2.19}$$

And p_n , i.e. the probability of the harmonic oscillator in its n -th state, takes the form,

$$p_n = \left(1 - \exp\left[-\frac{\hbar\omega}{k_B T}\right]\right) \exp\left[-\frac{\bar{n}_{\text{th}}\hbar\omega}{k_B T}\right],\tag{2.20}$$

where the ground state probability is given by $p_0 = 1/(\bar{n}_{\text{th}} + 1)$.

Alternatively, we can obtain the equation of motion for the annihilation operators \hat{b} ,

$$\frac{d\hat{b}}{dt} = -\left(i\Omega_m + \frac{\Gamma_m}{2}\right)\hat{b} + \sqrt{\Gamma_m}\delta\hat{b}_{\text{in}}(t), \quad (2.21)$$

where the noise operators associated with the input fluctuations are given by,

$$\begin{aligned} \langle \delta\hat{b}_{\text{in}}^\dagger(t)\delta\hat{b}_{\text{in}}(0) \rangle &= \bar{n}_{\text{th}}\delta(t) \\ \langle \delta\hat{b}_{\text{in}}(t)\delta\hat{b}_{\text{in}}^\dagger(0) \rangle &= (\bar{n}_{\text{th}} + 1)\delta(t). \end{aligned} \quad (2.22)$$

The Fourier transform of Eq. 2.21 gives,

$$\hat{b}(\omega) = \chi_m(\omega)\sqrt{\Gamma_m}\delta\hat{b}_{\text{in}}(\omega), \quad (2.23)$$

where we introduce the mechanical susceptibility,

$$\chi_m(\omega) = \frac{1}{\Gamma_m/2 - i(\omega - \Omega_m)}. \quad (2.24)$$

We can obtain the double-sided displacement noise spectral density,

$$\begin{aligned} S_{xx}(\omega) &= \int dt e^{i\omega t} \langle \hat{x}(t)\hat{x}(0) \rangle \\ &= x_{\text{zpf}}^2 (S_{\hat{b}^\dagger\hat{b}^\dagger}(\omega) + S_{\hat{b}\hat{b}}(\omega)) \\ &= x_{\text{zpf}}^2 |\chi_m(-\omega)|^2 \Gamma_m \bar{n}_{\text{th}} + x_{\text{zpf}}^2 |\chi_m(\omega)|^2 \Gamma_m (\bar{n}_{\text{th}} + 1). \end{aligned} \quad (2.25)$$

The double-sided noise spectrum results in different strength in the positive and negative frequency components, which is due to the vacuum fluctuation of the mechanical oscillator. Such difference indicates the different strength of releasing and absorbing mechanical energy, as the quantum harmonic oscillator cannot sustain a process where its vacuum state is annihilated. This *sideband asymmetry* provides a self-calibrated quantum thermometry of the mechanical oscillator, especially for low phonon occupation. The phonon occupancy and temperature of the mechanical oscillator can be obtained,

$$\begin{aligned} \bar{n}_{\text{th}} &= \left(\frac{S_{xx}(+\Omega_m)}{S_{xx}(-\Omega_m)} - 1 \right)^{-1} \\ T &= \frac{\hbar\Omega_m}{k_B} \left[\ln \left(\frac{S_{xx}(+\Omega_m)}{S_{xx}(-\Omega_m)} \right) \right]^{-1}. \end{aligned} \quad (2.26)$$

2.3 Optical Cavity

Here we consider the dynamics between an optical cavity coupled to a bosonic continuum bath, similar to the mechanical modes. The optical cavity are coupled to two independent bath, the internal loss at rate κ_0 and the waveguide modes at rate κ_{ex} . We can thus obtain the equation of motion for the intracavity field \hat{a} .

$$\frac{d\hat{a}}{dt} = -\left(i\omega_c + \frac{\kappa}{2}\right)\hat{a} + \sqrt{\kappa_0}\delta\hat{a}_0 + \sqrt{\kappa_{\text{ex}}}\hat{a}_{\text{in}}(t), \quad (2.27)$$

with the cavity resonant frequency ω_c and the total optical decay rate $\kappa = \kappa_0 + \kappa_{\text{ex}}$. $\delta\hat{a}_0$ corresponds to the vacuum fluctuation. The optical cavity is excited with an input field of frequency ω_L ,

$$\hat{a}_{\text{in}}(t) = (|\bar{a}_{\text{in}}| + \delta\hat{a}_{\text{in}}(t)) e^{-i\omega_L t}, \quad (2.28)$$

where \bar{a}_{in} is the mean coherent input field amplitude and $\delta\hat{a}_{\text{in}}(t)$ is the field fluctuation.

We can write the above equation in the rotating frame of the pumping laser,

$$\frac{d\hat{a}}{dt} = \left(i\Delta - \frac{\kappa}{2}\right)\hat{a} + \sqrt{\kappa_0}\delta\hat{a}_0 + \sqrt{\kappa_{\text{ex}}}\hat{a}_{\text{in}}(t), \quad (2.29)$$

where $\Delta = \omega_L - \omega_c$.

This results in the averaged intracavity field,

$$\bar{a} = \frac{\sqrt{\kappa_{\text{ex}}}}{\kappa/2 - i\Delta} |\bar{a}_{\text{in}}|, \quad (2.30)$$

and the mean intracavity photon number,

$$\bar{n}_{\text{cav}} = |\bar{a}|^2 = \frac{\kappa_{\text{ex}} |\bar{a}_{\text{in}}|^2}{\Delta^2 + (\kappa/2)^2} = \frac{4}{\kappa} \left(\frac{\kappa_{\text{ex}}/\kappa}{1 + (4\Delta^2/\kappa^2)} \right) \frac{P_{\text{in}}}{\hbar\omega_L}, \quad (2.31)$$

where P_{in} is the input power to the optical cavity.

For a single-sided cavity, such as the Optomechanical Crystal (OMC) in this thesis, the normalized reflection from the cavity takes the form,

$$R_c(\Delta) = 1 - \frac{4\eta_c(1-\eta_c)}{1 + (4\Delta^2/\kappa^2)}, \quad (2.32)$$

where the coupling efficiency of the cavity is defined by $\eta_c = \kappa_{\text{ex}}/\kappa$. When the pumping

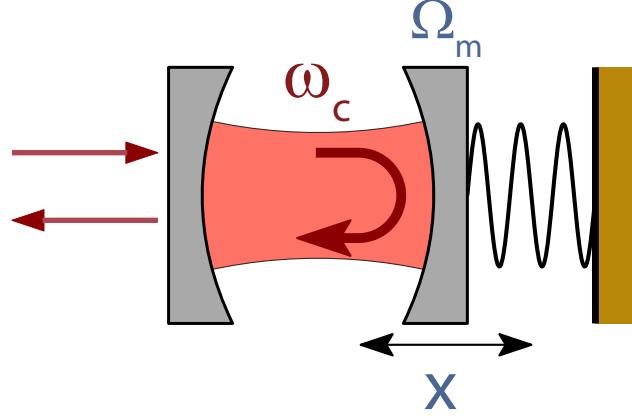


Figure 2.1 – **Schematic of a generic optomechanical system with a laser-driven optical Fabry-Pérot cavity and a vibrating end mirror.** The optical cavity has resonant frequency of ω_c , while the vibrating mirror has a vibrating frequency of Ω_m . Optical light is sent into the cavity and reflected back from one end mirror.

frequency is far off the cavity resonance, i.e. $|\Delta| \gg \kappa$, the normalized reflection approaches unity. When on resonance, the reflection is given by $R_c(0) = 1 - 4\eta_c(1 - \eta_c)$, which equals to zero when $\eta_c = 0.5$. In this case, the reflection from the cavity is completely suppressed. The Lorentzian dip in the cavity reflection can be adopted to calibrate the optical decay rate κ . The η_c however, requires additional knowledge of the coupling, where the cavity is either overcoupled or undercoupled. This can be verified by comparing different external coupling rates or via the phase response in a coherent cavity response measurement.

2.4 Quantum Optomechanics

Cavity optomechanics studies the coupling between light and mechanical motion due to radiation pressure. Such system could be intuitively described as a simple Fabry-Pérot (FP) cavity with one end mirror fixed and the other free end mirror mounted on a harmonic spring, as shown in Fig. 2.1. The cavity length is modulated by the mechanical motion x of the vibrating end mirror at its vibrational frequency Ω_m . This in turn leads to a modulation of the cavity resonance frequency ω_c and results in the dispersive coupling between the mirror vibration and the cavity field. It is useful to consider the Hamiltonian of the optomechanical system,

$$\hat{H} = \hbar\omega_c(\hat{x})\hat{a}^\dagger\hat{a} + \hbar\Omega_m\hat{b}^\dagger\hat{b}, \quad (2.33)$$

Chapter 2. Theory

where the optical cavity frequency $\omega_c(\hat{x})$ is a function of the displacement of the vibrating mirror. For small cavity frequency perturbation, we can expand the cavity frequency to the first order of the displacement,

$$\omega_c(\hat{x}) \approx \omega_c + \hat{x} \frac{\partial \omega_c}{\partial x}. \quad (2.34)$$

We can define the vacuum optomechanical coupling,

$$g_0 = \frac{d\omega_c}{dx} x_{\text{zpf}}. \quad (2.35)$$

This corresponds to the cavity frequency shift per zero-point fluctuation, where $x_{\text{zpf}} = \sqrt{\frac{\hbar}{2m_{\text{eff}}\Omega_m}}$ is the zero-point motion with m_{eff} as the effective mass. The radiation pressure force on the mirror is given by,

$$\hat{F}_{\text{rad}} = -\hbar \frac{g_0}{x_{\text{zpf}}} \hat{a}^\dagger \hat{a}, \quad (2.36)$$

which is enhanced by the intracavity photon number.

Before we proceed further, we note that other types of optomechanical couplings exist as well, such as the quadratic coupling in membrane-in-the-middle experiments [50], where the cavity frequency is shifted quadratically to the mirror displacement. The cavity linewidth can be also modulated by the mirror displacement, which is referred as dissipative coupling [106, 107]. The coupling can also arise due to the photothermal heating of the mechanical motion, i.e. the bolometric effects [108]. However, we consider only the linear dispersive coupling of the intracavity field to the mirror displacement.

We can write the Hamiltonian of the system including the driving and dissipation as,

$$\hat{H} = \hbar\omega_c \hat{a}^\dagger \hat{a} + \hbar\omega_m \hat{b}^\dagger \hat{b} + \hbar g_0 \hat{a}^\dagger \hat{a} (\hat{b} + \hat{b}^\dagger) + \hat{H}_{\text{diss}} + \hat{H}_{\text{drive}}, \quad (2.37)$$

where \hat{H}_{diss} and \hat{H}_{drive} correspond to Hamiltonian of the dissipation and the external driving.

The quantum Langevin equations can be obtained,

$$\begin{aligned} \dot{\hat{a}} &= -\left(i\omega_c + \frac{\kappa}{2}\right) \hat{a} - ig_0 (\hat{b} + \hat{b}^\dagger) \hat{a} + \sqrt{\kappa_{\text{ex}}} \hat{a}_{\text{in}}(t) + \sqrt{\kappa_0} \delta \hat{a}_{\text{vac}}(t) \\ \dot{\hat{b}} &= -\left(i\Omega_m + \frac{\Gamma_m}{2}\right) \hat{b} - ig_0 \hat{a}^\dagger \hat{a} + \sqrt{\Gamma_m} \hat{b}_{\text{in}}(t). \end{aligned} \quad (2.38)$$

Here we introduce the vacuum fluctuation field $\delta \hat{a}_{\text{vac}}(t)$ due to the internal cavity loss. We

excite the optical cavity with laser field $\hat{a}_{\text{in}}e^{-i\omega_L t}$, where ω_L is the laser frequency and \hat{a}_{in} is the input field amplitude. The input field, the intracavity field and the mirror motion can be decomposed into two components, the static and the fluctuation terms respectively,

$$\begin{aligned}\hat{a}_{\text{in}}(t) &= \bar{a}_{\text{in}} + \delta\hat{a}_{\text{in}}(t) \\ \hat{a}(t) &= \bar{a} + \delta\hat{a}(t) \\ \hat{b}(t) &= \bar{b} + \delta\hat{b}(t).\end{aligned}\tag{2.39}$$

The steady amplitude for optics and vibration can be obtained,

$$\begin{aligned}\bar{a} &\sim \frac{\sqrt{\kappa_{\text{ex}}}\bar{a}_{\text{in}}}{-i\bar{\Delta} + \kappa/2} \\ \bar{b} &= \frac{-ig_0\bar{n}_{\text{cav}}}{i\Omega_{\text{m}} + \Gamma_{\text{m}}/2},\end{aligned}\tag{2.40}$$

where $\bar{n}_{\text{cav}} = |\bar{a}|^2$ is the intracavity photon number. The resulting radiation pressure force displaces the equilibrium position of the mirror, and thus leads to a new cavity frequency $\omega_c + g_0(\bar{b} + \bar{b}^*)$, resulting in the new detuning $\bar{\Delta} = \Delta - g_0(\bar{b} + \bar{b}^*)$. We note that, for small driving field, such displacement is small compared to the cavity linewidth and can be absorbed in the laser detuning. For simplicity, we replace $\bar{\Delta}$ with Δ in the rest of this thesis.

Accordingly, we can obtain the quantum Langevin equations for the fluctuation terms for the optical and mechanical field in the rotating frame of the driving frequency,

$$\begin{aligned}\delta\dot{\hat{a}} &= \left(i\Delta - \frac{\kappa}{2}\right)\delta\hat{a} - ig\left(\delta\hat{b} + \delta\hat{b}^\dagger\right) + \sqrt{\kappa_{\text{ex}}}\delta\hat{a}_{\text{in}} + \sqrt{\kappa_0}\delta\hat{a}_{\text{vac}} \\ \delta\dot{\hat{b}} &= -\left(i\Omega_{\text{m}} + \frac{\Gamma_{\text{m}}}{2}\right)\delta\hat{b} - ig\left(\delta\hat{a}^\dagger + \delta\hat{a}\right) + \sqrt{\Gamma_{\text{m}}}\delta\hat{b}_{\text{in}},\end{aligned}\tag{2.41}$$

where we introduce the effective optomechanical coupling rate $g = g_0\sqrt{\bar{n}_{\text{cav}}}$.

The optical and mechanical noise operators satisfy the following noise correlations,

$$\begin{aligned}\langle\delta\hat{a}_{\text{in}}(t)\delta\hat{a}_{\text{in}}^\dagger(t')\rangle &= \alpha\delta(t-t') \\ \langle\delta\hat{a}_{\text{in}}^\dagger(t)\delta\hat{a}_{\text{in}}(t')\rangle &= 0 \\ \langle\delta\hat{a}_{\text{vac}}(t)\delta\hat{a}_{\text{vac}}^\dagger(t')\rangle &= \alpha\delta(t-t') \\ \langle\delta\hat{a}_{\text{vac}}^\dagger(t)\delta\hat{a}_{\text{vac}}(t')\rangle &= 0 \\ \langle\delta\hat{b}_{\text{in}}(t)\delta\hat{b}_{\text{in}}^\dagger(t')\rangle &= \bar{n}_{\text{th}}\delta(t-t') \\ \langle\delta\hat{b}_{\text{in}}^\dagger(t)\delta\hat{b}_{\text{in}}(t')\rangle &= (\bar{n}_{\text{th}} + \beta)\delta(t-t')\end{aligned}\tag{2.42}$$

Chapter 2. Theory

Here α describes the fluctuation in the optical field while β describes the zero-point fluctuation in the mechanical motion. In general, α (for a quantum limited laser) and β equal to one. A treatment of a non-quantum-limited laser is performed later in this thesis.

This set of equations can be easily solved in the Fourier domain, where we define,

$$\begin{aligned}\hat{A}[\omega] &= \int dt \hat{A}(t) e^{i\omega t} \\ \hat{A}^\dagger[\omega] &= \int dt \hat{A}^\dagger(t) e^{i\omega t} = (\hat{A}[-\omega])^\dagger.\end{aligned}\tag{2.43}$$

The quantum Langevin equations in the Fourier domain are given by,

$$\begin{aligned}\delta \hat{a}(\omega) &= \chi_c(\omega) \left(-ig \left(\delta \hat{b} + \delta \hat{b}^\dagger \right) + \sqrt{\kappa_{\text{ex}}} \delta \hat{a}_{\text{in}} + \sqrt{\kappa_0} \delta \hat{a}_{\text{vac}} \right) \\ \delta \hat{a}^\dagger(\omega) &= \chi_c^*(-\omega) \left(ig \left(\delta \hat{b} + \delta \hat{b}^\dagger \right) + \sqrt{\kappa_{\text{ex}}} \delta \hat{a}_{\text{in}}^\dagger + \sqrt{\kappa_0} \delta \hat{a}_{\text{vac}}^\dagger \right) \\ \delta \hat{b}(\omega) &= \chi_m(\omega) \left(-ig \left(\delta \hat{a}^\dagger + \delta \hat{a} \right) + \sqrt{\Gamma_m} \delta \hat{b}_{\text{in}} \right) \\ \delta \hat{b}^\dagger(\omega) &= \chi_m^*(-\omega) \left(ig \left(\delta \hat{a}^\dagger + \delta \hat{a} \right) + \sqrt{\Gamma_m} \delta \hat{b}_{\text{in}}^\dagger \right),\end{aligned}\tag{2.44}$$

where the optical and mechanical susceptibility take the form,

$$\chi_c(\omega) = \frac{1}{\kappa/2 - i(\omega + \Delta)}\tag{2.45}$$

$$\chi_m(\omega) = \frac{1}{\Gamma_m/2 - i(\omega - \Omega_m)}.\tag{2.46}$$

From Eq. 2.44, we can easily obtain the relation between field operators $D = (\delta \hat{a}, \delta \hat{a}^\dagger, \delta \hat{b}, \delta \hat{b}^\dagger)^T$ and the input noise operators $D_{\text{in}} = (\delta \hat{a}_{\text{in}}, \delta \hat{a}_{\text{in}}^\dagger, \delta \hat{a}_{\text{vac}}, \delta \hat{a}_{\text{vac}}^\dagger, \delta \hat{b}_{\text{in}}, \delta \hat{b}_{\text{in}}^\dagger)^T$, where $D = M \cdot L \cdot D_{\text{in}}$. We introduce M and L ,

$$M = \begin{pmatrix} \chi_c^{-1}(\omega) & 0 & -ig & -ig \\ 0 & [\chi_c^*(-\omega)]^{-1} & ig & ig \\ -ig & -ig & \chi_m^{-1}(\omega) & 0 \\ ig & ig & 0 & [\chi_m^*(-\omega)]^{-1} \end{pmatrix}^{-1}\tag{2.47}$$

and

$$L = \begin{pmatrix} \sqrt{\kappa_{\text{ex}}} & \sqrt{\kappa_0} & 0 & 0 & 0 & 0 \\ 0 & 0 & \sqrt{\kappa_{\text{ex}}} & \sqrt{\kappa_0} & 0 & 0 \\ 0 & 0 & 0 & 0 & \sqrt{\Gamma_m} & 0 \\ 0 & 0 & 0 & 0 & 0 & \sqrt{\Gamma_m} \end{pmatrix}.\tag{2.48}$$

Coherent response of the cavity to the input field can be obtained by the relation between of $\delta \hat{a}$ and $\delta \hat{a}_{\text{in}}$ from the matrix components ($M \cdot L$). The mirror vibration due to the radiation pressure, can result in a modified cavity response compared to the original optical susceptibility, such as in the optomechanically induced transparency [109, 110]. Such radiation pressure can also change the dynamical response of the mirror motion to the thermal noise, by modifying the damping rate and also the vibrating frequency. This can lead to the damping or heating of the vibration, where the former is called sideband cooling.

The output field $\delta \hat{a}_{\text{out}} = \delta \hat{a}_{\text{in}} - \sqrt{\kappa_{\text{ex}}} \delta \hat{a}$, can be decomposed into the sum of all the input noise operators. By far, we have shown the detailed procedure to obtain the output field with the input noises. In some cases, there can be additional noise sources, such as cavity frequency noise or laser noise, which can be incorporated accordingly. The output field can be measured accordingly through direct detection or linear detection.

Now we choose a simple example to explore the theoretical quantum limits in the displacement measurement with resonant probing, i.e. $\Delta = 0$,

$$\begin{aligned} \delta \hat{a}_{\text{out}}(\omega) &= \delta \hat{a}_{\text{in}}(\omega) - \frac{\sqrt{\eta_c \kappa}}{\kappa/2 - i\omega} \left(-i \frac{g_0}{x_{\text{zpf}}} \bar{a} \delta x(\omega) + \sqrt{\kappa_{\text{ex}}} \delta \hat{a}_{\text{in}}(\omega) + \sqrt{\kappa_0} \delta \hat{a}_{\text{vac}}(\omega) \right) \\ \delta F_{\text{rad}}(\omega) &= -\hbar \frac{g_0}{x_{\text{zpf}}} \bar{a} \left(\delta \hat{a}(\omega) + \delta \hat{a}^\dagger(\omega) \right). \end{aligned} \quad (2.49)$$

Linear measurement of the output field phase quadrature, $\delta q_{\text{out}}(\omega) = i \left(-\delta a_{\text{out}}(\omega) + \delta a_{\text{out}}^\dagger(\omega) \right)$, such as in a balanced homodyne measurement, results in the symmetrized noise spectral density [111],

$$\bar{S}_{qq}^{\text{out}}(\omega) = \frac{1}{2} \left(S_{qq}^{\text{out}}(+\omega) + S_{qq}^{\text{out}}(-\omega) \right) = 1 + \frac{4\bar{a}^2 g_0^2 \eta_c \kappa}{\omega^2 + (\kappa/2)^2} \frac{\bar{S}_{xx}(\omega)}{x_{\text{zpf}}^2}, \quad (2.50)$$

which includes a constant background due to the shot noise. This constitutes the fundamental displacement measurement imprecision,

$$\bar{S}_{xx}^{\text{im}}(\omega) = \frac{\omega^2 + (\kappa/2)^2}{4\bar{a}^2 g_0^2 \eta_c \kappa} x_{\text{zpf}}^2, \quad (2.51)$$

which is inversely proportional to the intracavity photon number and also the cavity coupling efficiency η_c . Note that we assume a lossless detection of the output field.

The force spectral density of the quantum back-action can be calculated from Eq. 2.49,

$$\bar{S}_{FF}^{\text{ba}}(\omega) = \frac{\bar{a}^2 \kappa \hbar^2}{\omega^2 + (\kappa/2)^2} \frac{g_0^2}{x_{\text{zpf}}^2}, \quad (2.52)$$

which scales linearly with the intracavity photon number.

The product of the \bar{S}_{xx}^{im} and \bar{S}_{FF}^{ba} satisfies the relation,

$$\bar{S}_{xx}^{\text{im}}(\omega) \cdot \bar{S}_{FF}^{\text{ba}}(\omega) = \frac{\hbar^2}{4\eta_c} \geq \frac{\hbar^2}{4}. \quad (2.53)$$

The total mechanical noise spectral density takes the form,

$$\bar{S}_{xx}^{\text{tot}}(\omega) = \bar{S}_{xx}^{\text{im}}(\omega) + \bar{S}_{xx}^{\text{ba}}(\omega) + \bar{S}_{xx}^{\text{th}}(\omega), \quad (2.54)$$

which includes three contributions, i.e. the measurement imprecision, quantum back-action, and thermal Brownian motion. The quantum back-action increased displacement measurement noise is given by,

$$\bar{S}_{xx}^{\text{ba}}(\omega) = \frac{\bar{S}_{FF}^{\text{ba}}(\omega)}{\left| m(\Omega_m^2 - \omega^2 - i\omega\Gamma_m) \right|^2}. \quad (2.55)$$

For simplicity, we look at the displacement spectral density at frequency of Ω_m . By choosing the proper intracavity photon number, we can minimize the total added noise, $\bar{S}_{xx}^{\text{add}}(\Omega_m) = \bar{S}_{xx}^{\text{im}}(\Omega_m) + \bar{S}_{xx}^{\text{ba}}(\Omega_m)$. The minimum added noise equals to the displacement noise of the zero-point motion,

$$\bar{S}_{xx}^{\text{add}}(\Omega_m) \geq \bar{S}_{xx}^{\text{zpf}}(\Omega_m) = \hbar / m_{\text{eff}} \Omega_m \Gamma_m, \quad (2.56)$$

which is the standard quantum limit for a displacement measurement. In addition to this, $\bar{S}_{xx}^{\text{th}}(\Omega_m) = 2\bar{n}_{\text{th}} \bar{S}_{xx}^{\text{zpf}}(\Omega_m)$ at the high temperature limit.

Displacement measurement noise spectral density versus the probing strength is given in Fig. 1.4, which shows the standard quantum limit. To decrease the measurement imprecision, strong probing of the mechanical motion is required. Over the last years, measurements with imprecision at and below the SQL were demonstrated in the microwave and optical domain [52, 62]. The quantum-back action was firstly observed in cryogenic environment [64–66] and more recently even observed at room temperature [91–93]. This opens the door to the QND

displacement measurement to surpass the SQL.

2.5 Bichromatic Optomechanics

In a simple quantum optomechanical system, the mechanical motion leads to frequency modulation of the cavity field. Such frequency modulation will naturally generate motional sidebands on both sides of the probing frequency. The scattering of the thermomechanical sidebands may have different strength due to optical cavity transduction. In the resolved sideband regime ($\Omega_m \gg \kappa$), the lower and upper motional sideband transitions allow a myriad of protocols, from sideband cooling [61, 112], state swap [101], to squeezing [81–85], and entanglement [113], by selectively driving upper and lower motional sidebands of cavity.

In this section, we will introduce the theoretical treatment for the back-action evading measurement together with schemes to perform self-calibrated quantum sideband thermometry and dissipative mechanical squeezing, which all require bichromatic pumping, close to the red and blue motional sidebands of the cavity.

The input field takes the form $\hat{a}_{\text{in}} = a_c e^{-i\omega_c t} + a_b e^{-i\omega_b t} + \delta \hat{a}_{\text{in}}$, where $a_{c(b)}$ and $\omega_{c(b)}$ are the amplitude and frequency of the cooling tone (blue probe), and $\delta \hat{a}_{\text{in}}$ corresponds to the input noise. The two tones are separated by $2(\Omega_m + \delta)$, and the mean of their frequencies is detuned from the cavity resonance by Δ . The mechanical mode is coupled to the optical field through radiation pressure.

For simplification, we transform into a rotating frame with respect to $H_0 = \hbar(\omega_c + \Delta) \hat{a}^\dagger \hat{a} + \hbar(\Omega_m + \delta) \hat{b}^\dagger \hat{b}$. We can linearize the intracavity optical field $\hat{a} \rightarrow \bar{a} + \delta \hat{a}$ and the mechanical displacement $\hat{b} \rightarrow \bar{b} + \delta \hat{b}$, where $\bar{a} = \sqrt{\bar{n}_c} e^{-i\omega_c t} + \sqrt{\bar{n}_b} e^{-i\omega_b t}$ and $\bar{n}_{b(c)}$ is the intracavity photon number due to the blue probe (cooling tone). Applying the rotating-wave approximation in the sideband-resolved regime, we can obtain the effective Hamiltonian,

$$\hat{H}_{\text{RWA}} = -\hbar \delta \hat{a}^\dagger \delta \hat{a} \Delta - \hbar \delta \hat{b}^\dagger \delta \hat{b} \delta - \hbar \left[(g_b \delta \hat{b}^\dagger + g_c \delta \hat{b}) \delta \hat{a}^\dagger + (g_c \delta \hat{b} + g_b \delta \hat{b}^\dagger) \delta \hat{a} \right], \quad (2.57)$$

where $g_b = g_0 \sqrt{\bar{n}_b}$ and $g_c = g_0 \sqrt{\bar{n}_c}$ are the enhanced coupling rates for the blue and cooling tone.

We obtain the quantum Langevin equations for the field fluctuations,

$$\begin{aligned}
 \delta \dot{\hat{a}} &= \left(i\Delta - \frac{\kappa}{2}\right) \delta \hat{a} + i(g_c \delta \hat{b} + g_b \delta \hat{b}^\dagger) + \sqrt{\kappa_{\text{ex}}} \delta \hat{a}_{\text{in}} + \sqrt{\kappa_0} \delta \hat{a}_{\text{vac}} \\
 \delta \dot{\hat{a}}^\dagger &= \left(-i\Delta - \frac{\kappa}{2}\right) \delta \hat{a}^\dagger - i(g_c \delta \hat{b}^\dagger + g_b \delta \hat{b}) + \sqrt{\kappa_{\text{ex}}} \delta \hat{a}_{\text{in}}^\dagger + \sqrt{\kappa_0} \delta \hat{a}_{\text{vac}}^\dagger \\
 \delta \dot{\hat{b}} &= \left(i\delta - \frac{\Gamma_m}{2}\right) \delta \hat{b} + i(g_c \delta \hat{a} + g_b \delta \hat{a}^\dagger) + \sqrt{\Gamma_m} \delta \hat{b}_{\text{in}} \\
 \delta \dot{\hat{b}}^\dagger &= \left(-i\delta - \frac{\Gamma_m}{2}\right) \delta \hat{b}^\dagger - i(g_c \delta \hat{a}^\dagger + g_b \delta \hat{a}) + \sqrt{\Gamma_m} \delta \hat{b}_{\text{in}}^\dagger.
 \end{aligned} \tag{2.58}$$

Here we redefine the optical and mechanical susceptibility as,

$$\begin{aligned}
 \chi_c(\omega) &= \frac{1}{\kappa/2 - i(\omega + \Delta)} \\
 \chi_m(\omega) &= \frac{1}{\Gamma_m/2 - i(\omega + \delta)}.
 \end{aligned} \tag{2.59}$$

Solving Eq. (2.58) in the Fourier domain, we obtain,

$$\begin{aligned}
 \delta \hat{a} &= \chi_c(\omega) [\sqrt{\kappa_{\text{ex}}} \delta \hat{a}_{\text{in}}(\omega) + \sqrt{\kappa_0} \delta \hat{a}_{\text{vac}}(\omega) + i g_c \delta \hat{b} + i g_b \delta \hat{b}^\dagger] \\
 \delta \hat{a}^\dagger &= \chi_c^*(-\omega) [\sqrt{\kappa_{\text{ex}}} \delta \hat{a}_{\text{in}}^\dagger(\omega) + \sqrt{\kappa_0} \delta \hat{a}_{\text{vac}}^\dagger(\omega) - i g_c \delta \hat{b}^\dagger - i g_b \delta \hat{b}] \\
 \begin{pmatrix} \delta \hat{b}(\omega) \\ \delta \hat{b}^\dagger(\omega) \end{pmatrix} &= i \frac{M(\omega)}{N(\omega)} \left[\sqrt{\kappa_{\text{ex}}} \begin{pmatrix} \delta \hat{a}_{\text{in}} \\ \delta \hat{a}_{\text{in}}^\dagger \end{pmatrix} + \sqrt{\kappa_0} \begin{pmatrix} \delta \hat{a}_{\text{vac}} \\ \delta \hat{a}_{\text{vac}}^\dagger \end{pmatrix} \right] \\
 &\quad + \frac{\sqrt{\Gamma_m}}{N(\omega)} \begin{pmatrix} \chi_m^{*-1}(-\omega) - i\Sigma^*(-\omega) & -i\Pi(\omega) \\ i\Pi(\omega) & \chi_m^{-1}(\omega) + i\Sigma(\omega) \end{pmatrix} \begin{pmatrix} \delta \hat{b}_{\text{in}} \\ \delta \hat{b}_{\text{in}}^\dagger \end{pmatrix},
 \end{aligned} \tag{2.60}$$

where

$$\begin{aligned}
 M(\omega) &= \begin{pmatrix} \chi_c(\omega) g_c (\chi_m^{*-1}(-\omega) + G^2 \chi_c^*(-\omega)) & \chi_c^*(-\omega) g_b (\chi_m^{*-1}(-\omega) + G^2 \chi_c(\omega)) \\ \chi_c(\omega) g_b (\chi_m^{-1}(\omega) + G^2 \chi_c^*(-\omega)) & \chi_c^*(-\omega) g_c (\chi_m^{-1}(\omega) + G^2 \chi_c(\omega)) \end{pmatrix} \\
 N(\omega) &= \chi_m^{-1}(\omega) \chi_m^{*-1}(-\omega) + i \chi_m^{*-1}(-\omega) \Sigma(\omega) - i \chi_m^{-1}(\omega) \Sigma^*(-\omega) + G^4 \chi_c(\omega) \chi_c^*(-\omega)
 \end{aligned} \tag{2.61}$$

and

$$\Pi(\omega) = -i g_c g_b [\chi_c(\omega) - \chi_c^*(-\omega)] \tag{2.62}$$

$$\Sigma(\omega) = -i [g_c^2 \chi_c(\omega) - g_b^2 \chi_c^*(-\omega)] \tag{2.63}$$

$$G^2 = g_c^2 - g_b^2. \tag{2.64}$$

We've now introduced the general theoretical treatment to the bichromatic pumping of the optomechanical system. In the following subsections, we will look into some specific measurement schemes.

Sideband Cooling

One of the main challenges for sub-SQL measurement is the large thermal noise. The mechanical oscillators are typically precooled under cryogenic environment. Further laser cooling techniques are developed to cool the mechanical oscillator close to the ground state [55, 56]. Here we briefly review the most simplest case, i.e. single tone sideband cooling, where $g_b = 0$, $\delta = 0$ and $\Delta = 0$. We obtain the quantum Langevin equations in the Fourier domain,

$$\begin{aligned}\chi_c^{-1}(\omega)\delta\hat{a}(\omega) &= ig_c\delta\hat{b}(\omega) + \sqrt{\kappa}\delta\hat{a}_{\text{in}}(\omega) \\ \chi_m^{-1}(\omega)\delta\hat{b}(\omega) &= ig_c\delta\hat{a}(\omega) + \sqrt{\Gamma_m}\delta\hat{b}_{\text{in}}(\omega),\end{aligned}\tag{2.65}$$

where we assume that the cavity is extremely overcoupled ($\eta_c = 1$).

The phonon annihilation operator can be expressed in terms of the input noise operators,

$$\hat{b}(\omega) = \tilde{\chi}_m(\omega) \left(\sqrt{\Gamma_m}\delta\hat{b}_{\text{in}}(\omega) + ig_c\sqrt{\kappa}\chi_c(\omega)\tilde{\chi}_m(\omega)\delta\hat{a}_{\text{in}}(\omega) \right).\tag{2.66}$$

Here we introduce the dressed mechanical susceptibility due to the dynamical back-action,

$$\tilde{\chi}_m(\omega) = \frac{\chi_m(\omega)}{1 + g_c^2\chi_c(\omega)\chi_m(\omega)},\tag{2.67}$$

In the weak coupling regime, $g_c \ll \kappa$, it can be simplified,

$$\tilde{\chi}_m(\omega) = \frac{1}{(\Gamma_m + \Gamma_{\text{opt}})/2 - i\omega},\tag{2.68}$$

with the optomechanical damping rate $\Gamma_{\text{opt}} = 4g_c^2/\kappa$. The dynamical back-action due to the radiation pressure force leads to an increased mechanical damping rate $\Gamma_{\text{tot}} = \Gamma_m + \Gamma_{\text{opt}}$.

From the mechanical noise spectrum,

$$S_{\hat{b}\hat{b}}(\omega) = \int_{-\infty}^{\infty} \frac{d\omega'}{2\pi} \langle \hat{b}^\dagger(\omega') \hat{b}(\omega) \rangle,\tag{2.69}$$

the final occupancy can be obtained,

$$\bar{n}_f = \int_{-\infty}^{\infty} \frac{d\omega}{2\pi} S_{\hat{b}\hat{b}}(\omega) = \frac{\Gamma_m \bar{n}_{\text{th}}}{\Gamma_m + \Gamma_{\text{opt}}}. \quad (2.70)$$

Dynamical back-action results in net cooling of the mechanical motion by coupling to the cold optical reservoir. We note that, the above calculation is performed with the rotating-wave approximation, where the quantum back-action limit from the cooling tone, i.e. $\kappa^2/16\Omega_m^2$, is neglected due to the large sideband resolution Ω_m/κ . Besides, the input laser is assumed to be quantum-limited, where the non-quantum-limited case is discussed in the Appendix. The excess noise in the laser leads to additional back-action heating [114].

The thermomechanical sideband can be measured by a quantum-limited linear detection, such as homodyne or heterodyne detection. In our case, due to the high mechanical frequency, we perform a balanced heterodyne detection of the output field, which is mixed with a strong local oscillator. More details on the balanced heterodyne detection is in the Appendix. The measured single-sided heterodyne noise spectrum corresponds to the symmetrized autocorrelator of the photocurrent, $S_I(\Omega) = \frac{1}{2} \int_{-\infty}^{\infty} \langle \{\hat{I}_{\text{out}}(t+t'), \hat{I}_{\text{out}}(t')\} \rangle e^{i\Omega t} dt$. When normalized to the shot noise, it is given by

$$S_I(\Omega + \Delta_{\text{LO}}) = 1 + \eta \Gamma_{\text{tot}} \frac{\bar{n}_f \Gamma_{\text{opt}}}{\Gamma_{\text{tot}}^2/4 + \Omega^2}, \quad (2.71)$$

where Δ_{LO} is the frequency difference between the LO oscillator and the cavity frequency and η is the total detection efficiency and $\Gamma_{\text{tot}} = \Gamma_m + \Gamma_{\text{opt}}$.

For simplicity, Δ_{LO} is assumed to be positive in our case. The noise spectrum consists of two parts, the shot noise floor and the thermomechanical sideband. The area of the thermomechanical sideband, $A_s = \int (S_I(\Omega) - 1) d\omega$, can be adopted for the mechanical noise thermometry,

$$\bar{n}_f = \frac{A_s / \bar{n}_c}{A_s^0 / \bar{n}_c^0} \frac{k_B T}{\hbar \Omega_m}, \quad (2.72)$$

by anchoring the mode area at the lowest power with intracavity photon number \bar{n}_c^0 , and sideband area A_s^0 . This requires that, the mechanical mode is well thermalized to the thermal reservoir at the lowest power, where the temperature can be accurately read out by a thermometer. This however can be a big issue for measurements at cryogenic temperatures, where the device thermalization is typically limited by the material properties [115] and also the cooling power of the cryostat.

Sideband Asymmetry

The mode temperature of a mechanical oscillator can be measured with self-calibrated quantum thermometry utilizing the quantum property of the harmonic oscillator. As mentioned earlier, for a quantum harmonic oscillator, the double-sided displacement noise spectral density is different for the negative and positive frequency components. For example, in Raman scattering, the Stokes and the anti-Stokes sidebands are imbalanced. Motional sideband asymmetry has been also observed in optomechanical systems [67–70]. The origin and the interpretation of such asymmetry however critically depend on how to perform the optomechanical measurement [70, 116, 117]. In a photon counting experiment, the sideband asymmetry relies on the quantum properties of the mechanical motion; while in a linear measurement such as heterodyne detection, it comes from the correlation between the measurement imprecision and the quantum back-action[70].

Here we introduce the theoretical treatment of the quantum optomechanical measurement of such sideband asymmetry in a balanced heterodyne detection. We assume a simple case of weak bichromatic balanced pumping of an optomechanical system. The two driving tones are placed symmetrically close to the red and blue sidebands with the same powers, where $g_c = g_b = g$, $\Delta = 0$. The effective Hamiltonian takes the form,

$$\hat{H}_{\text{RWA}} = -\delta\hbar\delta\hat{b}^\dagger\delta\hat{b} - \hbar g\left(\delta\hat{b}^\dagger + \delta\hat{b}\right)\left(\delta\hat{a}^\dagger + \delta\hat{a}\right). \quad (2.73)$$

We obtain the quantum Langevin equations in the Fourier domain,

$$\begin{aligned} \chi_c^{-1}(\omega)\delta\hat{a}(\omega) &= ig\delta\hat{b}(\omega) + ig\delta\hat{b}^\dagger(\omega) + \sqrt{\kappa}\delta\hat{a}_{\text{in}}(\omega) \\ \chi_m^{-1}(\omega)\delta\hat{b}(\omega) &= ig\delta\hat{a}(\omega) + ig\delta\hat{a}^\dagger(\omega) + \sqrt{\Gamma_m}\delta\hat{b}_{\text{in}}(\omega). \end{aligned} \quad (2.74)$$

We obtain the phonon annihilation operator in terms of the input noises,

$$\delta\hat{b}(\omega) = \chi_m(\omega)\left(\sqrt{\Gamma_m}\delta\hat{b}_{\text{in}}(\omega) + ig\sqrt{\kappa}\chi_c(\omega)\delta\hat{a}_{\text{in}}(\omega) + ig\sqrt{\kappa}\chi_c(\omega)\delta\hat{a}_{\text{in}}^\dagger(\omega)\right). \quad (2.75)$$

The mechanical susceptibility remains the same, due to the vanished dynamical back-action. We note that, additional quantum back-action heating is present in such bichromatic pumping scheme due to amplitude fluctuations in the pumping field. The mechanical displacement

noise spectrum can be obtained,

$$S_{xx}(\omega) = \int dt e^{i\omega t} \langle \hat{x}(t) \hat{x}(0) \rangle \quad (2.76)$$

$$= x_{\text{zpf}}^2 |\chi_m(-\omega)|^2 \Gamma_m (\bar{n}_{\text{th}} + \bar{n}_{\text{ba}}) + x_{\text{zpf}}^2 |\chi_m(\omega)|^2 \Gamma_m (\bar{n}_{\text{th}} + \bar{n}_{\text{ba}} + \beta),$$

where the $\bar{n}_{\text{ba}} = 4g^2/\kappa\Gamma_m\alpha$. In such balanced two-tone measurement ($\delta \neq 0$), the phonon occupation is increased due to the quantum back-action, i.e. $\bar{n}_f = \bar{n}_{\text{th}} + \bar{n}_{\text{ba}}$.

A linear balanced heterodyne detection of the cavity output field, results in a single-sided output noise spectrum,

$$S_I(\Omega + \Delta_{\text{LO}}) = 1 + \eta\Gamma_m |\chi_m(-\Omega)|^2 \frac{4g^2}{\kappa} \left(\bar{n}_f + \frac{\beta}{2} - \frac{\alpha}{2} \right) + \eta\Gamma_m |\chi_m(\Omega)|^2 \frac{4g^2}{\kappa} \left(\bar{n}_f + \frac{\beta}{2} + \frac{\alpha}{2} \right). \quad (2.77)$$

Here α and β correspond to the zero-fluctuation for the laser light and the mechanical motion respectively, which both equal to 1. However, this reveals the origin of the sideband asymmetry in the balanced heterodyne detection. Instead of from the quantum property of a mechanical oscillator, it is due to the quantum correlation between the measurement imprecision and quantum back-action. In the actual measurement, the two thermomechanical sidebands are separated by $2|\delta| \gg \Gamma_m$, such that there is no spectral overlap between the sidebands. Such sideband asymmetry can be adopted for self-calibration of the mechanical oscillator close to the ground state, which doesn't require the knowledge of the temperature of the thermal reservoir and the mechanical damping rate.

Sideband Cooling with Self-calibration

We have shown the theoretical treatment of single tone sideband cooling and motional sideband asymmetry. One might think of combining these two experiments, to perform a self-calibrated sideband cooling. Here we consider a two-tone pumping scheme where a strong cooling tone near the lower motional sideband is applied for sideband cooling, while an additional weaker blue probe is applied near the upper motional sideband for self-calibration. By measuring the resonantly-enhanced anti-Stokes and Stokes scattered sidebands, proportional to \bar{n}_f and $\bar{n}_f + 1$, respectively, the mean phonon occupancy of the oscillator \bar{n}_f can be determined. The mechanical susceptibility, which is modified by the radiation pressure from

the two tones, is defined as,

$$\chi_{\text{eff}}(\omega) = \frac{\chi_m^{*-1}(-\omega) - i\Sigma^*(-\omega)}{N(\omega)} \approx \frac{1}{(\Gamma_m + \Gamma_{\text{opt}})/2 - i(\omega + \delta - \delta\Omega_m)}. \quad (2.78)$$

In the weak-coupling regime ($\Gamma_{\text{opt}} \ll \kappa$), the effective damping rate of the mechanical oscillator becomes $\Gamma_{\text{eff}} = \Gamma_m + \Gamma_{\text{opt}}$, where the optomechanical damping rate (in the resolved-sideband limit) is $\Gamma_{\text{opt}} = -\Gamma_b + \Gamma_c$, and Γ_b and Γ_c take the form

$$\Gamma_{b(c)} = \bar{n}_{b(c)} g_0^2 \left(\frac{\kappa}{\kappa^2/4 + (\Delta \pm \delta)^2} \right). \quad (2.79)$$

The optical spring effect is given by

$$\delta\Omega_m = \bar{n}_b g_0^2 \left(\frac{\Delta + \delta}{\kappa^2/4 + (\Delta + \delta)^2} \right) + \bar{n}_c g_0^2 \left(\frac{\Delta - \delta}{\kappa^2/4 + (\Delta - \delta)^2} \right). \quad (2.80)$$

From the Wiener-Khinchin theorem, the two-sided mechanical displacement noise spectrum is calculated in the lab frame as

$$\begin{aligned} \frac{S_{xx}(\omega)}{x_{\text{zpf}}^2} &= S_{\hat{b}\hat{b}}(\omega) + S_{\hat{b}^\dagger\hat{b}^\dagger}(\omega) \\ &= \frac{\Gamma_m(\bar{n}_{\text{th}} + 1) + \Gamma_c}{(\omega - \Omega_{\text{eff}})^2 + \Gamma_{\text{eff}}^2/4} + \frac{\Gamma_m\bar{n}_{\text{th}} + \Gamma_b}{(\omega + \Omega_{\text{eff}})^2 + \Gamma_{\text{eff}}^2/4}. \end{aligned} \quad (2.81)$$

The final mechanical occupation, in the sideband resolved limit, is given by

$$\bar{n}_f = \frac{\Gamma_m\bar{n}_{\text{th}} + \Gamma_b}{\Gamma_{\text{eff}}}. \quad (2.82)$$

In the two-tone pumping scheme, the quantum back-action (QBA) from the blue probe can become dominant even when there is no heating due to optical absorption, as is evident from the second term in the numerator of Eq. (2.82).

When coupled to both the optical and thermal reservoirs, the zero point fluctuation of the dressed mechanical mode becomes,

$$\tilde{\beta} = \frac{\alpha(\Gamma_c - \Gamma_b) + \Gamma_m\beta}{\Gamma_{\text{eff}}}. \quad (2.83)$$

For $\alpha = 1$ (i.e. a quantum limited laser field) and $\beta = 1$, we see that also $\tilde{\beta} = 1$.

We note that Eq. (2.82) is formulated using the rotating-wave approximation, where the QBA

from the cooling tone is neglected [118–120], if the system is deep in the resolved-sideband regime. In the following, we explain this conclusion using a Raman-scattering picture that addresses QBA from both the cooling tone and the blue probe [119]. Without the mechanical damping, the mean phonon occupancy of the optomechanical crystal cavity \bar{n}_{\min} is given by the detailed balance expression

$$\frac{\bar{n}_{\min} + 1}{\bar{n}_{\min}} = \frac{\Gamma_b^{AS} + \Gamma_c^{AS}}{\Gamma_b^S + \Gamma_c^S}, \quad (2.84)$$

where $\Gamma_{b(c)}^{AS}$ and $\Gamma_{b(c)}^S$ correspond to the anti-Stokes and Stokes scattering rate, respectively, of the blue probe (cooling tone). Now, $\Gamma_c^{AS} \equiv \Gamma_c$ and $\Gamma_b^S \equiv \Gamma_b$, whereas Γ_b^{AS} and Γ_c^S take the form

$$\begin{aligned} \Gamma_b^{AS} &= \bar{n}_b g_0^2 \left(\frac{\kappa}{\kappa^2/4 + (\Delta + \delta + 2\Omega_m)^2} \right) \\ \Gamma_c^S &= \bar{n}_c g_0^2 \left(\frac{\kappa}{\kappa^2/4 + (\Delta - \delta - 2\Omega_m)^2} \right). \end{aligned} \quad (2.85)$$

The imbalanced Stokes and anti-Stokes scattering from both the cooling tone and the blue probe leads to a net optomechanical damping of the mechanical oscillator $\Gamma_{\text{opt}} = \Gamma_b^{AS} + \Gamma_c^{AS} - \Gamma_b^S - \Gamma_c^S \approx \Gamma_c - \Gamma_b$. The minimum phonon occupancy \bar{n}_{\min} is therefore given by

$$\bar{n}_{\min} = \frac{\Gamma_c^S + \Gamma_b}{\Gamma_{\text{opt}}}. \quad (2.86)$$

The stochastic QBA force from both tones produces a residual phonon occupancy of the optomechanical crystal cavity. In the deep resolved-sideband regime ($\kappa \ll \Omega_m$), such that $\Gamma_c^S \ll \Gamma_{\text{opt}}$, the QBA from the cooling tone is negligible. After including the mechanical damping Γ_m , \bar{n}_f takes the form in Eq. (2.82), where the QBA from only the blue probe is considered.

Similar in the sideband asymmetry measurement, a balanced heterodyne detection can be adopted for the output optical field. The frequency difference between the local oscillator and the mean frequency of the two pumping tones is Δ_{LO} , assuming $0 < -\delta < \Delta_{\text{LO}}$. The measured single-sided heterodyne noise spectrum, when normalized to the shot noise, is given by

$$S_I(\Omega + \Delta_{\text{LO}}) = 1 + \eta \Gamma_{\text{eff}} \left[\frac{(\bar{n}_f + 1)\Gamma_b}{\Gamma_{\text{eff}}^2/4 + (\Omega + \delta)^2} + \frac{\bar{n}_f \Gamma_c}{\Gamma_{\text{eff}}^2/4 + (\Omega - \delta)^2} \right], \quad (2.87)$$

Equation (2.87) can be used to determine the phonon occupancy \bar{n}_f from the asymmetry of the motional sidebands, considering the detuning dependent scattering rate.

Back-action Evasion

Due to the Heisenberg uncertainty principle, continuous linear displacement measurement is limited by the standard quantum limit. To surpass this limit, quantum non-demolition measurement can be performed. Following the original idea of Thorne, a two-tone back-action evading measurement scheme can be implemented by driving the optomechanical system periodically [35, 36]. Instead of performing the displacement measurement, one can measure a single quadrature of the displacement while completely giving up the information on the other quadrature. Now we go through the theoretical treatment of such two-tone back-action evading measurement, where two pumping tones of the same power are placed exactly at the red and blue sideband of the cavity, i.e. $\delta = 0$ and $\Delta = 0$. The effective Hamiltonian takes the form,

$$\hat{H}_{\text{RWA}} = -\hbar g (\delta \hat{b}^\dagger + \delta \hat{b}) (\delta \hat{a}^\dagger + \delta \hat{a}), \quad (2.88)$$

We can define the amplitude and phase quadratures for the optical field in the interaction picture,

$$\begin{aligned} \hat{Q} &= \frac{\delta \hat{a}^\dagger + \delta \hat{a}}{\sqrt{2}} \\ \hat{P} &= i \frac{\delta \hat{a}^\dagger - \delta \hat{a}}{\sqrt{2}}, \end{aligned} \quad (2.89)$$

where

$$[\hat{Q}, \hat{P}] = i. \quad (2.90)$$

And the two unitless mechanical quadratures¹ can be defined accordingly in the interaction picture,

$$\begin{aligned} \hat{X}_1 &= \frac{\delta \hat{b}^\dagger + \delta \hat{b}}{\sqrt{2}} \\ \hat{X}_2 &= i \frac{\delta \hat{b}^\dagger - \delta \hat{b}}{\sqrt{2}}, \end{aligned} \quad (2.91)$$

¹The displacement operator can be decomposed to the two rotating quadratures, $\hat{x} = \sqrt{2} x_{\text{zpt}} (\hat{X}_1 \cos(\Omega_m t) + \hat{X}_2 \sin(\Omega_m t))$, where $\hat{X}_1 = 1/\sqrt{2} (\hat{b} e^{+i\Omega_m t} + \hat{b}^\dagger e^{-i\Omega_m t})$ and $\hat{X}_2 = -i/\sqrt{2} (\hat{b} e^{+i\Omega_m t} - \hat{b}^\dagger e^{-i\Omega_m t})$.

where

$$[\hat{X}_1, \hat{X}_2] = i. \quad (2.92)$$

The input quadrature operators satisfy the following noise correlation,

$$\begin{aligned} \langle \hat{X}_{1,\text{in}}(t) \hat{X}_{1,\text{in}}(t') \rangle &= (\bar{n}_{\text{th}} + 1/2) \delta(t - t') \\ \langle \hat{X}_{2,\text{in}}(t) \hat{X}_{2,\text{in}}(t') \rangle &= (\bar{n}_{\text{th}} + 1/2) \delta(t - t') \\ \langle \hat{X}_{1,\text{in}}(t) \hat{X}_{2,\text{in}}(t') \rangle &= i/2 \delta(t - t') \\ \langle \hat{X}_{2,\text{in}}(t) \hat{X}_{1,\text{in}}(t') \rangle &= -i/2 \delta(t - t') \\ \langle \hat{Q}_{\text{in}}(t) \hat{Q}_{\text{in}}(t') \rangle &= 1/2 \delta(t - t') \\ \langle \hat{P}_{\text{in}}(t) \hat{P}_{\text{in}}(t') \rangle &= 1/2 \delta(t - t') \\ \langle \hat{Q}_{\text{in}}(t) \hat{P}_{\text{in}}(t') \rangle &= i/2 \delta(t - t') \\ \langle \hat{P}_{\text{in}}(t) \hat{Q}_{\text{in}}(t') \rangle &= -i/2 \delta(t - t'). \end{aligned} \quad (2.93)$$

We can obtain the effective Hamiltonian,

$$\hat{H}_{\text{RWA}} = -\hbar 2g \hat{Q} \hat{X}_1, \quad (2.94)$$

which consists only the coupling term between the optical quadrature \hat{Q} and mechanical quadrature \hat{X}_1 . The quantum Langevin equations of the field quadratures can be obtained in the Fourier domain,

$$\begin{aligned} \chi_c^{-1}(\omega) \hat{Q}(\omega) &= \sqrt{\kappa} \hat{Q}_{\text{in}}(\omega) \\ \chi_m^{-1}(\omega) \hat{X}_2(\omega) &= \sqrt{\Gamma_m} \hat{X}_{2,\text{in}}(\omega) + 2g \hat{Q}(\omega) \\ \chi_c^{-1}(\omega) \hat{P}(\omega) &= \sqrt{\kappa} \hat{P}_{\text{in}}(\omega) + 2g \hat{X}_1(\omega) \\ \chi_m^{-1}(\omega) \hat{X}_1(\omega) &= \sqrt{\Gamma_m} \hat{X}_{1,\text{in}}(\omega). \end{aligned} \quad (2.95)$$

We see that the \hat{X}_1 quadrature is not affected by the measurement, while \hat{X}_2 is additionally coupled to the optical fluctuation \hat{Q} . The noise spectral density for the two mechanical quadratures can be calculated accordingly,

$$\begin{aligned} \bar{S}_{X_1 X_1}(\omega) &= \frac{1}{2} \int \frac{d\omega'}{2\pi} \langle \{ \hat{X}_1(\omega'), \hat{X}_1(\omega) \} \rangle = \frac{\Gamma_m}{(\Gamma_m/2)^2 + \omega^2} (\bar{n}_m^{\text{th}} + 1/2) \\ \bar{S}_{X_2 X_2}(\omega) &= \frac{1}{2} \int \frac{d\omega'}{2\pi} \langle \{ \hat{X}_2(\omega'), \hat{X}_2(\omega) \} \rangle = \frac{\Gamma_m}{(\Gamma_m/2)^2 + \omega^2} (\bar{n}_m^{\text{th}} + 2\bar{n}_{\text{ba}} + 1/2), \end{aligned} \quad (2.96)$$

where $\bar{n}_{\text{ba}} = \frac{4g^2}{\kappa\Gamma_m}$. We see that the quadrature \hat{X}_1 remains unaffected, while an increased

measurement back-action $2\bar{n}_{\text{ba}}$ is imprinted on the other mechanical quadrature \hat{X}_2 . The output field can be measured by a balanced heterodyne detection. The noise spectrum density, normalized to the vacuum noise level, is given by,

$$S_I(\Omega + \Delta_{\text{LO}}) = 1 + \eta \Gamma_m |\chi_m(\Omega)|^2 \frac{4g^2}{\kappa} (2\bar{n}_{\text{th}} + \beta). \quad (2.97)$$

When increasing the probing strength g , the imprecision keeps decreasing and no back-action is seen by the measurement record. Such BAE measurement can be in principle adopted to perform sub-SQL measurement of the mechanical motion. In practise, excess back-action appears at high probing power, such as the microwave source noise and the optical absorption, which precludes the perfect BAE measurements [79, 80, 121]. Besides, one needs to distinguish different noise sources or processes during the measurement, such as in the evaded back-action or sideband asymmetry measurement [122].

In the optical domain, a sweep of two-tone frequency separation δ can be performed, while maintaining other parameters, such as g and Δ . For $|\delta| \gg \Gamma_m$, the sideband asymmetry is restored, where the phonon occupancy $\bar{n}_f = \bar{n}_{\text{th}} + \bar{n}_{\text{ba}}$ can be calibrated via the asymmetric thermomechanical sidebands. A transition between the sideband asymmetry and back-action evasion can thus be observed. To observe the evasion of the measurement back-action more easily, the mechanical oscillators are typically prepared at low phonon occupancy, using cryogenic precooling or laser cooling. However, this requires additional pumping tones, which results in complex dynamics in the optomechanical system, such as the Floquet dynamics due to Kerr-type nonlinearities [122].

Dissipative Mechanical Squeezing

In the back-action evading measurement, the quadrature fluctuation \hat{X}_1 is completely decoupled from the measurement quantum back-action. Conditional squeezing of the mechanical motion can be in principle obtained from BAE measurements, during a given run of experiment [36]. However, after averaging on many measurement runs, the minimum measured mechanical quadrature from the output noise spectrum is the zero-point motion. Unconditional squeezing of the mechanical motion can be achieved using reservoir engineering [123], where the optical cavity can be seen as a bath whose force noise is squeezed [124]. The scheme is similar to the BAE measurement, while the cooling tone is stronger than the blue probe, i.e. $\delta = 0$, $\Delta = 0$ and $g_c > g_b$. We can obtain the effective Hamiltonian with

Chapter 2. Theory

rotating-wave-approximation,

$$\hat{H}_{\text{RWA}} = -\hbar \left[(g_b \delta \hat{b}^\dagger + g_c \delta \hat{b}) \delta \hat{a}^\dagger + (g_c \delta \hat{b} + g_b \delta \hat{b}^\dagger) \delta \hat{a} \right]. \quad (2.98)$$

For $g_c \neq g_b$, we introduce a Bogoliubov-mode annihilation operator,

$$\hat{\beta} = \delta \hat{b} \cosh r + \delta \hat{b}^\dagger \sinh r, \quad (2.99)$$

where the squeezing parameter r satisfies $\sinh r = g_b/g_c$. The Hamiltonian can be rewritten,

$$\hat{H} = -\hbar G (\delta \hat{a}^\dagger \hat{\beta} + \delta \hat{a} \hat{\beta}^\dagger), \quad (2.100)$$

where $G = \sqrt{g_c^2 - g_b^2}$. Using an unbalanced two-tone pumping scheme, we can sideband cool the Bogoliubov mode $\hat{\beta}$. The vacuum state of $\hat{\beta}$ is the squeezed vacuum, where the squeezing operator is given by,

$$\hat{S}(r) = \exp \left[r (\hat{b} \hat{b} + \hat{b}^\dagger \hat{b}^\dagger) / 2 \right]. \quad (2.101)$$

The quantum Langevin equations for the Bogoliubov mode and the optical field are given by,

$$\begin{aligned} \chi_c^{-1}(\omega) \delta \hat{a} &= \sqrt{\kappa} \delta \hat{a}_{\text{in}} + iG \hat{\beta} \\ \chi_m^{-1}(\omega) \hat{\beta} &= \sqrt{\Gamma_m} \hat{\beta}_{\text{in}} + iG \delta \hat{a}. \end{aligned} \quad (2.102)$$

The mode occupation of the Bogoliubov mode can be obtained easily,

$$\bar{n}_\beta = \int_{-\infty}^{\infty} \frac{d\omega}{2\pi} S_{\beta\beta}(\omega) = \frac{\Gamma_m}{\Gamma_{\text{tot}}} \bar{n}_\beta^{\text{th}}, \quad (2.103)$$

where $\Gamma_{\text{tot}} = \Gamma_m + 4G^2/\kappa$ and the thermal occupation of the Bogoliubov mode takes the form,

$$\bar{n}_\beta^{\text{th}} = \left(\frac{g_c}{G} \right)^2 \bar{n}_{\text{th}} + \left(\frac{g_b}{G} \right)^2 (\bar{n}_{\text{th}} + 1). \quad (2.104)$$

The dynamical back-action from the two-tone driving cools the Bogoliubov mode, where the output noise spectrum can be obtained,

$$S_I(\Omega + \Delta_{\text{LO}}) = 1 + \eta \Gamma_{\text{tot}} \frac{\bar{n}_\beta \Gamma_{\text{opt}}}{\Gamma_{\text{tot}}^2/4 + \Omega^2}, \quad (2.105)$$

where the optomechanical damping rate is given by $\Gamma_{\text{opt}} = 4(g_c^2 - g_b^2)/\kappa$.

Ground state cooling of $\hat{\beta}$ directly results in the unconditional mechanical squeezing,

$$2\langle\hat{X}_1^2\rangle = e^{-2r} \left[1 + 2\langle\hat{\beta}^\dagger\hat{\beta}\rangle + \langle\hat{\beta}\hat{\beta}\rangle + \langle\hat{\beta}^\dagger\hat{\beta}^\dagger\rangle \right]. \quad (2.106)$$

From the noise spectrum, we could not however obtain the quadrature variance directly. Asserting the Cauchy-Schwarz inequality, the squeezing occupation obeys rigorous bounds from the phonon occupancy of the Bogoliubov mode [124],

$$\begin{aligned} \langle\hat{X}_1^2\rangle &\leq e^{-2r} \left[1 + 2\langle\hat{\beta}^\dagger\hat{\beta}\rangle \right] \\ \langle\hat{X}_1^2\rangle &\geq e^{-2r} \left[0.5 + 2\langle\hat{\beta}^\dagger\hat{\beta}\rangle \right]. \end{aligned} \quad (2.107)$$

The variance of mechanical quadrature \hat{X}_1 takes the form,

$$\langle\hat{X}_1^2\rangle = \frac{\Gamma_m}{\Gamma_{\text{tot}}} \left(\bar{n}_{\text{th}} + \frac{1}{2} \right) + \frac{2(g_c - g_b)^2}{\kappa\Gamma_{\text{tot}}}, \quad (2.108)$$

While for the other quadrature \hat{X}_2 , the variance takes the form,

$$\langle\hat{X}_2^2\rangle = \frac{\Gamma_m}{\Gamma_{\text{tot}}} \left(\bar{n}_{\text{th}} + \frac{1}{2} \right) + \frac{2(g_c + g_b)^2}{\kappa\Gamma_{\text{tot}}}. \quad (2.109)$$

The reservoir engineering results in a reduced variance in quadrature \hat{X}_1 and increased variance in quadrature \hat{X}_2 . We can infer the quadrature variance indirectly from Eq. 2.108 [125], which requires perfect knowledge of the system dynamics, such as additional parametric effects. Alternatively, one can perform an independent back-action evasion measurement of the two quadratures directly. However, this requires additional pumping tones, which results in complex dynamics in the optomechanical system, such as the Floquet dynamics [122]. Besides, the BAE measurement can be limited by the excess heating and also fundamental two-tone instability [126].

3 Experimental System

Over the last decade, a wide range of optomechanical systems are studied, where the mass of the mechanical oscillator ranges from zg (e.g. cold atoms [127]), to fg (e.g. microdisk [128]) and to g (suspended macroscopic mirrors) [58]. However, measurements in the quantum regime with such mechanical oscillators are rather limited and challenging. One of the greatest challenges is the thermal noise. The average phonon excitation of a mechanical oscillation is $\bar{n}_{\text{th}} = \frac{k_B T}{\hbar \Omega_m}$, which is proportional to the bath temperature and inversely proportional to the mechanical frequency. To observe quantum effects, a high frequency mechanical oscillator in cryogenic environment is preferred. Another challenge is that most of these experimental platforms are limited in the weak coupling regime, where the single photon coupling strength g_0 is much lower than the optical decay ($g_0 \ll \kappa$). One figure of merit is the so-called vacuum cooperativity $C_0 = \frac{4g_0^2}{\kappa\Gamma_m}$. In the last years, a lot of effort has been made to achieve high C_0 , which enables even the observation of the quantum back-action at room temperature despite the large decoherence rate $\bar{n}_{\text{th}}\Gamma_m$ [92].

In this chapter, we will discuss in detail the optomechanical device and the cryogenic setup for the quantum optomechanical measurements outlined in this thesis.

3.1 Optomechanical Crystal

To achieve stronger optomechanical coupling, one intuitive idea is to reduce the mode volume of the optical and mechanical resonator, to enhance the interaction between photonic and phononic field with large field overlap. The smaller effective mass results in higher mechanical frequency, thus lower mean phonon occupation. However, the loss rates for the optical and mechanical field are accordingly increased due to the small mode volume.

Over the last several decades, the field of photonic crystal has witnessed great advancements in the ultra-high-Q optical cavities with untra-small mode volume [129, 130]. The periodic patterning of the photonic structures forms photonic bandgap similar to the electronic bandgap in condensed matter physics. Such devices have enabled optical cavities with extremely high quality factors and small mode volumes [131, 132]. Similar ideas can be also implemented for the mechanical motion, where the periodic structures can form a phononic bandgap [49, 133]. The phononic defect mode can be confined very well in the center of structures.

The vacuum optomechanical coupling, which represents the cavity frequency shift per zero-point displacement, is given by,

$$g_0 = \frac{d\omega_o}{d\alpha} x_{\text{zpf}} = \frac{d\omega_o}{d\alpha} \sqrt{\frac{\hbar}{2m_{\text{eff}}\Omega_m}}, \quad (3.1)$$

with α a generalized coordinate, x_{zpf} the zero-point displacement and m_{eff} the effective mass. To obtain the cavity frequency shift with respect to the change of α , a first-order electromagnetic field perturbation theory could be employed, which results in

$$\frac{d\omega_o}{d\alpha} = -\frac{\omega_o}{2} \frac{\int dx \frac{d\varepsilon(x)}{d\alpha} |E(x)|^2}{\int dx \varepsilon(x) |E(x)|^2}, \quad (3.2)$$

where the $E(x)$ is the electric field vector while the ε is the permittivity. Two main contributions for the optomechanical coupling are considered, i.e. the moving boundary [134] and the photoelastic effect [135]. The former one can be interpreted as a vibration induced cavity length change which is purely from volume deformation of the cavity, while the later one can be considered as the refractive index change due to the dynamic stresses which is purely from changes in dielectric constants within the cavity. Overall, this results in the total optomechanical coupling rate, $g_0 = g_{\text{mb}} + g_{\text{pe}}$ [136], where $g_{\text{mb}} = \left. \frac{d\omega_o}{d\alpha} \right|_{\text{mb}} x_{\text{zpf}}$ and $g_{\text{pe}} = \left. \frac{d\omega_o}{d\alpha} \right|_{\text{pe}} x_{\text{zpf}}$. The moving boundary contribution g_{mb} can be obtained by [134],

$$\left. \frac{d\omega_o}{d\alpha} \right|_{\text{mb}} = -\frac{\omega_o}{2} \frac{\oint (Q \cdot \hat{n}) (\Delta\varepsilon E_{\parallel}^2 - \Delta\varepsilon^{-1} D_{\perp}^2) dS}{\int E \cdot D dV}, \quad (3.3)$$

where the Q is the normalized displacement and \hat{n} is the outward facing surface normal, D is the displacement field, and the subscripts \perp and \parallel correspond to the field components perpendicular and parallel to the surface. Besides,

$$\Delta\varepsilon = \varepsilon_1 - \varepsilon_2 \text{ and } \Delta\varepsilon^{-1} = \varepsilon_1^{-1} - \varepsilon_2^{-1}, \quad (3.4)$$

where $\varepsilon_{1,2}$ corresponds to the two material permittivities of the boundary interface. In our case, we define the effective mass of the mechanical oscillator,

$$m_{\text{eff}} = \frac{\int dx \rho(x) |Q(\alpha, x)|^2}{\alpha^2} = \int dx \rho(x) |q(x)|^2. \quad (3.5)$$

The photoelastic contribution can be calculated from the photoelastic shift for an general refractive index tensor,

$$\frac{d\varepsilon}{d\alpha} = -\varepsilon \left(\frac{pS}{\varepsilon_0} \right) \varepsilon, \quad (3.6)$$

while $\frac{\partial \varepsilon_{ij}}{\partial \alpha} = -\varepsilon_0 n^4 p_{ijkl} S_{kl}$. Here p is the rank-four photo-elastic tensor and S is the strain tensor. We obtain the first-order correction due to the photoelastic effect,

$$\begin{aligned} \left. \frac{d\omega_o}{d\alpha} \right|_{\text{pe}} &= \frac{\omega_o \varepsilon_0 n^4}{2} \int_{\text{Si}} dV \left[2 \text{Re} \{ E_x^* E_y \} p_{44} S_{xy} + 2 \text{Re} \{ E_x^* E_z \} p_{44} S_{xz} + 2 \text{Re} \{ E_y^* E_z \} p_{44} S_{yz} \right. \\ &\quad + |E_x|^2 (p_{11} S_{xx} + p_{12} (S_{yy} + S_{zz})) + |E_y|^2 (p_{11} S_{yy} + p_{12} (S_{xx} + S_{zz})) \\ &\quad \left. + |E_z|^2 (p_{11} S_{zz} + p_{12} (S_{xx} + S_{yy})) \right] / \int E \cdot D dV, \end{aligned} \quad (3.7)$$

where $(p_{11}, p_{12}, p_{44}) = (-0.094, 0.017, -0.051)$ [135, 136]. The optomechanical coupling rate can be numerically simulated with Finite Element Method (FEM).

Silicon optomechanical crystals (OMCs) [49, 136] that couple an optical mode at telecommunication wavelength and a co-localized mechanical mode at GHz frequency exhibit several exceptional features, including some of the largest vacuum optomechanical coupling rates ($g_0/2\pi \sim 1$ MHz) [136] as well as ultralong phonon lifetime [137]. They have been employed in a wide range of experiments, such as continuous quantum measurements [60, 121, 122], and probabilistic preparation of quantum states [96, 97, 138]. The compatibility of these systems with planar nanofabrication technology and their scalability have motivated studies of optomechanical topological phenomena [139, 140], frequency conversion [102] and coupling to superconducting qubits [103, 104].

Our optomechanical system is an optomechanical crystal (OMC) [49] adopting the design that reported previously [136]. Figure 3.1(a) shows the unit cell of the OMC structure, which is a rectangular silicon beam with a removed ellipse in the center. Figure 3.1(b) shows the photonic band structures, where a full bandgap is formed at telecom frequencies. Figure 3.1(c) shows the phononic band structures, where a phononic partial bandgap is present. A defect in the pattern is designed to co-localize photons and phonons. The defect is introduced by

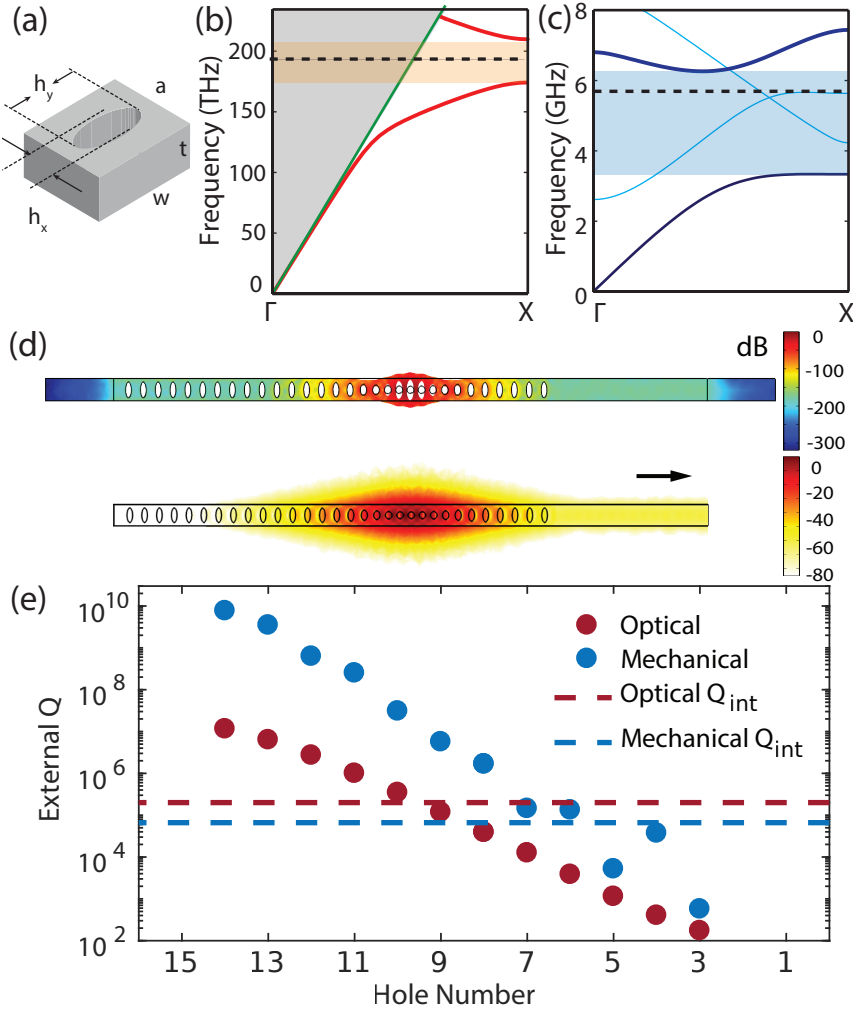


Figure 3.1 – **Design of the OMC.** (a) Nominal unit cell structure of the OMC with $(a, t, w, h_x, h_y) = (436, 220, 529, 165, 366)$ nm [136]. (b) The optical band diagram shows the dispersion of different modes in a one-dimensional lattice of unit cells. The light brown area in the middle represents a full optical bandgap at optical telecom frequencies. (c) The phononic band diagram shows the dispersion of different modes. The blue area in the middle shows a partial phononic bandgap at frequency from 3-6 GHz. (d) Simulated mechanical (top) and optical (bottom) field distribution of the OMC. (e) Simulated optical and mechanical external Q vs. number of holes of the front mirror, adjacent the defect section of OMC. When the number of holes is increased, both optical (red dot) and mechanical (blue dot) external Q increases. The dashed lines correspond to the measured intrinsic Q of the optical (red) and mechanical (blue) mode in [136].

varying the ellipticity and the pitch between the holes in a smooth and progressive way in order to minimize the scattering loss and maximize the optomechanical coupling [136], as shown in Fig. 3.1(d) from FEM simulation with Comsol. The pitch and hole sizes follow a smooth Gaussian function from the unit cell to the central defect. The optimal design results in a simulated $g_0/2\pi = 870\text{ kHz}$, of which $g_{\text{mb}}/2\pi = 930\text{ kHz}$ and $g_{\text{pe}}/2\pi = -60\text{ kHz}$ [136]. We note that, the moving boundary and the photoelastic contributions have different signs, which is extremely sensitive to the cavity design and material property [141–144]. By controlling the number of holes on each side of the defect, a single-sided geometry is realized to couple the light into the OMC, where the front input coupling mirror has less holes than the high-reflectivity mirror, as shown in Fig. 3.1(d). In such a single-sided cavity, the optical field can be efficiently coupled in and out while the mechanical mode maintains localized. Figure 3.1(e) shows the simulated external Q of the optical and mechanical modes vs. the hole number of the front mirror. Increasing the number of holes in the front mirror leads to an increased external Q of both optical and mechanical mode. However in practice, the mechanical Q is much lower, limited by material and fabrication imperfections, and hence not affected by hole number. By comparing to the measured intrinsic optical Q , a proper hole number for the front mirror is chosen in the actual design, while the hole number of the high-reflectivity mirror is kept fixed.

3.2 Taper Coupling

We tailor the design of the OMC for operations in the cryostat, which enables us to couple the light into the OMC by tapered fiber. To avoid the perturbation of the mechanical mode due to the taper coupling, we optimize our design by adding a waveguide in parallel to the nanobeam as shown in Fig. 3.2. The nanobeam is extended to introduce a coupling waveguide, into which light can be evanescently coupled by positioning a tapered optical fiber of diameter $\sim 1\text{ }\mu\text{m}$. The height, width and coupling length of the coupling waveguide are optimized accordingly to achieve maximum coupling. For a tapered fiber of diameter $\sim 1\text{ }\mu\text{m}$, it has an effective index of around 1.17 as shown in the dashed line in Fig. 3.3. The effective index of the silicon waveguide versus the width is shown in the blue curve, assuming a device layer thickness of 220nm for wavelength of 1550 nm. To ensure perfect mode matching between the waveguide TE mode and the optical mode of the tapered fiber, the width of the waveguide is chosen to be $\sim 280\text{ nm}$.

When the taper approaches the coupling waveguide, the modes start to hybridize, similar to the energy level splitting in a diatomic molecule. This results in two hybridized modes with

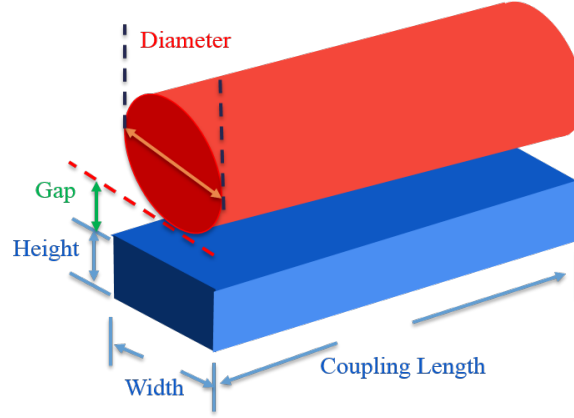


Figure 3.2 – **Optical Coupling between the waveguide and optical tapered fiber.** The tapered fiber of diameter $\sim 1\mu\text{m}$ is shown in red. The coupling waveguide is shown in blue with parameters such as width, height and coupling length indicated.

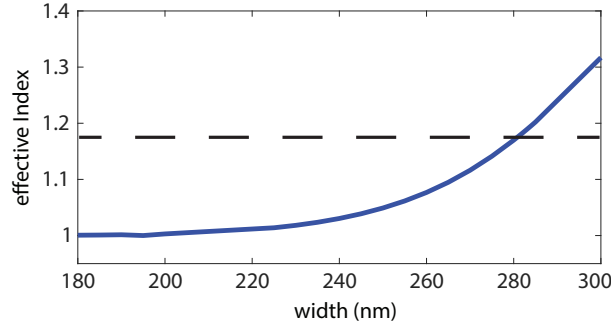


Figure 3.3 – **Effective index of the waveguide TE mode.** The blue curve shows the effective index versus the waveguide width. The dashed line corresponds to the tapered fiber of a diameter of $\sim 1\mu\text{m}$.

different effective index n_{eff} and different propagation constants β . To achieve a perfect field transfer between the waveguide and the taper, the coupling length between them is set by,

$$L_c = \frac{\pi}{\Delta\beta} = \frac{\lambda}{2\Delta n_{\text{eff}}}, \quad (3.8)$$

where $\delta\beta$ and Δn_{eff} are the difference in the propagation constant and the effective index of the two hybridized modes respectively, and λ is the optical wavelength. The optimal length is determined by the coupling strength between the tapered fiber and the waveguide, which is set by the gap in between. Figure 3.4 shows the optimal coupling length versus the gap between the tapered fiber and the coupling waveguide. When the taper touches the waveguide, a shortest coupling length could be obtained. To meet the phase matching condition, the waveguide is designed with width of $0.28\mu\text{m}$ to be mode matched with the

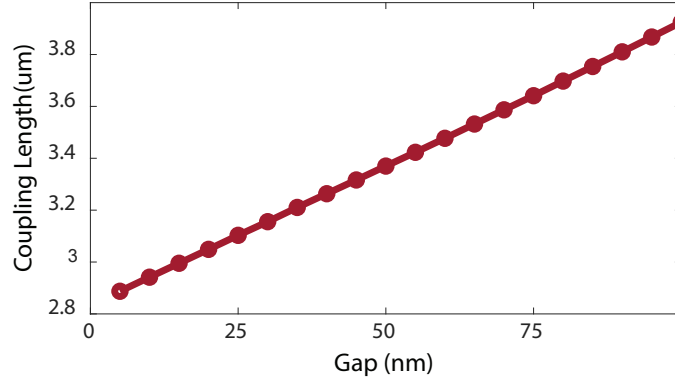


Figure 3.4 – **Optimal coupling length versus the gap between the taper and the waveguide.** The taper is assumed to have a diameter of $1\mu\text{m}$ and the width of the waveguide is chosen to be $\sim 2.9\mu\text{m}$.

taper with a diameter of $1\mu\text{m}$. The optimal coupling length for the waveguide is $\sim 2.9\mu\text{m}$. In order to reduce the scattering loss, the nanobeam width, i.e. 529nm , is tapered down to 280nm adiabatically, which follows a three-order polynomial function of the waveguide length. Besides, we force the derivative of the polynomial function to be zero at the both ends of the tapering section. We verify the simulation with both FEM simulations with Comsol and Finite Difference Time Domain simulations with Lumerical, which gives a $\eta_{\text{wg}} > 90\%$ in an ideal coupling case. Due to phase mismatch between the waveguide and the tapered fiber, we obtain typical single-pass waveguide coupling efficiencies $\eta_{\text{wg}} > 50\%$ experimentally.

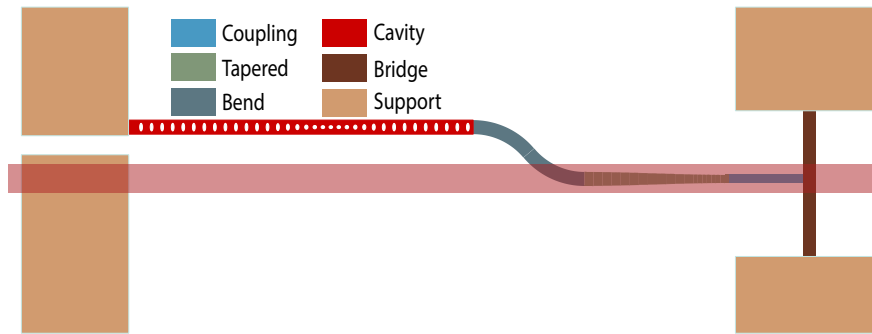


Figure 3.5 – **Device design.** The OMC is shown in red. The bended waveguide is shown in dark green. The tapered waveguide section is shown in light green. The coupling waveguide is shown in light blue. The supporting bridge is shown in dark brown and the pads are shown in light brown. The tapered fiber is shown in light red.

The full design for the device is shown in Fig. 3.5. To suspend the device layer, we implement a waveguide bridge support, which is connected to two supporting pads before the coupling waveguide. This leads to roughly 10% of scattering loss. On the other side, the nanobeam

is directly connected to a supporting pad. In the earlier designs, we choose to use the same waveguide bridge to support the other side of the taper, which however introduces a lot of fiber vibrations during the optical measurement. This in return leads to large power fluctuation. During actual measurements, we intentionally introduce a tilt for the taper alignment, where the taper touches the isolated supporting pad before touching the front supporting bridge, which eliminates the taper vibration.

3.3 Fabrication

The fabrication of silicon OMC with high accuracy is challenging and reiterative, which starts with the design and ends with characterization of the properties of the devices. However, the properties of the finalized OMC are typically far from the original targeted designs. This requires improvements at any of the fabrication steps: design, electron beam lithography, device etching, photolithography, mesa etching, sample cleaning and undercut. Due to the nano-scale dimension and required high accuracy, the available methods are quite restrictive. Because of the sensitivities to all sorts of perturbations during the fabrication, it is very important to attempt to do everything along the way exactly the same, to control all the parameters.

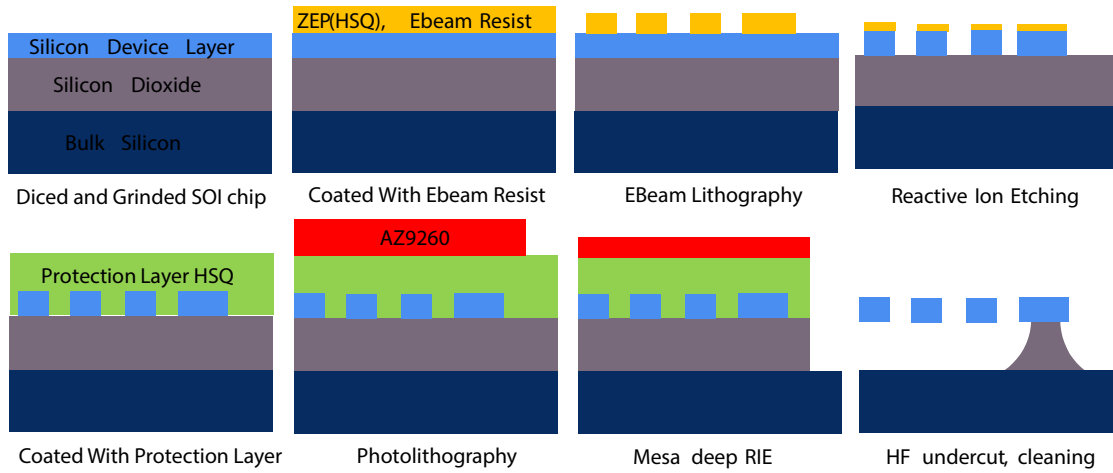


Figure 3.6 – **Fabrication Process Flow.** Dark blue layer is the substrate silicon. Gray layer is the buried oxide. Light blue layer is the silicon device layer. Yellow layer is the Ebeam resist. Two types of different Ebeam resists are adopted in this thesis, i.e. ZEP and HSQ. Red layer is the photoresist AZ9260, while the green layer is a protection layer of HSQ.

Figure 3.6 shows the fabrication steps. Starting from standard 8" Silicon On Insulator (SOI) wafer (Soitec), we dice it into 1.5cm × 1.5cm chips with backside oxide layer removed and

also substrate silicon grinded, which leads to a final thickness of 380 μ m for the whole chip for later convenience during cleaving. It has a silicon device layer of 220 nm and 2 μ m buried oxide layer. We pattern our chips with electron beam lithography (EBL). Before doing EBL, the chip is cleaned with oxygen plasma for surface activation. Then it is coated with Ebeam resist. Throughout this thesis, two types of Ebeam resists are tested, ZEP520 and Hydrogen silsesquioxane (HSQ). The different results from these two resists are summarized in the Appendix. To achieve higher resolution and stability, the parameters are optimized during the EBeam job preparation step with proximity effect correction and electron beam writing order. After the exposure and development, the chip is mounted on a silicon carrier wafer for etching.

A reactive ion etching (RIE) step is followed to etch the silicon device layer. As the verticality of the sidewalls and surface roughness here are critical for the optical scattering loss, the gas ratio, gas flow and also the etching time is optimized. After the device layer etching, the ebeam resist is removed by Remover 1165 and Piranha (a mixture of sulfuric acid and hydrogen peroxide).

To open an area for taper fiber coupling, an additional photolithography and deep RIE are applied to create a mesa structure. Before continuing the photolithography step, one protection layer of HSQ is coated and baked at 450 degree for 1 hour to prevent the device layer from contacting the photoresist. After this, we coat the chip with photoresist AZ9260 and perform the photolithography. Then the silicon dioxide and the substrate silicon are etched to isolate the final structure from surroundings for later measurement.

After removing all the resist, the device layer is undercut in diluted 10% hydrofluoric acid to suspend the device on test by removing the silicon dioxide. Following an additional Piranha cleaning step to remove organic residuals, the sample is finally dipped into 2% hydrofluoric acid to terminate the device surface with hydrogen atoms.

A typical scanning electron microscope image of the finalized sample is shown in Fig. 3.7(a). In this case, we use ZEP as the ebeam resist and fluorine based pseudo-Bosch process for the RIE step. The zoom-in image is shown on the right in Fig. 3.7(b,c), where the OMC shows perfect verticality and surface roughness of the sidewalls. In the fabrication, a systematic study of the etching process together with the EBL at CMI EPFL is performed, which is detailed in the Appendix of this thesis.

Besides the sidewall verticality and surface roughness, the geometric variations during the entire process also play a very important role, as the optomechanical coupling and the optical loss are rather sensitive to the geometric change. A step by step imaging during the entire

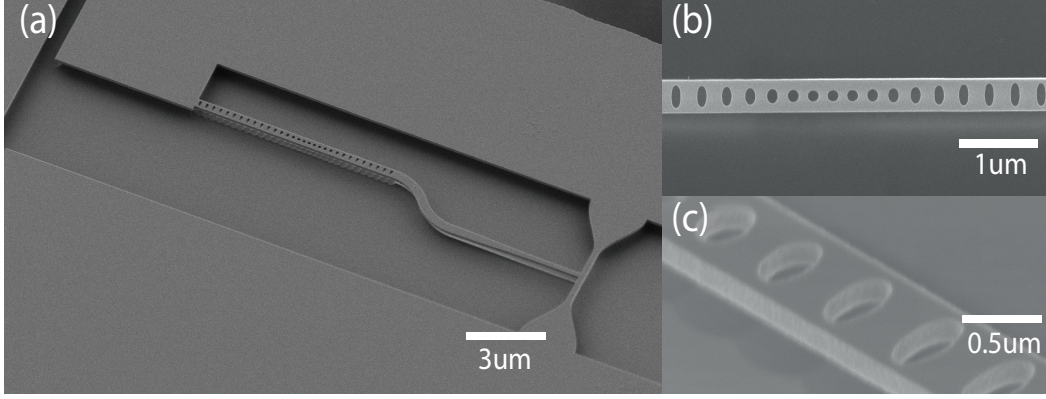


Figure 3.7 – **Scanning Electron Microscope Image of the fabricated sample** (a) SEM image of the entire OMC structure. (b) Top view of the OMC nanobeam. (c) Tilted view of the OMC with details of the sidewalls.

process is always necessary. In the end of our fabrication process, we implement an image processing procedure to analyze the SEM picture with the pixel information saved in the meta file.

The result for a processed image is shown in Fig. 3.8. In this case, the SEM picture has a pixel size of 3.56 nm/pixel and the width of the nanobeam is calibrated to be around 530.5 nm close to the target value 529 nm. The elliptical holes are analyzed with corresponding numbers shown. For each OMC cavity, we take two SEM pictures scanning both horizontally and vertically. For example, for a horizontally placed OMC, the nanobeam width and the semi-minor y axes(vertical) are more accurate when scanning vertically. We perform such analysis statistically on tens of cavities on the same chip to obtain detailed information for the nanobeam and ellipses. Here h_x corresponds to the semi-major x axes (horizontal) while h_y corresponds to the semi-minor y axes(vertical). The p is the pitch. The difference between the obtained averaged results and the design parameters are shown in Fig. 3.8(b). For the ellipses, h_x and h_y shows anti-correlation while the pitch is quite stable. The difference between the averaged fitted values and design parameters is fed into the next run of fabrication with adjusted parameters. For each batch of samples, we typically keep 20 cavities for image processing.

3.4 Experimental System Details

3.4.1 Room Temperature Measurement

The sample is firstly characterized at room temperature to obtain basic properties of OMC, such as the optical resonant wavelength λ and decay rate κ , mechanical frequency Ω_m and

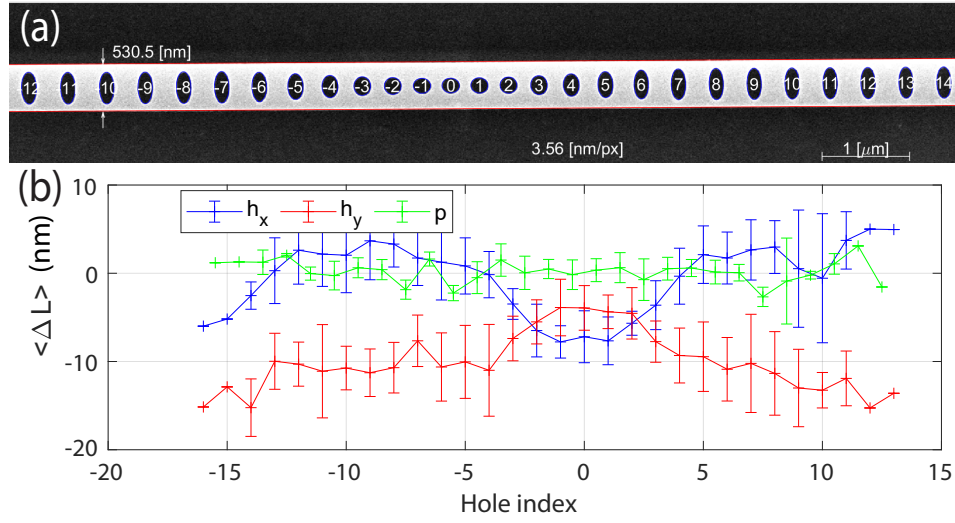


Figure 3.8 – **Image processing of the SEM picture of the silicon OMC.** (a) A typical processed SEM picture of the OMC with a resolution of 3.56nm/pixel. The holes in the nanobeam are analyzed and labeled with corresponding number. (b) Statistic variances of the ellipse sizes and pitches compared to the designed parameters over 20 cavities with same design for reference. h_x corresponds to the semi-major x axes (horizontal) while h_y corresponds to the semi-minor y axes(vertical). p is the pitch, which indicates the position of each ellipse.

damping rate Γ_m and vacuum optomechanical coupling rate g_0 . A typical room temperature characterization setup is shown in Fig. 3.9. As shown in Fig. 3.9(b), the chip is mounted on a stage with three-dimensional access through a piezo-positioner of nanometer resolution. A top camera with a long working distance objective is used for device imaging. A tapered fiber is glued on a glass holder for optical coupling.

The optical resonance is probed by scanning the piezo voltage of an external-cavity diode laser(ECDL). The reflected light from the cavity is calibrated with a fiber-loop reference cavity which has a free spectral range(FSR) of 158 MHz. In typical measurements, we obtain $\eta_{wg} \sim 50\%$, which however critically depends on the coupling condition and also the wavelength. Figure 3.10 shows the normalized optical reflection from the OMC that we used in the work demonstrating laser cooling to the zero-point energy [145], which is one of the best samples we obtained in this thesis in terms of optical linewidth. The optical reflection is normalized to the off-resonant values, which shows a deep in the reflection around cavity resonance. The normalized reflection is calibrated with a fiber-loop reference cavity with a Lorentzian fit as shown in the green curve in Fig. 3.10, from which we obtain a $\kappa \sim 2\pi \times 220$ MHz. In this case, the cavity is undercoupled, which gives $\kappa_{ex} \sim 2\pi \times 70$ MHz. We note that, the coupling depth

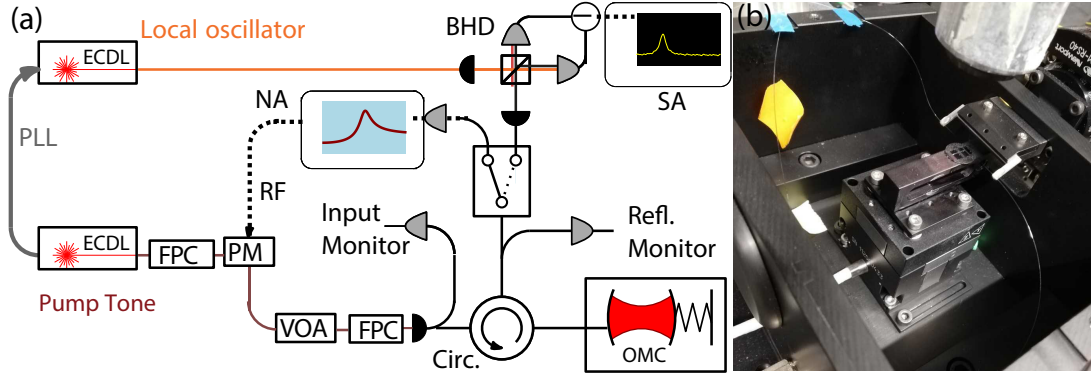


Figure 3.9 – **Room temperature characterization setup.** (a) Scheme of the measurement setup. PM, phase modulator; VOA, variable optical attenuator; FPC, fiber polarization controller; BHD, balanced heterodyne detector; SA, spectrum analyzer; NA, network analyzer; PLL, phase-locked loop. (b) Photo of the characterization setup.

on resonance is given by the expression,

$$R = \frac{(\kappa_{\text{ex}} - \kappa_0)^2}{(\kappa_{\text{ex}} + \kappa_0)^2}. \quad (3.9)$$

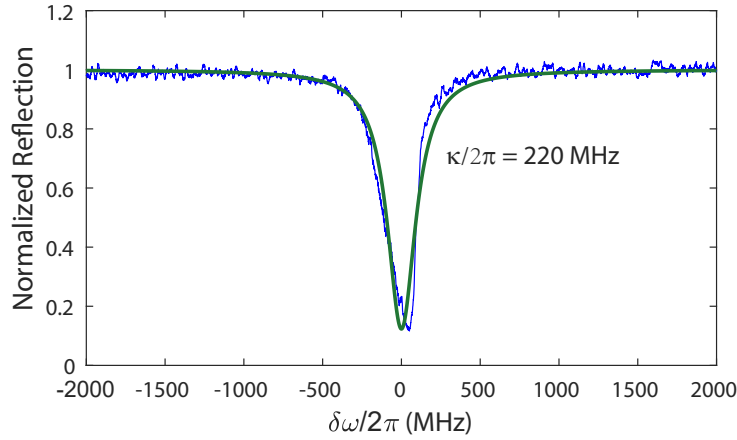


Figure 3.10 – **Optical characterization of the OMC.** The normalized reflection from the OMC with $\kappa/2\pi = 220$ MHz is shown in blue curve, which is normalized to the off-resonance reflection. A Lorentzian fit of the normalized reflection is shown in green curve.

For critically coupled cavities, i.e. $\kappa_{\text{ex}} = \kappa_0$, the normalized reflection on resonance is zero. However, we could not differentiate κ_{ex} and κ_0 simply from the normalized reflection from such one-sided cavities.

The number of holes in the in-coupling mirror controls its reflectivity and, hence, the external coupling rate, which is verified by numerical simulations. To validate this, within the same

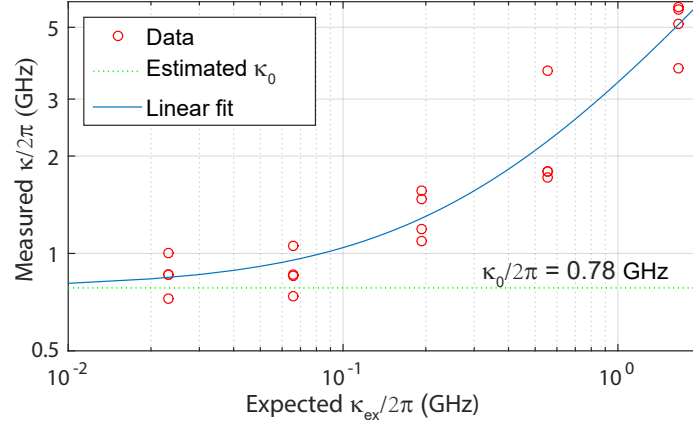


Figure 3.11 – **OMCs of different external coupling rates**. Open circles show the measured κ . Green dashed line shows the estimated κ_0 . The blue curve shows a linear fit of the measured κ to the estimated κ_0 . The cavities are from the same chip and have the same OMC design with different hole numbers in the in-coupling mirror to control the external coupling rate. The averaged intrinsic loss is $\kappa/2\pi = 0.78$ GHz.

batch, we sweep the number of holes for the low reflectivity mirror of the OMC, while maintaining the same hole number for the high reflectivity mirror. In our mask design, we place several OMCs with different number of holes adjacently, which leads to different external coupling rate κ_{ex} while maintaining approximately the same κ_0 .

In Fig. 3.11, we show statistically κ_{ex} and κ for tens of OMCs on the same chip. The measured κ ranges from $2\pi \times 800$ MHz to $2\pi \times 6$ GHz with hole number of low reflectivity mirror changed from 13 to 10. We could estimate the external coupling rate and the intrinsic loss, which are presented also in Fig. 3.11. With different holes number, we could see that the external coupling rate κ_{ex} is changed from $2\pi \times 40$ MHz (under-coupled) to $2\pi \times 7$ GHz (over-coupled), while the intrinsic loss is not changed that much. Here we choose to show one batch of cavities with $\kappa_0 \sim 2\pi \times 0.78$ GHz, as the variation of the coupling depth are more evident for κ_{ex} swept from tens of MHz to few GHz instead of the best OMC with $\kappa = 2\pi \times 0.22$ GHz . A linear fit is applied to the measured optical decay rate between κ_{ex} and κ . By adding the number of holes in the OMC, the external coupling decreases, as shown in the left side of Fig. 3.11.

Figure 3.9(a) shows the scheme of the characterization setup. For basic room temperature characterization, two lasers are utilized, one pumping tone and one local oscillator which is phased-locked to the pumping tone through a phase-lock-loop with a frequency separation of around the mechanical frequency. The pumping tone is sent through a fiber polarization controller (FPC) and phase modulator for weak probe generation, which later passes through a variable optical attenuator to control the power sent to the OMC. The input power and

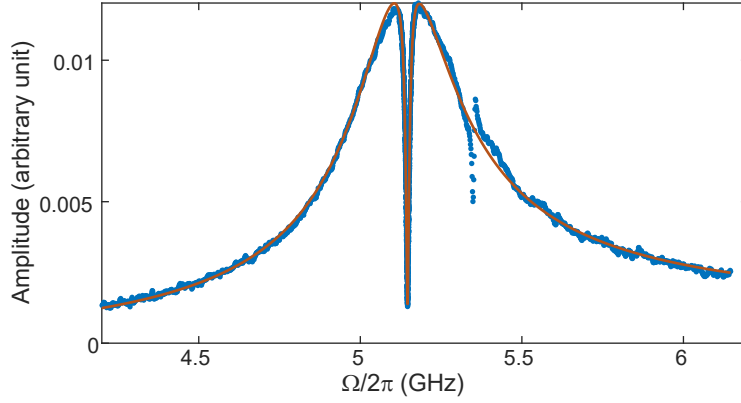


Figure 3.12 – **Coherent Response Measurement.** The blue curve shows the reflected cavity response of the cavity in Ref. [145] with $\kappa/2\pi = 220$ MHz for single tone pumping at power of $\sim 500\mu\text{W}$ with frequency close to the red sideband. The red curve is a fit to a theoretical model of the optomechanically-induced transparency.

reflected power are continuously monitored by two power meters respectively.

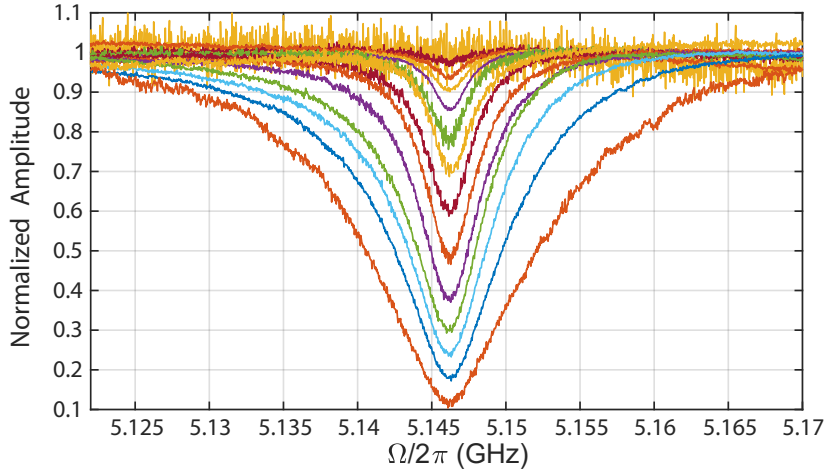


Figure 3.13 – **Optomechanical Induced Transparency of different pumping powers.** Fine sweep of the probing tone around the optical resonance of the cavity in Ref. [145] of $\kappa/2\pi = 220$ MHz with different pumping tone powers. The y-axis shows the reflection amplitude from the VNA normalized by the corresponding pumping powers.

The circulator feeds the reflected light to the detection stage. To achieve the desired tuning of the tones relative to the optical resonance, we send the reflected light to a coherent response setup, employing a network analyzer driving a phase modulator on the master laser [109]. For silicon, the optical absorption prevents one from injecting too much power into the cavity. Such nonlinear optical effect is much stronger at room temperature due to the large thermorefractive effect, and leads to thermal instability. As a result, the reflected optical signal

are amplified by an EDFA and filtered by an optical filter to suppress the amplified spontaneous emission noise, and detected by a fast photodiode with 12 GHz bandwidth. Besides, the reflected signal is mixed with a strong (~ 7 mW) local oscillator in a balanced heterodyne detection scheme, and the noise power spectral density of the subtracted photocurrent is analyzed using a spectrum analyzer.

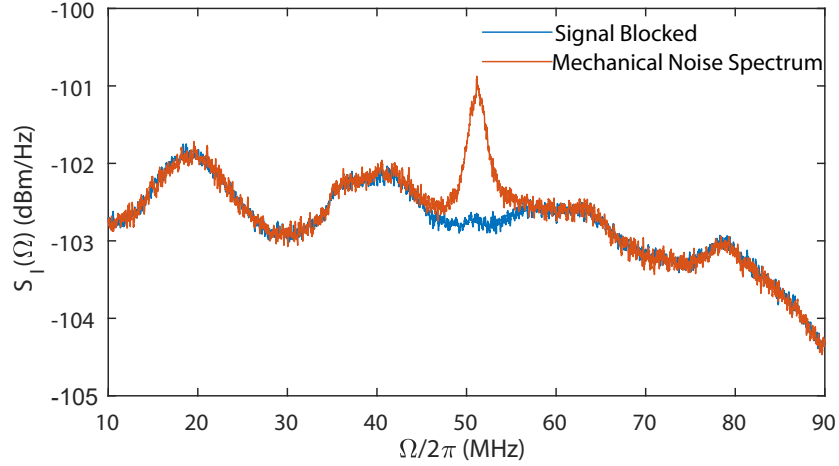


Figure 3.14 – **Incoherent noise spectrum from heterodyne detection.** Typical noise spectrum from BHD in the single-tone power-sweep measurements with $\Delta_c \sim -\Omega_m$. The shot noise spectrum with signal blocked is shown in blue while the noise spectrum of the thermo-mechanical sideband is shown in red.

A typical coherent response measurement is shown in Fig. 3.12. In this case, the pumping tone is red detuned by $-\Omega_m$ relative to the cavity resonance. A weak probe generated from the PM is scanning around the cavity resonance. In Fig. 3.12, a destructive interference is present in the broad cavity response. The dip in the cavity reflection around the mechanical frequency arises from the destructive interference of the direct detection of amplitude modulation caused by the two beating tones and the phase modulation imparted by the mechanical oscillator motion driven by the amplitude-modulated radiation-pressure. This is the optomechanically induced transparency due to radiation pressure force [109, 110]. The fit is shown in the red curve in Fig. 3.12 with a theoretical model [110]. We note that, in the fitting curve of Fig. 3.12, we only consider the fundamental mechanical mode with mechanical frequency $\Omega_m/2\pi \sim 5.145$ GHz. As quite evident in Fig. 3.12, a second mechanical mode of $\Omega_m/2\pi \sim 5.36$ GHz is coupled to the optical field with much lower optomechanical coupling rate. In this thesis, we focus on the quantum measurement of the fundamental mechanical mode.

The coherent response measurement is a standard measurement procedure to determine the pumping tone detuning relative to the cavity resonance Δ and also the optical linewidth κ . We

can thus calculate the intracavity photon number \bar{n}_c .

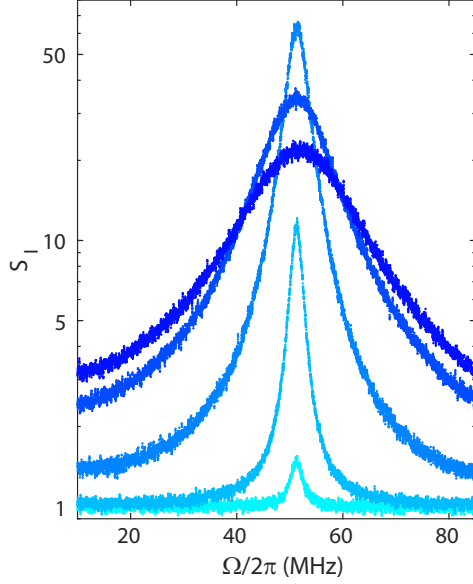


Figure 3.15 – Noise spectrum of balanced heterodyne detection. The noise spectrum is normalized to the shot noise floor and is taken with the cavity used in Ref. [145] at room temperature at different pumping powers for sideband cooling with the cooling tone close to the red sideband.

A series of measurements at different powers for sideband cooling can be performed while maintaining the pumping frequency around the red sideband ($\Delta = -\Omega_m$). The increased pumping power leads to the increased optomechanical damping rate. In Fig. 3.13, a zoomed view of the response measurement for probe frequency around the mechanical frequency is presented for different powers. When the pumping power increases, the dip in the cavity response becomes deeper and broader, which indicates the optomechanical damping of the mechanical oscillator, and can be utilized for the calibration of vacuum optomechanical coupling rate through $\Gamma_{\text{tot}} = \Gamma_m + \bar{n}_c \frac{4g_0^2}{\kappa}$, when pumping on the red sideband ($\Delta = -\Omega_m$).

We note that, for blue detuning, the radiation pressure force leads to an effective amplification of the mechanical motion. One will observe the optomechanically-induced-

absorption(OMIA), where a constructive interference could be present in the broad cavity response around the mechanical frequency.

We perform a quantum-limited measurement of the scattered thermomechanical sideband with balanced heterodyne detection, where the optical reflected light is mixed with a LO of high power (~ 6 mW). In our case, the LO is phased locked to the pumping laser on the blue side with a frequency separation of around the mechanical frequency. Typical incoherent noise spectra from the BHD are shown in Fig. 3.14. The blue curve corresponds to the shot noise and is obtained by blocking the signal beam in the BHD. We note that the uneven shot noise floor originates from the frequency dependent gain of the balanced detector, which has a bandwidth of 80 MHz. The red curve corresponds to the thermomechanical noise spectrum in the single-tone power-sweep measurements with the lowest intracavity photon number ($\bar{n}_c \sim 1$). For convenience, we normalize the noise spectrum to the shot noise.

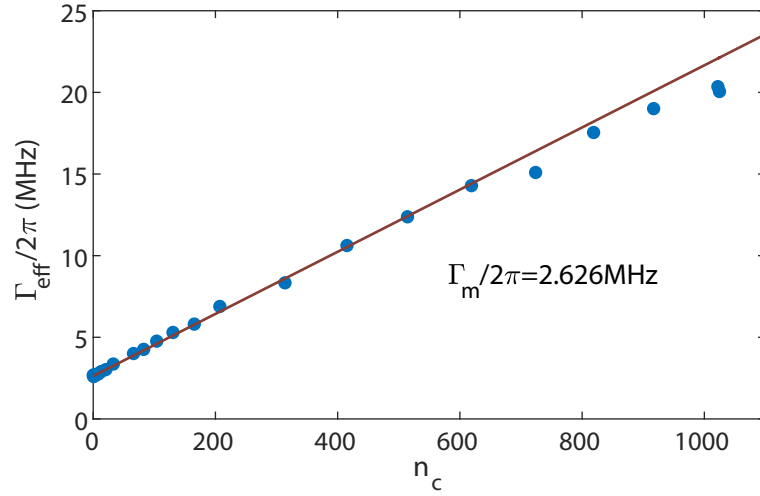


Figure 3.16 – **Effective mechanical damping rate at different intracavity photon number for sideband cooling at room temperature.** The blue dots show the fitted Γ_{eff} from the noise spectrum at different powers of the cavity used in Ref. [145]. The red line shows a linear fit of Γ_{eff} , from which the intrinsic damping rate Γ_m and vacuum optomechanical coupling rate g_0 can be obtained.

Figure 3.15 shows the single-sided noise spectrum consisting of the scattered thermomechanical sidebands from sideband-cooling measurements at different powers. Accordingly, we use a Lorentzian function to fit the noise spectrum in Fig. 3.15,

$$S_{\text{fit}}(\omega) = c + \frac{\Gamma_{\text{eff}} A_s}{\Gamma_{\text{eff}}^2/4 + (\omega - \omega_0)^2}, \quad (3.10)$$

where c , A_s , ω_0 and Γ_{eff} are the fitting parameters. c corresponds to the noise background. A and ω_0 correspond to the area and center frequency of the sideband from the cooling tone, with effective linewidth Γ_{eff} . From the fitted noise spectrum, we can obtain Γ_{eff} for each intracavity photon number.

For $\Delta = -\Omega_m$, Γ_{eff} has a linear dependence of \bar{n}_c as shown in Fig. 3.16. A linear fit of Γ_{eff} to \bar{n}_c results in a mechanical damping rate $\Gamma_m/2\pi \sim 2.626$ MHz and vacuum optomechanical coupling rate $g_0/2\pi \sim 1.06$ MHz. The phonon occupancy can be determined using mechanical noise thermometry by anchoring the normalized thermomechanical noise area to the room temperature thermal bath,

$$\bar{n}_f = \frac{A_s/\Gamma_s}{A_s^0/\Gamma_s^0} \frac{k_B T}{\hbar \Omega_m} \frac{\Gamma_m}{\Gamma_s^0 + \Gamma_m}. \quad (3.11)$$

where A_s^0 and Γ_s^0 are the sideband area and the scattering rate of the cooling tone at a specific

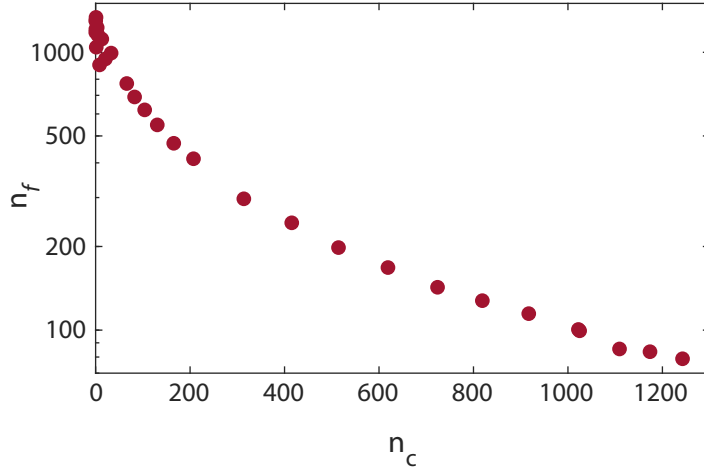


Figure 3.17 – **Final phonon occupancy at different cooling tone intracavity photon numbers.** This is performed on the cavity used in Ref. [145] with a linewidth $\kappa/2\pi = 220$ MHz for sideband cooling at room temperature.

anchor data point. In this case, it is assumed that the mechanical mode temperature T is given by the resistive thermometer and there is no excess heating at the anchor point with the lowest intracavity photon number. The mean phonon occupancy of the mechanical oscillator is $\bar{n}_{\text{th}} \simeq k_B T / \hbar \Omega_m$ when the mechanical mode is in equilibrium with the thermal reservoir. In the case of negligible optomechanical damping ($\Gamma_s^0 \ll \Gamma_m$), Eq. (3.11) can be simplified to $\bar{n}_f = \frac{A_s/\Gamma_s}{A_s^0/\Gamma_s^0} \frac{k_B T}{\hbar \Omega_m}$. In the power-sweep series, $\Delta_c = -\Omega_m$, we have $\bar{n}_f = \frac{A_s/n_c}{A_s^0/n_s^0} \frac{k_B T}{\hbar \Omega_m}$.

The calibrated final occupancy versus different intracavity photon number is presented in Fig. 3.17. At the highest pumping power ($\bar{n}_c \sim 1170$), we achieve a minimum phonon occupancy ~ 78.8 , which corresponds to a mechanical mode temperature of ~ 19.5 .

As mentioned above, the ultrahigh optical Q and small mode volume of the OMC can lead to high intracavity photon number and strong optomechanical coupling. However, this also leads to a reduced threshold for undesired optical nonlinearity [146]. In silicon, these nonlinearities become appreciable at elevated optical power levels, as the Kerr-type nonlinearities and two photon absorptions. This results in both temperature rise and additional cavity frequency change. These undesired optical nonlinearity also impose a practical limit on the number of photons inside a cavity to achieve the strong optomechanical coupling, especially at room temperature due to the large refractive-optical effect. For room temperature laser cooling, the final occupation can be further reduced for example by improving the mechanical damping rate by decreasing the gas pressure.

3.4.2 Cryogenic Measurement

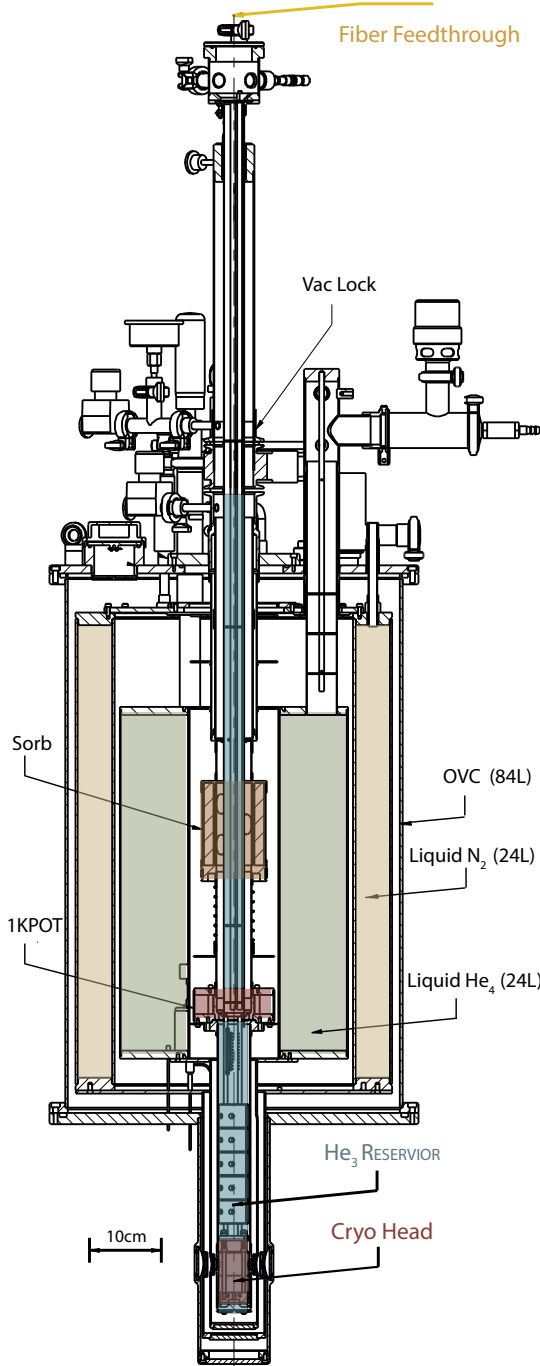


Figure 3.18 – Design of Heliox TL Cryostat

One of the greatest challenges for quantum measurement of mechanical motion is the mechanical decoherence, which is determined by the thermal bath. For this reason, most of the quantum optomechanical experiments are performed in cryogenic environment.

Cryogenically cooled optomechanical crystals are promising platforms for various quantum optomechanical experiments [96, 97, 147], mainly due to their GHz-scale mechanical frequencies. For a OMC at temperatures in the millikelvin range in a dilution refrigerators, it should be at its ground state $\bar{n}_{th} \ll 1$. However, the vacuum environment combined with the nanobeam geometry and reduced thermal conductivity of silicon at cryogenic temperatures [115], lead to large absorption heating even at very low probing powers [148]. This severely limits both the minimum achievable phonon occupation and the optomechanical cooperativity, set by the number of intracavity photons. Besides, extremely weak optical pulses have to be adopted in such measurements [96, 97, 147, 148].

We choose instead to use a ^3He *buffer gas* cryostat (Oxford Instruments HelioxTL), which provides sufficient thermalization of the sample to the gaseous ^3He , as shown in Fig. 3.18. On the top loading insert, there is a fiber feedthrough where light is guided from room temperature into the cryostat for opti-

cal measurement, as shown in yellow. The vacuum lock in the middle of the probe allows high degree of thermal isolation between room temperature and the cryogenic environment. Several successive layers further guarantees the thermal isolation, including an outer vacuum chamber (OVC) of pressure below 10^{-5} mbar, a liquid nitrogen reservoir at 77K (shown in light brown) and inner liquid ^4He reservoir at 4K (shown in light green). These layers are isolated by an inner vacuum chamber. The bottom of the probe is loaded in the *gaseous* ^3He environment as shown in light blue. ^3He has a critical temperature of around 3.3K. Below this, it can be liquefied at sufficiently high pressures. A 1KPot can be filled with liquid ^4He and further pumped to decrease the temperature. This leads to the condensation of the ^3He . A sorption pump is adopted to further reduce the vapour pressure above the ^3He surface, where ^3He adsorbs to a sorb with very large surface area. This allows access to temperature down to 300mK. At temperature of 1K, for our OMC with mechanical frequency of around 5GHz, the mean phonon occupancy is ~ 4 . The sorb temperature controls the pressure of the ^3He reservoir and thus the temperature. This is tuned by a sorb needle valve, which determines the amount of liquid ^4He that passes through. We note that both the 1KPot and the sorb are pumped by scroll pumps which are placed in a separate room around 10m away, to reduce the excess vibration in optical measurements.

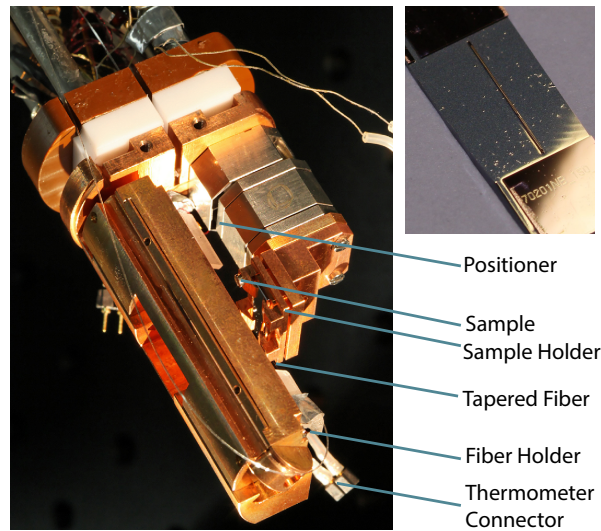


Figure 3.19 – **Preparation of the Cryohead.** On the left is the cryohead with the tapered fiber and the chip mounted. Details of the nano-positioner, sample holder, tapered fiber, fiber holder, thermometer connector are shown. On the top right is the photo of a typical chip with about 100 cavities on it for characterization.

The cryohead is placed at the bottom of the loading insert as shown in dark brown in Fig. 3.18, where we mount the sample and all the sensors. The HelioxTL comes with an optical window access with special coating to reduce excess radiation heating. This provides us with

large flexibility for optical coupling. The preparation of the cryogenic setup starts from the cryohead, which is shown in Fig. 3.19. The sample under test is shown on the top right. As mentioned previously, we sweep the number of the holes in the OMC to adjust the external coupling rate. Besides, we apply additional corrections to the hole sizes and the beam width to achieve proper optical resonant wavelength. FEM simulations show that such corrections lead to negligible degradation to the optical quality factor and optomechanical coupling rate when the applied corrections are within ± 15 nm. This corresponds to a resonant wavelength range of tens nanometers. As a result, around 100 cavities are patterned on each sample for characterization. The sample is mounted on a copper sample holder, which is fixed to a two-axes nano-positioner. This gives lots of flexibility for coupling the sample to the tapered fiber, which is glued on a glass fiber holder with UV glue, i.e. Norland Optical Adhesive 81. The UV glue has a refractive index around 1.5, which is similar to glass, and introduces no excess scattering loss around the glue region. The contact region on the glass holder has been intentionally roughened to ensure robust adhesion. We note that, both the UV glue and the glass holder survive very well after cooling down of the Heliox insert despite the drastic temperature change. Under UV radiation, the UV glue cures to a hard film but it will not become brittle. It has a small amount of resiliency that provides strain relief from vibrations or temperature extremes, and insures long term performance of the adhesive bond. Cryogenic thermometers are mounted on the bottom of the cryohead, which is located around several centimeters away from the sample and provides accurate readout of the sample temperature, ranging from mK to room temperature.

For all the cavities of each sample, we typically adopt the same waveguide design for the taper coupling. Before loading the Heliox insert, we adjust the taper position to achieve optimal coupling efficiency to the OMC, which critically depends on the taper diameter. We intentionally introduce a gentle tilt of the tapered fiber to ensure that the taper touches the supporting pad first. As shown in the bottom of Fig. 3.19, the fiber forms a "U" shape, which may result in excess bending loss. Although we focus on only the cavity reflection, the bending loss can introduce excess heat load at low temperatures.

As mentioned in the sample fabrication section, the native oxide of the silicon OMC typically leads to increased mechanical dissipation at low temperatures, due to the lattice mismatch between silicon device layer and the native oxide. For this reason, we terminate the silicon device layer with hydrogen atom before cooling down. The sample is cleaned with Piranha solution and dipped into a diluted HF solution(5%) for few seconds. We then immediately mount the sample on the probe. After pre-alignment of the taper and the sample again, the

cryohead shown in Fig. 3.19 is then screwed inside a copper cage to protect the taper and the nano-positioner during the loading and unloading of the Heliox insert. We take special care to the fiber arrangement to avoid unwanted scattering loss during the probe preparation by monitoring the fiber transmission continuously.

The Heliox insert is then mounted on top of the cryostat and pumped by a scroll pump to a pressure below 10^{-3} mbar within one hour to avoid further oxidation of the OMC. A leak test is performed on the Heliox insert, especially around the valves, connectors, clamps, and the fiber feedthrough, to ensure perfect vacuum. Before loading the Heliox insert, the ^3He in the cryostat is typically collected in a large volume ^3He dump (15L) using a cryo pump, which is disconnected from the ^3He reservoir. We then load the Heliox insert slowly and pump the vacuum lock continuously, with the output gas analyzed by a leak detector. The sorb temperature is kept below 20K to avoid drastic temperature decrease. To ensure sufficient thermalization of the Heliox insert, we introduce a small amount of ^3He of pressure ~ 1 mbar into the cryostat. The temperature decreases slowly at a rate of $\sim 0.3\text{K}/\text{min}$. The insert is thermalized slowly to the cryostat overnight with the taper transmission, cryostat parameters monitored continuously.

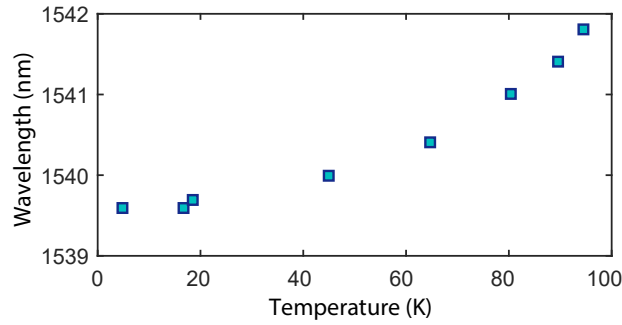


Figure 3.20 – **Optical resonant wavelength of OMC versus the cryostat temperature.** The resonant wavelength of an OMC with $\kappa/2\pi = 1.6\text{GHz}$ [122] is measured by a wavemeter at low pumping powers around $1\mu\text{W}$ with the cryostat pressure around 1 mbar.

The temperature decrease leads to the refractive index change of the silicon due to the thermorefractive effect. In Fig. 3.20, we show the optical resonant wavelength of a typical OMC cavity versus the cryostat temperature below 100K. The temperature decrease leads to a decreased optical resonant wavelength, i.e. $dn/dT > 0$. We note that the thermorefractive effect is much weaker for lower temperatures in the range of 1 K to 20 K [149]. Besides, for temperature below 4 K, intracavity photons shift the optical resonance to higher frequencies, due to a combination of thermo-optic and thermal expansion effects in silicon. As a result, the optical resonant wavelength decreases by around 15 nm from room temperature to the base

temperature of the cryostat. When the probe reaches the ^3He bath temperature around 4K, the cold buffer gas provides additional thermalization of the OMC sample despite the drastically decreased thermal conductivity of silicon at cryogenic temperatures [115]. In Fig. 3.21 we

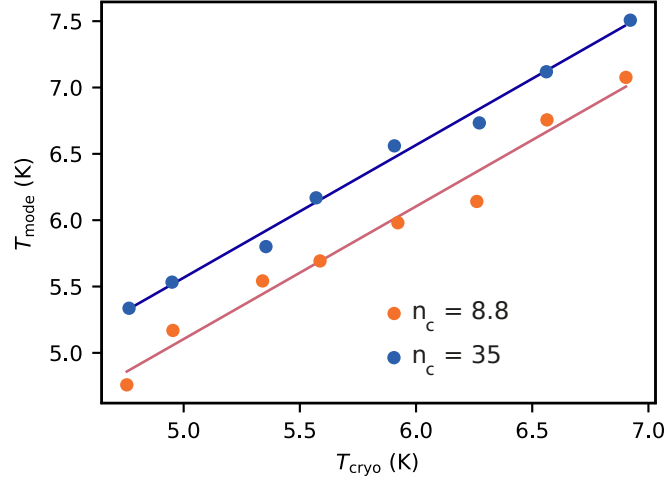


Figure 3.21 – **Laser power induced heating of the mechanical mode.** Mechanical mode temperature of an OMC with $\kappa/2\pi = 1.6\text{GHz}$ [122] versus cryostat temperature at different pumping powers which correspond to intracavity photon number $n_c = 8.8$ and $n_c = 35$, with sample pressure $\sim 25\text{mbar}$. The temperature is controlled by the heater close to the sample.

show the mechanical mode temperature of a typical OMC as a function of the temperature of the cryostat for two different pump powers, corresponding to mean intracavity photon number of 8.8 and 35, keeping the buffer gas pressure constant at 25mbar. The mechanical mode temperature is consistently higher for the higher input power, giving clear indication of optical absorption heating. The cryostat can not even be thermalized at a pressure of 25 mbar.

Working in a buffer gas environment enables us to substantially improve the thermalization of our optomechanical system. The pressure of the buffer gas is controlled by a sorption pump, and enables us to achieve much lower heating at the expense of higher mechanical damping rate due to the gas damping. For quantum measurement of the mechanical motion of the OMC, there is thus an optimal working condition in terms of gas pressure. Such thermalization performance can be verified by series of sideband cooling measurements, with a single cooling tone applied at the lower mechanical sideband, $\Delta = -\Omega_m$. In the well-resolved sideband regime, dynamical backaction provides additional damping $\Gamma_{\text{opt}} = C\Gamma_m$ where $C = C_0\bar{n}_c$ is the optomechanical cooperativity for mean intracavity photons \bar{n}_c . The mean thermal occupation of the oscillator is lowered to,

$$\bar{n}_f = \frac{\Gamma_m \bar{n}_{\text{th}} + \Gamma_{\text{opt}} n_{\text{qbl}}}{\Gamma_m + \Gamma_{\text{opt}}} = \frac{\bar{n}_{\text{th}} + C n_{\text{qbl}}}{1 + C}, \quad (3.12)$$

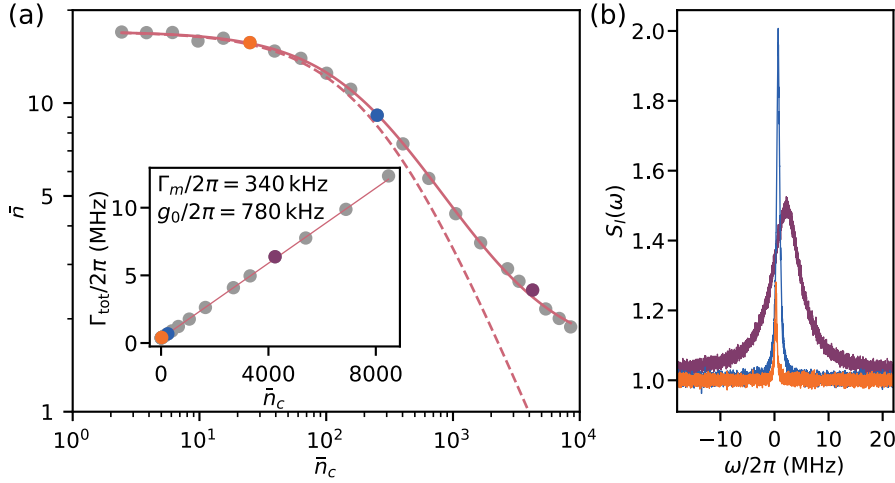


Figure 3.22 – **Sideband cooling of the mechanical mode of the cavity used in Ref. [122] at 4K.** (a) Mechanical occupation \bar{n} vs. \bar{n}_c from the mechanical noise thermometry. \bar{n} is anchored to the cryostat temperature, $\bar{n}_{\text{th}} = 17$, at lowest cooling power. The solid line is a fit to the simple heating model (3.13) with α and \bar{n}_{th} as free parameters, and the dashed line shows cooling in absence of absorption heating. The inset shows total mechanical damping Γ_{tot} vs. \bar{n}_c , with a linear fit used to extract the mechanical damping rate Γ_m and the optomechanical coupling rate g_0 . (b) Noise spectra $S_I(\omega)$, normalized to the shot noise level, at three different points.

where \bar{n}_{th} is the mean thermal occupation of the environment and $n_{\text{qbl}} = \kappa^2 / (16\Omega_m^2)$ is the quantum limit of sideband cooling [55, 56], which is negligible for sideband-resolved systems.

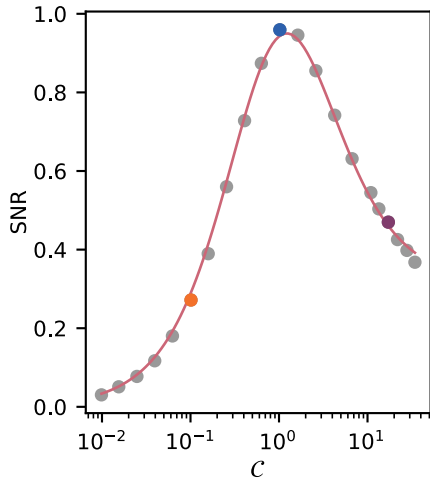


Figure 3.23 – **Signal-to-noise ratio (SNR) vs. the cooperativity C with a fit to the model (3.14) with free parameters η and heating α .** The measurement is performed on the OMC of $\kappa/2\pi = 1.6\text{GHz}$ [122] at 4K of pressure $\sim 160\text{mbar}$.

The simplest treatment of optical absorption heating is provided by the linear model $\bar{n}_{\text{th}} \rightarrow \bar{n}_{\text{th}} + \alpha \bar{n}_c$, where α is the extraneous heating of the bath in terms of oscillator phonons per intracavity photon. Within this model, we have

$$\bar{n}_f = \frac{\bar{n}_{\text{th}} + \alpha \bar{n}_c}{1 + C}, \quad (3.13)$$

the asymptotic quantum limit n_{qbl} is effectively replaced by the heating limit of α/C_0 phonons. In this model, we find the signal-noise-ratio (SNR), defined as the peak of $S_I(\omega)$ relative to the noise floor,

$$\text{SNR} = \frac{4\eta C \bar{n}_f}{1 + C} = 4\eta \frac{(\bar{n}_{\text{th}} + [\alpha/C_0]C)C}{(1 + C)^2}, \quad (3.14)$$

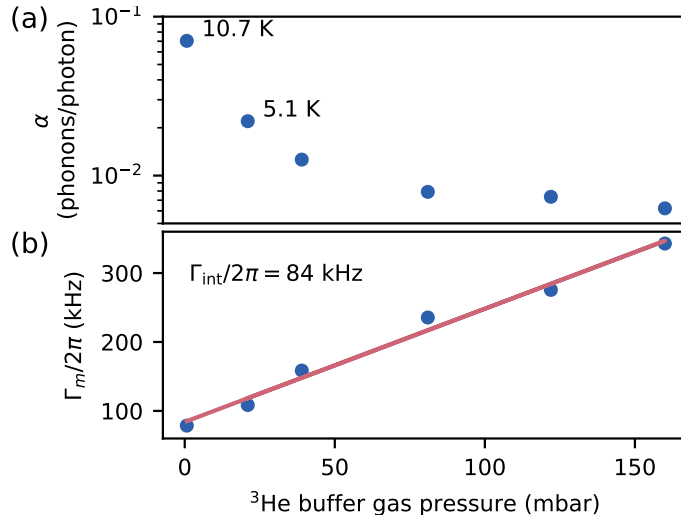


Figure 3.24 – **Effect of the buffer ^3He gas pressure on sideband cooling of an OMC of $\kappa/2\pi = 1.6\text{GHz}$ [122].** The ^3He gas pressure is controlled by adjusting the sorb temperature. (a) Oscillator heating α vs. gas pressure. Measurements were done at cryostat temperature of 4.5 K except for low pressures, where insufficient thermalization leads to elevated bath temperatures, as indicated in (b). (b) Mechanical damping vs. gas pressure. The linear field yields intrinsic damping $\Gamma_{\text{int}}/2\pi = 84\text{kHz}$.

where η is the overall detection efficiency.

Figure 3.22(a) shows sideband cooling of an sample with $\kappa/2\pi \sim 1.6\text{GHz}$ at cryostat temperature of 4 K with the buffer gas pressure at 160 mbar [122]. In order to calibrate \bar{n}_f , we assume the heating is negligible at the point of lowest power ($\bar{n}_c \sim 2$) and the oscillator is completely thermalized to the cryostat. We infer \bar{n}_f from the area of the noise spectra (Fig. 3.22(b)). The SNR of the spectra is shown in Fig. 3.23. We can thus fit the data of Fig. 3.22(a) and Fig. 3.23 using Eqs. (3.13) and (3.14) respectively, which gives extraneous heating of $\alpha = 6.3 \times 10^{-3} = 1.5C_0$ and overall efficiency $\eta = 0.04$.

To more accurately quantify the optical absorption heating rate, we studied this effect by performing sideband cooling measurements at different buffer gas pressures, with the results shown in Fig. 3.24. As expected, increasing the pressure leads to a decreased extraneous heating α (Fig. 3.24a) at the cost of additional mechanical damping due to gas damping (Fig. 3.24(b)). The intrinsic mechanical damping rate is $\Gamma_{\text{int}}/2\pi \sim 84\text{kHz}$. The excess mechanical damping rate due to the gas damping has a linear dependence to the ^3He buffer gas pressure, i.e. $\Gamma_{\text{gas}}/P \sim 2\pi \times 1.5\text{kHz/mbar}$. The combined effect of gas damping and thermalization results in theoretical cooling limits α/C_0 of 1.3–1.5 phonons at pressure of 160 mbar. We note that, at pressure of $\sim 0\text{mbar}$, we achieve a minimum \bar{n}_f of 5.7 due to extremely large

absorption heating, despite the low Γ_m . Besides, for pressures below 20 mbar, the cryostat temperature can't even be thermalized to the ^4He reservoir temperature, due to the deficient thermalization.

The experiments shown above are performed under gaseous ^3He environment around 4K. As mentioned previously, the cryostat can be operated in a regime, where the ^3He in the sample reservoir is condensed and further pumped to reduce the temperature. This enables the sample to reach temperature below 4 K, thus lowers the required input power for ground state cooling.

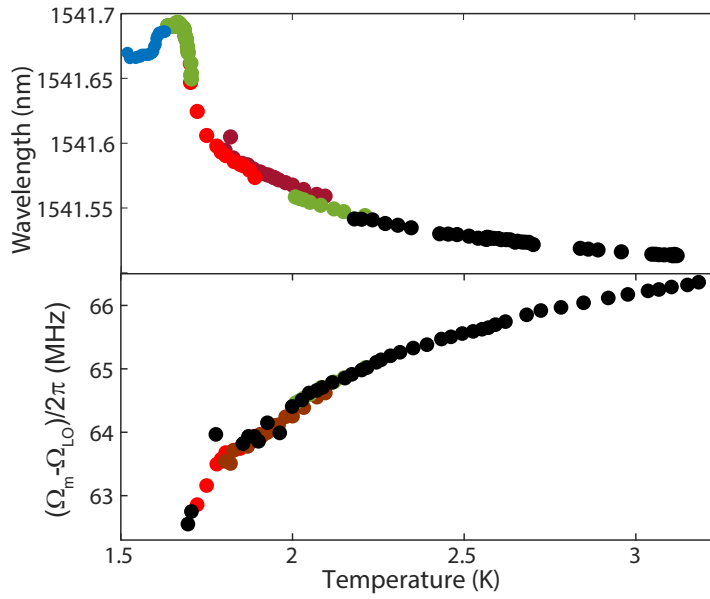


Figure 3.25 – Optical resonant wavelength and mechanical frequency of the OMC below 4K. The sample has $\kappa/2\pi = 1.6\text{GHz}$ [122]. The temperature is controlled by the 1KPot and sorb temperatures. Upper panel, optical resonant wavelength versus temperature at low temperatures measured by a wavelength meter. The wavelength is monitored by a coherent response measurement with cooling tone at $\Delta \sim -\Omega_m$ of low intracavity photon number ~ 1.5 . Lower panel, mechanical frequency versus temperature at low temperatures, shown as the frequency difference between Ω_m and LO locking frequency Ω_{LO} . The mechanical frequency is fitted from the noise spectrum in the BHD. Different colors correspond to different measurement runs, which shows consistent results.

Figure 3.25 shows the optical resonant wavelength and the mechanical frequency versus the temperature below 4K when the ^3He is cooled down by the 1KPot. The cavity, used in Ref. [122], is probed by a weak cooling tone of intracavity photon number around 1.5. The laser detuning is maintained at $\Delta \sim -\Omega_m$, which is continuously monitored by the response measurement. The mechanical noise spectrum is taken immediately from the balanced heterodyne detection

to obtain the mechanical damping rate and the mechanical frequency. The frequency shown in the lower panel of Fig. 3.25 is fitted from the mechanical noise spectrum with a Lorentzian function, which is the difference between the mechanical frequency and locking frequency of the local oscillator. In Fig. 3.25, the temperature above 1.7K is controlled by the 1KPot temperature, where ^3He is not yet completely condensed. By decreasing the 1KPot temperature, lower ^3He sample reservoir temperature can be achieved. We keep sorb temperature above 30K, to release all the ^3He . As shown in Fig. 3.25, the temperature decrease leads to large wavelength increase and mechanical frequency decrease. The different colors in Fig. 3.25 correspond to different measurement runs, which give consistent results. As the sorb temperature keeps decreasing, it starts to pump the condensed ^3He on the sample surface, leading to a decreased resonant wavelength. We attribute such OMC property changes to the condensed ^3He on the surface of the device. The optical frequency change is due to the larger refractive index of liquid ^3He , i.e. 1.03, compared to vacuum or gaseous ^3He . The optical frequency change is given by the expression,

$$\frac{\Delta\omega}{\omega_0} = -\frac{1}{2} \frac{\iiint_{\text{He}} (n_{\text{He}}^2 - 1) |E_0(\vec{r})|^2 d\vec{r}}{\iiint_{\text{all}} n^2(\vec{r}) |E_0(\vec{r})|^2 d\vec{r}}, \quad (3.15)$$

where $E_0(r)$ is the electric field distribution, n_{He} is the refractive index of the ^3He . The mechanical frequency decrease is due to the mass loading of the ^3He on the surface of OMC, which is given by the expression, $\frac{\Delta\Omega_m}{\Omega_m} = -\frac{\Delta m}{2m}$, where m is the effective mass of the mechanical mode. Preliminary analysis of the wavelength change shows that there is a condensed ^3He layer with maximum thickness of $\sim 10\text{ nm}$, which is verified with FEM simulations. In this sense, an optomechanical spectroscopy of the thin film ^3He is performed with high sensitivity and low optical probing power due to the ultra-small mode volume and also strong optomechanical coupling rate.

The study of liquid and superfluid helium has been an interesting research subject in the quantum optomechanics community in recent years, given the interest in the field of superfluids. There have been various experimental optomechanical platforms [150–159]. Optomechanical experiments with superfluid/fluid ^4He have been performed, where quantum measurement and control of the superfluid ^4He have been explored [150–154, 156–159]. In the Bowen group, microtoroidal resonators are utilized to study the excitations of superfluid ^4He , the vortex formation, as well as the development of theoretical tools in such systems [151, 159]. The Harris group uses the degrees of freedom offered by liquid or superfluid helium as the mechanical part of the system [150, 154]. This interesting approach directly takes advantage of the optics-fluid coupling, where motional sideband asymmetry of the mechanical mode of the

superfluid is observed. Tang's group investigates the sensing capabilities of a microtoroidal resonator submerged in microfluidic channels as well in superfluid helium [157]. Our result shows an interesting direction quantum optical measurement with nanoscale ^3He thin film, which remains unexplored in the past. The behavior between these two fluids is fundamentally different, with ^4He as boson while ^3He as fermion. In addition, the optomechanical crystals can be adopted for fluid and superfluid helium study, given their very low effective mass (100s fg) and high quality factors, thus providing a far greater sensitivity for mass sensing with quantum limited optical detection.

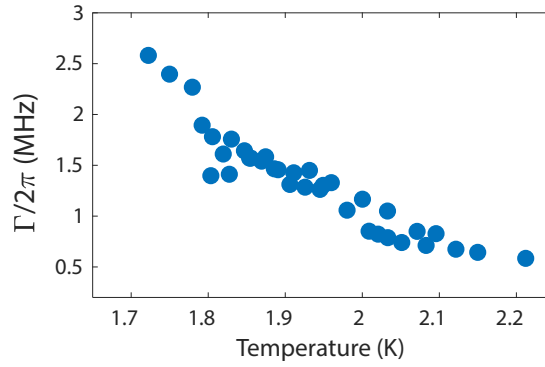


Figure 3.26 – **Mechanical damping rate below 4K.** The measurement is performed under the same condition as Fig. 3.25 on the same OMC [122]. The damping rate is fitted from the mechanical noise spectrum in BHD with pumping frequency maintained at $\Delta \sim -\Omega_m$ at low intracavity photon number ~ 1.5 .

We note however, due to mass loading of the ^3He , excess mechanical damping appears under condensation, as shown in Fig. 3.26. The large mechanical damping rate Γ above 2.2K is due to the high ^3He pressure, similar to the previous measurements at 4K. For lower temperatures, the mechanical mode is broadened due to ^3He condensation, which can lead to extremely large damping rate $\sim 2\pi \times 3$ MHz for temperatures below 1.7K, more than one order of magnitude larger than the intrinsic mechanical damping rate. Despite the large mechanical damping rate, the quantum limited detection of the thermomechanical sideband enables optomechanical measurement of the thin-film ^3He condensed on the OMC device layer with sufficient signal-to-noise ratio even under such low temperatures. Due to the broadened mechanical damping rate, the condensation of the ^3He limits the laser sideband cooling for low input powers. At high input powers, the optical absorption heating leads to the evaporation of the ^3He and restores the mechanical damping rate and also the mechanical frequency. Besides, the condensed ^3He may provide better thermalization of the sample due to the ^3He evaporation. This is investigated in more details in the work related to the laser cooling to the zero-point energy of the nanomechanical oscillator in this thesis [145].

4 Floquet Dynamics in Quantum Measurements of Mechanical Motion

In this chapter, we show that *Floquet dynamics* can arise in motional sideband asymmetry measurements due to presence of Kerr-type nonlinearities [122]. Floquet dynamics gives rise to an artificially modified motional sideband asymmetry by redistributing thermal and quantum fluctuations among the initially independently scattered thermomechanical sidebands. For pump tones exhibiting large frequency separation, the dynamics is suppressed and accurate quantum noise thermometry demonstrated. We develop a theoretical model based on Floquet theory that accurately describes our observations. The resulting dynamics can be understood as resulting from a *synthetic gauge field* among the Fourier modes, which is created by the phase lag of the Kerr-type response. This novel phenomenon has wide-ranging implications for schemes utilizing several pumping tones, as commonly employed in backaction-evading measurements and dissipative mechanical squeezing. Our observation may equally well be used for optomechanical Floquet engineering, e.g. generation of topological phases of sound by periodic time-modulation.

4.1 Floquet dynamics

Floquet dynamics results from periodic modulation of quantum systems. This has been developed theoretically and experimentally over the last decades in different areas in physics. Early application of the Floquet theorem dealt with a two-level quantum system interacting with strong oscillating fields [160, 161]. Utilizing Floquet theorem, a temporal analog of the Bloch theorem, a lot of exotic phenomenon has been explored in wide range of quantum systems with the control of time-periodic external fields [161–163]. For example, by time dependent perturbations in systems that are topologically trivial in equilibrium, new topological phases can be generated in non-equilibrium conditions, which is the so-called Floquet topologi-

cal insulators [164] and opens new avenues in the search of quantum materials. Similarly concepts have also been implemented in the photonic and acoustic systems with temporal modulation, to generate artificial gauge field and the topology protected one-way edge state [165–167]. More recently, Floquet engineering techniques have been adopted in experiments with many-body quantum systems [162, 163, 168, 169].

Although Floquet engineering has been applied to different fields of physics, here we show the Floquet dynamics is observed in quantum optomechanical measurements. We demonstrate experimentally and describe theoretically how the Kerr-type nonlinearities, *i.e.* light-induced cavity frequency shifts [79, 146, 170], can lead to Floquet dynamics in the presence of multiple drive tones, coupling of originally independent thermomechanical sidebands (e.g. Stokes and anti-Stokes sidebands) and modification of the scattering rates. This mechanism affects quantum measurements of mechanical motion, and we specifically demonstrate it leads to an artificially modified quantum sideband asymmetry.

We specifically analyze this new dynamics in the context of motional sideband asymmetry [67–70], which has received significant attention as it is a signature of the quantum-mechanical nature of the interaction between light and engineered mechanical oscillators. The anti-Stokes scattering (resulting in blue-shifted radiation) rate scales with \bar{n} , while the Stokes scattering rate scales with $\bar{n} + 1$, where \bar{n} denotes the average thermal occupation of the vibrational mode [111]. The ratio of the two scattering rates is given by the Boltzmann factor $\exp(-\hbar\Omega_m/k_B T)$, where Ω_m is the frequency of the oscillator and T its mode temperature, which therefore allows for absolute and self-calibrated quantum noise thermometry. Such motional sideband asymmetry has been observed in the quantized motion of laser-cooled trapped ions [171] and cold atoms in optical lattices [172] and used for thermometry in solids [173–175] and molecules [176], and it is commercially used in fiber optical distributed temperature measurements [177]. To exploit sideband asymmetry in optomechanical system for absolute thermometry without the need for calibration [91], understanding all noise contributions, such as laser noises [71, 178, 179], is crucial.

The thermal Kerr-type nonlinearity is shown to modify the motional sideband asymmetry, giving lower temperatures than the actual ones by artificially augmenting the sideband ratio. Counterintuitively, the coupling of the sidebands due to the Kerr-type nonlinearity and the induced artificial asymmetry are even present when operating far (*i.e.* $\times 10$) above the characteristic thermal response of the system. It can only be eliminated by separating the driving tones in frequency far beyond the bandwidth of the Kerr-type nonlinearity, as verified by independent measurements. The intrinsic motional sideband asymmetry is then restored,

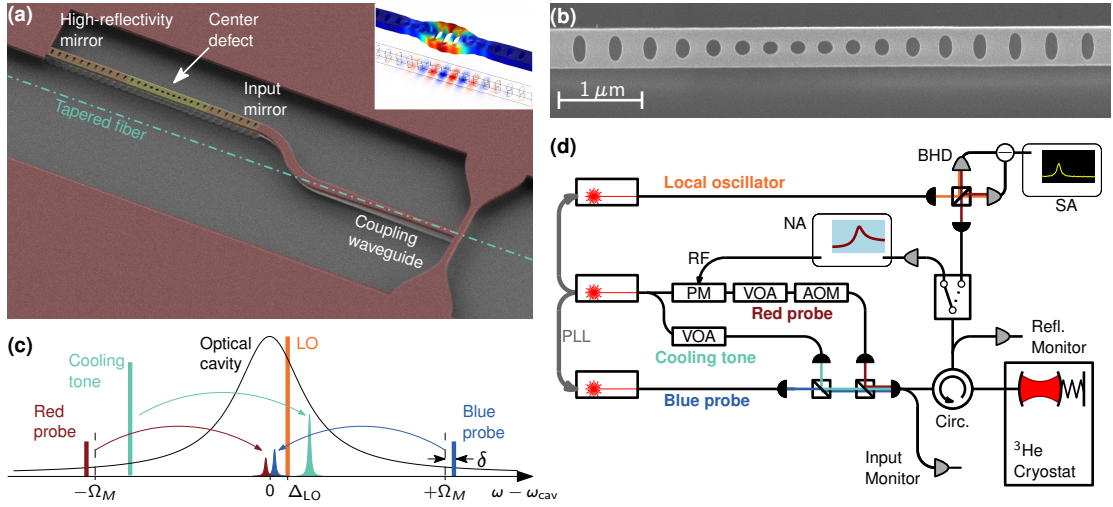


Figure 4.1 – Optomechanical crystal and experimental setup. (a) False-color SEM image of the silicon optomechanical crystal cavity with a waveguide for laser input coupling. The path of the tapered fiber is indicated. The inset shows the simulated mechanical breathing mode and optical mode. (b) SEM image of the cavity. (c) Scheme for motional sideband asymmetry measurement using two probe tones and a cooling tone. (d) Experimental setup. PM, phase modulator; VOA, variable optical attenuator; AOM, acousto-optical modulator; BHD, balanced heterodyne detector; SA, spectrum analyzer; NA, network analyzer; PLL, phase-locked loop.

and enables performing self-calibrated thermometry.

4.2 Experimental Results

Our experimental system is an OMC [136], as shown in Fig. 6.2. Optically, the device functions as a single-sided cavity with a partially transmitting input mirror. Light is evanescently coupled from a tapered optical fiber into a waveguide that forms part of the nanobeam with efficiency exceeding 50%. The optical resonance is at 1540 nm with a linewidth of $\kappa/2\pi = 1.6$ GHz, of which $\kappa_{\text{ex}} = 0.3\kappa$ are extrinsic losses to the input mirror. The optical mode is optomechanically coupled to a mechanical breathing mode of frequency $\Omega_m/2\pi = 5.3$ GHz, strongly confined due to a phononic bandgap, with an intrinsic linewidth of $\Gamma_{\text{int}}/2\pi = 84$ kHz. This places the system in the resolved sideband regime [180], i.e. $\Omega_m > \kappa$, as required for ground-state cooling [55, 56]. The measured optomechanical coupling rate is $g_0/2\pi = 780$ kHz. Our system is passively cooled to low initial thermal occupancy at 4.5 K (thermal occupancy at bath temperature $\bar{n}_{\text{th}} \simeq 17$) using a ^3He buffer gas cryostat. The buffer gas provides additional mechanical damping, increasing Γ_{int} by several 10s kHz to the actual mechanical linewidth Γ_m [145]. The buffer gas environment enables greatly enhanced thermalization of the oscillator and is necessary for cooling close to the ground state, unlike previous measurements under

vacuum [60, 96, 97, 147, 148, 181].

To measure motional sideband asymmetry, we employ two probe tones, around upper and lower motional sidebands, and in addition apply a strong tone near the lower sideband for sideband cooling (Fig. 6.2c). Such multi-tone probing scheme has been applied in previous experiments in the microwave domain [70, 182]. The two weak equal-power probes (about $n_c = 100$ mean intracavity photons each) are applied at frequencies $\omega_{\text{cav}} \pm (\Omega_m + \delta)$. The cooling tone is blue-detuned from the lower probe by the frequency Ω_{mod} , where $\Gamma_m \ll \Omega_{\text{mod}} \ll \kappa$. The red-detuned probe will generate a resonantly enhanced anti-Stokes Raman process, where a probe photon is upconverted in frequency from $-\Omega_m - \delta$ to $-\delta$, while destroying a phonon in the mechanical oscillator. The converse occurs for the blue-detuned probe, where a probe photon is downconverted from $\Omega_m + \delta$ to δ while creating a phonon, thus forming the resonant enhanced Stokes sideband. The experimental setup is shown in Fig. 6.2d. We use balanced heterodyne detection for quantum-limited measurement of the scattered thermomechanical sidebands in the output spectrum. The overall detection efficiency is $\eta \simeq 4\%$. We measure the symmetrized autocorrelator of the photocurrent $S_I(\omega) = \frac{1}{2} \int_{-\infty}^{\infty} \langle \hat{I}_{\text{out}}(t + t') \hat{I}_{\text{out}}(t') \rangle e^{i\omega t} dt$, where the average over t' is denoted by an overbar [70, 183]. The one-sided heterodyne spectrum takes the form (in the resolved sideband limit)

$$S_I(\omega + \Delta_{\text{LO}}) = 1 + \eta \Gamma_{\text{tot}} \left\{ \frac{\Gamma_m C_{\text{red}} \bar{n}}{\Gamma_{\text{tot}}^2/4 + (\omega + \delta)^2} + \frac{\Gamma_m C_{\text{cool}} \bar{n}}{\Gamma_{\text{tot}}^2/4 + (\omega + \delta - \Omega_{\text{mod}})^2} + \frac{\Gamma_m C_{\text{blue}} (\bar{n} + 1)}{\Gamma_{\text{tot}}^2/4 + (\omega - \delta)^2} \right\}, \quad (4.1)$$

where we have introduced cooperativities $C_{\text{red,blue,cool}} \equiv 4g_{r,b,c}^2/(\kappa\Gamma_m)$, the light-enhanced optomechanical coupling $g_{r,b,c} \equiv g_0 \sqrt{\bar{n}_{r,b,c}}$, reduced occupancy $\bar{n} = \Gamma_m \bar{n}_{\text{th}}/\Gamma_{\text{tot}}$, local oscillator detuning $\Delta_{\text{LO}} = \omega_{\text{LO}} - \omega_{\text{cav}}$, and incorporated the effect of sideband cooling into a broadened mechanical linewidth $\Gamma_{\text{tot}} \simeq \Gamma_m(1 + C_{\text{cool}})$. In the last expression we assume weak probe tones of equal strength, such that they do not contribute to the total mechanical damping, and taken the good cavity limit $\kappa/\Omega_m \rightarrow \infty$, thus neglecting the quantum backaction limit to optomechanical cooling [55, 56], which is of no importance here. We further assume that the cavity linewidth is much larger than the detuning and effective mechanical linewidth $\kappa \gg \delta, \Gamma_{\text{tot}}$, such that the optical susceptibility can be evaluated on resonance, and neglect classical laser noise. Equation (4.1) is normalized to the shot noise floor, includes the overall detection efficiency η , and we have chosen to show only sidebands close to resonance, the others are heavily suppressed due to the cavity resonance.

For our measurement, the red and blue cooperativities are chosen to be equal $C_{\text{red}} = C_{\text{blue}} \equiv C$, such that the Lorentzian probe tone sidebands centered around $\Delta_{\text{LO}} \pm \delta$ have weights pro-

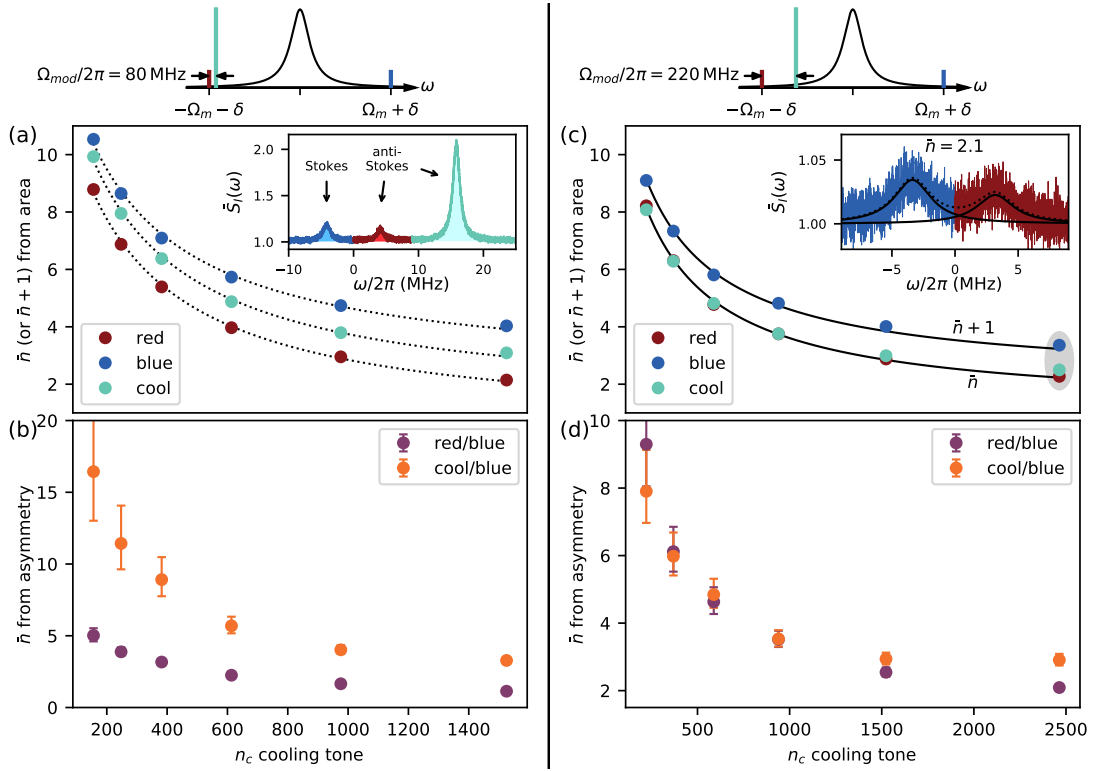


Figure 4.2 – **Artificial and quantum sideband asymmetry in optomechanical sideband cooling.** In (a), (b), the cooling tone is detuned 80 MHz from red-detuned probe. (a) Inferred \bar{n} ($\bar{n} + 1$) from anti-Stokes (Stokes) mechanical sidebands, based on total thermomechanical noise. Inset: Example of an actual observed noise spectrum, colored for different tones as in the main panel. (b) The occupancy \bar{n} obtained from motional sideband asymmetry, obtained both from the ratio of red- and blue-detuned probes, and the ratio of cooling tone and blue-detuned probe, which shows strong disagreement. Error bars represent ± 20 MHz tuning accuracy. (c), (d) show the data corresponding to (a), (b), respectively, only with the cooling tone detuned 220 MHz from red-detuned probe, where the effect of the thermal Kerr-type nonlinearity is strongly diminished. In (c), the lower curve is a fit according to the model with the average asymmetry of the last two points, shown in (d), used for calibration; one quantum is added to result in the upper curve, coinciding with the Stokes sideband data. Inset (c) shows spectra of the last data point.

portional to $C\bar{n}$ and $C(\bar{n} + 1)$. The asymmetry can be interpreted as a consequence of either quantum backaction (i.e., the optical input vacuum fluctuations) or of the mechanical commutation relations, depending on the detection scheme as well as the detector model used [70, 116, 117]. From the sidebands we extract \bar{n} either directly using noise thermometry or sideband asymmetry, as in previous optomechanical experiments [68, 69]. Raman thermometry can be done using the cooling tone sideband instead of the red-detuned probe sideband, as long as one accounts for the difference in optomechanical coupling. Classical laser noise, which can be a source of artificially enhanced asymmetry [71, 178, 184] is not affecting our measurements.

Throughout the experiment, the power of the cooling tone is increased, lowering the mechanical occupancy \bar{n} through sideband cooling, while the probe tones are held constant. Figure 4.2a,b we show thermometry results for a detuning of the red-probe from the cooling tone of $\Omega_{\text{mod}}/2\pi = 80\text{MHz}$. In Fig. 4.2a we use the total sideband power to infer \bar{n} ($\bar{n} + 1$) from the anti-Stokes (Stokes) mechanical sidebands, plotted against the cooling tone intracavity photons. Strikingly, the curves of the cooling tone and red-detuned probe *do not coincide*, making it impossible to associate \bar{n} with either. The discrepancy is also reflected in Fig. 4.2b, where *quantum sideband asymmetries* of either of the two anti-Stokes sidebands compared to the Stokes sideband yield *different* \bar{n} . We next repeat the measurement with larger separation between the red-detuned probe and the cooling tone, with $\Omega_{\text{mod}}/2\pi = 220\text{MHz}$ (Fig. 4.2c,d). The inferred \bar{n} from both anti-Stokes sidebands *now show excellent agreement* (Fig. 4.2c), and \bar{n} inferred from motional sideband asymmetry also agree within experimental errors (Fig. 4.2d). Our measurements thus show that the presence of the cooling tone, when tuned closely to the red-detuned probe, modifies the quantum-mechanical motional sideband asymmetry.

To investigate this phenomenon further, we perform an auxiliary experiment, shown in Fig. 4.3a. Omitting the blue-detuned probe, we apply two *equal power* tones near the lower mechanical sideband (still referred to as red-detuned probe and cooling tone). As illustrated in Fig. 4.3a, the observed anti-Stokes sidebands are not equal even for $\Omega_{\text{mod}} \ll \kappa$, with the higher-frequency sideband stronger, in disagreement with standard optomechanical theory. Keeping the red-detuned probe fixed at $\Delta = -\Omega_m$ and scanning the cooling tone, Fig. 4.3b shows the ratio of the two sidebands, normalized to the expected bare optomechanical response, vs. Ω_{mod} . The normalized ratio decreases with Ω_{mod} , only reaching the expected behavior at $\Omega_{\text{mod}} \sim 200\text{MHz}$. Note that, depending on the power used, the ratio may be very large for small Ω_{mod} , e.g. exceeding 2 for $\Omega_{\text{mod}}/2\pi = 20\text{MHz}$ in Fig. 4.3b. Figure 4.3c shows the noise spectra at low $\Omega_{\text{mod}}/2\pi = 4\text{MHz}$ for increasing tone power, where additional higher-

order sidebands, spaced by Ω_{mod} , are observed. These measurements point to the presence of a cavity nonlinearity, which couples the thermomechanical sidebands and modifies the observed asymmetry.

The existence of cavity nonlinearities due to e.g. thermal effects is not unusual and has been observed in both bulk optical cavities as well as ultrasmall optical mode volume resonators [146, 185–187]. While there are several potential sources for a “Kerr-type” effect, we consider the photothermorefractive frequency shift (PTRS) as the dominant mechanism. Physically, photons circulating in the cavity are absorbed, leading to heating, and thus shifting of the cavity resonance (e.g., via the temperature dependent refractive index). The temperature deviation δT is governed in the simplest case by a single timescale and temperature-independent absorption

$$\delta \dot{T}(t) = -\gamma_{\text{th}} \delta T(t) + g_{\text{abs}} |\bar{a}(t)|^2. \quad (4.2)$$

Here the absorption rate is given by g_{abs} , and the thermalization rate by γ_{th} . In the presence of two tones, the cavity field intensity beats $n_c(t) = |\bar{a}(t)|^2 \propto \text{const} + \cos(\Omega_{\text{mod}} t)$, which, via the absorption heating, causes a periodic modulation of the cavity frequency, captured by the detuning

$$\Delta_{\text{th}}(t) = \Delta_k \exp(i\Omega_{\text{mod}} t) + \text{c.c.} \quad (4.3)$$

where

$$\Delta_k = \frac{g_{\text{PT}} g_{\text{abs}} \bar{a}_c \bar{a}_r}{\sqrt{\gamma_{\text{th}}^2 + \Omega_{\text{mod}}^2}} e^{-i\phi_{\text{th}}}, \quad \phi_{\text{th}} = \tan^{-1} \left(\frac{\Omega_{\text{mod}}}{\gamma_{\text{th}}} \right). \quad (4.4)$$

Here \bar{a}_c, \bar{a}_r are the amplitudes of the intracavity fields produced by cooling tone and red-detuned probe, and g_{PT} relates cavity frequency shift to temperature deviation via $\Delta_{\text{th}} = g_{\text{PT}} \delta T$. Consequently the static thermal cavity shift per mean intracavity photon is given by $g_{0,\text{th}} = g_{\text{PT}} g_{\text{abs}} / \gamma_{\text{th}}$. In principle, the nonlinear cavity frequency shift could have a number of origins, which can be included in Δ_k . Here for simplicity we consider only the PTRS (4.3), such that Δ_k is given by Eq. (4.4). Additional Kerr-type nonlinearities are discussed in the end of Sec. 6.3.

The cavity frequency modulation mediates processes in which photons are scattered from a frequency ω to $\omega \pm \Omega_{\text{mod}}$, which causes coupling of the sidebands with strength Δ_k . In Section 6.3, we incorporate the PTRS into standard optomechanical theory to model our experiments,

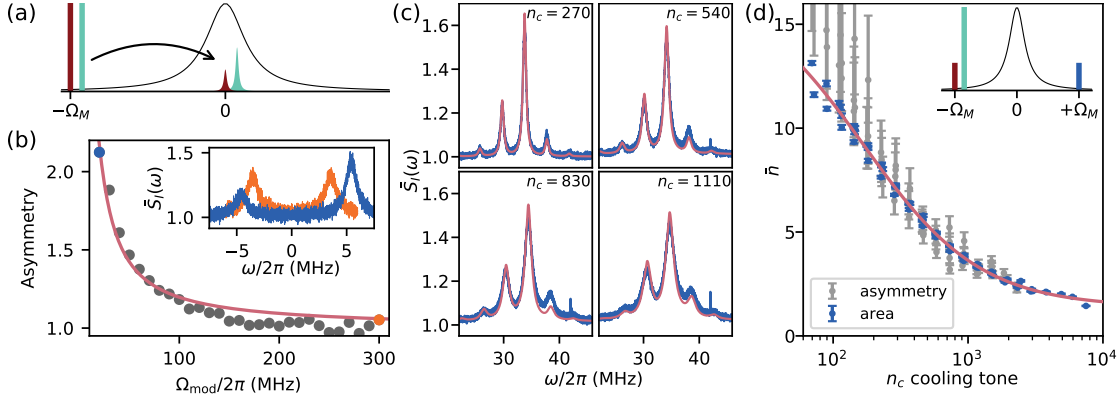


Figure 4.3 – **Observation of asymmetric noise spectra due to Kerr-type nonlinearity.** (a) Pumping scheme with two equal red-detuned pumps. (b) The peak ratio of the observed spectra, relative to the ratio expected from bare optomechanical response, vs. Ω_{mod} for constant power of $n_c = 640$ intracavity photons, showing decreased effect for higher modulation frequencies. The inset shows the spectra for data points of the same color in the main panel. (c) Increasing the pump power for a constant $\Omega_{\text{mod}}/2\pi = 4$ MHz, showing higher-order Fourier modes. Also shown are fits to the analytic model of Sec. 6.3. (d) Calibration of sideband cooling using motional sideband asymmetry, with $\Omega_{\text{mod}}/2\pi = 220$ MHz, free from Kerr-type artificial asymmetry. The oscillator is cooled down to $\bar{n} = 1.5$ phonons.

and use a Floquet approach, based on writing the cavity and mechanical annihilation operators as sums of Fourier modes, to solve the time-dependent quantum Langevin equations. In the first approximation, corresponding to retaining the dominant Fourier modes, the output spectrum takes the same form as above (4.1) but with modified cooperativities

$$\tilde{C}_{\text{red}} = C_{\text{red}} \left| 1 - 2i g_c \Delta_k / (g_r \kappa) \right|^2, \quad (4.5a)$$

$$\tilde{C}_{\text{cool}} = C_{\text{cool}} \left| 1 - 2i g_r \Delta_k^* / (g_c \kappa) \right|^2, \quad (4.5b)$$

leaving the ideal theory [Eq. (4.1)] otherwise unchanged. Importantly, these expressions can lead to an asymmetry when Δ_k is complex even when $g_r = g_c$. This explains our observations in Fig. 4.3b, where the cavity is driven by two equal-strength pumps, and asymmetric sidebands are observed. The asymmetry diminishes as Ω_{mod} is increased beyond the bandwidth γ_{th} . A fit to this simple model shown in Fig. 4.3b is in good agreement and captures this general behavior. In this case of $\Omega_{\text{mod}} \gg \gamma_{\text{th}}$ we find that the approximation Eq. (4.5) is sufficient to describe our data, with added Fourier modes producing no change to the fitted curve. From the fit we obtain the two quantities characterizing Δ_k (4.4), $\gamma_{\text{th}}/2\pi \sim 6$ MHz and $g_{\text{abs}} g_{\text{PT}}/4\pi^2 \sim 10 \text{ MHz}^2$, with other parameters determined independently. Deviations from the data at high frequencies may be accounted for by considering additional Kerr-type effects of higher bandwidths or more complicated thermal behavior than that afforded by Eq. (4.2), however we keep the

simplicity of our model and emphasize that for $\Omega_{\text{mod}}/2\pi = 220$ MHz used in Fig. 4.2c,d and all our subsequent motional sideband asymmetry measurements, we consistently observe the same normalized sideband power (i.e. same \bar{n}) for both cooling tone and red-detuned probe (within experimental errors of $\sim 5\%$), confirming the weakness of Kerr-type effects, and allowing to operate in a regime where the quantum sideband asymmetry arising from optomechanical quantum correlations can be observed. We also note that the coupling of red and blue tones is negligible as their spacing is $2\Omega_m \gg \gamma_{\text{th}}$.

In order to capture the Floquet dynamics observed in Fig. 4.3c, where a series of thermomechanical sidebands are generated, more Fourier modes have to be included (six optical and five mechanical; see Fig. 4.4). The relative weight of the higher order sidebands is in good agreement with the data. Strong thermal effects at $\Omega_{\text{mod}}/2\pi = 4$ MHz lead to distortion in the cavity linewidth measurement, introducing large detuning errors, leading to large uncertainties in cavity parameters. The fits shown in Fig. 4.3c yield $\gamma_{\text{th}}/2\pi$ in the range 4–8 MHz and $g_{\text{abs}}g_{\text{PT}}/4\pi^2 \sim 6\text{--}17$ MHz², in close agreement with Fig. 4.3b. In order to further confirm our model, we have carried out pump-probe response measurements of the cavity. We found the bandwidth of power induced cavity frequency shifts (likely thermal in origin) ~ 10 MHz, in agreement with the results presented here.

Next, we turn back to sideband measurements at $\Omega_{\text{mod}}/2\pi = 220$ MHz, where only the quantum asymmetry is prominent. Figure 4.3d shows an extended set of measurements done at cryostat temperature of 4.4 K and buffer gas pressure of 140 mbar, including occupancies \bar{n} inferred from both motional sideband asymmetry and power in the cooling sideband. Inferring \bar{n} from motional sideband asymmetry is straightforward, however the probes must be weak to avoid extraneous heating of the oscillator. The much-larger signal-to-noise ratio of the cooling sideband is more suitable for determination of \bar{n} for the highest cooling powers. Referring to Eq. (4.1) and neglecting the weak probes, we see that apart from the easily-measured optomechanical parameters, accurate knowledge of the quantity $\eta \bar{n}_{\text{th}}$ is required. Moreover, extraneous heating due to optical absorption modifies the actual bath occupancy from that measured, $\bar{n}_{\text{th}} \rightarrow \bar{n}_{\text{th}} + \alpha n_c$, where α is the added bath phonons per intracavity photon. Thus, at least one of the parameters $\eta, \bar{n}_{\text{th}}, \alpha$ needs to be independently determined. It is often difficult to obtain accurate measurement of these parameters. Here we use the sideband asymmetry at an intermediate data point to compute \bar{n} and, unequivocally, η , providing calibration for the entire cooling curve of Fig. 4.3d.

The two main sources of measurement error are tuning accuracy, estimated at $\pm 2\pi \times 20$ MHz = $\pm 0.0125\kappa$, that leads to slightly different cavity response seen by the two probes (error bars

in Figs. 4.2 and 4.3d), and error in estimate of Lorentzian peaks of the sidebands, that yield different \bar{n} values for the two flavors of asymmetry used in Fig. 4.2b,d (see inset of Fig. 4.2c). The former error is dominant for large \bar{n} (small asymmetry), while the latter is dominant at strong cooling powers hence low signal-to-noise ratios (for example the last point in Fig. 4.2d). For every data point in Fig. 4.3d, we add these errors in quadrature. We then compute η and its uncertainty using weighted average. The final result, $\eta = 0.044 \pm 0.005$ remains essentially the same if we take the last few, minimum error points. This calibration gives $\bar{n} = 1.5 \pm 0.2$ (40% ground-state occupation) for the minimum occupation in Fig. 4.3d. In addition, fitting the entire data set yields bath thermal occupation $\bar{n}_{\text{th}} = 17.5$ and extraneous heating of $\alpha = 1.3C_0$.

4.3 Theory

In optomechanical measurements, precise knowledge and precision measurements of the sources and processes that contribute to the noise spectrum are imperative, such as thermorefractive noise [62, 188] and noise in drive tones [114, 178, 179, 184].

To describe our experiment we take the standard optomechanical model in a rotating frame

$$\hat{H}_{\text{OM}}/\hbar = [\Delta_{\text{th}}(t) - \Delta] \hat{a}^\dagger \hat{a} + \Omega_m \hat{b}^\dagger \hat{b} - g_0 \hat{a}^\dagger \hat{a} (\hat{b} + \hat{b}^\dagger), \quad (4.6)$$

but include the PTRS (via Δ_{th}) as well as optical and mechanical baths. A standard calculation [43, 189] gives quantum Langevin equations, which we linearize around the mean intracavity field $\hat{a}(t) = \bar{a}(t) + \delta \hat{a}(t)$ (and the same for the mechanical mode) to obtain the equations for linear optomechanics [43]

$$\begin{aligned} \delta \dot{\hat{a}} &= \left\{ i[\Delta - \Delta_{\text{th}}(t)] - \frac{\kappa}{2} \right\} \delta \hat{a} + i g(t) (\delta \hat{b} + \delta \hat{b}^\dagger) + \sqrt{\kappa} \delta \hat{a}_{\text{in}}, \\ \delta \dot{\hat{b}} &= \left(-i\Omega_m - \frac{\Gamma_m}{2} \right) \delta \hat{b} + i[g(t) \delta \hat{a}^\dagger + g^*(t) \delta \hat{a}] + \sqrt{\Gamma_m} \hat{b}_{\text{in}}, \end{aligned} \quad (4.7)$$

where $\Delta \approx -\Omega_m$ is the average detuning of the pumps from the cavity, $g(t) = g_0 \bar{a}(t) \exp[i(\omega_{\text{cav}} + \Delta)t]$ is the modulated light-enhanced optomechanical coupling strength, and the input noises obey $\langle \delta \hat{a}_{\text{in}}(t) \delta \hat{a}_{\text{in}}^\dagger(t') \rangle = \delta(t - t')$ and $\langle \hat{b}_{\text{in}}(t) \hat{b}_{\text{in}}^\dagger(t') \rangle = (\bar{n}_{\text{th}} + 1) \delta(t - t')$ (as well as standard commutation relations). Langevin equations with periodic time-dependence can be analyzed with a recently developed method [190]. Note that closely related models have been studied in the context of levitated optomechanics [191, 192], where instead of the cavity, the mechanical resonator frequency is modulated.

In the experiment, we apply up to three tones to the cavity: a strong cooling tone, as well

as weak red- and blue-detuned probes. Since the blue-detuned probe is very far detuned from the other two tones, it remains unaffected and we will not consider it in this section. Cooling tone and red-detuned probe are close to the red sideband, separated in frequency by Ω_{mod} , as is shown in Fig. 4.3a. Neglecting all other effects, the resulting intracavity field $\bar{a}(t) = \bar{a}_r e^{-i(\omega_{\text{cav}} + \Delta)t} + \bar{a}_c e^{-i(\omega_{\text{cav}} + \Delta + \Omega_{\text{mod}})t}$.

We model the PTRS [170, 193] through Eq. (4.2) in conjunction with $\Delta_{\text{th}}(t) = g_{\text{PT}} \delta T(t)$ as discussed above. In our level of approximation we neglect the effect of the PTRS on the mean intracavity field, such that we can solve directly for the temperature deviation. Since a constant temperature shift leads to a static frequency shift which can be absorbed into the overall detuning Δ , we only consider the time-dependent part

$$\delta T(t) = g_{\text{abs}} \int_{-\infty}^t 2\bar{a}_c \bar{a}_r e^{-\gamma_{\text{th}}(t-t')} \cos(\Omega_{\text{mod}} t') dt' = \frac{2g_{\text{abs}} \bar{a}_c \bar{a}_r}{\sqrt{\gamma_{\text{th}}^2 + \Omega_{\text{mod}}^2}} \cos(\Omega_{\text{mod}} t - \phi_{\text{th}}), \quad (4.8)$$

where the phase lag

$$\phi_{\text{th}} = \tan^{-1}(\Omega_{\text{mod}} / \gamma_{\text{th}}) \quad (4.9)$$

arises due to the finite thermalization time. Equation (4.8) yields the PTRS displayed in Eqs. (4.3) and (4.4). The phase ϕ_{th} plays a crucial role in the observed asymmetric response. Note that if Δ_{th} is positive, the cavity resonance is blue-shifted. Absorption of photons in the cavity can also lead to a delayed photothermal force on the mechanical oscillator due to the photo-thermo-elastic effect [194–197], which in turn leads to a cavity frequency shift via the optomechanical coupling. In our experiment the photothermal body force is negligible due to the high mechanical frequency relative to the thermal bandwidth, thus we focus on the photo-thermo-refractive effect.

If the two pumps lie close to the red sideband ($\Delta \approx -\Omega_m$), and the modulation frequency is much smaller than Ω_m , as is the case here, we can neglect terms rotating at $2\Omega_m$ in a rotating-wave approximation. However, the resulting equations still have an explicit time-dependence, which can be removed by splitting the fields $\delta \hat{a}$ and $\delta \hat{b}$ into Fourier modes [190]

$$\begin{aligned} \delta \hat{a}(t) &= \sum_n \exp(in\Omega_{\text{mod}} t) \delta \hat{a}^{(n)}(t), \\ \delta \hat{b}(t) &= \sum_n \exp(in\Omega_{\text{mod}} t) \delta \hat{b}^{(n)}(t), \end{aligned} \quad (4.10)$$

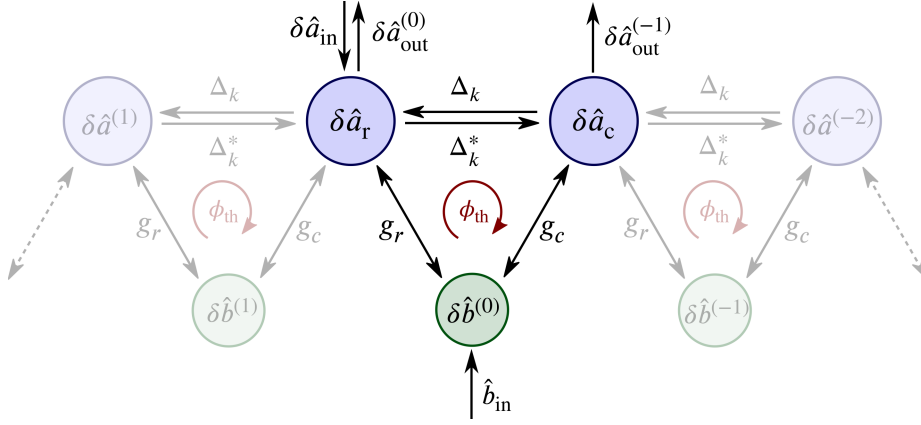


Figure 4.4 – **An illustration of the infinite array of coupled Fourier modes.** The map to Fourier modes (4.10) introduces an infinite set of coupled Langevin equations, which has to be truncated at some order to obtain a solution. Due to the two pumps (cooling and red-detuned probe), thermomechanical noise incident on mode $\delta\hat{b}^{(0)}$ is distributed onto $\delta\hat{a}_r$ and $\delta\hat{a}_c$, generating two sidebands. The cavity Fourier modes are coupled due to a cavity Kerr-type nonlinearity $[\Delta_k$ (4.4)]. This effect modifies the sideband weight, which to lowest order (considering only the bold three-mode system) can be accounted for with new effective optomechanical couplings (4.5), but in general leads to more sidebands (Fig. 4.3c), modeled by including more Fourier modes in the description. Notably, due to the finite response time, the coupling between the Fourier modes is *complex*, with the phase ϕ_{th} given in Eq. (4.9).

at the cost of introducing an infinite set of coupled equations of motion

$$\begin{aligned}
 \delta\dot{\hat{a}}^{(n)} &= \left(i\tilde{\Delta} - in\Omega_{\text{mod}} - \frac{\kappa}{2} \right) \delta\hat{a}^{(n)} + \delta_{n,0}\sqrt{\kappa}\delta\hat{a}_{\text{in}} \\
 &\quad + i \left(g_c\delta\hat{b}^{(n+1)} + g_r\delta\hat{b}^{(n)} - \Delta_k^*\delta\hat{a}^{(n+1)} - \Delta_k\delta\hat{a}^{(n-1)} \right), \\
 \delta\dot{\hat{b}}^{(n)} &= \left(-in\Omega_{\text{mod}} - \frac{\Gamma_m}{2} \right) \delta\hat{b}^{(n)} \\
 &\quad + i \left(g_c\delta\hat{a}^{(n-1)} + g_r\delta\hat{a}^{(n)} \right) + \delta_{n,0}\sqrt{\Gamma_m}\hat{b}_{\text{in}},
 \end{aligned} \tag{4.11}$$

which are depicted as lattice in Fig. 4.4. Here, $g_{r,c} = g_0\bar{a}_{r,c}$ and we have written $\Delta_{\text{th}}(t) = \Delta_k \exp(i\Omega_{\text{mod}}t) + \text{c.c.}$, and defined the residual detuning $\tilde{\Delta} = \Omega_m + \Delta \ll \kappa$, which presents only a small correction and will thus be neglected in the following.

The Fourier modes we have introduced are sometimes called auxiliary modes [99], frequency-shifted operators [191], or sidebands. The explicitly time-dependent terms in the linearized equations of motion (E.6) couple the Fourier modes. This off-diagonal coupling (in Fourier space) is suppressed by the response of the modes (especially the narrow mechanical mode), such that good approximations are obtained with only few Fourier modes.

For now, we assume that only the central modes $\delta\hat{a}_r \equiv \delta\hat{a}^{(0)}$, $\delta\hat{a}_c \equiv \delta\hat{a}^{(-1)}$, $\delta\hat{b}^{(0)}$ are nonzero.

These modes are shown in bold colors in Fig. 4.4 and are most relevant as they contain the most thermomechanical noise. This reduces the equations of motion (4.11) to the matrix equation

$$\begin{pmatrix} \chi_{\text{opt}}^{-1}(\omega) & -ig_r & i\Delta_k \\ -ig_r & \chi_m^{-1}(\omega) & -ig_c \\ i\Delta_k^* & -ig_c & \chi_{\text{opt}}^{-1}(\omega + \Omega_{\text{mod}}) \end{pmatrix} \begin{pmatrix} \delta \hat{a}_r \\ \delta \hat{b}^{(0)} \\ \delta \hat{a}_c \end{pmatrix} = \begin{pmatrix} \sqrt{\kappa} \delta \hat{a}_{\text{in}} \\ \sqrt{\Gamma_m} \hat{b}_{\text{in}} \\ 0 \end{pmatrix}, \quad (4.12)$$

where we have defined the susceptibilities

$$\chi_{\text{opt}}^{-1}(\omega) = \kappa/2 - i(\omega + \tilde{\Delta}), \quad \chi_m^{-1}(\omega) = \Gamma_m/2 - i\omega. \quad (4.13)$$

Note that the Kerr-type effect thus leads to a coupling of the Fourier modes $\delta \hat{a}_c$ and $\delta \hat{a}_r$, captured by Δ_k . The noise spectrum contains mostly noise from the mechanical oscillators, such that we can neglect $\delta \hat{a}_{\text{in}}$. Applying the red-detuned probe and the cooling tone introduces optical damping, yielding an effective susceptibility $\chi_{\text{m,eff}}^{-1}(\omega) = \Gamma_m(1 + C_{\text{red}} + C_{\text{cool}})/2 - i\omega$. Given the approximation (4.12), the spectrum reads

$$S_I(\omega + \Delta_{\text{LO}}) = 1 + \eta \kappa \bar{n} \Gamma_m \left| \frac{g_r - ig_c \Delta_k \chi_{\text{opt}}(\Omega_{\text{mod}} + \omega)}{\chi_{\text{opt}}^{-1}(\omega) \chi_{\text{m,eff}}^{-1}(\omega)} \right|^2 + \eta \kappa \bar{n} \Gamma_m \left| \frac{g_c - ig_r \Delta_k^* \chi_{\text{opt}}(\omega - \Omega_{\text{mod}})}{\chi_{\text{opt}}^{-1}(\omega) \chi_{\text{m,eff}}^{-1}(\omega - \Omega_{\text{mod}})} \right|^2, \quad (4.14)$$

where we have neglected the frequency dependence of the cavity response, and introduced the overall detection efficiency η [183, 189]. This spectrum can be understood as follows: thermomechanical noise is filtered by the mechanical response $\chi_{\text{m,eff}}$ and is scattered to the optical modes, where it interferes with itself. In the Fourier mode corresponding to the red-detuned probe sideband, the amplitudes g_r and $ig_c \Delta_k \chi_{\text{opt}}(\Omega_{\text{mod}})$ add. The rate g_r comes from scattering directly into that Fourier mode, whereas $ig_c \Delta_k \chi_{\text{opt}}(\Omega_{\text{mod}})$ has the clear interpretation of noise scattering first into cooling mode $\delta \hat{a}_c$ with amplitude g_c , where it picks up the optical susceptibility $\chi_{\text{opt}}(\Omega_{\text{mod}})$, and then hopping from there onto the red-detuned probe mode with amplitude Δ_k .

We find that even for equal pump strength ($g_r = g_c$) the thermomechanical sideband weights can differ, *as long as Δ_k has a nonzero phase*. This phase occurs only if Ω_{mod} and γ_{th} are comparable, in which case the phase lag of the thermal response behind the intracavity field [Eq. (4.3)] is non-trivial. This phase is conjugated between the clockwise and counterclockwise

process, allowing us to interpret it as a synthetic gauge field ϕ_{th} threading the triangles in Fig. 4.4. From this point of view, the interpretation is similar to the non-reciprocal noise scattering observed in the optomechanical isolator [98], and the optoelectromechanical transducer [198], except that here the phase arises dynamically, among the virtual Fourier modes, whereas in these examples the phase is a direct consequence of the phase relation of drives. In the more relevant case for thermometry, $g_r \ll g_c$, we can neglect the backaction of the probe tones and Eq. (4.14) reverts to the ideal theory (4.1), but now with the modified optomechanical cooperativities displayed above [Eq. (4.5)]. The three-mode approximation is sufficient for fitting our data in Fig. 4.3b, where mostly $\Omega_{\text{mod}} \gg \gamma_{\text{th}}$.

For strong driving and small $\Omega_{\text{mod}} \sim \gamma_{\text{th}}$, the interaction Δ_k between the optical Fourier modes is enhanced [Eq. (4.4)], and thus higher-order Fourier modes are populated, and more sidebands appear in the output spectrum. This is precisely what we observe in Fig. 4.3c. The higher-order sidebands can be modeled by including more Fourier modes (faint color in Fig. 4.4). The matrix in Eq. (4.12) is straightforwardly generalized to larger systems. It can then be shown [190] that the normal-ordered time-averaged noise spectrum is given by

$$S^N(\omega) = \sum_n \int \frac{d\omega'}{2\pi} \langle \delta \hat{a}_{\text{out}}^{(n)\dagger}(\omega + n\Omega_{\text{mod}}) \delta \hat{a}_{\text{out}}^{(-n)}(\omega') \rangle. \quad (4.15)$$

The heterodyne spectrum we quote above is related through $S_I(\omega + \Delta_{\text{LO}}) = 1 + \eta S^N(\omega)$. In Fig. 4.3c, to capture the full Floquet dynamics, we fit the data to this model including 6 optical Fourier modes and 5 mechanical Fourier modes [i.e. $d^{(2)} \dots d^{(-3)}$, $b^{(2)} \dots b^{(-2)}$ in Fig. 4.4].

We note that the intrinsic Kerr effect also leads to a cavity frequency shift $\Delta_{\text{Kerr}}(t) = g_{\text{Kerr}} |\bar{a}(t)|^2$ without a phase lag. The coupling strength g_{Kerr} can be estimated through [199]

$$g_{\text{Kerr}} = -\omega_{\text{cav}} \frac{n_2}{n_0} \frac{\hbar \omega_{\text{cav}} c}{V_{\text{mode}} n_0}, \quad (4.16)$$

where n_0 is the linear refractive index, n_2 the Kerr coefficient, V_{mode} the mode volume, and c the speed of light. For our system we find $g_{\text{Kerr}}/2\pi \sim -13$ kHz, considerably weaker than the PTRS which has a static, single intracavity photon coupling $g_{0,\text{th}}/2\pi = 1.7$ MHz. Additionally, the optomechanical interaction itself gives rise to an instantaneous Kerr-type frequency shift, $\Delta_{\text{OM}}(t) = g_{\text{OM}} |\bar{a}(t)|^2$ with $g_{\text{OM}} = -2g_0^2/\Omega_m \simeq -2\pi \times 230$ Hz [43], negligible in our system compared to the PTRS as well. The optomechanical Kerr effect, however, can be strong in other systems [200, 201]. The intrinsic and optomechanical Kerr effects are instantaneous and thus independent of pump spacing.

4.4 Frequency Response Measurement

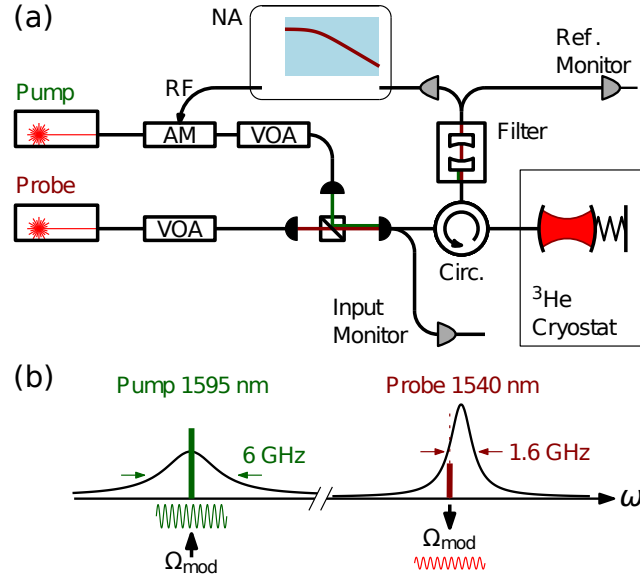


Figure 4.5 – **Cavity frequency response measurement.** (a) Experimental setup. AM, amplitude modulator. (b) Measurement scheme. An amplitude modulated pumping tone is applied to the an optical mode at wavelength of around 1600 nm. A weak probe is sent to the fundamental optical mode which transduce the frequency modulation to amplitude modulation.

To verify our theory further, and to discern contributions from different Kerr-type nonlinearities, we performed a cavity frequency response measurement [54, 187], shown in Fig. 4.5. In this pump-probe scheme, a pump laser is applied to a secondary wide optical resonance at 1595 nm, while a probe laser is tuned to the slope of the main optical resonance at 1540 nm (Fig. 4.5b) The pump laser is amplitude-modulated with variable frequency Ω and the corresponding shift of the cavity resonance is monitored via the probe laser. A bandpass optical filter at the output removes the reflected pump light to avoid cross-talk from the pump modulation.

The frequency response curve corresponds to a combination of low-pass filter behavior, attributed to different physical mechanisms that dominate at different frequencies [202]. In our case we found it best described by three low-pass components

$$\delta\omega = \left(\frac{a_1}{1 + i\Omega/\Omega_1} + \frac{a_2}{1 + i\Omega/\Omega_2} + \frac{a_3}{1 + i\Omega/\Omega_3} \right) \delta n_c, \quad (4.17)$$

with $\delta\omega$ the cavity frequency modulation, δn_c the intracavity photon number modulation, and Ω_i and a_i the bandwidths and amplitudes, respectively, of the three filters. Note that neither the intrinsic Kerr effect plateau, nor the mechanical oscillator response, were observed in our measurements, which were dominated by detector noise at GHz frequencies.

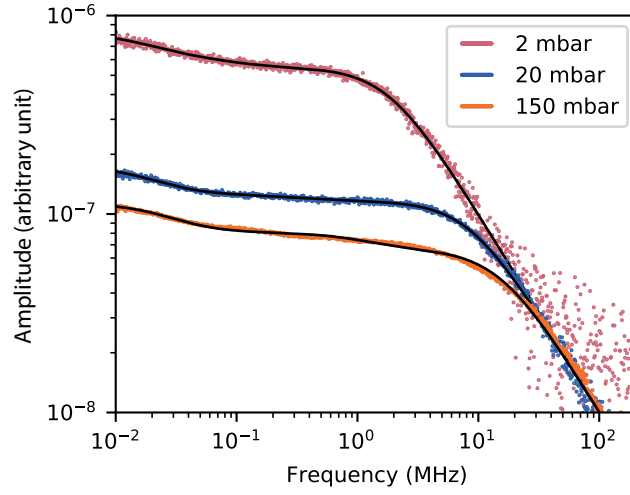


Figure 4.6 – **Cavity frequency response at different pressures.** The cavity response at three different pressures is shown in dotted curve, fitted with a three low-pass model.

Figure 4.5c shows our cavity frequency response for different buffer gas pressures, with the extracted bandwidths summarized in Table 4.1, from which several conclusions can be drawn. First, at 150 mbar the highest frequency Ω_3 around 15 MHz, agrees with the bandwidth of the Kerr-type effect studied in Sec. 4.2, which reinforces our observations (the lower frequencies are too low to be observed). Second, all bandwidths increase with pressure, indicating the role of the buffer gas in improving the thermalization of the cavity. In the range 2–150 mbar, The higher bandwidths $\Omega_{2,3}$ increase by an order of magnitude. Thus, the cavity response measurement plays a key role in understanding the Kerr-type nonlinearities studied in this work.

Pressure (mbar)	2	20	150
$\Omega_1/2\pi$ (kHz)	16.5	17.6	24.6
$\Omega_2/2\pi$ (MHz)	0.07	0.30	1.10
$\Omega_3/2\pi$ (MHz)	1.84	8.62	15.4

Table 4.1 – Bandwidth from fitting the response measurements of Fig. 4.5 with the three low-pass model (4.17).

4.5 Excess Laser Noise

External cavity diode lasers are well-known to have an excess noise in the GHz range, due to the damped relaxation oscillation caused by carrier population dynamics. This is the main contribution for GHz excess noise for diode lasers. As this frequency is close to the mechanical

frequency, it is necessary to quantify the phase noise of the diode laser that we are using [179, 184]. The presence of the excess laser phase noise leads to a limited sideband cooling performance. On the other hand, the effect of excess laser noise on the sideband asymmetry has been extensively studied [71, 178, 184] in both sideband resolved and sideband unresolved regimes. In a heterodyne detection scheme, the sideband imbalance is due to the correlation between imprecision and backaction from the probing tones. This is true also when the probing tones are not quantum limited, for example a laser with phase noise or a microwave source with thermal occupation. This can therefore lead to an artificially increased asymmetry. As a consequence it is imperative that the lasers are quantum noise limited in amplitude and phase quadrature.

Here we give an estimation of the effect from the measured excess laser noise on sideband asymmetry. We take into consideration of the excess noise in the amplitude and phase quadratures, defined as C_{qq} and C_{pp} respectively, as in [71]. To quantify the excess noise in the amplitude quadrature C_{qq} , we measure the power spectral density \bar{S}_p of the photocurrent at mechanical frequency Ω_m to the incident optical power through direct detection, where $\bar{S}_p = 2(\hbar\omega_L)^2 \langle \dot{n} \rangle (1 + 2C_{qq}) = \bar{S}_p^{\text{shot}} + \bar{S}_p^{\text{ex}}$. The excess amplitude noise leads to a deviation of $\bar{S}_p^{\text{ex}} = 4(\hbar\omega_L)^2 \langle \dot{n} \rangle C_{qq}$ from the shot noise power spectral density, which becomes visible at high optical power (100s μW to few mW). At the mechanical frequency $\Omega_m/2\pi = 5.3\text{ GHz}$, for typical probing power (0.5–2 μW) we use in the sideband asymmetry measurement, $C_{qq}(\Omega_m) < 10^{-4}$, which is negligible. The excess noise in the phase quadrature C_{pp} can be modeled as $C_{pp} = \langle \dot{n} \rangle S_{\phi\phi}^{\text{ex}}$, where $S_{\phi\phi}^{\text{ex}}$ is the phase noise spectral density of the laser. The phase noise of the laser is characterized with a narrow filter cavity, which transduces the phase fluctuation of the input field to amplitude fluctuation. For the laser (Toptica CTL) at typical current 300 mA, the relaxation oscillation frequency is around 1.94 GHz with a frequency noise spectral density of $S_{\omega\omega}(\Omega_{\text{relax}}) = 2 \times 10^6 \text{ rad}^2\text{Hz}$. At the mechanical frequency, the characterized frequency noise spectral density $S_{\omega\omega}(\Omega_m)$ is less than $10^5 \text{ rad}^2\text{Hz}$. For the typical probing power, C_{pp} is below 10^{-3} . As a result, the excess laser noise in both quadratures at typical probing power at the Fourier frequency of 5.3 GHz are negligible compared to the quantum fluctuations of the light.

4.6 Conclusion

Rapid advances in cavity optomechanics over the last decade now enable quantum control of mechanical oscillators using electromagnetic radiation. Here we have shown that quantum effects such as motional sideband asymmetry can be masked by classical nonlinearities, that

lead to modification of the effective scattering rates between thermomechanical sidebands of closely-tuned applied drives due to Floquet dynamics. Such phenomena can have substantial impact and introduce additional dynamics in those schemes utilizing continuous monitoring of the mechanical oscillator with multiple tones, such as backaction-evading measurement [121, 203], mechanical quantum squeezing [83, 84, 124, 125, 182] and dissipative optical squeezing [204], entanglement of two mechanical oscillators [205, 206], optomechanical non-reciprocity [98–100]. The observed Floquet dynamics can be exploited for future optomechanical Floquet engineering with time periodic modulation, such as generation of optomechanical topological phases and continuous variable quantum information [207]. Our study indicates the rich physics that remains to be explored when considering the optomechanical Hamiltonian in conjunction with other types of interactions, such as Kerr-type interactions as outlined here.

5 Optical Back-action Evading Measurement of a Mechanical Oscillator

Quantum mechanics imposes a limit on the precision of a continuous position measurement of a harmonic oscillator, as a result of quantum backaction arising from quantum fluctuations in the measurement field. A variety of techniques to surpass this standard quantum limit have been proposed, such as variational measurements, stroboscopic quantum non-demolition and *two-tone back-action evading (BAE) measurements*. The latter proceed by monitoring only one of the two non-commuting quadratures of the motion. This technique, originally proposed in the context of gravitational wave detection, has not been implemented using optical interferometers to date.

In this chapter, we demonstrate continuous two-tone back-action evading measurement in the optical domain of a localized GHz frequency mechanical mode of a silicon optomechanical crystal cryogenically and optomechanically cooled in a ^3He buffer gas cryostat close to the ground state [121]. We explicitly show the transition from conventional to backaction-evading measurement, employing quantum-limited optical heterodyne detection, and observe up to 0.67 dB (14%) reduction of total measurement noise.

5.1 Introduction

In a continuous measurement of the position \hat{x} of a harmonic oscillator, quantum backaction (QBA) of the measuring probe on the momentum \hat{p} ultimately limits the attainable precision [30, 208], restricting ultrasensitive measurements of force or motion. For an interferometric position measurement, in which a mechanical oscillator is parametrically coupled to a cavity, the trade-off arising from measurement imprecision (i.e. detector shot noise) and QBA force noise on the mechanical oscillator, dictates a minimum added noise equivalent to the oscilla-

tor's zero-point fluctuations, $x_{\text{zpf}} = \sqrt{\hbar/2m\Omega_m}$, referred to as the Standard Quantum Limit (SQL), originally studied in the context of gravitational wave detection [25, 30, 209] (here m is the mass, and Ω_m the angular frequency of the mechanical oscillator). Recent advances in the field of cavity optomechanics [43] which utilizes nano- or micro-mechanical oscillator coupled to optical or superconducting microwave cavities, have allowed reaching the regime where the QBA arising from radiation pressure quantum fluctuations becomes relevant. In particular, imprecision noise far below that at the SQL has been obtained [52, 210], thus entering the QBA-dominated regime; QBA has been observed [63, 64, 66]; and sensitivities approaching the SQL have been demonstrated [66, 74–76].

Quantum non-demolition (QND) techniques, first proposed by Thorne, Braginsky *et al.* [25, 31–33, 35], allow beating the SQL by minimizing or evading the effects of QBA. One technique to surpass the SQL, applicable to measurements far from the mechanical resonance frequency Ω_m , utilizes quantum correlations in the probe (due to ponderomotive squeezing [71–73, 211]), known as ‘variational readout’ [87, 88]. This technique has recently been demonstrated in a cryogenic micromechanical oscillator coupled to an optical cavity [89, 90], and in a room temperature nano-optomechanical system for quantum-enhanced force measurements [91, 92]. Another possibility is utilizing squeezed light, a technique applied to gravitational wave detectors [88, 94, 212]. More recent schemes include measurements of the collective motion in a hybrid system composed either of two mechanical oscillators (as demonstrated for an electromechanical system [213, 214]), or a mechanical and a ‘negative mass’ oscillator (demonstrated using an atomic ensemble [215, 216]).

Another type of QND measurement, backaction-evading (BAE) measurements introduced by Thorne *et al.* [35], allow avoiding QBA entirely by measuring only one of the two slowly-varying amplitude and phase quadratures \hat{X} and \hat{Y} , defined by $\hat{x}(t) \equiv \sqrt{2}x_{\text{zpf}}[\hat{X}(t)\cos\Omega_m t + \hat{Y}(t)\sin\Omega_m t]$, which constitute QND observables. Unlike \hat{x} and \hat{p} , the conjugate observables \hat{X} and \hat{Y} are *decoupled* from each other during free dynamic evolution. By exclusively measuring \hat{X} (say), all QBA is diverted to \hat{Y} and is completely absent from the measurement record. By increasing coupling to the system (probe power), one can then arbitrarily reduce the imprecision noise, allowing in principle unlimited sensitivity in the measurement of one quadrature. In a cavity optomechanical system such backaction-evading (BAE) measurement is possible by amplitude-modulating a cavity-resonant probe at frequency Ω_m (Fig. 5.1a) [31, 32, 35], equivalent to two-tone probing on the upper and lower mechanical sidebands of the cavity (Fig. 5.1b) Two-tone BAE is applicable in the well-resolved sideband regime $\Omega_m \gg \kappa$, where κ is the cavity linewidth. In the opposite regime of a fast cavity $\kappa \gg \Omega_m$ one must resort

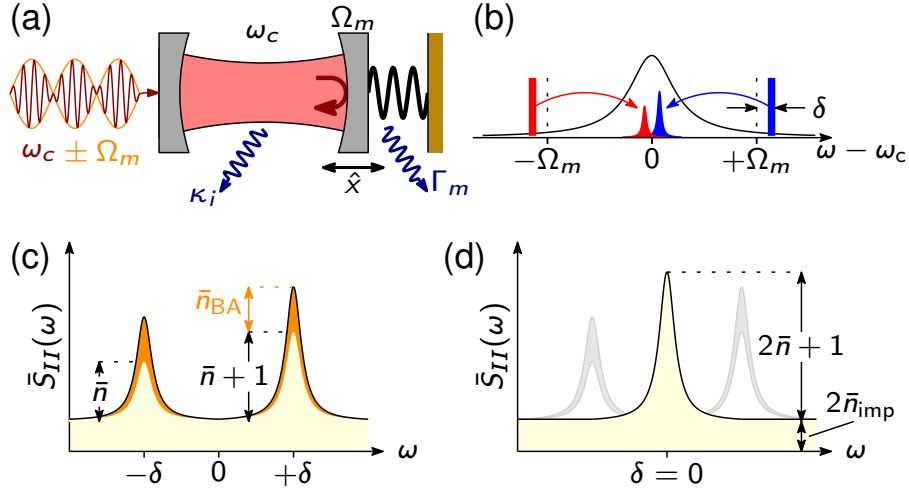


Figure 5.1 – **Backaction-evading measurement.** (a) Illustration of a cavity optomechanical system. Light in a cavity with optical resonance ω_c and full linewidth κ (of which κ_i intrinsic losses) is coupled to the position \hat{x} of a mechanical oscillator that has frequency Ω_m and linewidth Γ_m . In a BAE measurement, the probe is amplitude-modulated at the mechanical frequency Ω_m , coupling to the quadrature \hat{X} . (b) Frequency space configuration slightly detuned from BAE measurement, where the probe is modulated at $\Omega_m + \delta$. (c) Resulting power spectral density for an oscillator in a thermal state, showing the asymmetric Stokes and anti-Stokes scattered sidebands, plus the heating due to QBA. (d) When tuning to the BAE scheme $\delta = 0$, the two sidebands coalesce and the QBA is cancelled. The remaining imprecision noise \bar{n}_{imp} can be arbitrarily reduced by increasing probe power.

to stroboscopic QND measurements, requiring interaction times $\ll \Omega_m^{-1}$ [31, 35].

To date, such two-tone BAE measurement have exclusively been demonstrated in microwave optomechanical systems [77, 78], where they have also been utilized to perform tomography of states produced by schemes that produce reservoir-engineered squeezed [81–85] and entangled [205, 206] mechanical states. Yet, in all these experiments noise resulting from the use of a microwave amplifiers at elevated temperatures, resulted in substantially decreased efficiency and hindered beating the SQL [78]. Additionally, thermal noise at microwave frequencies can be non-negligible even at cryogenic temperatures, and requires careful calibration [70]. In contrast, optical homodyne or heterodyne detection is quantum-limited, and light is effectively a zero-temperature bath, allowing self-calibrated measurements of motion [67–70, 122]. Optomechanical systems using laser light have demonstrated quantum effects up to room temperature [91–93]. To date however, despite advances in operating in the QBA dominated regime in cavity optomechanics, BAE measurements in the optical domain have not been reported. BAE measurements are compounded by instabilities arising from the excitation of higher-order mechanical modes due to the $2\Omega_m$ intensity modulation, and are susceptible to

parametric instabilities [79, 80, 89].

5.2 Theory

The theory of dual-tone backaction-evading measurements in optomechanics has been treated earlier [36]. Here, we demonstrate a two-tone BAE measurement in the optical domain of an oscillator in a thermal state (average occupation \bar{n}), using quantum-limited balanced heterodyne detection (BHD). We first consider theoretically the scenario depicted in Fig. 5.1b–d, in which a cavity optomechanical system is interrogated with two tones detuned by $\pm(\Omega_m + \delta)$ from the cavity resonance and the two sidebands are detected using BHD.

The output optical field $\delta \hat{a}_{\text{out}} = \delta \hat{a}_{\text{in}} - \sqrt{\kappa} \delta \hat{a}$ is detected using balanced heterodyne detection, mixing it with a strong local oscillator with frequency $\omega_L + \Delta_{\text{LO}}$ (in the lab frame) on a beamsplitter and subtracting the detected intensity from the two beamsplitter output arms. This yields photocurrent with symmetrized PSD [217], $S_I(\omega) \propto S_{\delta \hat{a}_{\text{out}} \delta \hat{a}_{\text{out}}}(\Delta_{\text{LO}} + \omega) + S_{\delta \hat{a}_{\text{out}}^\dagger \delta \hat{a}_{\text{out}}^\dagger}(\Delta_{\text{LO}} - \omega)$. Apart from a white noise floor due to shot noise, both $S_{\delta \hat{a}_{\text{out}} \delta \hat{a}_{\text{out}}}(\omega)$ and $S_{\delta \hat{a}_{\text{out}}^\dagger \delta \hat{a}_{\text{out}}^\dagger}(\omega)$ contain information near $\omega \approx \Gamma_{\text{eff}}, \delta \ll \Delta_{\text{LO}}$. Hence the PSD will contain information near Δ_{LO} dominated by one of them. Henceforth we refer all measured PSDs to Δ_{LO} .

We specialize to the case $\Delta = 0$ and $g_b = g_c$, as in our experiment. We can also approximate $\chi_c(\omega) \approx \chi_c(0)$ since for our frequencies of interest $\omega \ll \kappa$. Including finite detection efficiency η finally yields the PSD, normalized to the vacuum noise level,

$$S_I(\omega) = 1 + \eta \Gamma_{\text{eff}}^2 C \left[\bar{n} |\chi_m(\omega - \delta)|^2 + (\bar{n} + 1) |\chi_m(\omega + \delta)|^2 + C |\chi_m(\omega - \delta) - \chi_m(\omega + \delta)|^2 \right] \quad (5.1)$$

where $\chi_m(\omega) = (-i\omega + \Gamma_{\text{eff}}/2)^{-1}$ is the mechanical susceptibility of the oscillator with total mechanical linewidth Γ_{eff} , η the overall detection efficiency, and $C = 4g_0^2 n_p / \kappa \Gamma_{\text{eff}}$ the optomechanical cooperativity proportional to the input power. For $\delta = 0$, the quadrature \hat{X} is given by $\hat{X} = \sqrt{\Gamma_{\text{eff}}/2} \chi_m(\omega) [b_{\text{in}}^\dagger(\omega) + b_{\text{in}}(\omega)]$ with PSD $\bar{S}_{XX}(\omega) = (\Gamma_{\text{eff}}/2)(2\bar{n} + 1) |\chi_m(\omega)|^2$. The first and second terms in brackets correspond to the anti-Stokes and Stokes scattered motional sidebands, respectively, having the Lorentzian shape of the mechanical susceptibility. These exhibit the well-known quantum sideband asymmetry [65, 122, 208, 218–222], resulting from the ratio $(\bar{n} + 1)/\bar{n}$ between absorption and emission rates. The last term in brackets is the QBA due to quantum noise in the probe light. When $\delta \gg \Gamma_{\text{eff}}$, QBA appears as heating of the oscillator, adding $\bar{n}_{\text{BA}} = C$ mean quanta (Fig. 5.1c). The two QBA components, which result from interaction with the positive and negative frequency parts of the probing field,

have opposite phase. When $\delta = 0$ QBA is cancelled, yielding a pristine measurement of the oscillator, $S_I(\omega) = 1 + \eta\Gamma_{\text{eff}}C\bar{S}_{XX}(\omega)$ with $\bar{S}_{XX}(\omega) = (\Gamma_{\text{eff}}/2)(2\bar{n} + 1)|\chi_m(\omega)|^2$ (Fig. 5.1d). In this case $2\bar{n}_{\text{BA}}$ quanta are added to the complementary quadrature [36]. In principle, one can then increase signal-to-noise ratio, (i.e. measurement sensitivity) indefinitely, with no deleterious effects on the measurement, simply by increasing probing power. However, even barring other technical limitations, we have neglected bad-cavity effects, $\bar{n}_{\text{bad}} = (\kappa/4\Omega_m)^2 C$, where photons scattered out of resonance interact with counter-propagating terms (neglected in the RWA) to induce QBA [36]. In our experiment $C \lesssim 10$ and $\bar{n}_{\text{bad}} \sim 10^{-2}$ is completely negligible.

5.3 Experimental Results

We performed a BAE measurement in a silicon OMC used in Ref. [122]. Optically, the device functions as a single-sided cavity with a partially transmitting input mirror. Light is evanescently coupled from a tapered optical fiber into a waveguide that forms part of the nanobeam (coupling efficiency exceeds 50%). The optical resonance is at 1540 nm with a linewidth of $\kappa/2\pi = 1.7$ GHz, of which $\kappa_{\text{ex}} = 0.3\kappa$ are extrinsic losses to the input mirror. The optical mode is optomechanically coupled to a mechanical breathing mode of frequency $\Omega_m/2\pi = 5.3$ GHz, strongly confined due to a phononic bandgap, and an intrinsic linewidth of $\Gamma_{\text{int}}/2\pi = 84$ kHz. This places the system in the resolved sideband regime [180]. The measured optomechanical coupling parameter is $g_0/2\pi = 780$ kHz.

The system is placed in a ^3He buffer gas cryostat (Oxford Instruments HelioxTL), which allows us to overcome the prohibitive optical absorption heating *in vacuo* that has limited operation with these devices to very low photon numbers [148] or pulsed operation [96, 97, 147, 148, 181]. We are thus able to operate at high probe powers where QBA is observable. The buffer gas causes additional damping, increasing the mechanical linewidth to $\Gamma_m = \Gamma_{\text{int}} + \Gamma_{\text{gas}}$. In addition to the BAE probes, we also apply a cooling tone red-detuned from the optical resonance, to lower the thermal occupation \bar{n}_f through optomechanical sideband cooling [180], $\bar{n}_f \simeq \bar{n}_{\text{th}}/(1 + C_{\text{cool}})$ with \bar{n}_{th} the occupation of the thermal environment. The cooling tone also provides additional damping due to dynamical backaction, $\Gamma_{\text{eff}} = \Gamma_m(1 + C_{\text{cool}})$, which is the effective linewidth seen by the BAE probes. Note that the balanced probes do not produce dynamical backaction. Here, $C_{\text{cool}} = C_0 n_c$ is the cooling tone cooperativity defined similarly to C but relative to the original linewidth Γ_m , with the single photon cooperativity $C_0 \equiv 4g_0^2/\kappa\Gamma_m$, and n_c the mean intracavity photons due to the cooling tone. The cooling tone is tuned $2\pi \times 220$ MHz away from the red-detuned BAE probe to mitigate the Floquet dynamics due to Kerr-type effects [122]. At low temperatures, intracavity photons shift the optical resonance

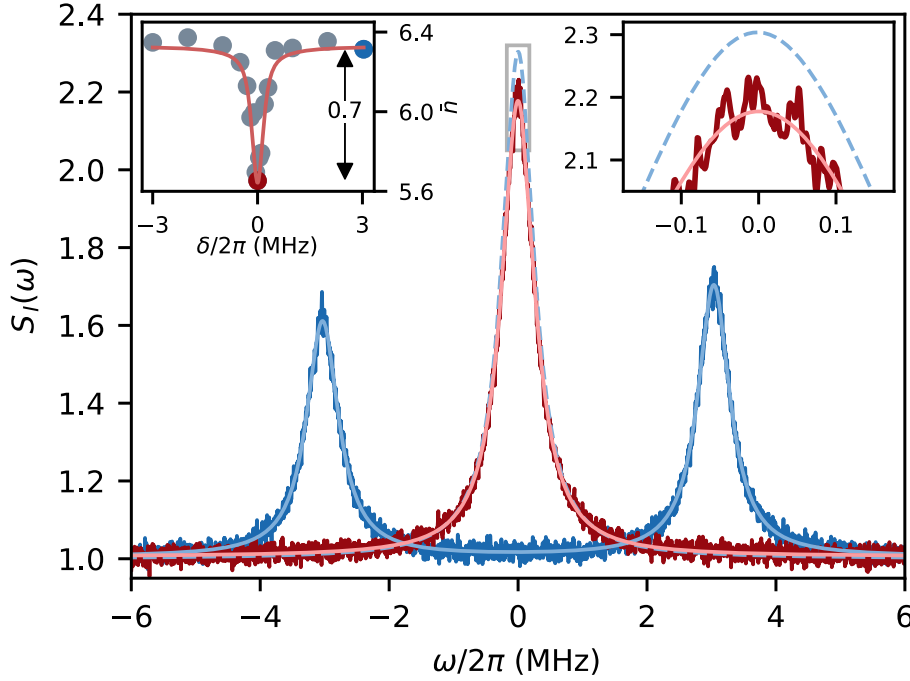


Figure 5.2 – **Experimental observation of backaction-evasion.** Data traces, normalized to the vacuum noise level, for non-BAE (blue) and BAE measurements (red) are shown with Lorentzian fits. The non-BAE sidebands exhibit motional asymmetry, used to self-calibrate the measurement in units of mechanical quanta. The sum of the non-BAE sidebands, indicated in dashed blue, is larger than in the BAE case (red) by 0.7 mechanical quanta. The right inset is a zoom of the indicated region. The left inset shows the inferred occupation \bar{n} as a function of the detuning δ . In this measurement $n_p = 290$, $n_c = 320$, and $C_{\text{cool}} = 3.8$.

to higher frequencies, due to a combination of thermo-optic and thermal expansion effects in silicon. The cavity is optically unstable when driven with the BAE probes alone (due to the blue-detuned probe), and an additional red-detuned (cooling) tone of sufficient power is required. In our system we have found empirically that we need $\bar{n}_c \gtrsim \bar{n}_p/2$ for stable operation. The measurement setup is the same as previous sideband asymmetry experiments. The two BAE probes (as well as the cooling tone) are derived from two phase-locked lasers. The three tones are combined in a free-space setup and coupled with the same polarization into a single mode fiber. By blocking each beam path we ascertain equal power for each probe, stable to within 1%. The light reflected from the oscillator is directed to a BHD setup, where it is mixed with a local oscillator generated by a third laser. By carefully characterizing our lasers we have determined that classical laser noise is negligible in our system. Specifically we operate far from the relaxation-oscillation peak of our diode laser [179, 184]. In order to accurately tune the probes across the optical resonance, we temporarily switch the reflected light to a coherent response measurement setup.

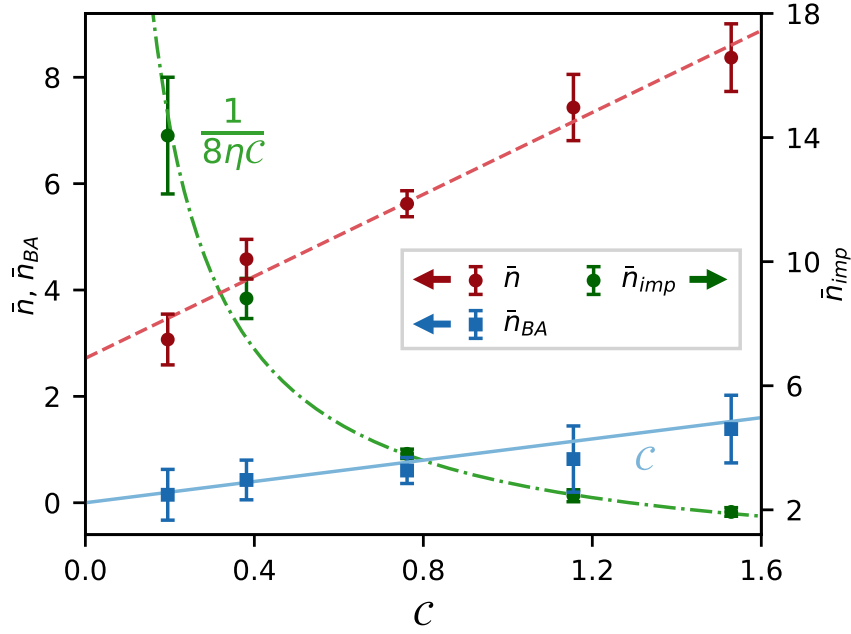


Figure 5.3 – **Effect of probe power on quantum backaction and optical absorption heating.** The measurements were carried out at 1.6 K and ^3He buffer-gas pressure of 30 mbar, with $n_c \simeq 420$ ($C_{cool} \simeq 5.0$). The occupation \bar{n} and the number of evaded QBA phonons \bar{n}_{BA} vs. independently-measured C are plotted on the left axis. The error bars are due to uncertainty in occupancy calibrated using quantum sideband asymmetry. The solid blue line plots $\bar{n}_{BA} = C$. The dashed red line is a linear fit to \bar{n} with slope βC where $\beta = 3.85$. The right axis shows the imprecision noise with a fit $\bar{n}_{imp} = 1/8\eta C$ yielding $\eta = 0.04$.

Figure 5.2 shows BAE measurement of the mechanical oscillator, taken at a cryostat temperature of 2.0 K ($\bar{n}_{th} \sim 7.9$) and buffer-gas pressure of 46 mbar. In this experiment, we vary the detuning $\delta/2\pi$ from +3 to -3 MHz. The total mechanical linewidth across the measurement is $\Gamma_{eff}/2\pi = 607 \pm 7$ kHz and the other measurement parameters are $\bar{n}_p = 290$, $\bar{n}_c = 320$, and $C_{cool} = 3.8$. When the probes are tuned away from the mechanical sidebands, $\delta/2\pi = 3$ MHz, the PSD exhibits motional sideband asymmetry that can be used to self-calibrate the measurement in terms of mechanical quanta (including QBA heating; see inset of Fig. 5.2), $\bar{n} + \bar{n}_{BA} = 6.3$ in this case [67–70, 122]. When tuning the probes on the mechanical sidebands, $\delta/2\pi = 0$ MHz, the total thermomechanical noise is reduced by 0.7 mechanical quanta, in perfect agreement with independently calculated $C = 0.7$. Thus more than 11% of the noise in the non-BAE case is due to QBA. This constitutes the first BAE measurement in the optical domain and the first with quantum-limited detection.

We now turn to discuss technical limitations of BAE measurement imposed by our system. In conventional cavity-based position measurement employing homodyne detection [75, 76], one refers the on-resonance readout to mechanical quanta, i.e., expressing the peak

of the measured PSD as $S_I^{\text{hom}}(\Omega_m) \propto \bar{n}_{\text{imp}}^{\text{hom}} + \bar{n}_{\text{BA}} + (\bar{n} + \frac{1}{2})$, where $\bar{n}_{\text{imp}}^{\text{hom}} = (16\eta C)^{-1}$ is the measurement imprecision due to shot noise (cf. Fig. 5.1d). The Heisenberg uncertainty relation requires $4\sqrt{\bar{n}_{\text{imp}}^{\text{hom}} \bar{n}_{\text{BA}}} \geq 1$. The SQL is achieved by minimizing the total added noise $\bar{n}_{\text{add}} = \bar{n}_{\text{imp}}^{\text{hom}} + \bar{n}_{\text{BA}}$ subject to this constraint, yielding $\bar{n}_{\text{add}}^{\text{SQL}} = (4\eta)^{-1/2}$ ($\frac{1}{2}$ for ideal measurement). In a BAE measurement there is no QBA component, however any device suffers extraneous heating due to optical absorption, adding excess heating backaction $\bar{n}_{\text{BA}}^{\text{th}} = \beta C$ analogous to \bar{n}_{BA} . Additionally, in heterodyne detection $\bar{n}_{\text{imp}} = (8\eta C)^{-1}$, due to twice the vacuum noise compared to homodyne detection ('image band'). The minimum added noise is $\bar{n}_{\text{add}}^{\text{th}} = \sqrt{\beta/2\eta}$. When $\beta < \frac{1}{2}$, BAE outperforms conventional measurement of the same efficiency.

Figure 5.3 shows a set of measurements done at 1.6 K ($\bar{n}_{\text{th}} \simeq 6.3$) and buffer-gas pressure of 30 mbar with variable probe power n_p and constant cooling tone power $n_c = 420$ (set by the maximum probe power). Both \bar{n} and \bar{n}_{BA} are plotted against the independently measured cooperativity C , with \bar{n}_{BA} in excellent agreement with theory (blue solid line, slope of 1), with maximum cancellation of $\bar{n}_{\text{BA}} = 1.4$ out of $\bar{n} + \bar{n}_{\text{BA}} = 9.8$ quanta, or 14% (reduction of 0.67 dB). The linear fit to \bar{n} yields $\beta = 3.85$. Thus, although QBA *is evaded* in our measurement, extraneous heating is still a limiting factor, as can be seen directly from Fig. 5.3. The imprecision noise is also in excellent agreement with theory and yields $\eta = 0.04$, in agreement with previous measurements [122] of the same system. Thus $4\sqrt{\bar{n}_{\text{imp}} \bar{n}_{\text{BA}}^{\text{th}}} = \sqrt{2\beta/\eta} = 13.88$. Compared to a measurement at the SQL with the same efficiency, the optimal added noise is $\bar{n}_{\text{add}}^{\text{th}} = 2.78 \times \bar{n}_{\text{add}}^{\text{SQL}}$.

5.4 Conclusion

In conclusion, we have explicitly demonstrated evasion of QBA for the first time in the optical domain, an important step for various quantum measurements with nanomechanical oscillators in the sideband resolved regime. Though the current generation of devices is limited by low efficiency and extraneous heating, improvements in design and fabrication already yield an intrinsic optical Q -factor improvement by a factor of ~ 5 , addressing both deficiencies [145]. This opens the path for creating motional squeezed states through reservoir engineering [124] demonstrated so far only in the microwave domain [83, 84, 125, 182] and dissipative squeezing of light [223] which remains elusive.

6 Two-tone Optomechanical Instability

In this chapter, we report a new type of optomechanical instability that arises in two-tone backaction-evading (BAE) measurements [126]. This is observed in the optical domain with a silicon optomechanical crystal and investigated systematically in the microwave domain with a micromechanical oscillator coupled to a microwave resonator. The parametric instability in balanced two-tone optomechanics results from single-mode squeezing of the mechanical mode in the presence of small detuning errors in the two pump frequencies. Counterintuitively, the instability occurs even in the presence of perfectly balanced intracavity fields and can occur for both signs of detuning errors. The instability imposes a fundamental limitation on BAE measurements as well as other two-tone schemes, such as dissipative mechanical squeezing.

6.1 Introduction

Interferometric position measurement of mechanical oscillators is the underlying principle of the Laser Interferometer Gravitational Observatory (LIGO) [28] and constitutes one of the most sensitive techniques for determining absolute distance available to date. In a similar vein, cavity optomechanical systems [43], which exploit radiation-pressure coupling of light and mechanical motion in micromechanical and nanomechanical systems, have achieved some of the most sensitive measurements of mechanical motion relative to the zero-point motion [75, 76]. In both settings, the quantum fluctuations of radiation pressure place a fundamental limitation on the displacement sensitivity [25, 30, 209]. Still, there can be other constraints, such as radiation-pressure nonlinearities. Parametric oscillatory instability [42, 51, 211, 224–228] is one of the most fundamental optomechanical effects predicted to limit the performance of the LIGO detector by constraining the optical power below the self-induced

oscillation threshold [227, 229–235]. It arises from the fact that radiation-pressure coupling is intrinsically nonlinear, giving rise—in addition to static optical bistability [236]—to rich nonlinear dynamics, leading to an intricate landscape of multiple stable attractors (dynamical multistability) [228, 237, 238] and classical chaos [239]. It can occur in single-tone pumping on the upper motional sideband (or blue detuned in the bad-cavity limit), which results from a two-mode squeezing interaction (nondegenerate parametric down-conversion) between the optical and mechanical modes. Radiation-pressure-induced parametric instability has been observed in cavity optomechanical systems [53] and, a decade later, in the Advanced LIGO detector itself [240]. Such dynamical instabilities in optomechanical systems place a limit to ultrasensitive displacement measurements which require high cooperativity.

Here, we report a new type of instability in optomechanical systems with bichromatic driving, resulting from single-mode squeezing (degenerate parametric down-conversion) of the mechanical mode, and is associated with the optical spring effect. More specifically, we observe such instability in two-tone backaction-evading (BAE) measurements [25, 31, 33, 35], which aim to surpass the standard quantum limit (SQL) of measurement of mechanical motion [30]. The *two-tone instability* reported here arises from deviations from the ideal BAE configuration where there is a finite-frequency detuning error with respect to both optical and mechanical resonance frequencies. The threshold for the onset of the instability depends on the magnitude of the tuning errors, and is also inversely proportional to the optical pump power. For any given experimental inaccuracy in the pump frequency, a finite instability threshold exists in two-tone experiments, which ultimately limits the maximum probe power and thus the achievable sensitivity. As we show, these limitations can be prohibitive for strong pumping powers aiming to surpass the SQL. The two-tone instability is intrinsic to the optomechanical interaction and does not arise from extraneous effects, in contrast to previously reported instabilities in BAE measurements associated with thermal effects [241] or two-level systems [80]. While our focus is on BAE measurements, it is important to note that the phenomenon reported here can affect other two-tone optomechanical protocols, such as dissipative mechanical squeezing. For example, in recent work on noiseless single-quadrature amplification of mechanical motion [242], the squeezing effect we report here produces significant deviations from the expected system behavior.

6.2 Observation of instability in two-tone pumping

In a BAE measurement the cavity, with resonance frequency ω_c , is probed with two pump tones of equal power, each tuned to the upper and lower motional sideband of the cavity,

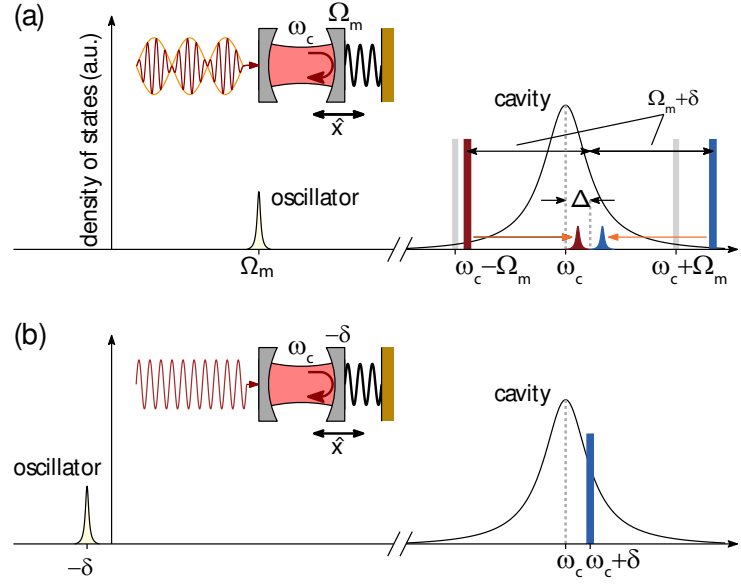


Figure 6.1 – Pumping scheme leading to two-tone instability. (a) Frequency-space representation of optical backaction-evading (BAE) measurement using two-tone pumping. An optomechanical system is pumped with two pumps that are placed on the lower and upper motional sideband of the cavity (shown in gray). Two detuning errors are introduced, due to imperfect knowledge of the mechanical oscillator frequency (δ), and due to imperfect symmetric spacing around the cavities' resonance frequency ω_c , as expressed by Δ . Also shown are the mechanical resonance at frequency Ω_m and the scattered mechanical sidebands. The inset shows an optomechanical system: a mechanical oscillator (position coordinate \hat{x}) that is the moving mirror of a Fabry-Perot cavity and that is coupled to the cavity mode by radiation pressure. (b) An equivalent system, in which the two-tone pumping is mapped to a Hamiltonian that exhibits the same dynamics as (a), consisting of a single continuous pump field applied at $\omega_c + \delta$ and with the mechanical oscillator frequency obeying the substitution $\Omega_m \rightarrow -\delta$. Note that δ and Δ have been exaggerated for clarity.

i.e., at $\omega_c \pm \Omega_m$. It can also be understood as a single pump tuned at ω_c with full amplitude modulation at the mechanical frequency Ω_m . In Fig. 6.1(a) we illustrate the scheme, and introduce a small detuning error $|\Delta| \ll \kappa$ of the symmetrically spaced tones with respect to the cavity resonance, as well as an error $|\delta| \sim \Gamma_m$ in modulation frequency. The two tones are detuned by $\Delta \pm (\Omega_m + \delta)$ from the cavity resonance. The mechanical motion, due to thermal noise and quantum back-action, imprints phase fluctuations on the reflected cavity field. The corresponding output noise spectrum of the two probes exhibits two Lorentzians separated by 2δ , also shown in Fig. 6.1(a). When $\Delta = \delta = 0$, an ideal BAE measurement is performed. The mechanical sidebands are superimposed on each other, but while thermal motion adds in quadrature, the quantum backaction noise is canceled from the measurement record. A hallmark of BAE measurements is witnessing, as δ is varied from a finite value to zero, a total

mechanical noise that is lower than the sum total of the two individual mechanical noise spectra. The total evaded backaction, expressed in units of mechanical quanta, is equal to the optomechanical cooperativity C , proportional to the probing power.

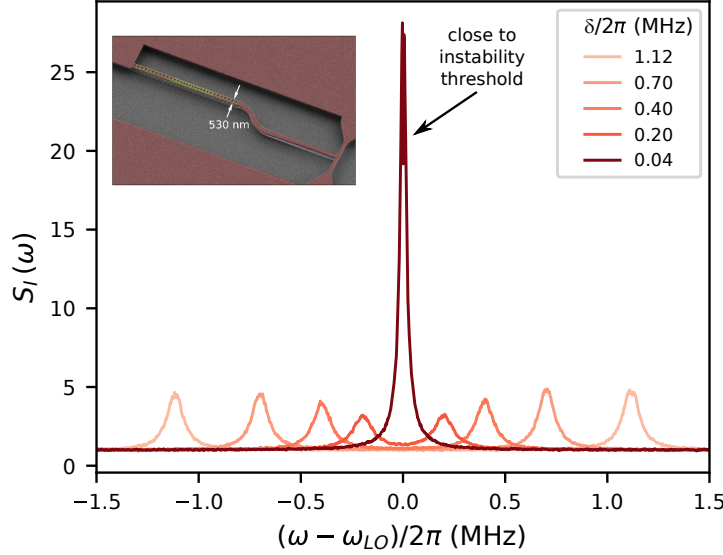


Figure 6.2 – Experimental observation of two-tone instability. BAE measurement in the optical domain with a silicon OMC (inset). The OMC has an optical decay rate of $\kappa/2\pi = 300$ MHz. A sequence of measurements is shown, where the mechanical sidebands are measured via quantum-limited heterodyne detection, normalized to the shot-noise level. Here, ω_{LO} is the optical frequency of the heterodyne local oscillator laser. In the sequence, the mechanical “tuning error” δ is varied from a positive value toward zero, where $\delta = 0$ ideally corresponds to a BAE measurement. Because of the cavity tuning error Δ , at $\delta/2\pi = 0.04$ MHz a strong increase in the total mechanical noise is observed, as well as narrowing of the sideband, instead of the expected decrease due to backaction cancellation.

As shown in Fig. 6.2, we observe the two-tone instability in a silicon OMC [112, 243] with a mechanical frequency $\Omega_m/2\pi \approx 5.2$ GHz, optical resonance wavelength $\lambda \approx 1540$ nm, and cavity linewidth $\kappa/2\pi = 300$ MHz (optical Q factor $\sim 6.5 \times 10^5$). The measured vacuum optomechanical coupling rate is $g_0/2\pi = 930$ kHz. In this chapter, the OMCs are patterned by electron beam lithography using 4% hydrogen silsesquioxane (HSQ) as a negative resist, different from previous chapters. Pattern transfer into the device layer is accomplished by inductively-coupled-plasma reactive ion etching (ICP-RIE) with a mixture of HBr and O_2 . The sample is measured in a ^3He buffer-gas cryostat (Oxford Instruments HelioxTL) [121, 122]. The buffer gas facilitates the thermalization of the sample, preventing deleterious optical absorption heating and allows strong pumping. The various measurements reported here were done at temperatures in the range 4.6–4.9 K, and pressures 32–160 mbar, resulting in a damping rate of $\Gamma_m/2\pi = 100$ –285 kHz.

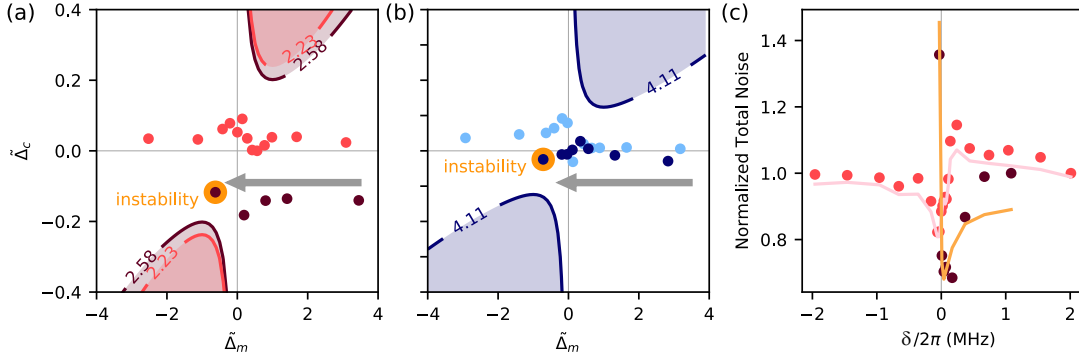


Figure 6.3 – Two-tone instability in the optical domain. (a) Two-tone BAE measurements (dark red and light red dots) scanning δ with Δ kept approximately constant. The $(\tilde{\Delta}_m, \tilde{\Delta}_c)$ coordinate of each measurement is plotted, where $\tilde{\Delta}_c \equiv \Delta/(\kappa/2)$ and $\tilde{\Delta}_m \equiv \delta/(\Gamma_m/2)$. The instability contours for the respective cooperativities, around $C \sim 2.2$ – 2.6 (contour label), are indicated with the same color. While one measurement sequence ($C = 2.23$) remains near $\tilde{\Delta}_c \approx 0$, the other ($C = 2.58$) encounters instability in the vicinity of its corresponding contour. The highlighted dot is the measurement right before instability. (b) Same as (a) with higher $C \sim 4.1$. Here the stable region is smaller, highlighting the difficulty of achieving stable operation due to the inaccuracy in $\tilde{\Delta}_c$. (c) Total noise power in the mechanical sidebands, normalized to 1 for large δ , for the two measurements sequences in (a). The sudden increase in power for the unstable data is evident. The solid lines are theoretical fits using the full Langevin equations.

Figure 6.3 shows examples of the BAE measurements of similar cooperativities $C \sim 2.2$ – 2.6 with δ scanned from positive to negative values, while holding Δ approximately constant. In the lower measurement Δ is farther from 0, bringing it in the vicinity of the domain of instability. This is the same measurement as Fig. 6.2. The separation between the data and the domain of instability is $\sim 2\pi \times 15$ MHz, well within the uncertainty in our measurement of Δ . Figure 6.3(b) shows similar data for higher cooperativity $C \sim 4$, where uncertainty in measurement of Δ precludes discerning between the stable and unstable behavior. Figure 6.3(c) shows the total mechanical noise in the data of Fig. 6.3(a), with the theoretical fit obtained from the Langevin equations (6.6). The data shown in light red, not encountering the instability, show imperfect, asymmetric BAE behavior (due to $\Delta \neq 0$). The dark red data show the amplified noise prior to the onset of instability.

6.3 Theory

It is well known that the anti-damping induced by pumping the cavity on the upper motional sideband (or blue detuning in the bad-cavity limit) can induce a parametric oscillatory instability. In principle, there exists another type of dynamical instability in this system, one

associated with the optical spring effect, i.e., a change in the restoring force induced by light. This cannot occur in the resolved-sideband regime, in the relevant case of weak coupling between the mechanical mode and the cavity field. Indeed, optomechanical systems typically employ high-quality-factor oscillators, where the shift in mechanical frequency due to dynamical backaction can be neglected. However, as we show below, this instability may arise when pumping with *two* tones close to the upper and lower mechanical sidebands [Fig. 6.1(a)], as in BAE measurements, for example. In fact, as we show, the situation when pumping with two tones and that for single-tone driving on the upper motional sideband are described by the same linearized equations.

We consider the balanced two-tone driving on the upper and lower motional sidebands. Following the theoretical treatment in the BAE measurement, we can obtain the Hamiltonian

$$\hat{H}/\hbar = -\delta \hat{a}^\dagger \delta \hat{a} \Delta - \delta \hat{b}^\dagger \delta \hat{b} \delta - g(\delta \hat{a} + \delta \hat{a}^\dagger)(\delta \hat{b} + \delta \hat{b}^\dagger), \quad (6.1)$$

where $\delta \approx 0$.

From the quantum Langevin equations [43, 105], we can obtain,

$$\left[\frac{\Gamma_m}{2} - i(\delta + \omega) + i\Sigma(\omega) \right] \delta \hat{b}(\omega) = -i\Sigma(\omega) \delta \hat{b}^\dagger(\omega) + \hat{b}_{\text{in}}(\omega), \quad (6.2)$$

where the self-energy (effective coupling) is given through

$$\Sigma(\omega) = \frac{2\Delta g^2}{(\kappa/2 - i\omega)^2 + \Delta^2}. \quad (6.3)$$

In Eq. (6.2) we have subsumed all noise contribution into a single generic noise input operator $\hat{b}_{\text{in}}(\omega)$, which does not play a role in the instability mechanism. So far we have not made any approximations (beyond the RWA in two-tone driving), and indeed Eq. (6.2) contains all the effects we wish to consider here. The self-energy Σ plays two roles. First, it couples $\delta \hat{b}^\dagger$ to $\delta \hat{b}$, thus acting like the coupling in a degenerate parametric oscillator. Second, as a self-energy, its real part renormalizes the frequency of the mechanical resonator and its imaginary part modifies the effective damping.

Two-tone instability.—In backaction-evading measurements, δ is small, as it represents a tuning error. This makes the right-hand side of Eq. (6.2) near resonant, such that it cannot be neglected. The instability arises in a way similar to a degenerate parametric oscillator [244]. Since κ is now a large parameter, we can neglect the frequency dependence of $\Sigma(\omega) \approx \Sigma(0) \equiv \Sigma \in \mathbb{R}$. Note that now the self-energy Σ coincides with the optical spring effect due to a

single drive detuned by Δ from cavity resonance. This allows us to recast Eq. (6.2) again as an equation of motion

$$\delta \dot{\hat{b}}(t) = \left[-\frac{\Gamma_m}{2} + i(\delta - \Sigma) \right] \delta \hat{b}(t) - i\Sigma \delta \hat{b}^\dagger(t) + \hat{b}_{\text{in}}(t). \quad (6.4)$$

This equation is the same quantum Langevin equation as one would write down for a damped degenerate parametric oscillator. It can intuitively be viewed as arising from an optical spring effect modulated at $2(\Omega_m + \delta)$. The dynamical matrix corresponding to Eq. (6.4) has eigenvalues $-\frac{\Gamma_m}{2} \pm i\sqrt{\delta(\delta - 2\Sigma)}$. For $2\Sigma < \delta$, the eigenvalues have a negative real part (damping $\Gamma_m/2$) and a finite imaginary part (effective frequency $\Delta_{\text{eff}} = \text{Re} \sqrt{\delta(\delta - 2\Sigma)}$). As Σ increases, first the effective frequency Δ_{eff} vanishes, at which point the damping of the modes starts to be modified. The vanishing of the effective mechanical frequency corresponds to the mechanical oscillation phase locking to the modulated optical field. The stability condition is

$$4g^2\delta\Delta < \left(\frac{\Gamma_m^2}{4} + \delta^2 \right) \left(\frac{\kappa^2}{4} + \Delta^2 \right). \quad (6.5)$$

The instability threshold can also be written in terms of normalized detunings $\tilde{\Delta}_c \equiv \Delta/(\kappa/2)$ and $\tilde{\Delta}_m \equiv \delta/(\Gamma_m/2)$, yielding $4C = (1 + \tilde{\Delta}_c^2)(1 + \tilde{\Delta}_m^2)/(\tilde{\Delta}_c\tilde{\Delta}_m)$. This equation can only be fulfilled for $C \geq 1$, and we plot its contours in Fig. 6.4. Note that Eq. (6.5) also predicts that the instability can occur for *both* negative and positive values of the two detuning errors (provided they have the same sign), in contrast to the parametric oscillatory instability.

Further understanding of the two-tone instability, and its distinction from the parametric oscillatory instability, can be achieved by examining the eigenvalues of the dynamical matrix, similar to the analysis performed in Ref. [245]. The Hamiltonian Eq. (6.1) leads to the quantum Langevin equations

$$\delta \dot{\hat{a}} = -(\kappa/2 - i\Delta)\delta \hat{a} + ig(\delta \hat{b} + \delta \hat{b}^\dagger) + \sqrt{\kappa}\delta \hat{a}_{\text{in}} \quad (6.6a)$$

$$\delta \dot{\hat{b}} = -(\Gamma_m/2 - i\delta)\delta \hat{b} + ig(\delta \hat{a} + \delta \hat{a}^\dagger) + \sqrt{\Gamma_m}\delta \hat{b}_{\text{in}}. \quad (6.6b)$$

Ignoring the input noise operators $\delta \hat{a}_{\text{in}}$ and $\delta \hat{b}_{\text{in}}$, which are irrelevant in the present analysis,

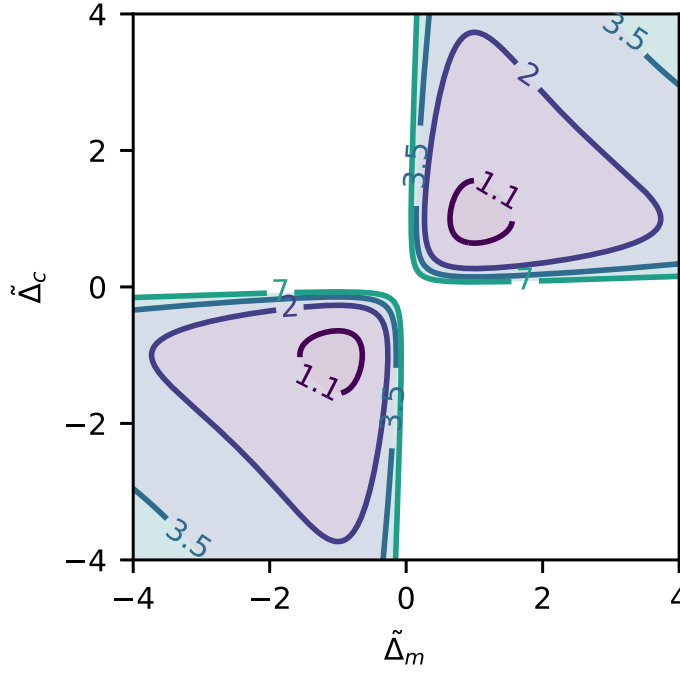


Figure 6.4 – **Domains of two-tone instability.** The onset of the two-tone instability is given by the condition Eq. (6.5) and depends only on $\tilde{\Delta}_m \equiv \delta / (\Gamma_m/2)$, $\tilde{\Delta}_c \equiv \Delta / (\kappa/2)$, and the cooperativity C . Here we plot the domains of instability as a function of $\tilde{\Delta}_m$ and $\tilde{\Delta}_c$ for different cooperativities C (given as the contour labels). As C increases the stable region in the vicinity of the origin $\tilde{\Delta}_m = \tilde{\Delta}_c = 0$ becomes smaller, reducing the range of $\tilde{\Delta}_m$ and $\tilde{\Delta}_c$ for which the system is stable.

the Langevin equations (6.6) can be written as a matrix equation $\dot{\mathbf{x}} = \mathbf{M}\mathbf{x}$, with

$$\mathbf{M} = \begin{pmatrix} -\kappa/2 & -\Delta & 0 & 0 \\ \Delta & -\kappa/2 & 2g & 0 \\ 0 & 0 & -\Gamma_m/2 & -\delta \\ 2g & 0 & \delta & -\Gamma_m/2 \end{pmatrix} \quad (6.7)$$

and

$$\mathbf{x} = [\delta \hat{a} + \delta \hat{a}^\dagger, i(\delta \hat{a}^\dagger - \delta \hat{a}), \delta \hat{b} + \delta \hat{b}^\dagger, i(\delta \hat{b}^\dagger - \delta \hat{b})]^T. \quad (6.8)$$

We note that this dynamical equation describes *both* single-tone pumping, with the equivalence $-\delta \rightarrow \Omega_m$, and two-tone pumping in the well-resolved sideband regime (Fig. 6.1). An eigenvalue of the matrix Eq. (6.7) with a positive real part leads to an exponentially increasing

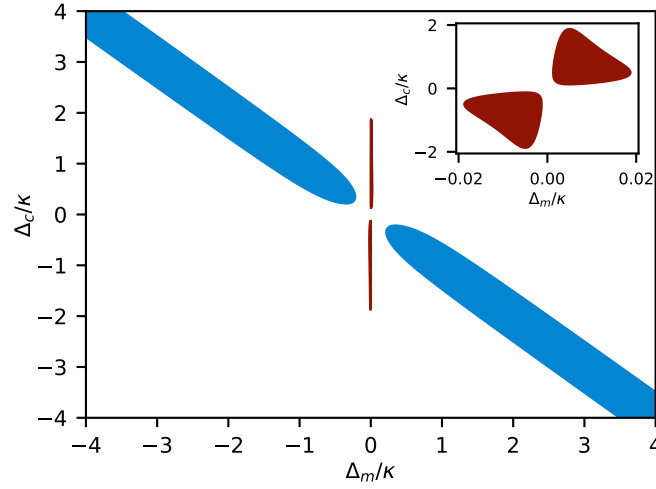


Figure 6.5 – **Instability domains from eigenvalue analysis.** Domains where an eigenvalue of the dynamical matrix Eq. (6.7) has positive real part, signaling an instability. The blue domain, in the neighborhood of $-\delta = \Omega_m \approx \Delta_c$, is the known parametric oscillatory instability. In this domain, the imaginary part of the eigenvalue is nonzero. In reality, the mechanical frequency is positive $\Omega_m > 0$, such that the lower right-hand part is unphysical. The red domain that occurs for $|\delta| \ll \kappa$ (enlargement shown in the inset) is the two-tone instability. In this domain $\delta\Delta > 0$, and the imaginary part of the eigenvalue is zero. The parameters used are $\kappa = 1$, $\Gamma_m = 10^{-2}$, and $C = 2$.

solution, and thus signals an instability. For such a dynamical linear time invariant system, we can apply the Routh–Hurwitz stability criterion, which also results in Eq. 6.5.

Figure 6.5 shows the domains of instability in the parameter space spanned by δ and Δ . These domains separate into two classes, corresponding to the parametric and two-tone instabilities. In one class, which corresponds to the conventional parametric oscillatory instability, the imaginary part of the offending eigenvalue is nonzero, corresponding to spiral dynamics [246]. The onset of the parametric oscillatory instability coincides with the transition from a stable to an unstable spiral. This class lies in the vicinity of the diagonal $\Delta \approx \Omega_m$, as expected (note that the regime $\delta = -\Omega_m > 0$, although mathematically possible, is unphysical in this case). The second class lies close to the origin, in particular $|\delta| \ll \kappa$, and corresponds to the two-tone instability. In this regime the eigenvalues are well approximated by the eigenvalues of Eq. (6.4) due to the slow dynamics of the optical field, and the instability domains are given by the simple condition (6.5). The eigenvalues are real and of opposite sign, corresponding to a saddle point, as expected from a degenerate parametric amplifier. In this picture, as the power ($\propto \Sigma$) is increased, the dynamics change from a stable spiral to a stable node and finally to a saddle point [246]. Figure 6.4 shows the domains of two-tone instability for different powers.

Apart from using locking techniques to reduce Δ , it may be possible to hold off the onset of the two-tone instability by using active feedback. Feedback techniques to counter the parametric oscillatory instability have been considered [247, 248]. In the case of the two-tone instability, the feedback force would naturally be applied on the measured quadrature (and as such is not of the viscous damping type).

6.4 Microwave Experiment

In the optical domain, pump frequency fluctuations and cavity frequency fluctuations are quite large. The control of the detuning errors is of great challenge, which makes it impossible to verify the theory above. To independently confirm the existence and universality of this phenomenon, the measurement is performed in an entirely different optomechanical system: an electromechanical system based on a mechanically-compliant vacuum-gap capacitor coupled to a superconducting microwave resonator placed in a dilution refrigerator [249, 250]. An overcoupled ($\kappa_{\text{ex}}/2\pi = 2.65\text{ MHz}$, $\kappa_0/2\pi = 0.16\text{ MHz}$) Al superconducting microwave resonator with a resonance frequency of $\omega_c/2\pi = 6.43\text{ GHz}$ is coupled (vacuum coupling rate $g_0/2\pi = 194\text{ Hz}$) to a mechanically compliant vacuum-gap capacitor ($\Omega_m/2\pi = 6.15\text{ MHz}$ and $\Gamma_m/2\pi \approx 20\text{ Hz}$). The chip was cooled to about 15 mK in a dilution refrigerator. Three microwave sources with a common frequency reference are sent to the microwave optomechanical system: two BAE pumps with frequencies $\omega_c + \Delta \pm (\Omega_m + \delta)$ and an additional cooling pump tuned to $\omega_c - \Omega_m - \delta_{\text{cool}}$, where $\delta_{\text{cool}}/2\pi = 400\text{ kHz}$. The cooling tone is applied to reduce the thermal noise and increase the mechanical damping rate to $\Gamma_{\text{eff}}/2\pi = 110\text{ Hz}$, allowing us to observe the narrowing of the mechanical sidebands when approaching the instability with better resolution.

Figure 6.6 shows two-tone instability in BAE experiment in the microwave domain, with a cooperativity of $C = 7$ (here, measurement backaction includes classical noise, which should also be canceled). We observe an exponential increase in the total noise as the detuning δ is decreased. As δ is decreased further, the noise saturates the HEMT amplifier in the detection chain, leading to an increased noise floor [Fig. 6.6, yellow curve]. The origin of this instability is not a spurious effect in the experiments, as is evident from the observation that the same behavior occurs in two very different optomechanical systems measured with very different equipment. Instead, as shown below, the instability is a direct consequence of the optomechanical interaction in the presence of the small tuning errors δ and Δ and depends only on these two parameters and the cooperativity. To validate Eq. (6.5), the threshold for the two-tone instability in terms of δ and Δ , a two-dimensional scan is performed [249, 250].

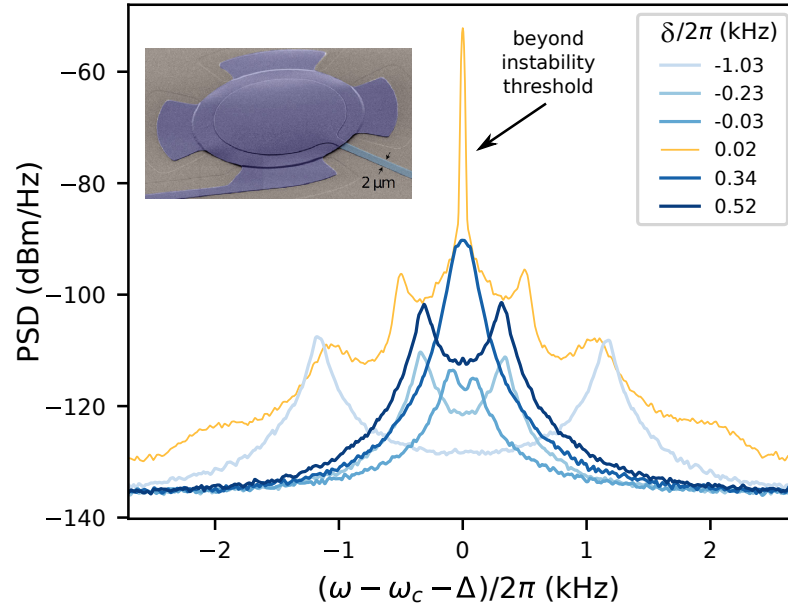


Figure 6.6 – **Experimental observation of two-tone instability in microwave domain.** BAE measurement in the microwave domain with a mechanically compliant capacitor coupled to a superconducting microwave resonator (inset). Measurements with both positive and negative values of δ are shown. The measurement at $\delta/2\pi = 0.02$ kHz occurs within the domain of instability (yellow curve), in which case the observed spectrum is distorted by saturation of the HEMT amplifier used in the detection chain. Note the logarithmic y axis.

Figures 6.7(a)–(c) show the total noise in the mechanical sidebands as a function of $\tilde{\Delta}_m$ and $\tilde{\Delta}_c$ for three different cooperativities C . Each horizontal cut in Figs. 6.7(a)–(c) corresponds to a measurement of the type shown in Fig. 6.2. The domains of instability are clearly evident as areas of increased noise (in red), in excellent agreement with Eq. (6.5) (black contours). In particular, instability only arises when $\tilde{\Delta}_m \tilde{\Delta}_c > 0$, as predicted from Eq. (6.5), and can arise both for red- ($\tilde{\Delta}_c < 0$) and blue-detuned ($\tilde{\Delta}_c > 0$) mean probe frequency. Figures 6.7(d)–(f) show the theoretical plots corresponding to Fig. 6.7(a)–(c), again in excellent agreement. Figures 6.7(g)–(i) show the horizontal cuts indicated in Fig. 6.7(b). The point $\tilde{\Delta}_m = \tilde{\Delta}_c = 0$ corresponds to a "perfect" BAE measurement, as can be seen in Fig. 6.7(g), where a 3 dB decrease in the total mechanical noise relative to $\tilde{\Delta}_m \neq 0$ due to cancellation of measurement backaction is evident.

The predicted decrease in size of the stable region with increasing pumping power is clearly evident in the experimental data depicted in Fig. 6.7, with $\tilde{\Delta}_c \lesssim 1/2C$ required to avoid instability [e.g., $\tilde{\Delta}_c \lesssim 0.04$ for $C = 14$ in Fig. 6.7(c)]. Overall, excellent agreement is obtained between theory and experiment, confirming our theoretical analysis and description of the effect. Thus, optomechanics imposes strict tuning accuracy for a given measurement sensi-

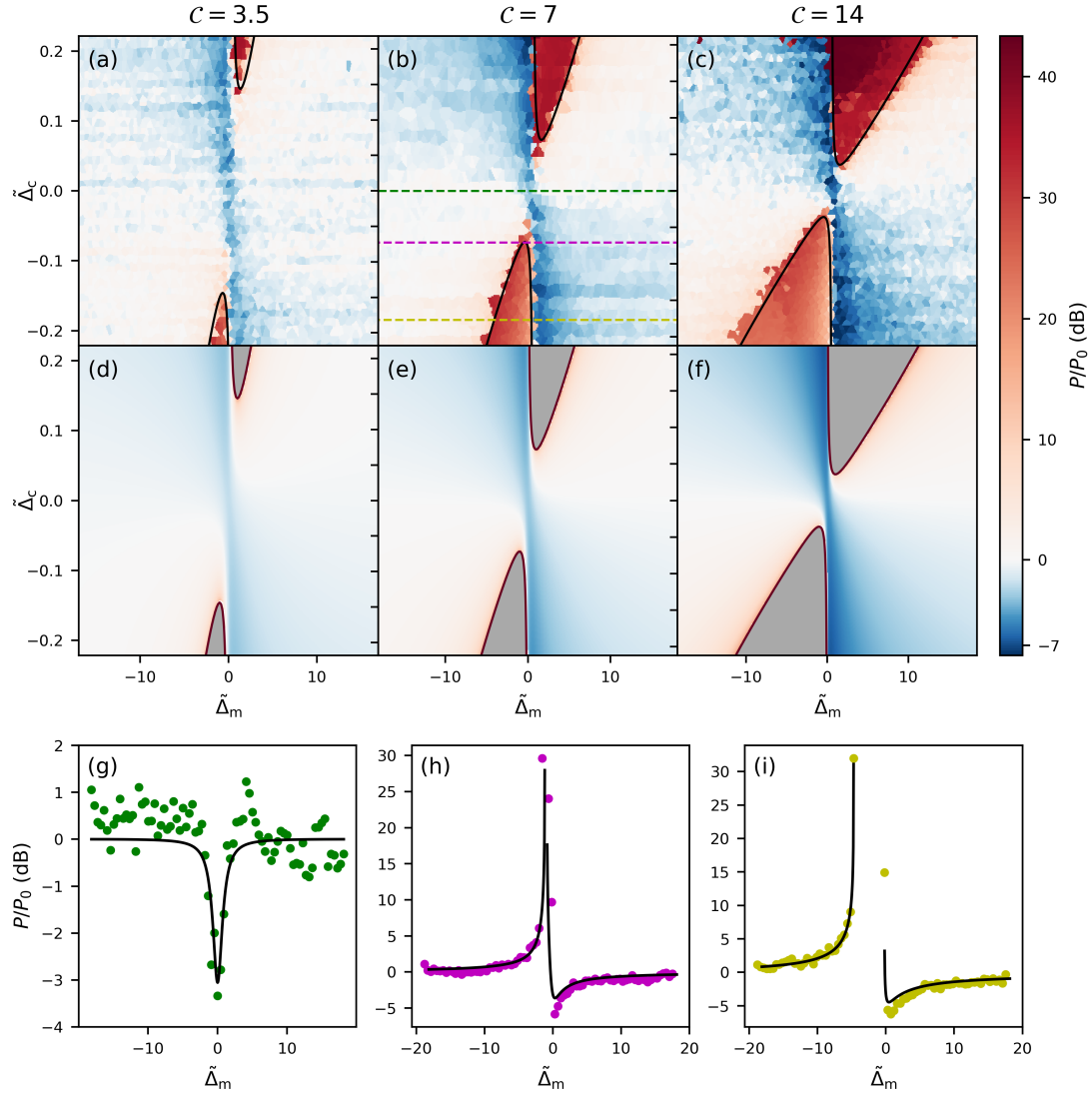


Figure 6.7 – Investigation of the two-tone instability in a circuit-electromechanical system. (a)–(c) Mapping of the total mechanical noise as a function of $\tilde{\Delta}_m$ and $\tilde{\Delta}_c$, for cooperativities $C = \{3.5, 7, 14\}$, respectively. The total power P in both mechanical sidebands in the output spectra is shown, normalized to the power P_0 at $(\tilde{\Delta}_m, \tilde{\Delta}_c) = (-18, 0)$ (no tuning error and far from the BAE regime). Since data points do not align on a regular grid (accounting for small changes in $\tilde{\Delta}_c$ along the horizontal scan), the rasterization was implemented using nearest-neighbor (Voronoi) partitioning. Solid black lines are instability thresholds from Eq. (6.5). (d)–(f) Theory plots corresponding to (a)–(c). Gray areas are unstable regions predicted by theory. (g)–(i) Cross sections of (b) for $\tilde{\Delta}_c = \{0, -0.07, -0.18\}$, respectively [nearest data points to horizontal dashed lines in (b)]. Solid black lines are theory predictions based on the full linear model.

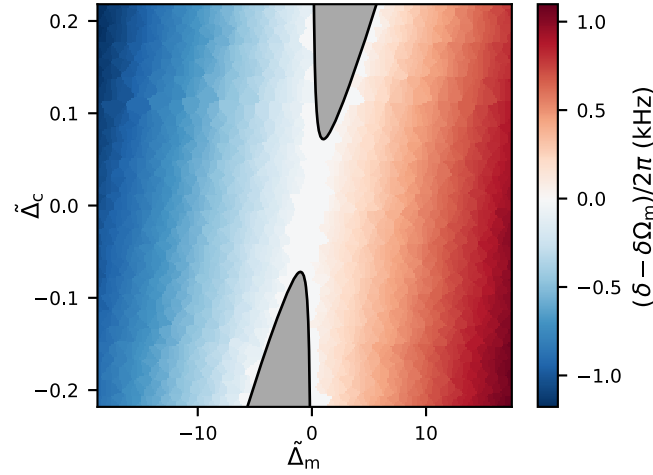


Figure 6.8 – **Vanishing of the effective mechanical frequency.** The plot shows the difference between the measured effective mechanical frequency and pump modulation frequency as a function of the detunings. Near the instability domain (shaded in gray), the two frequencies become equal, which corresponds to vanishing of the effective mechanical frequency in the rotating frame, confirming the theoretical treatment. Measurement is the same as in Fig. 6.7(b).

tivity in two-tone BAE measurements. In this case, measurement backaction is due to both quantum and classical noise in the two microwave tones. It is important to emphasize that for BAE measurements that allow measurements beyond the SQL, cooperativities of $C \gg \bar{n}_m$ are required, thus highlighting the stringent nature of the condition imposed by $\tilde{\Delta}_c \lesssim 1/2C$.

In Fig. 6.8 we plot the difference between δ and the change in effective mechanical frequency of the oscillator $\delta\Omega_m$ (due to the optical spring effect), for the same data as in Fig. 6.7(b). Near the onset of the two-tone instability, the two sidebands coincide, and this difference approaches zero; i.e., the effective mechanical frequency $\Omega_m + \delta\Omega_m$ becomes equal to the modulation frequency of the pump, $\Omega_m + \delta$. This corresponds to vanishing of the effective mechanical frequency in the frame rotating with the modulation frequency.

6.5 Conclusion

We report experimentally and explain theoretically a new type of dynamical instability that was previously unreported in cavity optomechanics. This instability is qualitatively different than the parametric oscillatory instability [225–227, 229, 237, 251], and originates from degenerate parametric amplification of the mechanical mode. Our work now demonstrates that the performance of emerging optomechanical experiments, such as backaction-evading

measurements aimed at surpassing the standard quantum limit [78, 121], generation of quantum squeezing [81, 213, 223, 252], and noiseless single-quadrature amplification [242], will be intrinsically constrained by another instability determined by tuning accuracy and coupling strength. Even below the instability threshold, these new dynamics need to be taken into account.

7 Laser cooling of a nanomechanical oscillator to the zero-point energy

Optomechanical cavities in the well-resolved-sideband regime are ideally suited for the study of a myriad of quantum phenomena with mechanical systems, including backaction-evading measurements, mechanical squeezing, and generation of non-classical states. For these experiments, the mechanical oscillator should be prepared in its ground state; residual motion beyond the zero-point motion must be negligible. The requisite cooling of the mechanical motion can be achieved using the radiation pressure of light in the cavity by selectively driving the anti-Stokes optomechanical transition. To date, however, laser-absorption heating of optical systems far into the resolved-sideband regime has prohibited strong driving. For deep ground-state cooling, previous studies have therefore resorted to passive cooling in dilution refrigerators. In this chapter, we employ a highly sideband-resolved silicon optomechanical crystal in a ^3He buffer gas environment at $\sim 2\text{ K}$ to demonstrate laser sideband cooling to a mean thermal occupancy of $0.09^{+0.02}_{-0.01}$ quantum (self-calibrated using motional sideband asymmetry), which is -7.4 dB of the oscillator's zero-point energy and corresponds to 92% ground state probability [145]. Achieving such low occupancy by laser cooling opens the door to a wide range of quantum-optomechanical experiments in the optical domain.

7.1 Introduction

Laser cooling techniques developed several decades ago [57, 253–255] have revolutionized many areas of science and technology, with systems ranging from atoms, ions and molecules [256–262] to solid-state structures and macroscopic objects [128, 263, 264]. Among these systems, mechanical oscillators play a unique role given their macroscopic nature and their ability to couple to diverse physical quantities [43]. Laser cooling of mechanical systems occurs via coupling of mechanical and electromagnetic degrees of freedom (optomechanical

coupling) and has been demonstrated with a wide range of structures [54–56, 60, 61, 66, 74–76, 265, 266]. It has led to the observation of radiation pressure shot noise [64], ponderomotive squeezing of light [67, 68], and motional sideband asymmetry [67–70].

Many optomechanical protocols, including mechanical squeezing [83, 84, 124, 125, 182], entanglement [205, 206], state swaps [101], generation of non-classical states [96, 97, 138, 147, 267], and back-action evading (BAE) measurements below the standard quantum limit (SQL) [77, 78, 121], require ground state preparation of a well-sideband-resolved system, where Stokes and anti-Stokes motional transitions can be driven selectively. In this case, driving of anti-Stokes transitions can be efficiently applied to damp the motion and sideband cool the system. The cooling limit is set by laser noise (classical or quantum) or by technical limitations, such as absorption heating, and determines the residual thermal noise. For the case of squeezing or BAE measurements, the amount of cooling beyond half quantum (equivalent to the zero point energy) determines the amount of squeezing or the amount to which the SQL on resonance is surpassed. Such deep ground-state preparation has been demonstrated in microwave optomechanical systems [61]. In the optical domain, however, cooling below half quantum has so far only been achieved in systems with low sideband resolution, i.e. in the bad-cavity limit [86] or using feedback cooling [76].

Silicon optomechanical crystals (OMCs) [49, 136] that couple an optical mode at telecommunication wavelengths and a co-localized mechanical mode at GHz frequencies exhibit several exceptional features, including large vacuum coupling rates ~ 1 MHz [136] as well as ultralong phonon lifetime [137]. They have been employed in a wide range of experiments, such as continuous quantum measurements [60, 121, 122], and probabilistic preparation of quantum states [96, 97, 138, 147]. The compatibility of these systems with planar nanofabrication technology and their scalability have motivated studies of optomechanical topological phenomena [139, 140], frequency conversion [102] and coupling to superconducting qubits [103, 104]. Yet despite these promising features, ground-state preparation of silicon OMCs has only been possible via passive cooling to milli-Kelvin temperatures in dilution refrigerators [148, 181]. Significant heating due to optical absorption—a consequence of the extremely small optical mode volume and inefficient thermalization [115]—has limited experiments to use of weak laser pulses [96, 97, 137, 138, 147] and precluded continuous measurements [121, 122, 148].

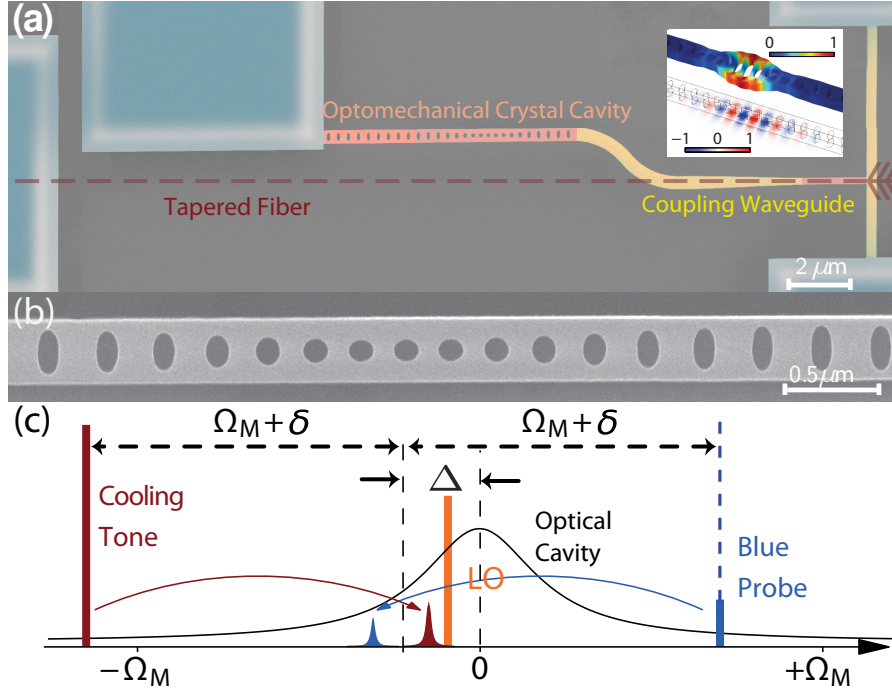


Figure 7.1 – **Optomechanical crystal and experimental scheme.** (a) False-color SEM image of the silicon optomechanical crystal cavity with a waveguide for input coupling of light. The path of the tapered fiber is indicated by the red dashed line. The inset shows the simulated mechanical breathing mode and optical mode. (b) SEM image of the central portion of the silicon optomechanical crystal cavity. (c) Measurement scheme using a cooling tone for sideband cooling and a blue probe for motional sideband asymmetry measurement. The local oscillator (LO) is used for detection and is not sent to the cavity.

7.2 Experimental System Details

As shown in Fig. 7.1(a,b), our system consists of a quasi-one-dimensional silicon optomechanical crystal [121, 122, 136]. The OMC is mounted in a ^3He cryostat (Oxford Instruments HelioxTL) operated at $\sim 2.0\text{K}$ and a buffer-gas pressure of $\sim 40\text{mbar}$, which ensures efficient thermalization of the device [121, 122]. A tapered optical fiber is used to couple light evanescently into the coupling waveguide (40% efficiency in this work). For characterization, we monitor the laser light reflected from the single-sided optical cavity. The optical resonance is at 1540nm with a total linewidth of $\kappa/2\pi \approx 255\text{MHz}$, of which the external coupling rate is $\kappa_{\text{ex}}/2\pi \approx 71\text{MHz}$.

The optical mode is coupled to a localized mechanical mode with frequency $\Omega_m/2\pi \approx 5.17\text{GHz}$ with an intrinsic damping rate $\Gamma_{\text{int}}/2\pi \approx 65\text{kHz}$. An independent measurement is performed at temperature of 4K and pressure of 40mbar , from which we obtain measured vacuum optomechanical coupling rate $g_0/2\pi = 1.08\text{MHz}$ and broadened mechanical damping rate

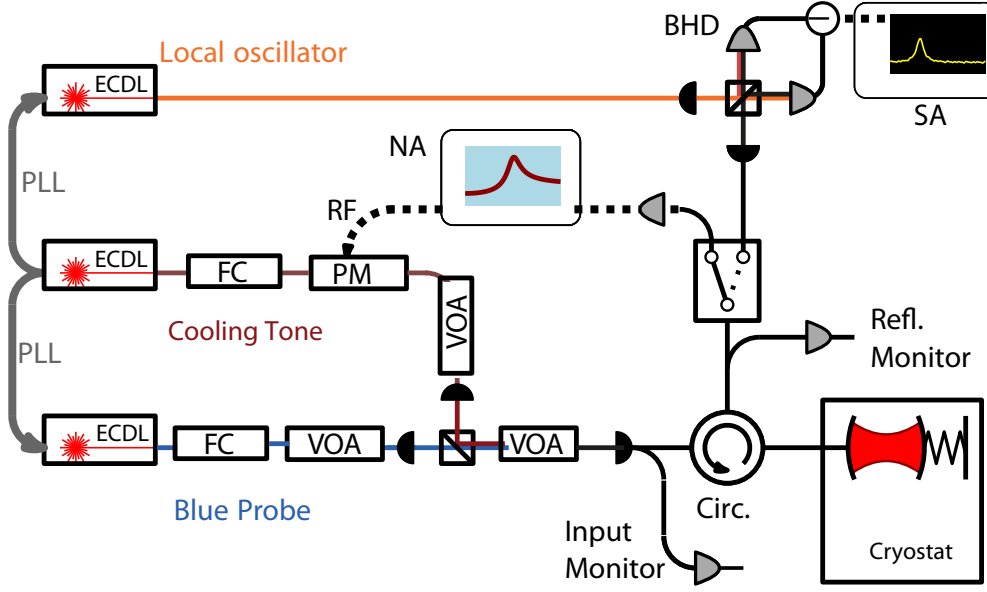


Figure 7.2 – **Experimental setup.** ECDL, external-cavity diode laser; FC, filter cavity; PM, phase modulator; VOA, variable optical attenuator; BHD, balanced heterodyne detector; SA, spectrum analyzer; NA, network analyzer; PLL, phase-locked loop.

$\Gamma_m/2\pi = 115 \pm 8 \text{ kHz}$ due to additional gas damping .

In this experiment, we choose to work at 2.0K and ^3He buffer gas pressure $\sim 40 \text{ mbar}$. A schematic of the experimental setup is shown in Fig. 7.2. Three external cavity diode lasers (ECDLs) generate the local oscillator (Toptica CTL 1550), cooling tone (Toptica CTL 1500), and blue probe (Toptica CTL 1500). The blue probe and local oscillator (LO) are phased-locked to the cooling tone. Different from previous chapters, both cooling tone and the blue probe are filtered by a 50 MHz bandwidth tunable Fabry-Perot filters which are locked to the respective tones using PDH lock technique, to reject the high frequency excess laser phase noise. The cooling tone passes through a phase modulator (PM), used to generate weak sidebands as probes for coherent optomechanical spectroscopy. The cooling tone and the blue probe are combined in free-space with the same polarization and sent into a single-mode fiber that enters the cryostat. A fiber-optic circulator feeds the reflected light to the detection stage, which can be toggled between two different paths. In the first path, the reflected light is sent to a fast photoreceiver connected to a network analyzer for coherent optomechanical spectroscopy, in which case the phase modulator is employed. In the second path, the reflected light is sent to a balanced heterodyne detection (BHD) setup, where it is mixed with a strong local oscillator ($\sim 8 \text{ mW}$) on balanced photodetectors. The power spectral density of the photocurrent is analyzed by a spectrum analyzer. In this case, the cooling tone is not phase

modulated.

Motional sideband asymmetry, a signature of the quantum nature of the optomechanical interaction, was recently observed in various optomechanical systems [67–70, 122] and used to perform self-calibrated thermometry of the mechanical oscillator close to its ground state [68–70, 122]. In our experiments, we adopt a two-tone pumping scheme [Fig. 7.1(c)], where a strong cooling tone near the lower motional sideband is applied for sideband cooling, while an additional weaker ‘blue probe’ is applied near the upper motional sideband. By measuring the resonantly-enhanced anti-Stokes and Stokes scattered sidebands, proportional to \bar{n}_f and $\bar{n}_f + 1$, respectively, the mean phonon occupancy of the oscillator \bar{n}_f can be determined. The frequencies of the two tones are separated by $2(\Omega_m + \delta)$, and their mean is detuned from the optical resonance frequency by Δ [Fig. 7.1(c)]. In the presence of the cooling tone and blue probe, the mechanical susceptibility is modified by the radiation pressure. The effective mechanical damping rate becomes $\Gamma_{\text{eff}} = \Gamma_m + \Gamma_{\text{opt}}$, with the total optomechanical damping rate (in the resolved-sideband regime) $\Gamma_{\text{opt}} = -\Gamma_b + \Gamma_c$, where

$$\Gamma_{b(c)} = \bar{n}_{b(c)} g_0^2 \left(\frac{\kappa}{\kappa^2/4 + (\Delta \pm \delta)^2} \right), \quad (7.1)$$

and \bar{n}_b and \bar{n}_c are the intracavity photon numbers of the blue probe and cooling tone, respectively. In the weak coupling regime, $\Gamma_{\text{opt}} \ll \kappa$, the effective mechanical frequency is $\Omega_{\text{eff}} = \Omega_m + \delta\Omega_m$, with

$$\delta\Omega_m = g_0^2 \left(\bar{n}_b \frac{\Delta + \delta}{\kappa^2/4 + (\Delta + \delta)^2} + \bar{n}_c \frac{\Delta - \delta}{\kappa^2/4 + (\Delta - \delta)^2} \right). \quad (7.2)$$

The mean final phonon occupancy is given by

$$\bar{n}_f = \frac{\Gamma_m \bar{n}_{\text{th}} + \Gamma_b}{\Gamma_{\text{eff}}}, \quad (7.3)$$

where \bar{n}_{th} is the mean phonon occupancy due to the thermal environment. Importantly, the second term in the numerator of Eq. (7.3) corresponds to quantum backaction (QBA) heating due to resonant Stokes transitions from the blue probe [Fig. 7.1(c)]. This is in contrast to off-resonant Stokes transitions from the cooling tone, which are completely negligible in the well-resolved sideband regime (here $\Omega_m/\kappa \simeq 20$) and set the quantum limit for sideband cooling [86, 118–120]. In our two-tone experiments, QBA heating due to the blue probe, $\Gamma_b/\Gamma_{\text{eff}}$, is comparable to the heating by the thermal bath at high probe powers and limits the cooling. Thus we perform both two-tone measurements for ancillary quantum thermometry and single-tone measurements to achieve maximum cooling power.

In each measurement, we first determine the detuning of the cooling tone from the cavity, $\Delta_c = \Delta - \Omega_m - \delta$ by performing a coherent cavity response measurement [110, 121]. We then obtain the thermomechanical noise spectrum by measuring the cavity output field using quantum-limited balanced heterodyne detection (BHD) with a strong phase-locked local oscillator (LO; ~ 8 mW). The frequency difference between the LO and the mean frequency of the two pumping tones is Δ_{LO} , where $0 < -\delta < \Delta_{LO}$. The measured heterodyne noise spectrum, normalized to the shot noise floor, is given by

$$S_I(\Omega) = 1 + \eta \Gamma_{\text{eff}} \left[\frac{(\bar{n}_f + 1) \Gamma_b}{\Gamma_{\text{eff}}^2/4 + (\Omega + \delta - \Delta_{LO})^2} + \frac{\bar{n}_f \Gamma_c}{\Gamma_{\text{eff}}^2/4 + (\Omega - \delta - \Delta_{LO})^2} \right], \quad (7.4)$$

where η is the overall detection efficiency. The second and third terms in Eq. (7.4) correspond to the scattered Stokes and anti-Stokes sidebands, which we use for self-calibrated thermometry of the oscillator.

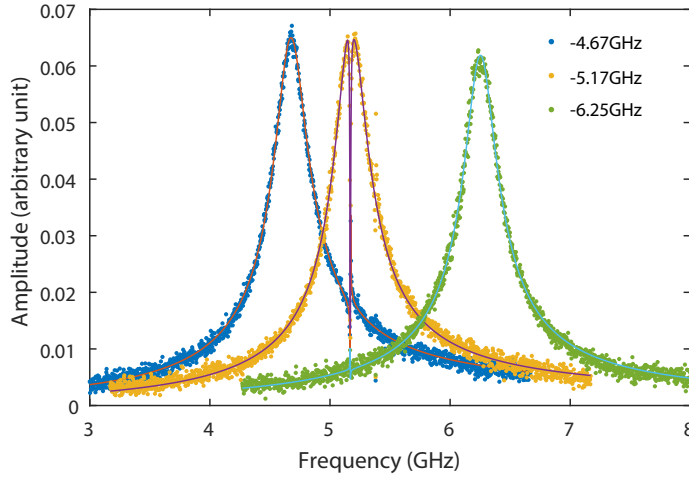


Figure 7.3 – **Coherent optomechanical spectroscopy.** Reflected cavity response for single tone detuning sweeps for various detunings of the cooling tone with respect to the optical resonance. The curve, including the optomechanically-induced transparency, is fitted with a theoretical model to obtain the Δ_c and κ .

Our scheme differs from previous experiments that utilize equal red and blue probes alongside a cooling tone [70, 122]. By using only two tones, we avoid coupling between scattered sidebands due to Floquet dynamics that may introduce errors in the inferred phonon occupancy [122]. We keep the ratio between the input powers of the cooling tone and the blue probe around 6, to achieve both sufficient cooling and a measurable anti-Stokes signal ($\propto \bar{n}_f$). From a series of two-tone measurements, we obtain a mean calibration coefficient between the normalized thermomechanical sideband area A_c/Γ_c and the phonon occupancy \bar{n}_f using Eq. (7.4), where A_c is the area of the sideband from the cooling tone. The calibration coeffi-

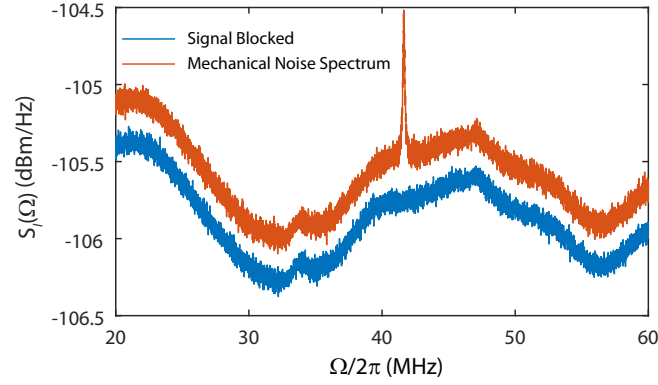


Figure 7.4 – **Incoherent noise spectrum from heterodyne detection.** Typical noise spectrum from BHD in the single-tone detuning-sweep measurements at $\Delta_c/2\pi \simeq -7.18$ GHz. The shot noise spectrum with signal blocked is shown in blue while the noise spectrum of the thermomechanical sideband is shown in red.

cient serves as an ancillary quantum thermometer for the mechanical mode, independent of the resistive thermometer mounted in the cryostat. For ground state cooling, we turn off the blue probe and perform single-tone sideband cooling measurements, keeping the same experimental conditions and calibration. From the measured thermomechanical noise spectrum, we can thus obtain the final occupancy using two independent calibrations, *i.e.*, the ancillary quantum thermometry and the mechanical noise thermometry, where for the latter the mechanical mode temperature is referenced to the cryostat thermometer.

7.3 Experimental Results

A single measurement consists of acquisition of the power spectral density for given system parameters (cooling tone power, detuning, etc.) and determination of the phonon occupancy using Eqs. (2.87) and (2.82), *i.e.* ancillary quantum thermometry and mechanical noise thermometry. This requires reliable characterizations of κ , \bar{n}_c , \bar{n}_b and Δ_c . A measurement proceeds as follows. First, we determine the individual input and reflected powers of the cooling tone and (for two-tone measurements) blue probe by blocking each in turn. For the two-tone experiments, we nominally set the blue probe power to be a factor of 6 weaker than the cooling tone. Second, we perform coherent optomechanical spectroscopy to determine Δ_c and κ . Third, we switch to the BHD setup and acquire the power spectral density of the photocurrent with the reflected signal sent to the BHD. We also take the shot-noise spectra for each measurement by blocking the reflected light from the BHD, to account for the LO power drift across measurements. Fourth, we record again the total input and reflected probe

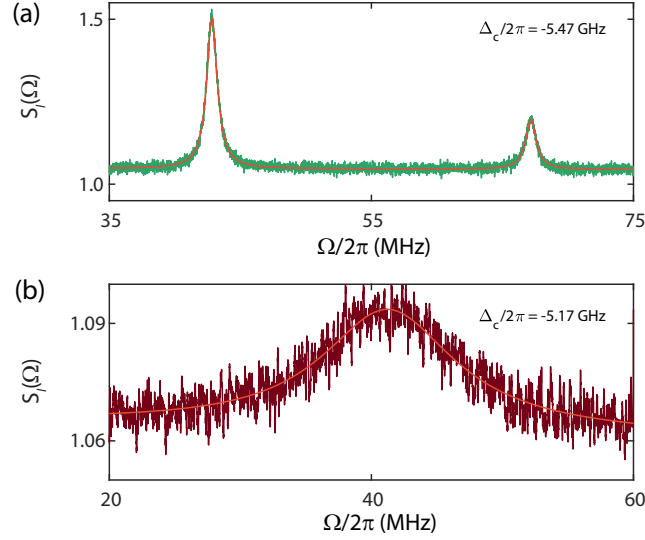


Figure 7.5 – **Fitting of the incoherent noise spectrum.** Typical noise spectrum from (a) a two-tone measurement with $\Delta_c/2\pi \simeq -5.47$ GHz, and (b) a single-tone measurement with $\Delta_c/2\pi \simeq -5.17$ GHz, along with the corresponding fitting curve.

powers. The probe powers fluctuate by less than 1% across measurements.

7.3.1 Coherent optomechanical spectroscopy

Figure 7.3 shows typical coherent optomechanical spectra at several different values of Δ_c for the single cooling tone detuning sweep measurements. The mechanical motion leads to destructive interference with the probe generated by the phase modulator, resulting in optomechanically induced transparency (OMIT) [109, 110] in the reflected cavity response. We fit the data with a theoretical model to extract κ and Δ_c , which are used along with the measured powers, to determine the intracavity photon numbers.

7.3.2 Calibration using sideband asymmetry

Typical incoherent noise spectra from the BHD are shown in Fig. 7.4. The blue curve corresponds to the shot noise and is obtained by blocking the signal beam in the BHD. We note that the uneven shot noise floor originates from the frequency dependent gain of the balanced detector. The red curve corresponds to the thermomechanical noise spectrum in the single-tone detuning-sweep measurements at $\Delta_c/2\pi \simeq -7.18$ GHz.

For convenience, we normalize the noise spectrum to the shot noise as shown in Fig. 7.5. Figure 7.5(a) shows the single-sided noise spectrum consisting of the scattered sidebands

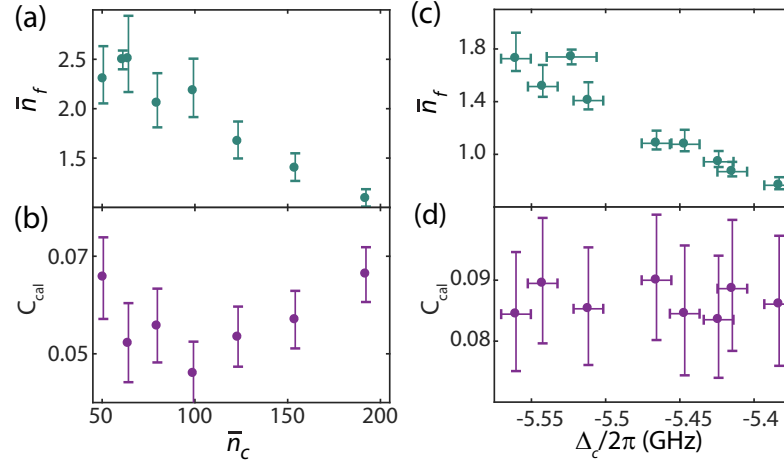


Figure 7.6 – **Ancillary Quantum Thermometry for power-sweep and detuning-sweep measurements.** (a) and (b), calibrated final occupancy and calibration coefficient (C_{cal}) from sideband asymmetry of power sweep measurements. C_{cal} is the ratio between the normalized sideband area and the calibrated \bar{n}_f . The error bars correspond the errors from the Lorentzian fitting of the noise spectrum. (c) and (d), calibrated final occupancy and calibration coefficient (C_{cal}) from sideband asymmetry of detuning sweep measurements. The error bars include the errors in the Lorentzian fitting of the noise spectrum and also the detuning uncertainty of 10 MHz.

from two-tone sideband asymmetry measurements. Accordingly, we use a fitting function with two Lorentzian terms,

$$S_{\text{fit}}(\omega) = c + \frac{\Gamma_{\text{eff}} A_1}{\Gamma_{\text{eff}}^2/4 + (\omega - \omega_1)^2} + \frac{\Gamma_{\text{eff}} A_2}{\Gamma_{\text{eff}}^2/4 + (\omega - \omega_2)^2}, \quad (7.5)$$

where c , A_1 , A_2 , ω_1 , ω_2 and Γ_{eff} are the fitting parameters. c corresponds to the noise background. A_1 (A_2) and ω_1 (ω_2) correspond to the area and center frequency of the sideband from the cooling tone (blue probe), with effective linewidth Γ_{eff} . From Eq. (2.87) we have $A_1 = \eta \Gamma_c \bar{n}_f$ and $A_2 = \eta \Gamma_b (\bar{n}_f + 1)$, where Γ_b and Γ_c are given by Eq. (2.79). We can therefore determine both the phonon occupancy

$$\bar{n}_f = \frac{A_1/\Gamma_c}{A_2/\Gamma_b - A_1/\Gamma_c}. \quad (7.6)$$

and the calibration coefficient

$$C_{\text{cal}} = A_2/\Gamma_b - A_1/\Gamma_c, \quad (7.7)$$

which fully calibrates the measurement.

In Fig. 7.6, we show the ancillary quantum thermometry for both the power-sweep and detuning-sweep measurements, including the phonon occupancy and the calibration coefficient. For the power-sweep measurements as shown in Fig. 7.6(a) and (b), we choose series of pumping powers, which ensure both sufficient laser cooling and measurable while non-overlapping Stokes and anti-Stokes sidebands [70]. For the detuning sweep measurements as shown in Fig. 7.6(c),(d) we choose series of Δ_c close to the red sideband to obtain sufficient laser cooling and measurable while non-overlapping Stokes and anti-Stokes sidebands. The different calibration coefficients between the power-sweep and detuning-sweep measurements are mainly due to the different coupling conditions of the tapered fiber. The averaged calibration coefficient along with the corresponding standard deviation is used for the ancillary quantum thermometry in the single-tone measurements.

The final occupancy can be determined from the sideband area,

$$\bar{n}_f = \frac{A_s}{\Gamma_s C_{\text{cal}}}, \quad (7.8)$$

where A_s and Γ_s are the sideband area and the scattering rate of the cooling tone for the single-tone measurement as shown in Fig. 7.5(b).

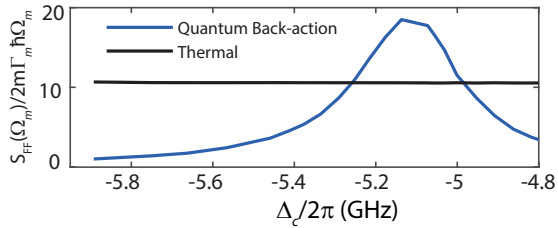


Figure 7.7 – Detuning dependence of quantum back-action in the two-tone ancillary quantum thermometry. The force spectral density at positive mechanical frequency $S_{FF}(+\Omega_m)$ for both the thermal force (black curve) and the QBA from the blue probe (blue curve) calculated from experimental values and normalized by $2m\Gamma_m\hbar\Omega_m$.

In Fig. 7.7, we compare the force noise spectral density at the positive mechanical frequency $S_{FF}(+\Omega_m)$ (responsible for heating the mechanical oscillator [208]) of the QBA from the blue probe and of the thermal force, as calculated from experimental parameters in a two-tone detuning sweep measurement. Here, we express $S_{FF}(+\Omega_m)$ in mechanical quanta via normalization by $2m\Gamma_m\hbar\Omega_m$, where m is the effective mass. While the thermal force spectral density is independent of detuning (equivalent to $\bar{n}_{\text{th}} \sim 10$ quanta), the force spectral density due to QBA from the blue probe (equivalent to Γ_b/Γ_m) peaks

around $\Delta_c/2\pi = -5.1$ GHz, where it dominates the thermal force noise.

7.3.3 Mechanical Noise Thermometry

The occupancy can also be determined using mechanical noise thermometry by anchoring the normalized thermomechanical noise area to the cryogenic thermometer,

$$\bar{n}_f = \frac{A_s/\Gamma_s}{A_s^0/\Gamma_s^0} \frac{k_B T}{\hbar \Omega_m} \frac{\Gamma_m}{\Gamma_s^0 + \Gamma_m}, \quad (7.9)$$

where A_s^0 and Γ_s^0 are the sideband area and the scattering rate of the cooling tone at a specific anchor data point. In this case, it is assumed that the mechanical mode temperature T is given by the resistive thermometer and there is no excess heating at the anchor point. The mean phonon occupancy of the mechanical oscillator is $\bar{n}_{th} \simeq k_B T / \hbar \Omega_m$ when the mechanical mode is in equilibrium with the thermal reservoir. In the case of negligible optomechanical damping ($\Gamma_s^0 \ll \Gamma_m$), Eq. (7.9) can be simplified to $\bar{n}_f = \frac{A_s/\Gamma_s}{A_s^0/\Gamma_s^0} \frac{k_B T}{\hbar \Omega_m}$. In the power-sweep series, $\Delta_c = -\Omega_m$, we have $\bar{n}_f = \frac{A_s/n_c}{A_s^0/n_s^0} \frac{k_B T}{\hbar \Omega_m}$.

7.3.4 Results of Sideband Cooling

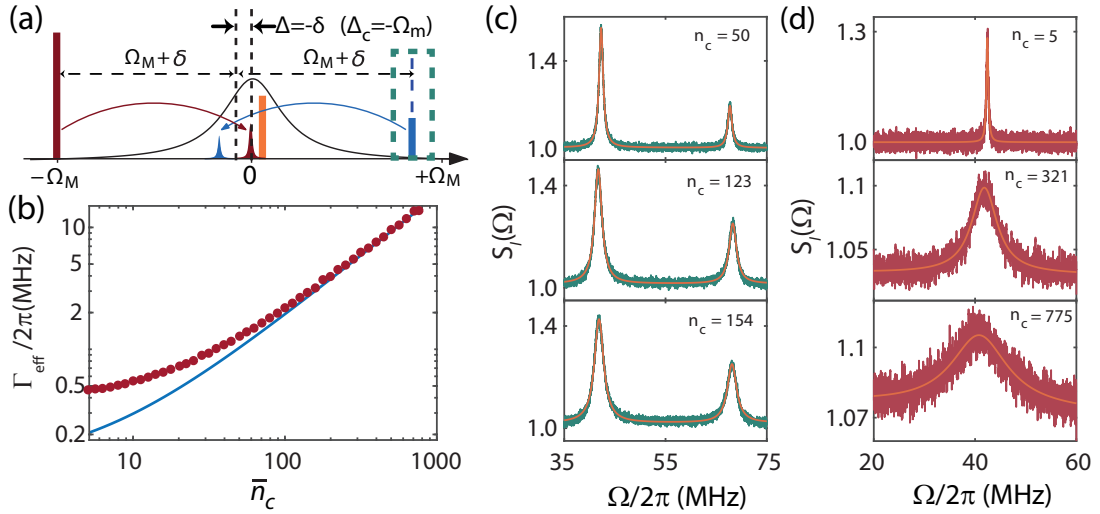


Figure 7.8 – Power dependence of sideband cooling. (a) Pumping scheme for the power sweep with a cooling tone at a fixed detuning of $-\Omega_m$ relative to the cavity resonance and an additional blue probe for sideband asymmetry calibration, as indicated in the dashed green box. The frequency separation between the cooling tone and blue probe is fixed at $2(\Omega_m + \delta)$. (b) Measured effective mechanical linewidth Γ_{eff} from the noise power spectral density vs. cooling tone intracavity photon number \bar{n}_c (red full circles) in single-tone measurements with a theoretical plot with experimental values (blue curve). (c) and (d) Single-sided noise spectra from balanced heterodyne detection normalized to the shot noise floor from two-tone and single-tone measurements, respectively, with corresponding fit curves, for various intracavity photon numbers.

As noted earlier, before and after each set of measurements, both the input powers and the reflected powers of the two tones are checked, and their fluctuation is less than 1%. Besides, for each set of measurements the reflection efficiency varies less than 1%, which eliminates the power/detuning dependence for the calibration efficiency. We adopt a detuning uncertainty of ± 10 MHz for Δ_c from the fitting error from the coherent optomechanical spectra in both the power-sweep and the detuning-sweep series of measurements. The detuning uncertainty is taken into consideration for the ancillary quantum thermometry and is included in the error bars of phonon occupancy calibration in addition to the Lorentzian fitting error from the noise spectrum. In a first set of measurements shown in Fig. 7.8, we vary the power of the

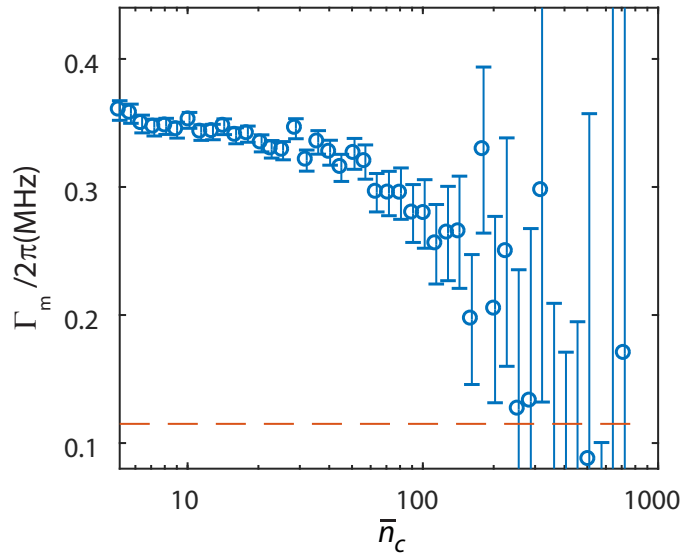


Figure 7.9 – **Mechanical Linewidth in the single-tone power-sweep measurements.** The measurement is performed with the OMC at temperature around 2K with ^3He condensed. Γ_m is inferred from the fitted Γ_{eff} and calculated Γ_c from experimental values. The error bars corresponds to the fitting error in the Γ_{eff} . A horizontal dashed line of $\Gamma_m/2\pi = 115\text{kHz}$ is shown for comparison.

pump tones while keeping $\Delta_c = -\Omega_m$ fixed for optimal sideband cooling. A blue probe, as indicated in the dashed green box in Fig. 7.8(a), is utilized only for ancillary sideband asymmetry measurements. Figure 7.8(b) shows the effective mechanical linewidth Γ_{eff} as a function of the cooling-tone intracavity photon number \bar{n}_c , obtained from the noise spectra in the single-tone experiments (red full circles) with a theoretical plot (blue curve) assuming a mechanical linewidth $\Gamma_m/2\pi = 115\text{kHz}$ and vacuum coupling rate $g_0/2\pi = 1080\text{kHz}$. As shown in Fig. 7.8(b), Γ_{eff} deviates from the theoretical value for low intracavity photon numbers. We attribute this to condensed ^3He on the surface of OMC, which degrades the mechanical linewidth at low powers but may improve the thermalization. We note that knowledge of Γ_m

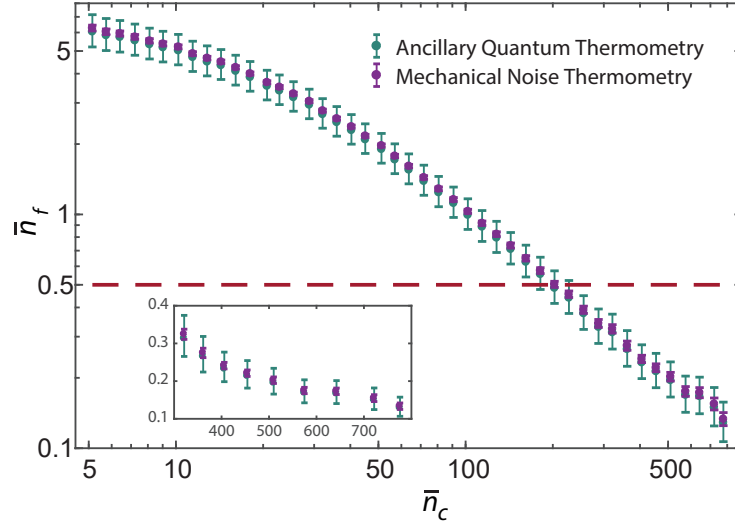


Figure 7.10 – **Final occupancy versus the cooling tone intracavity photon number.** Purple open circles are anchored to the cryostat thermometer temperature at the lowest values of \bar{n}_c . Green full circles utilize the averaged calibration coefficient obtained from the ancillary two-tone sideband-asymmetry measurements, where the error bars are given by both the errors in the Lorentzian fit and in the calibration coefficient. The inset shows an expanded view at the highest cooling powers. The horizontal red dashed line corresponds to $\bar{n}_f = 1/2$.

is required for the mechanical noise thermometry, as the additional optomechanical damping has to be considered. From independent single-tone sideband cooling measurements performed at a temperature of 4 K and pressure of 40 mbar, we obtain a mechanical damping rate $\Gamma_m/2\pi \sim 115$ kHz and vacuum optomechanical coupling rate $g_0/2\pi \sim 1.08$ MHz. The mechanical linewidth is larger for low input powers. This is due to condensed ^3He on the sample surface, as the lower temperatures ~ 2 K in the experiment are obtained by pumping a condensed ^3He reservoir. In Fig. 7.9, we show the inferred $\Gamma_m = \Gamma_{\text{eff}} - \Gamma_c$ for different \bar{n}_c , where Γ_c is calculated from the experimental values. The error bars correspond to the fitting error in Γ_{eff} . At low pumping powers, the SNR is decreased due to the broadened Γ_m . To have a measurable anti-Stokes signal in the noise thermometry, we start from intracavity photon number $\bar{n}_c = 5$, with calculated $\Gamma_c/2\pi = 93$ kHz based on experimental values. From the fitted effective mechanical linewidth Γ_{eff} , we estimate $\Gamma_m/2\pi \simeq 360$ kHz for $\bar{n}_c = 5$. This is adopted for the mechanical noise thermometry by anchoring at 2 K with $\bar{n}_c = 5$. Figure 7.8(c) and (d) show a series of noise spectra from the two-tone and single-tone measurements, respectively, at various values of \bar{n}_c along with Lorentzian fits. The noise spectra are normalized to the shot noise floor, obtained by blocking the signal beam in the BHD. The left and right thermomechanical sidebands shown in Fig. 7.8(c) are due to the cooling tone and the blue probe, respectively. We choose a series of pumping powers that ensures both sufficient laser

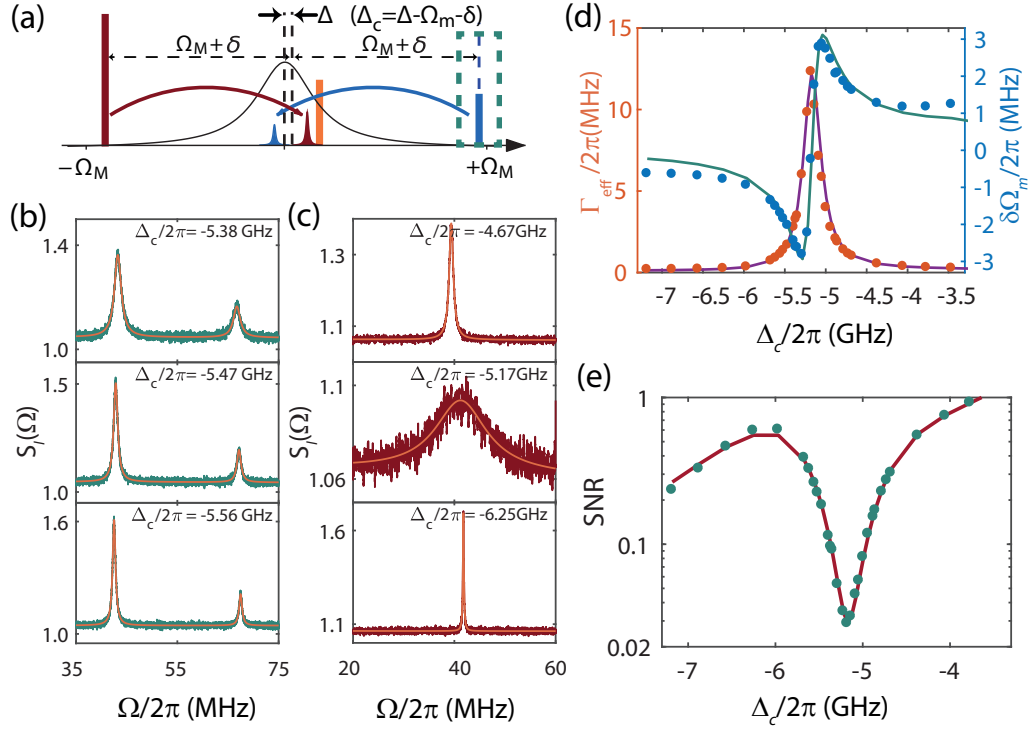


Figure 7.11 – **Detuning dependence of the sideband cooling.** (a) Pumping scheme for the detuning sweep where the detuning Δ_c of the cooling tone relative to the cavity resonance is varied. An additional blue probe is used for ancillary sideband asymmetry calibration, as indicated in the dashed green box. Frequency separation between the cooling tone and blue probe is fixed at $2(\Omega_m + \delta)$. (b) and (c) Single-sided noise spectra from the balanced heterodyne detection normalized to the shot noise floor from two-tone and single-tone measurements, respectively, with corresponding fit curves, for various detunings. (d) The fitted mechanical linewidth (red full circles, left axis) and optical spring effect (blue full circles, right axis), with corresponding theoretical plots based on experimental optomechanical parameters. (e) Signal-to-noise ratio (SNR) vs. Δ_c , with the fitting curve to a theoretical model which includes optical heating, with excess heating rate and overall detection efficiency as free fitting parameters.

cooling and measurable, non-overlapping Stokes and anti-Stokes sidebands [70]. As the power increases, the ratio of the areas of the red and blue sidebands, given by $\bar{n}_f \Gamma_c / (\bar{n}_f + 1) \Gamma_b$ [cf. Eq. (7.4)], decreases as the mechanical oscillator approaches the ground state ($\bar{n}_f \rightarrow 0$), as shown in Fig. 7.8(c). We thus obtain an averaged calibration coefficient between the normalized thermomechanical sideband area and the final occupancy from a series of ancillary quantum thermometry measurements. At high pumping powers, we observe an increase in the noise floor, as evident in the middle and bottom panels in Fig. 7.8(d). This originates from beating of the high signal power with excess noise of the LO around 5.17 GHz. Figure 7.10 shows the inferred mean phonon occupancy \bar{n}_f vs. \bar{n}_c from the single-tone measurements, calibrated using two independent methods. The green circles show the phonon occupancy calibrated

using the ancillary sideband asymmetry measurements. The purple open circles show the calibration using the cryostat thermometer by anchoring the lowest value of $\bar{n}_c \sim 5$ at 2.0 K. This calibration requires knowledge of Γ_m , which is estimated by subtracting the calculated value of Γ_{opt} at this power from the measured Γ_{eff} , to yield $\Gamma_m/2\pi \approx 360$ kHz. We note that Γ_m is unnecessary using ancillary quantum thermometry, making it an ideal independent quantum thermometer, as opposed to conventional mechanical noise thermometry. The two methods show excellent agreement. The minimum phonon occupancy achieved in this power-sweep experiment is $0.13^{+0.02}_{-0.02}$ (88% ground-state occupancy) and is reached at a cooling-tone intracavity photon number of $\bar{n}_c \approx 776$.

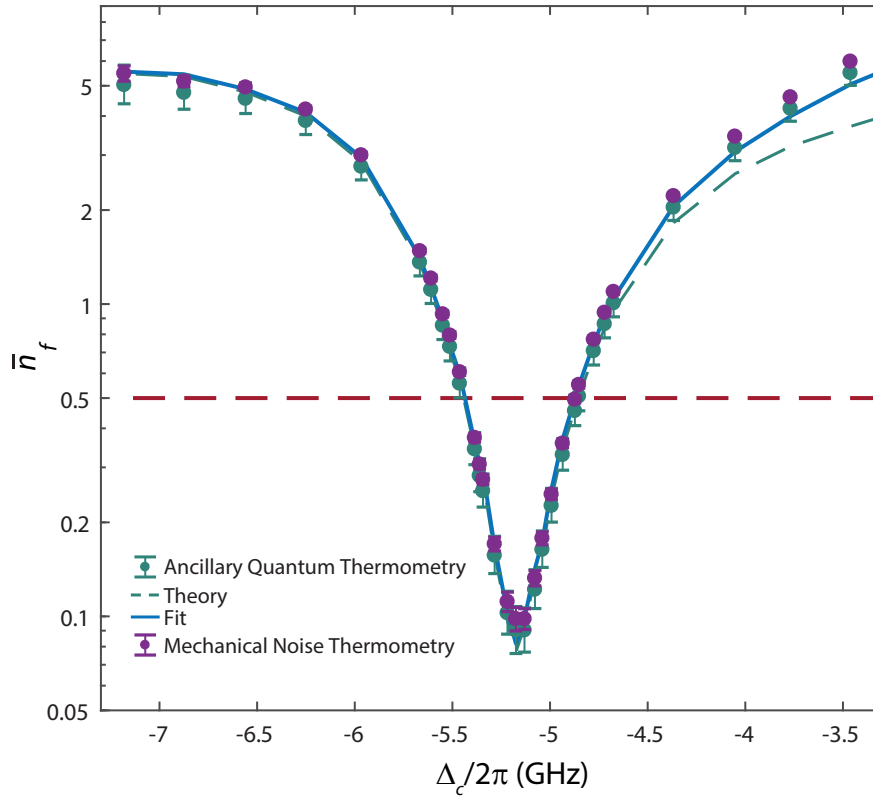


Figure 7.12 – **Final occupancy versus the cooling tone detuning in single-tone measurements.** Green full circles show calibration using the ancillary two-tone quantum thermometry. Dashed green curve shows a theoretical plot calculated from experimental optomechanical parameters assuming ideal thermalization. Blue curve shows a fitting curve incorporating excess optical heating. Error bars are given by the errors in the Lorentzian fits and in the calibration coefficient in two-tone sideband asymmetry. Purple full circles are anchored with cryostat thermometer at $\Delta_c/2\pi \approx -7.18$ GHz. The horizontal red dashed line corresponds to $\bar{n}_f = 1/2$.

In a second set of measurements, we vary the detuning Δ_c of the cooling tone with respect

to the cavity resonance, keeping the frequency separation of the blue probe in the ancillary measurement and that of the LO fixed at $2(\Omega_m + \delta)$ and Δ_{LO} , respectively [Fig. 7.11(a)]. Figure 7.11(b) and (c) each show a series of measured noise spectra normalized to the shot noise floor at various values of Δ_c , together with Lorentzian fits, from the two-tone and single-tone measurements. In the ancillary two-tone measurements, the input powers of the cooling tone and blue probe are $\sim 350 \mu\text{W}$ and $\sim 60 \mu\text{W}$ respectively, with a series of values of Δ_c to ensure sufficient laser cooling and measurable, non-overlapping Stokes and anti-Stokes sidebands. To infer \bar{n}_f via sideband thermometry, the detuning-dependent intracavity photon number and optical susceptibility for the two scattered sidebands must be taken into consideration. We obtain a mean calibration coefficient between the normalized thermomechanical sideband area and the final occupancy from the sideband asymmetry measurements. For single-tone measurements, the cooling tone input power is $\sim 500 \mu\text{W}$. Figure 7.11(d) shows the effective mechanical linewidth (red circles) and the optical spring effect (blue circles) obtained from a Lorentzian fit to the noise spectrum, with excellent agreement with the respective theoretical curves. We note that, due to the presence of high input power throughout the measurement, the mechanical linewidth degradation observed at low powers in the previous measurement [Fig. 7.8(b)] is absent. Figure 7.12 shows \bar{n}_f vs. Δ_c , where \bar{n}_f is calibrated from the thermomechanical sideband area from the single-tone sideband cooling measurements. Green circles are determined using the mean calibration factor obtained from sideband asymmetry measurements. The theoretical dependence calculated from experimental parameters (7.3) is shown as a green dashed curve for comparison. The theory curve is in excellent agreement with the data except in the region where the cooling tone approaches the cavity resonance, indicating residual optical heating [122, 148]. We fit the phonon occupancy with a model incorporating heating [blue curve in Fig. 7.12] that is both linear and quadratic in the number of intracavity photons. The fit indicates that the excess optical heating in our measurements has primarily a quadratic dependence, resulting in an increase in \bar{n}_{th} of $\sim 1.2 \times 10^{-6} \bar{n}_c^2$; the linear coefficient is negligible. This is different from previous experiments with large optical decay rate, where linear absorption heating dominates [122]. The quadratic dependence is suggestive of two-photon-absorption [146, 268]. We note that in any case such optical heating cannot come from excess laser noise [114, 178, 179, 184], for which the heating rate peaks at $\Delta_c = -\Omega_m$. For the noise thermometry, we anchor the calibration to 2.0 K, at farthest detuning of $\Delta_c/2\pi \approx -7.18 \text{ GHz}$. The resulting data are shown as purple full circles in Fig. 7.12. For $\Delta_c/2\pi = -7.18 \text{ GHz}$ with $\bar{n}_c = 330$, the estimated increase in \bar{n}_{th} due to quadratic heating is ~ 0.135 , which is negligible compared to the bare thermal bath occupation of 8.2 phonons. This indicates that the mechanical oscillator is well-thermalized despite the high pumping power. The minimum phonon occupancy, occurring close to the red mechanical sideband

($\Delta_c/2\pi \simeq -5.17$ GHz), is $\bar{n}_f = 0.09^{+0.02}_{-0.01}$, which is -7.4 dB of the zero-point energy. This places the mechanical oscillator at 92% ground state occupation. In Fig. 7.11(e), the signal-to-noise ratio vs. Δ_c for the thermomechanical noise spectrum is shown with a fit that includes the quadratic heating model in addition to the standard sideband cooling theory. The fit yields an overall detection efficiency $\eta \simeq 6.4\%$.

7.3.5 Excess laser noise

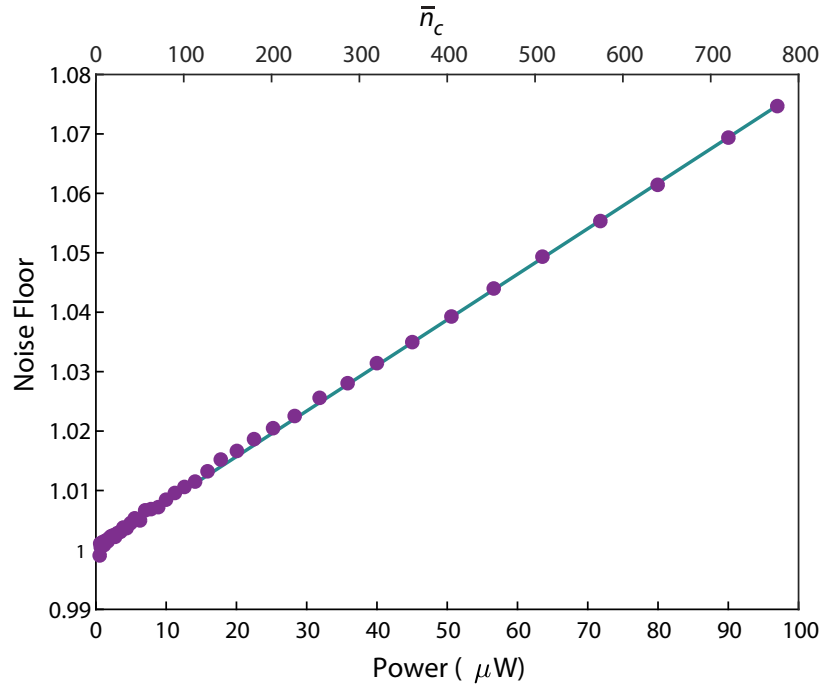


Figure 7.13 – **Noise floor vs. reflected power in single-tone power-sweep measurements.** Noise floor from the normalized noise spectra from the BHD in the single-tone power-sweep measurements (purple full circles), fitted with a green line. The lower x axis corresponds to the reflected power into the balanced heterodyne setup while the upper axis corresponds to the intracavity photon number. The increase of the noise floor at high powers is due the beating between the strong signal and LO.

Excess laser noise is known to constrain sideband cooling and to corrupt motional sideband asymmetry measurements [114, 117, 178, 179, 184]. As shown in our previous work [122], the excess laser frequency noise spectrum density $S_{\omega\omega}(\Omega)$ at frequency of 5.2 GHz is measured below $10^5 \text{ rad}^2/\text{Hz}$. In all the measurements, the pumping tones (cooling tone and blue probe) pass through narrow bandwidth filter cavity locked to the respective pumping tones to reject high frequency excess phase noise. In Fig. 7.13, we presented the noise floor fitted from the thermomechanical noise spectra in the balanced heterodyne measurements (purple full

circles), which increases linearly with the reflected power (intracavity photon number) in the single-tone power-sweep measurements (green line). In BHD, we choose a LO power of around 8 mW. The beating between the highest reflected power (100 μ W) and vacuum noise from the LO can lead to an increased noise floor by $\sim 1\%$. This can be eliminated in principle by passing the LO through a narrow bandwidth filter cavity. However, this will introduce large insertion loss and experimental complexity, thus is not implemented in our measurements. The noise floor increase observed in our heterodyne measurements originates from the beating between the high reflected power and excess noise of the LO around 5.17 GHz [122]. More details concerning the laser noise calibration are discussed in the Appendix of the thesis.

7.3.6 Conclusion

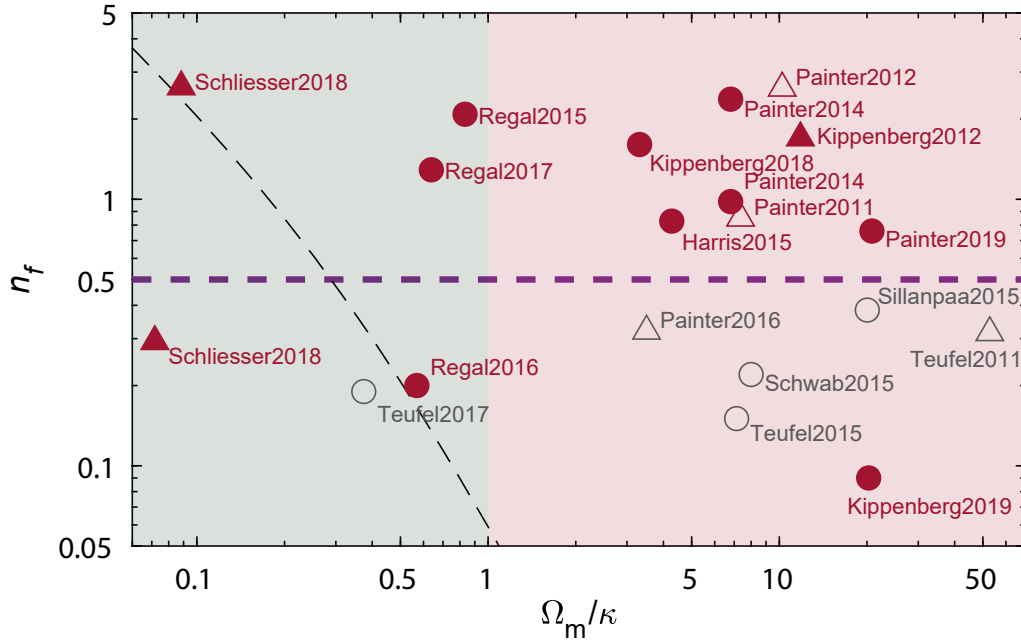


Figure 7.14 – **Recent advancement in laser cooling of mechanical resonators in various platforms.** Figure presented with final phonon occupation \bar{n}_f (logarithmic scale) vs. sideband resolution (Ω_m/κ). Gray and red markers correspond to microwave and optical platforms, respectively; \triangle and \circ correspond to noise thermometry and quantum sideband thermometry, respectively; open and solid markers correspond to quantum-limited and non-quantum-limited measurements, respectively. The dashed black curve corresponds to the quantum limit for sideband cooling. The green and the red area correspond to the Doppler regime and the sideband-resolved regime, respectively.

In conclusion, we have demonstrated high-fidelity sideband cooling to the zero-point energy of a localized GHz mechanical mode of a silicon OMC. The residual mean phonon occupancy is $0.09^{+0.01}_{-0.01}$ (92% ground state occupation). The system possess a unique blend of advanta-

geous properties, combining high mechanical frequency, large sideband resolution, negligible optical-absorption heating and the ability to be prepared in the ground state in the presence of strong probing. In Fig. 7.14, we show a summary of recent advancement in laser cooling of mechanical oscillators in various platforms using feedback or sideband cooling techniques, with a detailed comparison. Our result enables a large number of quantum optomechanical experiments that have remained elusive in the optical domain, including two-tone backaction-evading measurements reaching sub-SQL sensitivity [78, 121, 126], squeezed mechanical states [83, 84, 124, 125, 182], low-added-noise optomechanical transducers [98–100], as well as quantum-coherent operations such as state swapping [101] and entanglement generation [205, 206]. In addition, our results provide valuable insight to eventual microwave-optical transducer in piezoelectric optomechanical platforms with future promise of integration to superconducting qubits [101–104].

8 Quantum squeezing of mechanical motion with light

In quantum mechanics, a harmonic oscillator always has a zero-point energy even in its ground state. The position or the momentum of the harmonic oscillator always have unavoidable fluctuations, which are limited by the Heisenberg uncertainty principle. However, the minimum uncertainty for the position or the momentum can be manipulated, e.g. the uncertainty in position can be less than the zero-point motion while the large uncertainty is imprinted on the momentum. Such squeezed state has been obtained with optical light and atomic motion. In this chapter we will show our results on the quadrature squeezing of mechanical motion of an optomechanical crystal below the zero-point fluctuation using light.

8.1 Reservoir engineering

Squeezed states have received a lot of interest over the last decades [16, 269, 270] for quantum metrology and quantum technology. For example, the squeezed vacuum is implemented in LIGO for the enhanced sensitivity for the gravitation wave detection [94]. However, the quantum squeezing of a harmonic oscillator is extremely challenging due to the large thermal noise. In principle, parametric driving a harmonic oscillator can be used for the squeezing generation by modulating the spring constant at twice the mechanical frequency [271, 272], which is however limited by the 3-dB limit. To surpass such 3-dB limit, there have been a lot of theoretical proposals developed in the last decade. For example, back-action evading measurement together with a strong feedback force can be implemented [36, 273]. Alternatively a detuned parametric driving in addition to a feedback force can be used [274, 275]. Besides, mechanical squeezing can be achieved by injecting a squeezed light in to the cavity [276]. However, all these proposals are extremely challenging to realize in the optical and microwave domain.

Reservoir engineering, originally proposed in the trapped ion community by engineering the system-environment coupling [123], has also been proposed [124]. In such scheme, the optomechanical system is bichromatically driven at the upper and lower mechanical sidebands, while the red probe is stronger than the blue probe. In this case, the optical cavity can be seen as a bath whose force noise is squeezed. Over the last years, this has enabled the demonstration of mechanical squeezing in the microwave electromechanical systems [83, 84, 125, 182].

In the optical domain, the mechanical squeezing below the zero-point motion remains elusive. The main challenge is the thermal noise, which requires that ability of cooling the mechanical motion below half a quanta in the sideband resolved regime. The amount of attainable squeezing is directly limited by the final occupancy. Our result of laser cooling to the zero-point energy allows us to prepare the mechanical squeezed state. The generation of mechanical squeezing can be performed by a two-tone pumping scheme as discussed in the theory chapter. There are several challenges we want to highlight here. First of all, the optomechanical system may be subjected to other different dynamics that arises naturally under strong pumping, such as the power dependent cavity frequency and mechanical frequency. Despite that the red tone are much stronger than the blue tone in the two-tone pumping scheme, instability can appear. Secondly, the detection of the mechanical squeezing can be difficult. One can obtain the upper and lower bound of the mechanical quadrature variance from the Bogoliubov mode noise spectrum from the imbalanced two-tone pumping. One can also indirectly infer the quadrature variance from the noise spectrum of the Bogoliubov mode. Direct measurement of the mechanical quadratures can be performed with back-action evading measurement with an additional pair of blue and red probing tones. However, Floquet dynamics can arise in such multiple tones pumping scheme, when probing on the same optical resonance. This will result in extremely complex calibration. In principle, the probing tones can be applied to another optical mode. However, in our case, the second order optical resonance has much larger linewidth $\kappa > 2\pi \times 1 \text{ GHz}$ and much weaker coupling to the mechanical mode $g_0/2\pi < 200 \text{ kHz}$.

In the theory section, we have introduced the theoretical treatment for the dissipative squeezing. Similar to previous schemes, we consider an optomechanical system bichromatically driven on the upper and lower sidebands, with the cooling tone stronger than the blue probe. We consider the quantum Langevin equations of the optical and mechanical fluctuation field,

with rotating-wave approximation,

$$\begin{aligned}
 \delta \dot{\hat{a}} &= \left(i\Delta - \frac{\kappa}{2}\right) \delta \hat{a} + i(g_c \delta \hat{b} + g_b \delta \hat{b}^\dagger) + \sqrt{\kappa_{\text{ex}}} \delta \hat{a}_{\text{in}} + \sqrt{\kappa_0} \delta \hat{a}_{\text{vac}} \\
 \delta \dot{\hat{a}}^\dagger &= \left(-i\Delta - \frac{\kappa}{2}\right) \delta \hat{a}^\dagger - i(g_c \delta \hat{b}^\dagger + g_b \delta \hat{b}) + \sqrt{\kappa_{\text{ex}}} \delta \hat{a}_{\text{in}}^\dagger + \sqrt{\kappa_0} \delta \hat{a}_{\text{vac}}^\dagger \\
 \delta \dot{\hat{b}} &= \left(i\delta - \frac{\Gamma_m}{2}\right) \delta \hat{b} + i(g_c \delta \hat{a} + g_b \delta \hat{a}^\dagger) + \sqrt{\Gamma_m} \delta \hat{b}_{\text{in}} \\
 \delta \dot{\hat{b}}^\dagger &= \left(-i\delta - \frac{\Gamma_m}{2}\right) \delta \hat{b}^\dagger - i(g_c \delta \hat{a}^\dagger + g_b \delta \hat{a}) + \sqrt{\Gamma_m} \delta \hat{b}_{\text{in}}^\dagger.
 \end{aligned} \tag{8.1}$$

Here we assume g_c and g_b are real numbers. Regardless of the input noise terms, this is a linear time-invariant system under the two-tone optical driving. The stability of the system is given by the Routh–Hurwitz stability criterion,

$$\left(\Delta^2 + \frac{\kappa^2}{4}\right) \left(\left(\frac{1}{2} \left(\frac{4\kappa g_c^2 - 4\kappa g_b^2}{4\Delta^2 + \kappa^2} + \Gamma_m \right) \right)^2 + \delta^2 \right) \geq 2\delta\Delta (g_b^2 + g_c^2) - \frac{\Delta^2 (g_b^2 - g_c^2)^2}{\Delta^2 + \frac{\kappa^2}{4}}. \tag{8.2}$$

We note that, when $g_b = g_c = g$, such criterion restores to the stability criterion for the two-tone back-action evasion measurements, i.e.

$$\left(\Delta^2 + \frac{\kappa^2}{4}\right) \left(\frac{\Gamma_m^2}{4} + \delta^2 \right) \geq 4\delta\Delta g^2. \tag{8.3}$$

Compared to the BAE, the stability criteria is much more relaxed, due to the dynamical back-action.

Such stability condition can be viewed alternatively by looking at the field equations of the mechanical motion. Due to fast decay of the optical field, we can make the assumption of the adiabatic decay of the optical field,

$$\delta \hat{a} = \frac{i(g_c \delta \hat{b} + g_b \delta \hat{b}^\dagger) + \sqrt{\kappa_{\text{ex}}} \delta \hat{a}_{\text{in}} + \sqrt{\kappa_0} \delta \hat{a}_{\text{vac}}}{\frac{\kappa}{2} - i\Delta}. \tag{8.4}$$

For the mechanical field, we thus have,

$$\begin{aligned}
 \dot{\delta\hat{b}} = & \delta\hat{b} \left(\frac{g_b^2}{\frac{\kappa}{2} + i\Delta} - \frac{g_c^2}{\frac{\kappa}{2} - i\Delta} + \frac{2i\delta - \Gamma_m}{2} \right) + \frac{i\delta\hat{a}_{\text{in}}\sqrt{\kappa}g_c}{\frac{\kappa}{2} - i\Delta} \\
 & \delta\hat{b}^\dagger \left(\frac{g_b g_c}{\frac{\kappa}{2} + i\Delta} - \frac{g_b g_r}{\frac{\kappa}{2} - i\Delta} \right) + \frac{i\sqrt{\kappa}g_b\delta\hat{a}_{\text{in}}^\dagger}{\frac{\kappa}{2} + i\Delta} + \delta\hat{b}_{\text{in}}\sqrt{\Gamma_m} \\
 \dot{\delta\hat{b}}^\dagger = & \delta\hat{b}^\dagger \left(\frac{g_b^2}{\frac{\kappa}{2} - i\Delta} - i\delta - \frac{g_c^2}{\frac{\kappa}{2} + i\Delta} - \frac{\Gamma_m}{2} \right) - \frac{i\delta\hat{a}_{\text{in}}\sqrt{\kappa}g_b}{\frac{\kappa}{2} - i\Delta} \\
 & + \delta\hat{b} \left(\frac{g_b g_c}{\frac{\kappa}{2} - i\Delta} - \frac{g_b g_c}{\frac{\kappa}{2} + i\Delta} \right) - \frac{i\sqrt{\kappa}\delta\hat{a}_{\text{in}}^\dagger g_c}{\frac{\kappa}{2} + i\Delta} + \delta\hat{b}_{\text{in}}^\dagger \sqrt{\Gamma_m}.
 \end{aligned} \tag{8.5}$$

The detuning error of δ and Δ leads to the coupling between the $\delta\hat{b}$ and $\delta\hat{b}^\dagger$. As one tries to squeeze one quadrature, the detuning errors in the measurements, i.e. δ and Δ , lead to the anti-squeezing of the other quadrature, which can in turn degrade the obtained the squeezing. The coupling between the two quadratures may result in the instability in such measurements.

8.2 Experimental Results

We performed mechanical squeezing measurement in a silicon optomechanical crystal [122, 145]. Optically, the device functions as a single-sided cavity with a partially transmitting input mirror. Light is evanescently coupled from a tapered optical fiber into a waveguide that forms part of the nanobeam (coupling efficiency exceeds 50%). The optical resonance is at 1540 nm with a linewidth of $\kappa/2\pi \sim 255$ MHz, of which $\kappa_{\text{ex}}/2\pi = 71$ MHz are the external coupling rate to the waveguide. The optical mode is optomechanically coupled to a mechanical breathing mode of frequency $\Omega_m/2\pi = 5.19$ GHz, and an intrinsic linewidth of $\Gamma_{\text{int}}/2\pi = 65$ kHz. The measured vacuum optomechanical coupling rate is $g_0/2\pi = 1080$ kHz. The system is placed in a ^3He buffer gas cryostat (Oxford Instruments HelioxTL) at a temperature of around 1.8 K with a pressure of 55 mbar. The buffer gas environment provides sufficient thermalization and dissipates the heat from optical absorption at high pumping powers. This enables the strong two-tone probing of the OMC.

The experimental setup is the same as previous ground state cooling experiments. The local oscillator and the blue probe are phase locked to the cooling tone. Both the cooling tone and the blue probe pass through narrow filter cavities which are locked to the respective carrier via PDH lock technique to reject the high frequency laser phase noise. The two pumping tones are combined in a free-space setup and maintained with the same polarization into a single mode fiber. The reflected light is switched between a coherent response measurement and the

BHD setup. We transit between the sideband asymmetry measurements and the mechanical squeezing by sweeping the frequency separation $2(\Omega_m + \delta)$ with $\delta \geq 0$ while maintaining $\Delta \sim 0$. For each measurement, we adjust the cooling tone frequency with relative detuning of $\Delta_c = -\Omega_m + \delta$ from the coherent response measurement. The LO is locked on the right side of cooling by $\Omega_{LO} \sim \Omega + \delta + 2\pi \times 50 \text{ MHz}$.

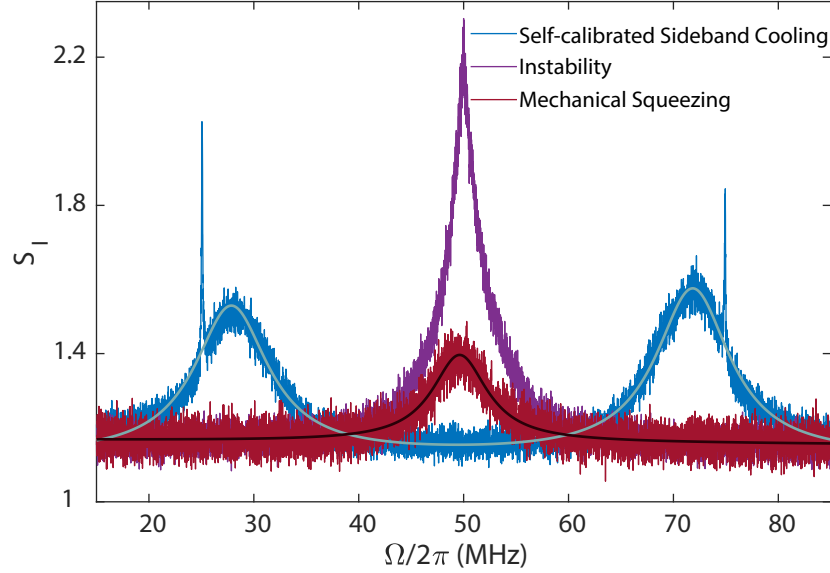


Figure 8.1 – **Experimental observation of mechanical squeezing.** The measurements are performed on an OMC used in Ref. [145] with an optical linewidth of $\kappa/2\pi = 255 \text{ MHz}$, at around 1.8 K with a pressure of 55 mbar . Balanced heterodyne noise spectrum normalized to the shot noise with different frequency separations, for self-calibrated sideband cooling (blue), two-tone instability (purple) and mechanical squeezing measurements. The sideband asymmetry noise spectrum is fitted with a double Lorentzian function (light blue) while the mechanical squeezing spectrum is fitted with a single Lorentzian function (black).

In Fig. 8.1, we show the observation of the mechanical squeezing. Total input power of $770 \mu\text{W}$ is sent to the OMC with a reflection efficiency around 16%, with a power ratio between the cooling tone and blue probe around 2.25. Due to the high pumping power, the mechanical linewidth is restored despite the condensed thin film liquid ^3He . In this measurement, we vary the detuning $\delta/2\pi$ from 25 to 0 MHz. The blue curve corresponds to the noise spectrum of the self-calibrated sideband cooling in the BHD. As the LO frequency is higher than both scattered thermomechanical sidebands, the fundamental anti-Stokes scattered sideband from the cooling tone is on the right while the Stokes scattered sideband from the blue probe is shown on the right. The noise spectrum is given by,

$$S_I(\Omega + \Delta_{LO}) = 1 + \eta \Gamma_{\text{eff}} \left[\frac{(\bar{n}_f + 1) \Gamma_b}{\Gamma_{\text{eff}}^2/4 + (\Omega + \delta)^2} + \frac{\bar{n}_f \Gamma_c}{\Gamma_{\text{eff}}^2/4 + (\Omega - \delta)^2} \right], \quad (8.6)$$

where η is the overall detection efficiency. $\Gamma_{b(c)}$ takes the form,

$$\Gamma_{b(c)} = \bar{n}_{b(c)} g_0^2 \left(\frac{\kappa}{\kappa^2/4 + \delta^2} \right). \quad (8.7)$$

From the sideband asymmetry measurement, the phonon occupation can be self-calibrated from the fitted sideband area A_c and A_b ,

$$\bar{n}_f = \frac{A_c / \bar{n}_c}{A_b / \bar{n}_b - A_c / \bar{n}_c}. \quad (8.8)$$

The fitted mechanical linewidth is $\Gamma_{\text{eff}}/2\pi = 8.85$ MHz, which is much larger than the mechanical damping rate. The sideband asymmetry measurement results in a mean final phonon occupancy of 1.167. The calibration coefficient between the phonon occupancy and the normalized sideband area is given by,

$$C_{\text{cal}} = A_b / \Gamma_b - A_c / \Gamma_c. \quad (8.9)$$

The obtained calibration coefficient is adopted to calibrate the mechanical squeezing spectrum.

In this case, due to the strong blue probe, most of the residual phonon occupancy comes from the QBA of the blue probe, despite the large damping rate. The red curve corresponds to the noise spectrum of a sideband-cooled Bogoliubov mode when $\delta \sim 0$. The noise spectrum takes the form,

$$S_I(\Omega + \Delta_{\text{LO}}) = 1 + \eta \Gamma_B \frac{\bar{n}_f^{\text{BG}} \Gamma_{\text{BG}}}{\Gamma_B^2/4 + (\Omega + \delta)^2}, \quad (8.10)$$

where Γ_B is the effective linewidth of the Bogoliubov mode and scattering rate of the Bogoliubov mode is given by $\Gamma_{\text{BG}} = \Gamma_c^{\text{BG}} - \Gamma_b^{\text{BG}}$. $\Gamma_{c/b}^{\text{BG}}$ are the scattering rate for the cooling tone and the blue probe in the mechanical squeezing, where $\Gamma_c^{\text{BG}}/\Gamma_b^{\text{BG}} = \bar{n}_c/\bar{n}_b$. We note that for the optical susceptibility of the Bogoliubov mode is $\chi_c^{\text{BG}}(\Omega) = 1/(\kappa/2 - \Omega)$, where $\delta = 0$ and $\Delta = 0$. The fitted Bogoliubov mode has an effective linewidth $\Gamma_{\text{BG}}/2\pi = 6.38$ MHz, which slightly narrower than the obtained mechanical linewidth for the self-calibrated sideband cooling. Using the obtained calibration coefficient, the resulting phonon occupancy for the Bogoliubov mode is $\bar{n}_{\text{BG}} = 0.8203 \pm 0.04 < 1$. The squeezing parameter is given by $r = \text{atanh}(\sqrt{\bar{n}_b/\bar{n}_c}) = 0.806$. We first check the lower and upper bound of the quadrature variance using the phonon occupancy

of the Bogoliubov mode,

$$\begin{aligned}\langle \hat{X}_1^2 \rangle &\leq e^{-2r} [1 + 2\bar{n}_{\text{BG}}] = 0.527 \pm 0.02 \\ \langle \hat{X}_1^2 \rangle &\geq e^{-2r} [0.5 + 2\bar{n}_{\text{BG}}] = 0.427 \pm 0.02.\end{aligned}\tag{8.11}$$

To infer the quadrature variance, we can fit the thermal decoherence rate \bar{n}_{th} of the mechanical under high pumping power. From the occupation of the Bogoliubov mode, we can obtain the thermal decoherence rate,

$$\bar{n}_{\text{th}}\Gamma_m = \bar{n}_{\text{BG}}\Gamma_{\text{tot}}\frac{\Gamma_{\text{BG}}}{\Gamma_c + \Gamma_b} \sim 2\pi \times 1.90 \text{ MHz}.\tag{8.12}$$

In the ideal case, i.e. $\delta = 0$ and $\Delta = 0$, the mechanical quadrature variance is given by,

$$\langle \hat{X}_1^2 \rangle = \frac{\Gamma_m(\bar{n}_{\text{th}} + 1/2) + \left(\sqrt{\Gamma_c^{\text{BG}}} - \sqrt{\Gamma_b^{\text{BG}}} \right)^2 / 2}{\Gamma_{\text{tot}}} = 0.43 \pm 0.02.\tag{8.13}$$

The estimated variance is close to the variance lower bound and -1.2 dB below the zero-point energy. The error bar here is given by the fitting of the noise spectrum.

8.3 Parametric effects

As shown in Fig. 8.1, the instability can surprisingly arise even with large effective damping when the detuning δ is close to zero. From the coherent response measurement, we obtain the static cavity response under strong two-tone pumping. Theoretical calculations show that under such pumping power, the required detuning uncertainty is close to the optical linewidth, which is extremely relaxed compared to the detuning uncertainty in our experiments, i.e. ± 10 MHz. We note that, the linewidth of the Bogoliubov mode is narrower than the scattered sidebands in the sideband asymmetry measurements. This indicates additional coupling between the two quadratures, e.g. due to excess parametric effects, such as power dependent mechanical and optical frequency change. One possibility is the cavity frequency oscillation due to the periodic absorption power in the cavity [122] to the photothermal effects. Such photothermal effect can lead to significant modification to the micro-cavity spectroscopy under strong driving considering the limited bandwidth for thermal process.

In our case, the intracavity field is given by $\hat{a} = \bar{a}_b e^{-i(\Omega_m + \delta)t} + \bar{a}_c e^{+i(\Omega_m + \delta)t} + \delta \hat{a}$. The optical

absorption leads to the temperature change,

$$\dot{\Delta T} = -\gamma_{\text{th}}\Delta T + g_{\text{abs}}|a|^2. \quad (8.14)$$

Considering that the thermal response bandwidth $\gamma_{\text{th}} \ll \Omega_m$, we can obtain a set of modified quantum Langevin equations for the field operators in the time domain,

$$\begin{aligned} \dot{\delta \hat{a}} &= \left(i\Delta - \frac{\kappa}{2}\right)\delta \hat{a} + \epsilon(|\bar{a}_c|^2 - |\bar{a}_b|^2)\delta \hat{a} - \frac{2\epsilon\bar{a}_c\bar{a}_b\gamma_{\text{th}}}{\Omega_m}\delta \hat{a}^\dagger + i\frac{2\epsilon\bar{a}_c\bar{a}_b}{\Omega_m}\delta \dot{\hat{a}}^\dagger \\ &\quad + i(g_c\delta \hat{b} + g_b\delta \hat{b}^\dagger) + \sqrt{\kappa_{\text{ex}}}\delta \hat{a}_{\text{in}} + \sqrt{\kappa_0}\delta \hat{a}_{\text{vac}} \\ \dot{\delta \hat{a}}^\dagger &= \left(-i\Delta - \frac{\kappa}{2}\right)\delta \hat{a}^\dagger + \epsilon(|\bar{a}_c|^2 - |\bar{a}_b|^2)\delta \hat{a}^\dagger - \frac{\epsilon 2\bar{a}_c\bar{a}_b\gamma_{\text{th}}}{\Omega_m}\delta \hat{a} - i\frac{\epsilon 2\bar{a}_c\bar{a}_b}{\Omega_m}\delta \dot{\hat{a}} \\ &\quad - i(g_c\delta \hat{b}^\dagger + g_b\delta \hat{b}) + \sqrt{\kappa_{\text{ex}}}\delta \hat{a}_{\text{in}}^\dagger + \sqrt{\kappa_0}\delta \hat{a}_{\text{vac}}^\dagger \\ \dot{\delta \hat{b}} &= \left(i\delta - \frac{\Gamma_m}{2}\right)\delta \hat{b} + i(g_c\delta \hat{a} + g_b\delta \hat{a}^\dagger) + \sqrt{\Gamma_m}\delta \hat{b}_{\text{in}} \\ \dot{\delta \hat{b}}^\dagger &= \left(-i\delta - \frac{\Gamma_m}{2}\right)\delta \hat{b}^\dagger - i(g_c\delta \hat{a}^\dagger + g_b\delta \hat{a}) + \sqrt{\Gamma_m}\delta \hat{b}_{\text{in}}^\dagger. \end{aligned} \quad (8.15)$$

where $\epsilon = g_{\text{abs}}g_{\text{th}}/\Omega_m$. The photothermal effects lead to the coupling between the $\delta \hat{a}$ and $\delta \hat{a}^\dagger$. We note that even with such high pumping powers, the additional terms in Eq. 8.15 due to parametric effects are completely negligible even taking the large value we obtained from Ref. [122]. This is mainly due to the small thermal bandwidth.

8.4 Conclusion

We've shown the mechanical squeezing with optical light using reservoir engineering technique. The inferred mechanical quadrature variance is -1.4 dB below the zero-point fluctuation. Besides, we observe two-tone instability in the squeezing measurements despite the large dynamical back-action. Independent measurement of both mechanical quadratures can be performed via a BAE measurement in the future. Our results enable future displacement and force sensing with enhanced sensitivity, such sub-SQL displacement measurement [89, 90]. Besides, it opens new avenue to non-classical mechanical state generations, such as the Schrodinger-cat state via phonon subtraction [267].

9 Summary and Outlook

9.1 Summary

In summary, we have shown our efforts towards the quantum measurement of mechanical motion at the standard quantum limit.

Floquet dynamics in quantum measurement of mechanical motion. We observe the Floquet dynamics in sideband asymmetry measurements on a silicon OMC sideband-cooled to 40% ground-state occupation. The Floquet dynamics, resulting from the multiple pump tones, gives rise to an artificially modified motional sideband asymmetry by redistributing thermal and quantum fluctuations among the initially independently scattered thermomechanical sidebands. A theoretical model developed based on Floquet theory accurately describes the observations, which results from a synthetic gauge field among the Fourier modes.

Optical Backaction-Evading Measurement of a Mechanical Oscillator. We demonstrate the first optical continuous two-tone backaction-evading measurement of a localized GHz frequency mechanical mode of Silicon OMC close to the ground state. We explicitly show the transition from conventional to backaction-evading measurement, employing quantum-limited optical heterodyne detection, and observe up to 0.67 dB (14%) reduction of total measurement noise.

Two-tone optomechanical instability. We observe two-tone optomechanical instability in the optical domain with a silicon OMC, and develop a theoretical model to this finding. This is investigated systematically in the microwave domain with a micromechanical oscillator coupled to a microwave resonator. Its origin can be understood in a rotating frame as the vanishing of the effective mechanical frequency due to an optical spring effect. This imposes a fundamental limitation on BAE measurements, as well as other two-tone schemes, such as

dissipative quantum mechanical squeezing.

Laser cooling of a silicon nanomechanical oscillator to the zero-point energy. We demonstrate state-of-art continuous-wave laser sideband cooling of a silicon OMC to a mean thermal occupancy of 0.09 quanta, verified via motional sideband asymmetry. The result overcomes previous heating limitations and highlights the promise of silicon optomechanical crystals for quantum-enhanced continuous displacement measurements, as low-added-noise optomechanical interfaces for signal transduction and integration with superconducting qubit technology.

Quantum squeezing of mechanical motion with light. We demonstrate the first quantum squeezing of mechanical motion with optical light using reservoir engineering technique. The inferred mechanical quadrature variance is -1.4 dB below the zero-point fluctuation. Besides, we observe two-tone instability in the squeezing measurements despite the large dynamical back-action. Our results enable future quantum enhanced displacement and force sensing and non-classical mechanical state generation.

9.2 Outlook

The feasibility of deep in the quantum back-action dominated regime, makes it possible for a wide range of quantum enhanced measurements, such as sub-SQL measurement of mechanical motion using two-tone BAE measurement. Besides, the high fidelity ground state preparation of the OMC allows more efficient protocols in the pulsed regime, where non-classical mechanical state can be generated. By coupling the quantum mechanical motion to other degrees of freedom, such as electromagnetic field and solid-state two-level systems, coherent quantum state transfer can be realized. For example, the ability of reaching the ground state highlights the promise of OMC as a mechanical interface between two optical frequencies, where coherent quantum-limited optical frequency conversion can be achieved. The unique cryogenic system with remarkable thermalization can be adopted also for other cryogenic experiments that require efficient heat dissipation, such as piezo-optomechanics and electro-optical systems for microwave-optical frequency conversion and potential integration with superconducting qubits.

A List of Symbols

Symbol	Meaning
\hat{a}	Photon annihilation operator
Δ	Relative detuning between the laser frequency ω_L and cavity resonance frequency ω_{cav} ,
κ	Overall cavity intensity decay rate, including input coupling and intrinsic losses, $\kappa = \kappa_{\text{ex}} + \kappa_0$.
$\chi_c(\omega)$	Optical susceptibility of the cavity, $\chi_c(\omega) = [\kappa/2 - i(\omega + \Delta)]^{-1}$
\bar{n}_{cav}	Mean cavity photon number, $\bar{n}_{\text{cav}} = \langle \hat{a}^\dagger \hat{a} \rangle$
\hat{b}	Phonon annihilation operator
Ω_m	Mechanical frequency
Γ_{int}	Intrinsic mechanical damping rate
Γ_m	Mechanical damping rate
x_{ZPF}	Mechanical zero-point fluctuation amplitude, $x_{\text{ZPF}} = \sqrt{\hbar/2m_{\text{eff}}\Omega_m}$
$\chi_m(\omega)$	Mechanical susceptibility, $\chi_m(\omega) = [\Gamma_m/2 - i(\omega - \Omega_m)]^{-1}$
$S_{xx}(\omega)$	Two-sided quantum noise spectrum, $S_{xx}(\omega) \equiv \int dt e^{i\omega t} \langle \hat{x}(t)\hat{x}(0) \rangle$
\bar{n}_{th}	Mean phonon number in thermal equilibrium, $\bar{n}_{\text{th}} = (e^{\hbar\Omega_m/k_B T} - 1)^{-1}$
g_0	Optomechanical vacuum coupling rate
C_0	Optomechanical vacuum cooperativity, $C_0 = 4g_0^2/\kappa\Gamma_m$
C	Optomechanical cooperativity, $C = 4\bar{n}_{\text{cav}}g_0^2/\kappa\Gamma_m$
Γ_{opt}	Optomechanical damping rate
$\delta\Omega_m$	Optical spring (mechanical frequency shift)
\bar{n}_f	Mean final occupancy of the mechanical resonator
$\hat{X}_{1,2}$	Mechanical quadratures, $\hat{X}_1 = 1/\sqrt{2}(\hat{b}e^{+i\Omega_m t} + \hat{b}^\dagger e^{-i\Omega_m t})$ and $\hat{X}_2 = -i/\sqrt{2}(\hat{b}e^{+i\Omega_m t} - \hat{b}^\dagger e^{-i\Omega_m t})$.
$S_I(\omega)$	Single-sided noise spectrum of the photocurrent

B Nano Fabrication

Throughout this thesis, different processes have been developed and tested for performance comparison. In the following sections, we will show the details of the fabrication process developed and at the Center of MicroNanoTechnology (CMi) at EPFL.

B.1 Fabrication Runcard

1. Substrate preparation

- (a) Protection coating of 8inch SOI wafer with AZ9260 of 5um
- (b) Cleaving into quarters
- (c) Backside oxide removal at Wetbench with BHF 7:1 for 40min
- (d) Photoresist strip at Wetbench with Microposit Remover 1165
- (e) Spin coating with AZ9260 of 10um
- (f) Softbake at Hotplate at 115°C for 90min
- (g) Backside Grinding with Disco DAG 810 for 325um
- (h) Chip dicing with Disco DAD 321 for 15mm×15mm
- (i) Photoresist Strip at Wetbench with Microposit Remover 1165

2. Electron Beam Lithography

- (a) Pattern Preparation.
 - i. Pattern generation with gdspy
 - ii. Layout Beamer

- A. Extraction of cells, layers or regions of interest
 - B. Layout operation (healing, tone-reversal, bias, Boolean functions), Resolution=5nm
 - C. E-Beam Proximity Effect Correction
 - D. Output formatter for our E-Beam machines
- iii. CJOB
 - A. Import gpf files
 - B. Choose proper dose,
 - C. Choose proper beamcurrent,
 - D. Export the job with estimated exposure time
- (b) Ebeam Lithography
 - Process A, HSQ as Ebeam resist
 - i. Surface Activation with Tepla300. O2 plasma, 200W, 45s, 200mL/min
 - ii. Spin coating of HSQ XR-1541-006 with 6500RPM of 120nm
 - iii. Exposure with Vistec EBPG5000
 - iv. Development at the wet bench with TMAH25% for 30s
 - Process B, ZEP as Ebeam resist
 - i. Surface Activation with Tepla300. O2 plasma, 200W, 45s, 200mL/min
 - ii. Spin coating of ZEP-520 (1%) with 6500RPM of 120nm
 - iii. Soft bake at 180 degree for 7min
 - iv. Exposure with Vistec EBPG5000
 - v. Development at the wet bench
- 3. Chip Mounting on 4 inch silicon carrier wafer
 - (a) Quickstick at 135 °C
- 4. Device Etching
 - HSQ as Ebeam resist
 - Process A, Hydrogen Bromide based etching
 - (a) STS Multiplex ICP, HBr with O₂, 1 min
 - Process B, Fluorine based etching
 - (a) Alcatel AMS200, C₄F₈withSF₆, 18 sec

ZEP as Ebeam resist

- (a) Alcatel AMS200, C_4F_8 with SF_6 , 3.5 min

5. Device Protection layer

- (a) Spin Coating with HSQ, 1000 RPM
- (b) Thermal curing Neytech QEX 450 °C, 1 hour

6. Photolithography

- (a) Chip Mounting
- (b) HMDS priming
- (c) Spin coating of AZ9260 with thickness of $6\mu m$
- (d) Soft bake at 115 °C for 5 min
- (e) Exposure with Suss MJB4 20s.
- (f) Development with $2 \times AZ400K + 7 \times H_2O$, 3 min

7. Deep RIE Mesa Etching

HSQ as Ebeam resist

- (a) Oxide etching, SPTS APS, He/ C_4F_8 , 7min
- (b) Silicon etching, Alcatel AMS200, C_4F_8 with SF_6 , 21 min

ZEP as Ebeam resist

- (a) HSQ etching, SPTS APS, He/ C_4F_8 , 1min
- (b) Silicon etching, Alcatel AMS200, C_4F_8 with SF_6 , 1 min
- (c) Oxide etching, SPTS APS, He/ C_4F_8 , 6min
- (d) Silicon etching, Alcatel AMS200, C_4F_8 with SF_6 , 21 min

8. Finalization

- (a) Unmount chip from silicon carrier wafer at 100 °C
- (b) Photoresist removal with Tepla300, O_2 plasma, 10 min
- (c) Undercut, diluted HF (10%), 3 min
- (d) Piranha Cleaning, $1 \times H_2O_2 + 3 \times H_2SO_4$ at 100 °C, 10 min
- (e) Manual cleaving of the chip
- (f) Surface treatment, diluted HF (1%), several seconds

B.2 Etching Test

Nanofabrication of the OMC is of great challenges due to the small feature size and geometric variations. The final properties of the OMC rely critically on the geometry, surface roughness, and the sidewall verticality. In this section, an etching test is performed with different silicon etching processes and different EBeam resists based on the existing facilities in our cleanroom. In the etching test, two different EBeam are analyzed, i.e. HSQ and ZEP520A. For HSQ, two different etching processes are investigated, i.e. Fluorine and HBr based etching. For ZEP, we study the performance of Fluorine based etching. The main aim is to obtain an optimized process for OMC fabrication by looking at the etching results in terms of the cross sections of the test pattern after cleaving.

After defining the pattern with EBeam resist, we use Inductively Coupled Plasma (ICP) Reactive Ion Etching (RIE) to etch the silicon on top layer of SOI chip. During the plasma etching, the coil of the ICP systems ionizes the etch gas which chemically attacks the material using a sufficient powerful RF source. After ionization, the plasma is accelerated towards the carrier wafer (in our case) fixed on the chuck. To increase the plasma density, one can increase the ICP power which increases the etching rate. As the momentum is determined by the chuck power, one can also increase the milling aspect of the etching. In our etching step, the wafer is held by the chuck either by mechanical clamping or electrostatic forces while the backside of wafer is under constant Helium flow and pressure. As a result, changes in Helium flow rate lead to the variations of the substrate temperature, which may impact the etching processes. Besides, the pressure changes the ion angular distribution and also the amount of lateral etching by affecting collisions between the ions. The overall gas flow rate is also important, especially when multiple gases are utilized. The etching time is determined by the etching condition and device layer thickness. Longer etching time is typically required for tougher material (Si_3N_4 over Si) and thicker material (again Si_3N_4 over Si), which tends to heat up the sample and can damage the resist.

Large variety of parameters influence the final result of the RIE step. To optimize an etching process, it requires extensive parameters search. Samples etched with different parameters are analyzed with scanning electron microscope (SEM). Once satisfied parameters are obtained for desired process, it is of great importance to maintain the reproducible conditions. One way is to maintain reproducible electrostatic and mechanical clamps to mount wafers in the chamber. However, for parameters search with smaller chip-size substrate, it is not suitable. Alternatively, we mount the SOI chip ($1.5\text{cm} \times 1.5\text{cm}$) onto the carrier wafer with quickstick which melts around 135°C .

B.2.1 Fluorine Based Etching - Pseudo-Bosch Etching

Different requirements for plasma etching are key to the outcome of desired patterns, which leads to different criteria when selecting a suitable etching process. Selectivity, defined as the ratio of the etching rate between the mask and the material, plays an important rule, since a process with high selectivity allows for thinner mask for devices with same thickness which enables higher fidelity lithography. One of the most commonly used process is Bosch etching process, where two gases are used, SF_6 and C_4F_8 . SF_6 would lead to isotropic etching leaving silicon tetrafluoride SiF_4 as etching product. If C_4F_8 is added, it would be ionized into CF_2 , C_2 and C_3 . Once they are deposited on the exposed surfaces, long polymer chains can form and protect these surfaces from additional etching. In Bosch process, alternating SF_6 based etching and C_4F_8 based deposition are used to obtain high aspect ratio with good selectivity. However, the two alternating processes end up with rough sidewalls. Here, a modified Bosch process is used, which is called "waveguide etch" or "Pseudo Bosch etch". The two gases are injected simultaneously. The significantly reduced etching rate and the high selectivity result in much smoother sidewalls.

B.2.2 Hydrogen Bromide Based Etching

One alternative process to the above mentioned "pseudo Bosch process" is to use HBr based chemistry combined with oxygen. HBr results in polymerization on polysilicon sidewalls while oxygen provides a thin oxide layer. As HBr is very selective to the oxide, it is especially useful for silicon-on-insulator(SOI) patterned by HSQ. With a high selectivity between 1:5 and 1:10 found in literature, it is possible to achieve resolution limits with thin layers of coated HSQ $\sim 100\text{nm}$.

B.2.3 Etching Results

The pattern for the etching tests is shown in Fig. B.1. It consists of groups of trenches and squares with different lengths ranging from 100nm to 500nm . Through each cleaving line, we can always hit one square or line of width with target feature size, which can reveal full information for different sizes with same etching parameters, regardless of the EBeam resist that is used. The main purpose for the etching test is to see the cross section and more importantly the sidewall after etching. We mount the $1.5\text{cm} \times 1.5\text{cm}$ chip on a 4-inch silicon carrier wafer, as required by our equipments. More importantly, it mitigates the effects of silicon loading during etching, i.e. the area-dependent etch conditions. With the silicon wafer

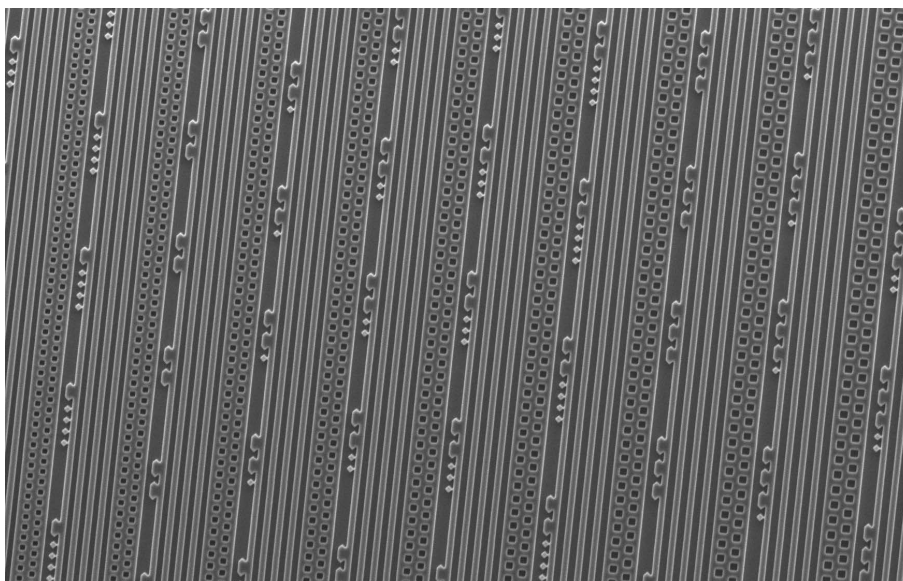


Figure B.1 – Pattern for the etching test

in the etch chamber, the amount of surface area on the chip being etched has a negligible impact on the loading condition, and allows for reproducible silicon etching regardless of the pattern size. Besides, this improves the thermalization of the chip with helium flow on the backside of the carrier wafer.

Before starting the etching test, we first give an overview of the parameters we use for HSQ (with AMS200 and STS) and also ZEP (with AMS200). The substrate chips are coated with HSQ-XR-1541-006 at the speed of 6500 RPM. The thickness of HSQ is around 120nm. We perform the etching test with AMS200 and STS respectively. For AMS200, the recipe we use is Si_opto, which is optimized to etch silicon. The parameters are as following:

1. SF_6 of 40sccm and C_4F_8 of 55 sccm
2. Plasma power: 1500W , RF forward: 30W
3. Temperature: 20° C

To obtain reproducible etching, we always perform an oxygen plasma cleaning for 10min of the etching chamber and prime for 10 min with the real process with a dummy wafer before the main etching process. This ensures the stability for helium flow and etching gas. The gas ratio of C_4F_8 and SF_6 is 1.375. The etch time is monitored by the end point detection (EPD). In this etching test, we tried 20sec, 28sec, 32sec respectively to cover different etching conditions, i.e. under-etching, about-etching and over-etching.

For STS for HBr, the recipe we use is HBr_Si with another step of Condi_Br before the main etching. The detailed steps for The Condi_Br are listed below:

1. Condi_Br

(a) O₂ plasma clean

- i. Power 700W
- ii. O₂: 10sccm
- iii. Time: 30min

(b) Breakthrough

- i. Ar: 20sccm
- ii. Plattern Power: 125W, Coil Power: 900W
- iii. Time: 15s
- iv. Chamber Pressure: 5mTorr

(c) Main Etching

- i. HBr: 20 sccm, O₂: 1 sccm
- ii. Plattern Power 60W, Coil Power 700W
- iii. Time: 30min
- iv. Chamber Pressure: 10mTorr

2. HBr_Si

(a) Sub_Si

- i. Cl: 50sccm
- ii. Plattern Power: 100W, Coil Power: 80W
- iii. Time: 10s
- iv. Chamber Pressure: 5mTorr

(b) Main Etching

- i. HBr: 20sccm, O₂: 1sccm(Optional)
- ii. Plattern Power 50W, Coil Power 900W
- iii. Time: 30min
- iv. Chamber Pressure: 2mTorr

For the first Condi_Br, it takes more 1 hour. To ensure the same etching rate for each run, we always etch a silicon wafer coated with photoresist first to check the reproducibility of

the etching rate by measuring the thickness of silicon after 5min. During the HBr_Si step, to stabilize the power, we start from 300W, then switch to 600W and in the end raise to 900W. Besides, the chamber pressure is preset as 10mTorr for plasma generation. When the power is stabilized at 900W, we manually change the chamber pressure from 10mTorr to 2mTorr. This usually takes additional 10 seconds. For the etching time, we preset it as 30 seconds, and stop manually since the machine recalculates the etching time when we change the power. In the etching test, we try the etching time with 60 seconds, 75 seconds and 90 seconds. After the etching, we unmounted the chip from the carrier wafer at the hotplate and remove the quickstick on the backside using Acetone and IPA. For better imaging of the bottom of the etched silicon, we put the chip into diluted HF (25%) for 3 minutes at room temperature and rinse with DI water for 1 minute.

For chips coated with ZEP520, the recipe we use is Si_opto_HR, the parameters are as following:

1. SF₆ of 25sccm and C₄F₈ of 63sccm
2. Plasma power: 1500W , RF forward: 15W
3. Temperature: 20° C

To obtain reproducible etching, we always also do an oxygen plasma cleaning for 10min and prime for 10min before the main etch with a dummy wafer. The temperature here is the same as Si_opto while the RF forward power is decreased from 30W to 15W, which enables slower etching. Besides, the gas ratio between C₄F₈ and SF₆ is increased from 1.375 to 2.52, which leads to smoother sidewall and also slower etching, since the flow rate of SF₆ is decreased quite a lot. The etching time here is chosen as 3minutes and 10seconds, 3minutes and 25seconds, and 3minutes and 40 seconds, which enable us to see the different etching conditions of silicon. After etching, we unmount the chip from the carrier wafer at the hotplate and remove the quickstick on the backside with Acetone and IPA. Then we stripped the remaining ZEP with UFT Remover and Piranha for 10min as described before. This will remove almost all the residues in the structures. For better imaging of the bottom of the etched silicon, we put the chip into diluted HF (25%) for 3minutes at room temperature and rinse with DI water for 1 minute.

To investigate the etching performance, we cleaved the chip with a diamond scribe and perform SEM imaging of the cross section and the sidewall of the etched silicon. Here we present the results we obtained from the etching test. Figure B.2 presents the results after etching, before and after undercut respectively for three different etching processes.

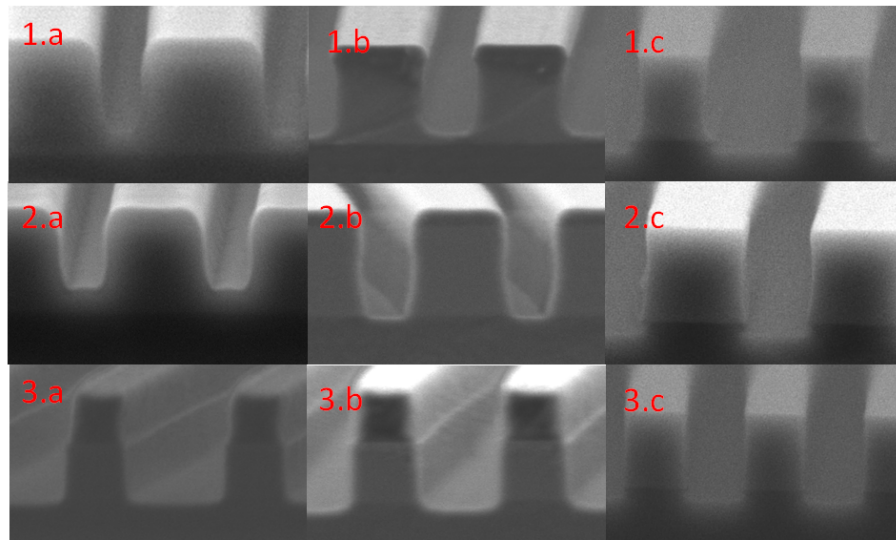


Figure B.2 – The etch test before and after undercut. 1.a(b) Silicon underetched (overetched) with Si_opto(HSQ) before undercut; 1.c Silicon about-etched with Si_opto(HSQ) after undercut; 2.a(b) Silicon underetched (overetched) with HBr_Si(HSQ) before undercut; 2.c Silicon about-etched with HBr_Si(HSQ) after undercut; 3.a(b) Silicon underetched (overetched) with Si_opto_HR(ZEP) before undercut; 3.c Silicon about-etched with Si_opto_HR(ZEP) after undercut.

Figure B.2 1.a(b) shows the results for chips coated with HSQ etched with AMS200 (Si_opto), the sidewall are far from perfect for both underetched and overetched samples. We could see curved sidewall on the bottom. The verticality of the sidewall is also far from satisfaction. Figure B.2 1.c shows the sidewalls after undercut, we could see large curvature on the bottom, where the silicon layer is not etched through and the etching doesn't ensure a good verticality. Figure B.2 2.a(b) shows the results for chips coated with HSQ while etched with STS (HBr_Si). The sidewalls are much better compared to Fluorine based etching for both under etched and overetched samples. HBr with oxygen leads to better sidewalls and verticality. The results also show that for wider groves, the sidewalls are more vertical than narrow ones. As this is a traditional problem in silicon etching with HBr, one way is to overetch the samples to get better verticality. One can increase the etch power and also etching time. However, the thickness of HSQ here is around 120nm, the overetching will kill almost all the coated HSQ in the end. Figure B.2 2.c shows the sidewalls after undercut, where the verticality is much better compared to the Fluorine based etching. Figure B.2 3.a(b) shows the results for chips coated with ZEP etched with AMS200 (Si_optoHR). The sidewalls are almost perfect compared to the etching results using HSQ with Fluorine Based and HBr based etching. We also obtain perfect verticality for narrow and wide groves. As the thickness of the coated ZEP is around 350nm, we still could still push limit to thinner ZEP for higher resolution, which requires

further parameters search. As it seems that there is a curved etch on the ZEP surface, which would probably lead to lower resolution or crack of the part of silicon. After stripping the ZEP with UFT Remover and Piranha and undercut, the sidewall is shown in Fig. B.2 3.c, which shows perfect verticality and surface roughness.

In this thesis, two different fabrication processes are adopted for the silicon device etching. Fluorine based Pseudo-Bosch etching process with ZEP as EBeam resist is developed at the CMI at EPFL. The HBr based etching process with HSQ as EBeam resist is developed at the Binnig and Rohrer Nanotechnology Center at IBM Research–Zurich, which includes the samples used in Chapter 6-8. The detailed fabrication process is presented in Ref. [277].

B.3 Image Processing

In the previous section, we show how we evaluate the different etching processes with different EBeam resists, such as HSQ and ZEP. Optomechanical properties of the OMC, however, depend also critically on the geometry of the finalized samples, such as the hole sizes and the beam width. A perfect understanding of feature size of the fabricated sample is important. As mentioned previously, we apply a proximity effect correction in the EBeam step to compensate the electron backward scattering during the Ebeam exposure. This is however not sufficient for the finalized OMC, where the etching process also matters. We develop a matlab-based image processing package to analyze the fabricated OMC from the SEM pictures. In Fig. B.3, we show the graphical user interface (GUI) for the image processing. The SEM pictures of the finalized OMC cavities is taken with a Zeiss Merlin SEM, scanning both vertically and horizontally, with nanometer resolution. The SEM picture is taken at a voltage of 5/10kV with a resolution of 1-10 nm/pixel. The meta files are saved in the tif file of the figures. The image processing procedure is shown in the following,

1. Re-orientation and cropping of the image to keep only the nanobeam
2. Wiener filter applied to reduce the image noise with Matlab function `wiener2`
3. Binarize the image with analyzed threshold to separate the nanobeam from the background
4. Boundaries detection with Matlab Image Processing Toolbox function `bwboundaries`
5. Improve edge detection accuracy by introducing subpixel precision
6. Fit of the ellipses and lines of extracted features

7. Determine the image scale from the pitch of the nanobeams

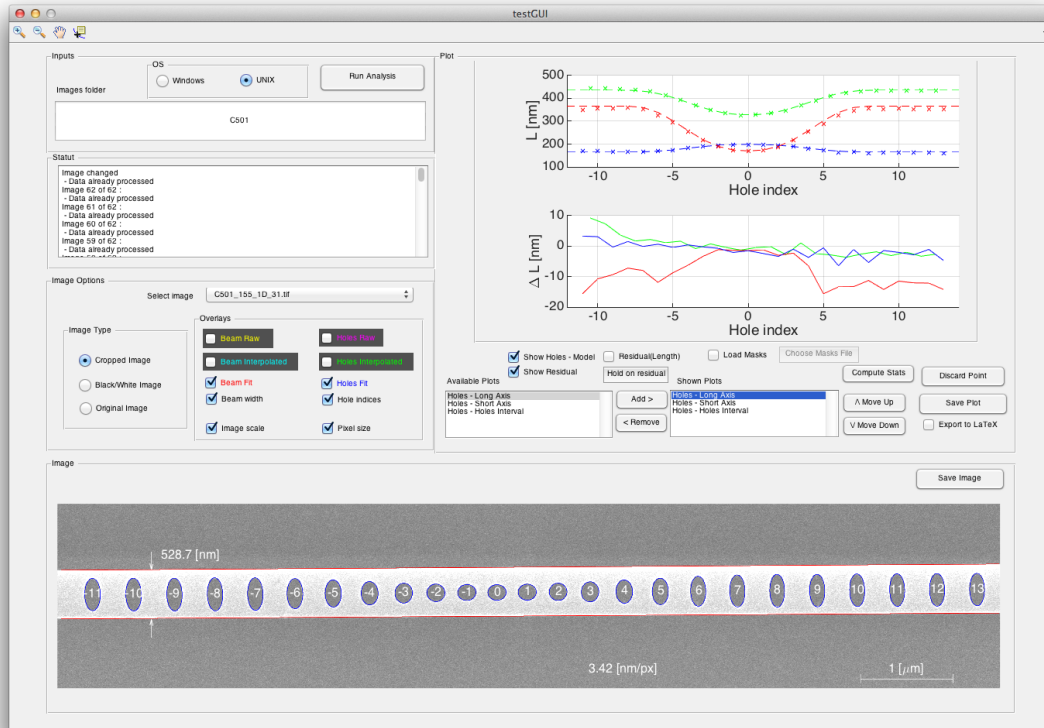


Figure B.3 – Graphical user interface for the image processing of the SEM pictures of the OMC developed in Matlab.

After the image processing, we compare the fitted results to the both the mask design and also the optimal design for the OMC by loading the Ebeam mask design. The individual plot for each cavity and statistical average can be selectively chosen in the GUI. The deviation of the actual fabricated OMC from the target design, such as the hole sizes, are fitted with a hole-number dependent Gaussian function plus a constant, where the constant typically matches the nanobeam width change. We apply a correction based on the statistic variations to the EBeam mask design in the next fab run. The fabrication process is subject to external conditions changes and the outcomes can differ slightly from batch to batch, especially for the obtained constant from the fitting of the corrections. As a result, we typically sweep the constant while keep the hole-number dependent Gaussian function fixed.

The code is available on Github from the following address: https://github.com/QINC-Lab/ImageProcessing_OMC.git.

C Optical Measurement

C.0.1 Coherent Response Measurement

For optical characterization and control, it is of utmost importance to tune the probing tones accurately around the optical resonance. Active locking the probing tone to the cavity or vice versa (e.g. using a Pound-Drever-Hall technique), are extremely useful for this purpose. For example, a narrow tunable filter cavity (50 MHz) can be locked to our pumping lasers to suppress the high frequency laser noises at ~ 5 GHz, as shown in our previous experiments. In lots of optomechanical measurements, e.g. sideband cooling, the laser has to be driven off resonant from the cavity. The relative detuning of the pumping laser to the cavity resonance thus becomes important, which can be obtained from the cavity coherent response. We use passive tuning of our master laser, from which the other tones are derived. From the response curve we extract accurate values of both laser detuning and optical linewidth.

Here we give details on the method. A simplified setup is shown in Fig. C.1. The laser is phase-modulated using RF output of a network analyzer (NA). This weak modulation generates two sidebands around the carrier on both sides. The carrier and sidebands are sent to the cavity and reflected via an optical circulator. They interfere on a fast photodetector with the photocurrent fed to the NA input. The demodulation of the RF signal results in a coherent cavity response, which measures the magnitude and phase of the S_{21} parameter.

The field amplitude incident on the cavity is given by

$$a_{\text{in}}(t) \simeq a_0 \left(1 + \frac{\beta}{2} e^{i\Omega t} - \frac{\beta}{2} e^{-i\Omega t} \right), \quad (\text{C.1})$$

with β the modulation index, a_0 the field amplitude and Ω the modulation frequency. The

Appendix C. Optical Measurement

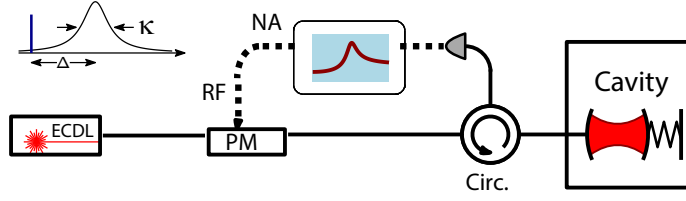


Figure C.1 – **Simplified setup for optical coherent response measurements.** A strong pumping tone is detuned from the cavity resonance by Δ . Weak probing tones are generated by a phase modulator (PM). The reflection from the cavity is collected for coherent response measurements.

modulation index is directly related to the RF power sent to the phase modulator from the NA at each modulation frequency Ω .

The reflected light is

$$a_{\text{out}}(t) \simeq a_0 \left[r(\Delta) + \frac{\beta}{2} r(\Delta + \Omega) e^{i\Omega t} - \frac{\beta}{2} r(\Delta - \Omega) e^{-i\Omega t} \right], \quad (\text{C.2})$$

with

$$r(\Delta) = 1 - \frac{\eta_c \kappa}{\kappa/2 - i\Delta}. \quad (\text{C.3})$$

The amplitude reflection coefficient at detuning Δ and $\eta_c \equiv \kappa_{\text{ex}}/\kappa$ the cavity coupling parameter. The magnitude of the S_{21} parameter, the Ω frequency component of the photocurrent $|a_{\text{out}}(t)|^2$, is given by (here and below we omit a constant scale factor)

$$|S_{21}(\Omega)| = \frac{\beta}{2} |r(\Delta) r^*(\Delta - \Omega) - r^*(\Delta) r(\Delta + \Omega)|. \quad (\text{C.4})$$

For laser detuning Δ much larger than the cavity linewidth κ , the coherent cavity response shows a perfect Lorentzian. The laser detuning and cavity linewidth can be calculated easily. Figure C.2 shows a typical coherent response measurement, which deviates significantly from a Lorentzian when $\Delta \sim \kappa$. Additionally, when scanning over a wide bandwidth, one has to consider the frequency dependence of β (due to phase modulator, rf cables, detector response etc.). A robust and reliable procedure to calibrate the frequency dependence of the entire detection chain is to take several traces at various detunings, and fit all of them simultaneously to Eq. (C.4) with only Δ variable across traces, and with a high-order polynomial in Ω as a prefactor. This prefactor is then applied in all subsequent fits. The inset in Fig. C.2 shows the frequency dependence of β given by the polynomial. We adjust probe detuning using this

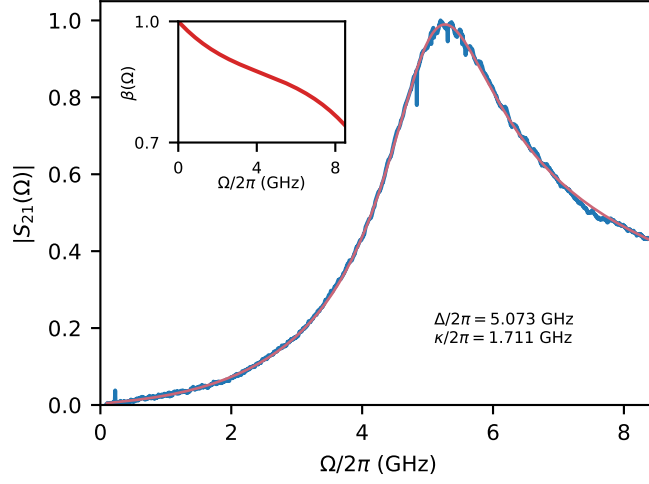


Figure C.2 – **Coherent response determination of detuning and linewidth.** An example of a measurement with a fit Eq. (C.4), yielding κ and Δ . A correction due to extraneous frequency-dependent response, measured and shown in the inset, is included in the fit.

method prior to each data point acquisition.

The coherent response measurement has been widely used in this thesis. For example, we calibrate the free spectral range of the fiber loop reference cavity $\sim 187\text{MHz}$. In laser noise measurement, where the phase noise is transduced to amplitude modulation by placing the laser off resonance, the cavity linewidth of the filter cavity and laser detuning can be obtained. By checking the cavity response measurement, we can check the stability of the cavity resonant frequency before and after a specific measurement, especially under cryogenic environment. Besides, it has been adopted for the measurement of optomechanically induced transparency with OMC, which can be additionally used for g_0 calibration [110]. We note that, a slightly modified version of this scheme is also implemented in the response measurement of the optical cavity by pumping at a second optical mode to rule out the thermal and Kerr response [122].

C.0.2 Balanced Heterodyne Detection

In quantum optomechanics, the mechanical motion generates Stokes and anti-Stokes sidebands. Quantum measurement of mechanical motion relies on the optical detection of these weakly scattered thermomechanical sidebands. This becomes particularly challenging for the measurements of the mechanical motion close to the zero-point energy. For example, in the case where the final occupancy $\bar{n}_f = 1$, the weight of the sideband compared to the carrier is $\sim 4g_0^2/(\Omega_m^2)$. Due to the rather weak vacuum optomechanical coupling rate, the ratio between

Appendix C. Optical Measurement

the scattered sideband and carrier can be as low as -70dB . Besides, in real measurements, the total detection efficiency of the photons leaving the cavity can be much lower than unity, due to different kinds of losses, such as the intracavity absorption, connector loss, fiber loss, mirror loss or inefficient photodiode.

Here we assume a signal to measure with field amplitude,

$$\hat{a}_{\text{sig}} = (\bar{a}_{\text{sig}} + \delta \hat{a}_{\text{sig}}) e^{-i\omega_s t} \quad (\text{C.5})$$

where ω_s is the frequency of the traveling optical field, \bar{a}_{sig} is the mean coherent field amplitude while $\delta \hat{a}_{\text{sig}}$ corresponds to the field fluctuation. Direct measurement of photon number at the photodiode is given by,

$$n_{\text{sig}} = \hat{a}_{\text{sig}}^\dagger \hat{a}_{\text{sig}} = \bar{a}_{\text{sig}}^2 + \bar{a}_{\text{sig}} (\delta \hat{a}_{\text{sig}} + \delta \hat{a}_{\text{sig}}^\dagger) + \delta \hat{a}_{\text{sig}}^\dagger \delta \hat{a}_{\text{sig}}, \quad (\text{C.6})$$

where the third term can be neglected. We note that, the measured photon flux consists of a constant \bar{a}_{sig}^2 , and the amplitude fluctuation term $\bar{a}_{\text{sig}} (\delta \hat{a}_{\text{sig}} + \delta \hat{a}_{\text{sig}}^\dagger)$. The measured photocurrent is thus dominated by a DC signal. Considering the large detector noise, the quantum-limited detection of the field fluctuation will be quite difficult as high powers are required which can easily saturate the photodiode. As a result, to measure weakly scattered sideband, direct detection is typically not ideal. One solution is to use an Erbium-doped fiber amplifier(EDFA) together with a filter cavity. We use such method to amplify the weak reflected light in the coherent cavity response measurement, especially for low pumping powers, due to the large noise-equivalent-power of the fast photodiode (14 GHz). However, amplification by an EDFA adds some noise to the original signal – mainly due to amplified spontaneous emission by $\sim 5 - 7\text{ dB}$. This results in extensive calibration of the noise process in the measured signal, such as the wavelength, power and gain dependent noise figure. A quantum limited detection of the weakly scattered sidebands is required. Here, we discuss the basic principles of balanced heterodyne detection. The scheme for the balanced heterodyne detection is shown in Fig. C.3. The signal is now is combined with a strong local oscillator(LO) through a balanced beam splitter. The LO has the field amplitude,

$$\hat{a}_{\text{LO}} = (\bar{a}_{\text{LO}} + \delta \hat{a}_{\text{LO}}) e^{-i\omega_{\text{LO}} t}, \quad (\text{C.7})$$

where the optical frequency $\omega_{\text{LO}} = \omega_s + \Omega_{\text{LO}}$, \bar{a}_{LO} is the mean field amplitude and $\delta \hat{a}_{\text{LO}}$ is the

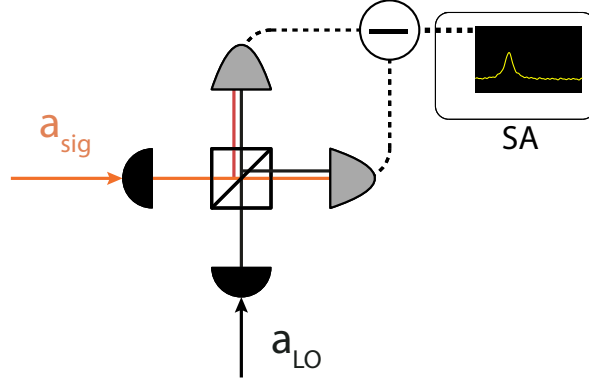


Figure C.3 – **Simplified setup for Balanced Heterodyne Detection.** a_{sig} and a_{LO} are the signal and the local oscillator, which are combined in a free space balanced heterodyne setup.

field fluctuation of the LO. The output field of the two paths,

$$\begin{aligned}\hat{a}_1 &= \frac{1}{\sqrt{2}} (\hat{a}_{\text{LO}} + i\hat{a}_{\text{sig}}) \\ \hat{a}_2 &= \frac{1}{\sqrt{2}} (i\hat{a}_{\text{LO}} + \hat{a}_{\text{sig}}),\end{aligned}\tag{C.8}$$

are collected onto two identical independent photodiodes. The photocurrent from the two photodiodes are subtracted, which results in the heterodyne signal,

$$\hat{I}_{\text{out}}(t) = i \left(\hat{a}_{\text{sig}}^\dagger(t) \hat{a}_{\text{LO}}(t) - \hat{a}_{\text{LO}}^\dagger(t) \hat{a}_{\text{sig}}(t) \right).\tag{C.9}$$

In the case of strong LO, where the LO power is much larger than the signal power, i.e. $|\bar{a}_{\text{LO}}| \gg |\bar{a}_{\text{sig}}|$, we can obtain,

$$\hat{I}_{\text{out}}(t) = e^{i\Omega_{\text{LO}}t} \bar{a}_{\text{LO}}^* \delta \hat{a}_{\text{sig}}(t) + e^{-i\Omega_{\text{LO}}t} \bar{a}_{\text{LO}} \delta \hat{a}_{\text{sig}}^\dagger(t),\tag{C.10}$$

The (time-averaged) autocorrelator of the signal is the heterodyne spectrum,

$$S_I(\omega)^{\text{het}} = \frac{1}{2} \int_{-\infty}^{\infty} \overline{\langle \hat{I}_{\text{out}}(t+t'), \hat{I}_{\text{out}}(t') \rangle} e^{i\omega t} dt,\tag{C.11}$$

where the overbar denotes averaging with respect to t' . Invoking commutation relations we normal-order the operators in Eq. (C.11)

$$\overline{\langle \hat{I}_{\text{out}}(t+t'), \hat{I}_{\text{out}}(t') \rangle} = |\bar{a}_{\text{LO}}|^2 \left[\overline{\delta \hat{a}_{\text{sig}}^\dagger(t+t') \delta \hat{a}_{\text{sig}}(t')} e^{-i\Omega_{\text{LO}}t} + \overline{\delta \hat{a}_{\text{sig}}^\dagger(t') \delta \hat{a}_{\text{sig}}(t+t')} e^{i\Omega_{\text{LO}}t} \right].\tag{C.12}$$

Appendix C. Optical Measurement

We can thus obtain the spectrum of the heterodyne photocurrent,

$$S_I^{\text{het}}[\Omega] = |\bar{a}_{\text{LO}}|^2 \left(S_{\hat{a}\hat{a}}^{\text{sig}}[\Omega + \Omega_{\text{LO}}] + S_{\hat{a}^\dagger\hat{a}^\dagger}^{\text{sig}}[\Omega - \Omega_{\text{LO}}] \right). \quad (\text{C.13})$$

The weak optical signal is amplified by the strong LO, where the noise spectral density from the balanced heterodyne detection far exceed the detector noise. By choosing proper frequency separation between the pumping frequency and the LO, it can optically mix down the measured noise from high frequency (GHz) to a low frequency range (MHz), which can be easily captured by a low-noise balanced photodiode. The balanced heterodyne measurements have been widely adopted in this thesis, especially for the quantum limited detection of the thermomechanical sidebands, such as in the ground state cooling, motional sideband asymmetry, back-action evading measurement and mechanical squeezing. In these measurements, the LO is derived from another laser which is phase locked to the master pumping laser. The locking frequency between the two lasers are typically set close to the mechanical frequency. What's more, BHD has been intensively adopted for ultra-low noise investigation, such as the laser noise and the cavity frequency noise, taking advantage of the flexibility of the locking scheme.

D Laser Noise

External cavity diode lasers are well-known to have an excess noise in the GHz range, due to the damped relaxation oscillation caused by carrier population dynamics. This is the main contribution for GHz excess noise for diode lasers. As this frequency is close to the mechanical frequency, it is necessary to quantify the phase noise of the diode laser that we are using [179, 184].

The presence of the excess laser phase noise leads to a limited sideband cooling performance [114, 178, 179, 184]. On the other hand, the effect of excess laser noise on the sideband asymmetry has been extensively studied [71, 178, 184] in both sideband resolved regime and Doppler regime. In a heterodyne detection scheme, the sideband imbalance is due to the correlation between imprecision and backaction from the probing tones. This is true also when the probing tones are not quantum limited, which can lead to an artificially increased asymmetry. As a consequence it is imperative that the lasers are quantum noise limited in amplitude and phase quadrature.

Before switching to the laser noise characterization, we first give a basic introduction on the noise properties. For a probing laser at frequency of ω_L , the amplitude $a_{\text{in}}(t)$ could be expressed as $a_{\text{in}}(t) = e^{-i\omega_L t}(\bar{a} + \delta\hat{a}_{\text{in}}(t))$, where \bar{a} is the mean photon flux amplitude and $\delta\hat{a}_{\text{in}}(t)$ is the field fluctuation.

The field quadratures are defined as

$$\delta\hat{q}_{\text{in}}(t) = \frac{\delta\hat{a}_{\text{in}}(t) + \delta\hat{a}_{\text{in}}^\dagger(t)}{\sqrt{2}}, \quad (\text{D.1a})$$

$$\delta\hat{p}_{\text{in}}(t) = \frac{\delta\hat{a}_{\text{in}}(t) - \delta\hat{a}_{\text{in}}^\dagger(t)}{i\sqrt{2}}, \quad (\text{D.1b})$$

where $[\delta \hat{q}_{\text{in}}(t), \delta \hat{p}_{\text{in}}(t')] = i\delta(t - t')$.

By introducing the $C_{i,j}$ ($i = p, q$) as excess noise in the field quadratures,

$$\begin{pmatrix} \delta \hat{q}_{\text{in}}(t) \delta \hat{q}_{\text{in}}(t') & \delta \hat{q}_{\text{in}}(t) \delta \hat{p}_{\text{in}}(t') \\ \delta \hat{p}_{\text{in}}(t) \delta \hat{q}_{\text{in}}(t') & \delta \hat{p}_{\text{in}}(t) \delta \hat{p}_{\text{in}}(t') \end{pmatrix} = \frac{1}{2} \begin{pmatrix} 1 + 2C_{qq} & i + 2C_{qp} \\ -i + 2C_{qp} & 1 + 2C_{pp} \end{pmatrix} \delta(t - t'), \quad (\text{D.2})$$

the input field satisfies the following relation,

$$\begin{pmatrix} \langle \delta a_{\text{in}}(t) \delta a_{\text{in}}(t') \rangle & \langle \delta a_{\text{in}}(t) \delta a_{\text{in}}^\dagger(t') \rangle \\ \langle \delta a_{\text{in}}^\dagger(t) \delta a_{\text{in}}(t') \rangle & \langle \delta a_{\text{in}}^\dagger(t) \delta a_{\text{in}}^\dagger(t') \rangle \end{pmatrix} = \frac{1}{2} \begin{pmatrix} C_{qq} - C_{pp} & 2 + C_{qq} + C_{pp} \\ C_{qq} + C_{pp} & C_{qq} - C_{pp} \end{pmatrix}. \quad (\text{D.3})$$

In order to measure the amplitude noise, we can employ direct detection of the photon flux. The power spectral density \bar{S} of the photocurrent of incident optical power is given by,

$$\bar{S}_p = 2(\hbar\omega_L)^2 \langle \dot{n} \rangle (1 + 2C_{qq}) = \bar{S}_p^{\text{shot}} + \bar{S}_p^{\text{ex}}. \quad (\text{D.4})$$

where $\langle \dot{n} \rangle$ is the photon flux. The noise spectral density of the shot noise and the excess amplitude noise are given by,

$$\begin{aligned} \bar{S}_p^{\text{shot}} &= 2(\hbar\omega_L)^2 \langle \dot{n} \rangle \\ \bar{S}_p^{\text{ex}} &= 4(\hbar\omega_L)^2 \langle \dot{n} \rangle C_{qq}. \end{aligned} \quad (\text{D.5})$$

We obtain the noise spectrum for different incident power around the mechanical frequency. A low powers, the noise spectrum increases linearly versus the incident powers, due to the shot noise. The deviation due to excess amplitude noise compared to the shot noise, starts to appear for high probing powers (100s μW to few mW). However, even for high incident powers (mW), the excess amplitude noise is much less than the shot noise, which is negligible.

The excess noise in the phase quadrature C_{pp} can be modeled as $C_{pp} = \langle \dot{n} \rangle S_{\phi\phi}^{\text{ex}}$, where $S_{\phi\phi}^{\text{ex}}$ is the phase noise spectral density of the laser. To obtain the excess noise in the phase quadrature,

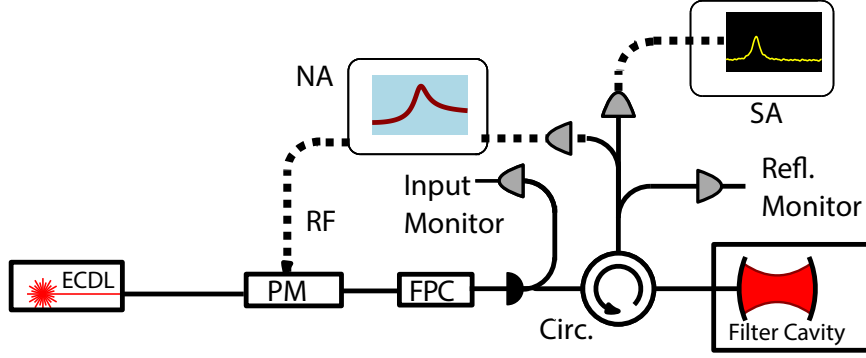


Figure D.1 – **Measurement Setup for the phase noise measurement with a filter cavity.** A RF tone from NA is sent to a phase modulator to generate the probing tones or the calibration tone. The reflected light is switched between the coherent response measurement to determine the detuning and the spectrum analyzer to obtain the noise spectrum for noise calibration.

a calibration of the laser phase noise is thus required. In our experiments, we are interested in the phase noise around the mechanical frequency around 5 GHz. A narrow cavity can be used to transduce the laser frequency noise to the amplitude noise which can be measured by direct detection. In principle, one can directly use the OMC for such phase noise calibration. However, due to the large bandwidth (\sim GHz), the transduction from the phase modulation to the amplitude modulation is insufficient for lasers with low phase noise. In our case, we choose to work with an external MicronOptics FFP-TF2 filter cavity with a linewidth \sim 50 MHz. The noise spectrum is firstly taken by direct detection of the reflected light with the laser far detuned from the filter cavity $S_I^A(\Omega)$, which consists of the amplitude noise and the detector noise. We then sweep the cavity detuning in order to measure the phase noise in the range from 0 to 6 GHz. During each sweep, a coherent cavity response measurement is performed to obtain the relative detuning Δ between the laser and the filter cavity. The total noise spectrum $S_I^{\text{tot}}(\Omega)$ is then captured with a spectrum analyzer together with a calibration tone located at the laser detuning frequency. The calibration tone is generated by a phase modulator with RF signal of frequency $|\Delta|$, of known modulation depth β . This enables the conversion of the recorded noise spectrum to the phase noise spectral density. As shown previously in the coherent cavity response measurement, the modulation depth β is frequency dependent. The frequency dependent modulation depth can be independently calibrated by comparing the power ratio between the generated first-order sideband and the carrier, which is essentially given by $\beta^2/4$. The phase noise spectral density can be obtained from the subtracted noise spectrum $S_I(\Omega) = S_I^{\text{tot}} - S_I^A$, which takes the form,

$$S_I(\Omega) = S_{\phi\phi}(\Omega) \frac{\kappa^2/4}{(\Omega - |\Delta|)^2 + \kappa^2/4} \frac{S_I(|\Delta|)}{S_{\phi\phi}(|\Delta|)}, \quad (\text{D.6})$$

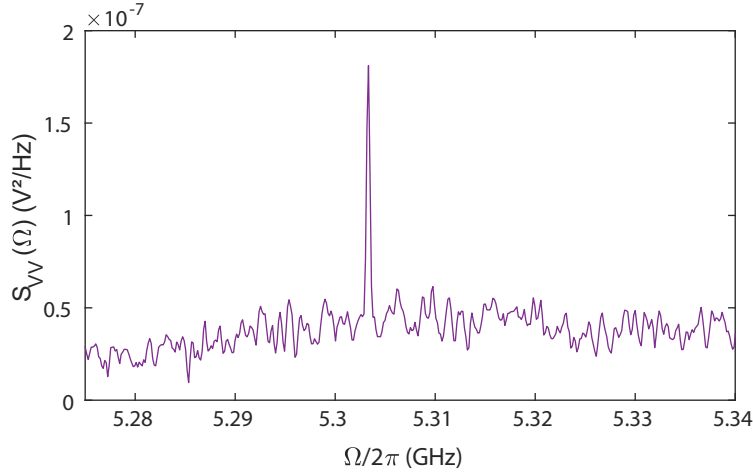


Figure D.2 – **Noise spectrum of the transduced phase noise around 5.3GHz.** The laser model used here is Toptica CTL1550. The direct detection of the cavity transduced amplitude fluctuation with a calibration tone around 5.303GHz with known modulation depth. The amplitude noise and the detector noise are subtracted.

where $S_{\phi\phi}(\Omega)$ is the phase spectral density. Using the calibration tone with known modulation depth β , the calibration between the total noise spectral density and the phase noise spectral density at the frequency $|\Delta|$ is given by,

$$\frac{S_I(|\Delta|)}{S_{\phi\phi}(|\Delta|)} = \frac{\int S_I^{\text{cal}}(\Omega) d\Omega}{\beta^2/4}. \quad (\text{D.7})$$

where $\int S_I^{\text{cal}}(\Omega) d\Omega$ corresponds to the integral of the noise spectral density of the calibration tone. The phase noise spectral density can be obtained,

$$S_{\phi\phi}(\Omega) = S_I(|\Delta|) \frac{\beta^2/4}{\int S_I^{\text{cal}}(\Omega) d\Omega} \frac{(\Omega - |\Delta|)^2 + \kappa^2/4}{\kappa^2/4}, \quad (\text{D.8})$$

which results in the frequency noise spectral density $S_{\omega\omega}(\Omega) = \Omega^2 S_{\phi\phi}(\Omega)$.

In Fig. D.2, typical noise spectrum of the transduced phase noise of the Totica CTL 1550 around 5.3GHz is shown with $S_{VV}(\Omega)$. The central peak corresponds to the calibration tone. The broad cavity transduced phase noise is also quite evident. The characterized frequency noise spectral density $S_{\omega\omega}(2\pi \times 5.3 \text{ GHz})$ is $\sim 3 \times 10^4 \text{ rad}^2/\text{Hz}$. In Fig. D.3, we show the calibrated frequency noise spectral density from 1GHz to 6GHz. For the laser (Toptica CTL 1550) at typical current 300 mA, the relaxation oscillation frequency is around 1.94 GHz with a frequency noise spectral density of $S_{\omega\omega}(\Omega_{\text{relax}}) \sim 2 \times 10^6 \text{ rad}^2/\text{Hz}$.

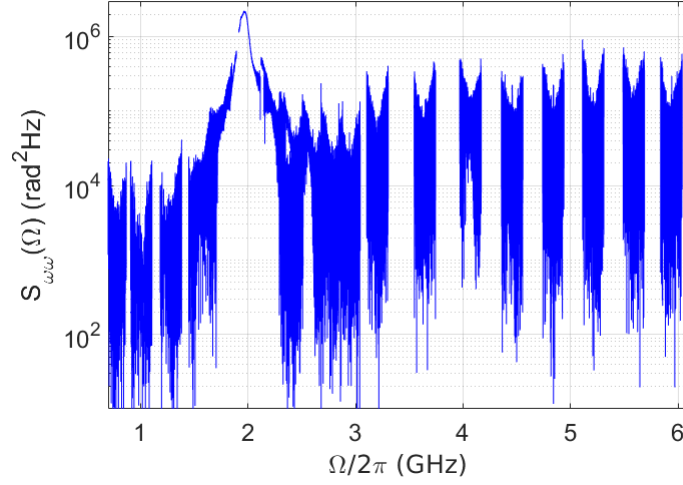


Figure D.3 – **Calibrated frequency noise spectral density of Toptica CTL1550.** The noise spectrum are jointly plotted for different frequency ranges by sweeping the relative detuning between the pumping laser and filter cavity resonance.

We perform the same frequency noise measurement with the New Focus Velocity series (TLB-6328), which turn out to have significantly higher phase noise compared to the Toptica CTL. The measured relaxation oscillation frequency is ~ 3.5 GHz. The overall frequency noise spectral density is more than one order of magnitude higher than the Toptica CTL around the mechanical frequency ~ 5 GHz.

Laser noise has been proven to limit the final occupancy for sideband cooling due to the excess heating from the excess classical noise. For a sideband resolved optomechanical system, the final phonon occupancy of the mechanical oscillator from sideband cooling, is given by,

$$\bar{n}_f = \frac{\kappa \bar{n}_{\text{th}} \Gamma_m}{4g_0^2 n_c} + \frac{\kappa^2}{16\Omega_m^2} + \frac{n_c}{\kappa} S_{\omega\omega}. \quad (\text{D.9})$$

The first term in Eq. D.9 corresponds to the standard laser cooling. The second term corresponds to the quantum limit of sideband cooling due to the quantum back-action. The excess heating due to the laser noise is given by $\frac{n_c}{\kappa} S_{\omega\omega}$, which scales linearly with the pumping power. The optimal final occupancy can be obtained,

$$\bar{n}_f^{\min} = \sqrt{\frac{\bar{n}_{\text{th}} S_{\omega\omega} \Gamma_m}{g_0^2}}, \quad (\text{D.10})$$

which is limited by the excess laser noise. For a OMC with $\Gamma_m \sim 2\pi \times 100$ kHz at 4K, the required laser frequency noise is $S_{\omega\omega} \sim 10^6 \text{ rad}^2/\text{Hz}$ to sideband cool to 1 phonon. For ultra-low phonon occupancy, e.g. 0.1, the frequency noise has to be two order of magnitude lower,

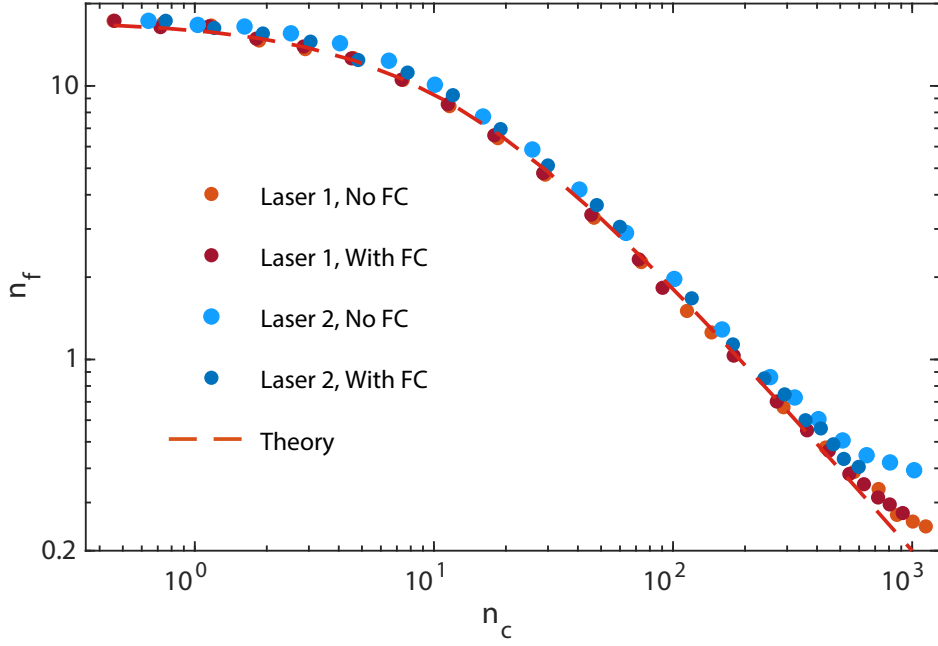


Figure D.4 – **Sideband cooling of OMC at 4K with two different lasers with and without a filter cavity.** The measurement is performed on an OMC used in Ref. [145], with an optical linewidth of $\kappa/2\pi = 250\text{MHz}$, at 4K with a pressure of $\sim 60\text{mbar}$. Laser 1 and Laser 2 are Toptica CTL 1550 and CTL1500 respectively. For each laser, we compare the cooling performance with and without a filter cavity. The filter cavity is locked to the pumping laser via PDH lock to suppress the high frequency noise. A theoretical curve calculated from experimental parameters is shown in dashed line for comparison.

which is however quite difficult to measure using direct detection. Perfect knowledge of the phase frequency noise at high frequency becomes extremely necessary. To reveal how the frequency noise affects the sideband cooling performance, Figure D.4 shows the cooling results for two Toptica lasers of different models, namely Toptica CTL 1550 and 1500, for an OMC at 4K. Both of these two lasers are tested with and without a filter cavity. The filter cavity with linewidth $\kappa \sim 2\pi \times 50\text{MHz}$ is locked to the respective pumping lasers using the PDH locking technique, which gives additional 20dB of phase noise suppression around the mechanical frequency. Besides, a theoretical cooling curve based on experimental parameters is shown in red dashed line for comparison. For low pumping powers, the sideband cooling results follow the theoretical curve very well. At high powers, e.g. $n_c \sim 1000$, a deviation from theoretical results of the final occupancy appears, mainly due the optical heating. The light blue dots, corresponding to the Toptcal CTL 1550 without the filter cavity, shows much larger deviation compared to the case with the filter cavity (dark blue dots), which clearly show the impact of the excess phase noise heating on the laser sideband cooling. For this reason, in our experiment of laser cooling to the zero-point energy and mechanical squeezing, the pumping

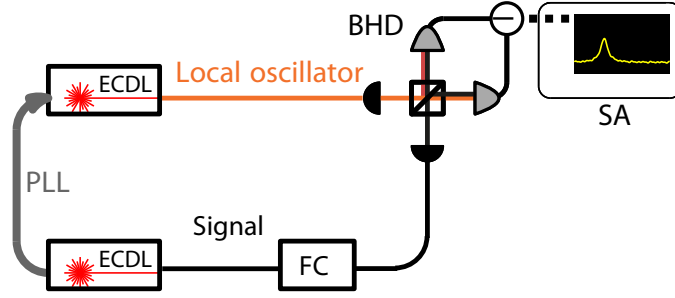


Figure D.5 – **Simplified setup for noise analysis with balanced heterodyne detection.** The low noise signal laser Toptica CTL1500 passes through a filter cavity to reject high bandwidth excess noise. The LO is phase locked to the signal at various frequencies, which is switched between two lasers, Toptica CTL1550 and Toptica CTL1500, respectively. The signal power is around $100\mu W$, while the LO power is set around 6mW.

tones pass through a narrow filter cavity for noise suppression at high frequencies. Due to the large insertion loss (PM and filter cavity) and experimental complexity, we don't implement such noise suppression to the local oscillator.

We note that, in the balanced heterodyne detection of the thermomechanical sideband at high pumping powers, we consistently observe an increased noise floor compared to the shot noise floor. Extensive exploration has been made to verify the origin of such noise floor increase, such as cavity frequency noise, fiber noise, Brillouin scattering, device noise (bulk acoustic wave), and laser noise. In Fig. D.5, a balanced heterodyne detection setup is adopted to have a quantum-limited measurement of the excess noise. Due to the finite bandwidth of the balanced photodiode (MHz), a slave local oscillator is phase locked to the master signal laser at various frequencies. For the signal laser, we choose a Toptica CTL 1500 model, which has quite low excess frequency noise at GHz frequency. The signal passes through a filter cavity which is locked to the carrier to reject the noise at high frequencies. The power of the signal laser before the beam splitter is around $100\mu W$, which is close to the highest reflected power we typically have in the sideband cooling experiments. The LO oscillator is switched between a Toptica CTL 1500 and 1550, with a power of $\sim 6mW$ before the beam splitter. We note that, for such noise analysis, a balanced homodyne detection can be adopted in principle. However, due to the lack of low NEP balanced detector at GHz bandwidth, we stay with the balanced heterodyne detection, which gives us the flexibility to have quantum-limited noise measurement in large frequency range.

The excess noise compared to the shot noise floor in the balanced heterodyne detection is shown in Fig. D.6. The signal laser, which is primarily adopted as the cooling tone in our

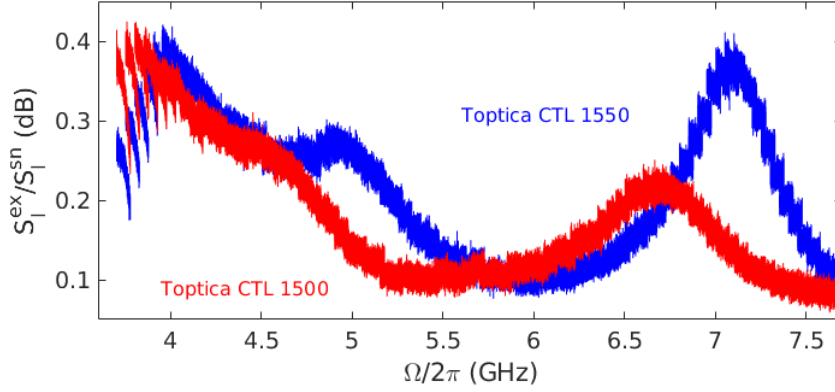


Figure D.6 – **Observed excess noise in the balanced heterodyne detection with different local oscillators.** The LO is phase locked at various frequencies away from the signal laser ranging from 3.6GHz to 7.8GHz. The BHD spectrum is taken for each locking frequency and jointly plotted, due to the finite bandwidth of the balanced photodiode (80 MHz).

experiments (Toptica CTL 1500), has a power of $\sim 100 \mu\text{W}$. We bypass all the unnecessary optical devices and paths, such as PM, attenuator, filter cavity, mirrors and tapered fiber. The result of the excess noise S_I^{ex} normalized to the shot noise S_I^{sn} using two different lasers for the LO is shown in blue (Toptica CTL 1550) and red (Toptica CTL 1500) curves. The two lasers gives different noise property at different frequencies. Due to the high signal laser power, the excess noise shown in Fig. D.6 can be much higher than the shot noise. It has two main contributions, the shot noise of the signal laser and the beating between the signal laser and the excess noise of LO at high frequency. The frequency dependent excess noise observed is mainly due to the LO excess noise. We note that, the Toptica CTL 1500 has relatively lower noise around the mechanical frequency. As a result, we use this model as the blue probe in our experiments and use Toptica CTL 1550 as the LO. As a side note, additional measurements also show that the noise performance doesn't change by introducing the optical devices used in the experiments for the signal laser path.

E Dissipation in optical micro-cavity spectroscopy

In optical micro-cavities, the electromagnetic field is enhanced due to small mode volume and low dissipation. This enables a wide range of parametric process at low powers, such as four-wave mixing, second-harmonic generation, and light matter interactions, such as the coupling to quantum emitters (cavity quantum electrodynamics) and mechanical motion (cavity optomechanics). Despite the strong confinement in the cavity, optical light dissipates to the environment due to different kinds of losses, such as external coupling, optical scattering and absorption. Optical absorption in the micro-cavities leads to an elevated temperature, which in turn modifies the cavity frequency, due to thermal expansion or thermorefractive effect. Such photothermal effects become more evident when the cavity is driven by a strong pumping field.

In cavity optomechanics, the mechanical motion is dispersively coupled to the light field in the cavity due to radiation pressure. Interestingly, early experiments showed that the light absorption can also be utilized to cool the mechanical motion due to the thermal delay, which is called the bolometric effect. The photothermalrefractive effects are known to lead to a static cavity frequency shift. The delayed nature of the thermal process in optical cavity is treated in the early work. We've shown that Floquet dynamics can arise in the multiple tone pumping schemes, where the Kerr-type nonlinearities can lead to the coupling between the independent thermomechanical sidebands.

In this section, we show how the micro-cavity is responding to the strong coherent pump and how the cavity spectroscopy is affected. We consider an optical cavity of resonant frequency ω_c and an input field $a_{\text{in}} = (\bar{a}_{\text{in}} + \delta a_{\text{in}})e^{-i\omega_L t}$ of frequency ω_L . We thus obtain,

$$\dot{\hat{a}} = \left\{ i [\Delta - \Delta_{\text{th}}(t)] - \frac{\kappa}{2} \right\} \hat{a} + \sqrt{\kappa_{\text{ex}}} \hat{a}_{\text{in}}, \quad (\text{E.1})$$

Appendix E. Dissipation in optical micro-cavity spectroscopy

where $\Delta_{\text{th}} = g_{\text{th}}\delta T$ is the frequency shift due to the photothermal effects.

$$\delta \dot{T}(t) = -\gamma_{\text{th}}\delta T(t) + g_{\text{abs}}|a(t)|^2, \quad (\text{E.2})$$

where g_{abs} is temperature increase per photon and γ_{th} is the thermal decay rate. The temperature change can be obtained accordingly,

$$\delta T(t) = \int_{-\infty}^t g_{\text{abs}} e^{-\gamma_{\text{th}}(t-s)} |a(s)|^2 ds. \quad (\text{E.3})$$

We can linearize the intracavity field $a(t) = \bar{a}(t) + \delta \hat{a}(t)$, where $\bar{a} = \sqrt{\bar{n}_c}$ is the mean field.

The field equation of the optical fluctuation δa can be obtained in the Fourier domain,

$$(-i(\Delta + \Omega) + \kappa/2)\delta \hat{a} = g_{\text{th}}g_{\text{abs}}\frac{n_c}{\Omega - i\gamma_{\text{th}}}\delta a + \sqrt{\kappa_{\text{ex}}}\delta \hat{a}_{\text{in}}. \quad (\text{E.4})$$

We define the optical susceptibility,

$$\chi_c^0(\Omega) = \frac{1}{\kappa/2 - i(\Delta + \Omega)} \quad (\text{E.5})$$

We see that under the strong pump, the field fluctuation experiences a modified cavity response,

$$\delta \hat{a} = \chi_c(\Omega)\sqrt{\kappa_{\text{ex}}}\delta \hat{a}_{\text{in}} \quad (\text{E.6})$$

where

$$\chi_c(\Omega) = \frac{1}{\kappa/2 - i(\Delta + \Omega) - g_{\text{th}}g_{\text{abs}}\frac{\bar{n}_c}{\Omega - i\gamma_{\text{th}}}} \quad (\text{E.7})$$

The thermal decay rate γ_{th} are typically in the order of kHz ~ MHz, which is typically lower than the cavity linewidth. For $\Omega \gg \gamma_{\text{th}}$, the fluctuation field sees an effective cavity linewidth,

$$\kappa_{\text{eff}} = \kappa - g_{\text{th}}g_{\text{abs}}\frac{2\bar{n}_c\Omega}{\Omega^2 + \gamma_{\text{th}}^2} \quad (\text{E.8})$$

and an effective detuning,

$$\Delta_{\text{eff}} = \Delta - \Delta_{\text{th}} - g_{\text{th}}g_{\text{abs}}\frac{\bar{n}_c\gamma_{\text{th}}}{\Omega^2 + \gamma_{\text{th}}^2} \quad (\text{E.9})$$

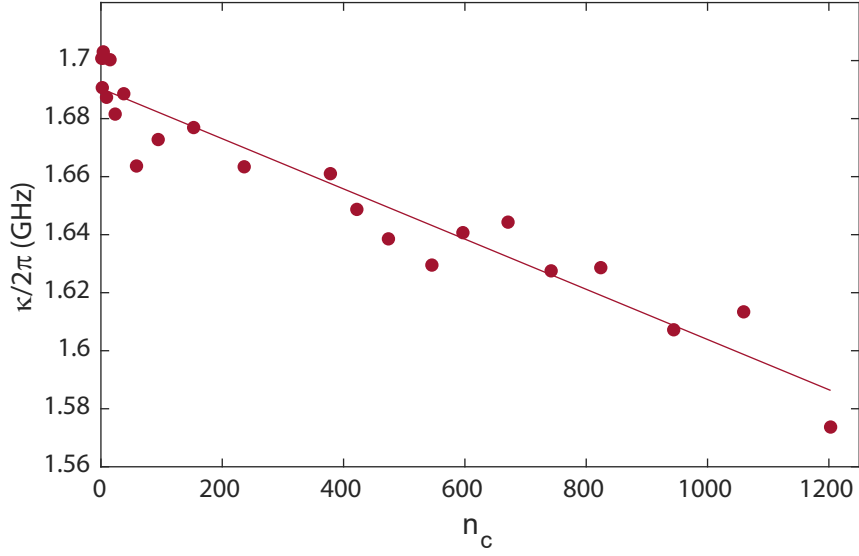


Figure E.1 – **Optical cavity linewidth vs. the intracavity photon number from the coherent response measurement.** The cavity used here is the same as in Ref. [122], which is placed in vacuum at temperature around 10K. The solid circles are from fitted from the coherent cavity response measurement at different intracavity photon numbers while maintaining the effective detuning to $-\Omega_m$.

where $\Delta_{th} = g_{abs}g_{th}\bar{n}_c/\gamma_{th}$ is the static frequency shift proportional to the mean intracavity photon number \bar{n}_c . The detuning can be typically compensated by tuning the pumping laser frequency $\bar{\Delta} = \Delta - \Delta_{th}$.

A coherent response measurement can be performed for such cavity under strong driving. From the cavity response, we can obtain the κ_{eff} under different powers. Due to nonlinear dynamics in the cavity, such as two-photon absorption and free-carrier absorption, the cavity linewidth typically increases when increasing the optical pumping power. However, in the case of positive g_{th} , which corresponds to negative thermorefractive effect (i.e. $dn/dT < 0$), the effective cavity linewidth can suprisingly decrease.

In Fig. E.1, the effective cavity linewidth is shown versus the intracavity number. The measurement is performed with an OMC of $\kappa/2\pi = 1.7$ GHz at 10K with pressure ~ 0.5 mbar. As the pumping powers increases, the effective linewidth decreases linearly, due to the optical heating. The fitted result infers,

$$g_{th}g_{abs}\frac{2\Omega_m}{\Omega_m^2 + \gamma_{th}^2} \sim 8.65 \times 10^4 \times 2\pi. \quad (E.10)$$

We thus can obtain,

$$g_{\text{th}}g_{\text{abs}}/(4\pi^2) \sim 227 \text{ MHz}^2, \quad (\text{E.11})$$

which indicates strong absorption heating of the optical cavity.

In a cavity optomechanical system, the optical field is coupled to the mechanical motion via radiation pressure,

$$\begin{aligned} \dot{\hat{a}} &= \left\{ i[\Delta - \Delta_{\text{th}}(t)] - \frac{\kappa}{2} \right\} \hat{a} + i g_0 \hat{a}(\hat{b} + \hat{b}^\dagger) + \sqrt{\kappa_{\text{ex}}} \hat{a}_{\text{in}}, \\ \dot{\hat{b}} &= \left(-i\Omega_m - \frac{\Gamma_m}{2} \right) \hat{b} + i g_0 \hat{a}^\dagger \hat{a} + \sqrt{\Gamma_m} \hat{b}_{\text{in}}, \end{aligned} \quad (\text{E.12})$$

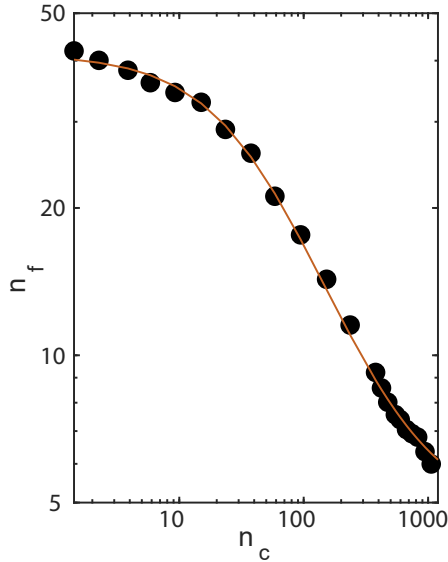


Figure E.2 – **Final phonon occupancy vs. the intracavity photon number.** The phonon occupancy is calibrated from mechanical noise thermometry in the balanced heterodyne noise spectrum with the effective laser detuning Δ_{eff} to $-\Omega$. The red curve corresponds to a fitting curve using a theoretical model with linear absorption.

We can obtain the quantum Langevin equation in the Fourier domain,

$$\begin{aligned} \chi_c^{-1}(\Omega) \delta a &= i g_0 \bar{a}(\delta b + \delta b^\dagger) + \sqrt{\kappa_{\text{ex}}} \delta a_{\text{in}} \\ \chi_m^{-1}(\Omega) \delta b &= i g_0 \bar{a}(\delta a + \delta a^\dagger) + \sqrt{\Gamma_m} \delta b_{\text{in}} \end{aligned} \quad (\text{E.13})$$

where $\chi_m(\Omega) = 1/(\Gamma_m - i(-\Omega_m + \Omega))$.

In case of $\Omega_m \gg \gamma_{\text{th}}$, for sideband cooling ($\Delta_{\text{eff}} = -\Omega_m$), the mechanical susceptibility is modified due to the radiation pressure,

$$\chi_m(\Omega) = \frac{1}{\Gamma_m - i(\Omega_m + \Omega) + 4\bar{n}_c g_0^2 / \kappa_{\text{eff}}} \quad (\text{E.14})$$

The total damping rate

$$\Gamma_{\text{tot}} = \Gamma_m + \frac{4\bar{n}_c g_0^2}{\kappa - g_{\text{th}}g_{\text{abs}} \frac{2\bar{n}_c \Omega_m}{\Omega_m^2 + \gamma_{\text{th}}^2}} \quad (\text{E.15})$$

Dynamical back-action comes from the imbalanced Stokes scattering and anti-Stokes scattering. In this case, the anti-Stokes scattering is enhanced further due to the effective cavity linewidth narrowing. In principle we can fit the power dependent mechanical linewidth to obtain the heating parameters.

The output noise spectrum from a balanced heterodyne detection is given by,

$$S_I(\Omega + \Delta_{\text{LO}}) = 1 + \eta_c \Gamma_{\text{tot}} \frac{\bar{n}_f \bar{n}_c 4g_0^2 / \kappa_{\text{eff}}}{\Gamma_{\text{tot}}^2 / 4 + \Omega^2}, \quad (\text{E.16})$$

In Fig.E.2, we show the calibrated final phonon occupancy from the balanced heterodyne detection when pumping on the red sideband at different powers. A theoretical model incorporating linear absorption heating is used for the fitting as shown in the red curve. The minimum phonon occupancy achieved is $\bar{n}_f \sim 5.5$ at $\bar{n}_c \sim 1200$. We note that, the calibration of the final occupancy relies on κ_{eff} . In our case, the cavity linewidth change over the entire power sweep is $\sim 10\%$, which results in negligible impact on the final occupancy calibration.

However, under high pumping power, the absorption induced effective cavity linewidth change can be comparable to the intrinsic scattering loss, for extremely high Q optical micro-cavities. Even though the actual intrinsic cavity linewidth may not change, it can have a large impact on the cavity spectroscopy due to the different effective linewidth and detuning.

Bibliography

- [1] A. Einstein, *Annalen der Physik* **322**, 132 (1905).
- [2] W. Heisenberg, *Zeitschrift für Physik* **43**, 172 (1927).
- [3] A. Einstein, B. Podolsky, and N. Rosen, *Physical Review* **47**, 777 (1935), publisher: American Physical Society.
- [4] N. Bohr, *Nature* **136**, 65 (1935), number: 3428 Publisher: Nature Publishing Group.
- [5] N. Bohr, *Physical Review* **48**, 696 (1935), publisher: American Physical Society.
- [6] D. Bohm, *Physical Review* **85**, 166 (1952), publisher: American Physical Society.
- [7] J. S. BELL, *Reviews of Modern Physics* **38**, 447 (1966), publisher: American Physical Society.
- [8] H. P. Robertson, *Physical Review* **34**, 163 (1929), publisher: American Physical Society.
- [9] V. B. Braginsky, F. Y. Khalili, and K. S. Thorne, *Quantum Measurement* (Cambridge University Press, 1992).
- [10] J. P. Gordon, H. J. Zeiger, and C. H. Townes, *Physical Review* **99**, 1264 (1955), publisher: American Physical Society.
- [11] A. L. Schawlow and C. H. Townes, *Physical Review* **112**, 1940 (1958), publisher: American Physical Society.
- [12] P. A. M. Dirac and N. H. D. Bohr, *Proceedings of the Royal Society of London. Series A, Containing Papers of a Mathematical and Physical Character* **114**, 243 (1927), publisher: Royal Society.
- [13] E. Fermi, *Reviews of Modern Physics* **4**, 87 (1932), publisher: American Physical Society.
- [14] R. J. Glauber, *Physical Review* **130**, 2529 (1963), publisher: American Physical Society.

Bibliography

- [15] L. MANDEL and E. WOLF, *Reviews of Modern Physics* **37**, 231 (1965), publisher: American Physical Society.
- [16] D. Stoler, *Physical Review D* **1**, 3217 (1970), publisher: American Physical Society.
- [17] H. P. Yuen, *Physical Review A* **13**, 2226 (1976), publisher: American Physical Society.
- [18] M. Xiao, L.-A. Wu, and H. J. Kimble, *Physical Review Letters* **59**, 278 (1987), publisher: American Physical Society.
- [19] Y. Aharonov and D. Bohm, *Physical Review* **122**, 1649 (1961), publisher: American Physical Society.
- [20] C. M. Caves, *Physical Review D* **23**, 1693 (1981), publisher: American Physical Society.
- [21] A. Aspect, *Physical Review D* **14**, 1944 (1976), publisher: American Physical Society.
- [22] A. Wheeler and W. Zurek, *Quantum Theory and Measurement* (Princeton University Press, 1983).
- [23] C. M. Caves, *Physical Review D* **26**, 1817 (1982), publisher: American Physical Society.
- [24] H. Araki and M. M. Yanase, *Physical Review* **120**, 622 (1960), publisher: American Physical Society.
- [25] V. B. Braginski^T and Y. I. Vorontsov, *Sov. Phys. Usp.* **17**, 8 (1975).
- [26] M. E. Gertsenshtein and V. I. Pustovoit, *Sov. Phys. JETP* **16**, 433 (1962).
- [27] R. Weiss, Quarterly Report of the Research Laboratory for Electronics, MIT Report No. 105 (1972).
- [28] LIGO Scientific Collaboration and Virgo Collaboration, *Physical Review Letters* **116**, 061102 (2016).
- [29] V. Braginsky, *Journal of Experimental and Theoretical Physics* **26**, 831 (1967).
- [30] C. M. Caves, *Physical Review Letters* **45**, 75 (1980), publisher: American Physical Society.
- [31] V. B. Braginsky, Y. I. Vorontsov, and K. S. Thorne, *Science* **209**, 547 (1980), publisher: American Association for the Advancement of Science Section: Articles.
- [32] C. M. Caves, K. S. Thorne, R. W. P. Drever, V. D. Sandberg, and M. Zimmermann, *Reviews of Modern Physics* **52**, 341 (1980).

-
- [33] V. B. Braginsky and F. Y. Khalili, *Reviews of Modern Physics* **68**, 1 (1996), publisher: American Physical Society.
- [34] W. G. Unruh, *Physical Review D* **18**, 1764 (1978), publisher: American Physical Society.
- [35] K. S. Thorne, R. W. P. Drever, C. M. Caves, M. Zimmermann, and V. D. Sandberg, *Physical Review Letters* **40**, 667 (1978), publisher: American Physical Society.
- [36] A. A. Clerk, F. Marquardt, and K. Jacobs, *New Journal of Physics* **10**, 095010 (2008).
- [37] M. Brune, S. Haroche, V. Lefevre, J. M. Raimond, and N. Zagury, *Physical Review Letters* **65**, 976 (1990), publisher: American Physical Society.
- [38] J. F. Roch, G. Roger, P. Grangier, J.-M. Courty, and S. Reynaud, *Applied Physics B* **55**, 291 (1992).
- [39] P. Grangier, J. A. Levenson, and J.-P. Poizat, *Nature* **396**, 537 (1998), number: 6711 Publisher: Nature Publishing Group.
- [40] A. Lupaşcu, S. Saito, T. Picot, P. C. de Groot, C. J. P. M. Harmans, and J. E. Mooij, *Nature Physics* **3**, 119 (2007), number: 2 Publisher: Nature Publishing Group.
- [41] L. S. Collaboration, *Physical Review D* **93**, 112004 (2016), publisher: American Physical Society.
- [42] V. Braginsky, A. Manukin, and T. M., *Journal of Experimental and Theoretical Physics* **31**, 829 (1970).
- [43] M. Aspelmeyer, T. J. Kippenberg, and F. Marquardt, *Reviews of Modern Physics* **86**, 1391 (2014).
- [44] S. Mancini, D. Vitali, and P. Tombesi, *Physical Review Letters* **80**, 688 (1998), publisher: American Physical Society.
- [45] C. Fabre, M. Pinard, S. Bourzeix, A. Heidmann, E. Giacobino, and S. Reynaud, *Physical Review A* **49**, 1337 (1994), publisher: American Physical Society.
- [46] K. Jacobs, P. Tombesi, M. J. Collett, and D. F. Walls, *Physical Review A* **49**, 1961 (1994).
- [47] S. Bose, K. Jacobs, and P. L. Knight, *Physical Review A* **56**, 4175 (1997).
- [48] P. F. Cohadon, A. Heidmann, and M. Pinard, *Physical Review Letters* **83**, 3174 (1999).

Bibliography

- [49] M. Eichenfield, J. Chan, R. M. Camacho, K. J. Vahala, and O. Painter, *Nature* **462**, 78 (2009).
- [50] J. D. Thompson, B. M. Zwickl, A. M. Jayich, F. Marquardt, S. M. Girvin, and J. G. E. Harris, *Nature* **452**, 72 (2008).
- [51] T. Carmon, H. Rokhsari, L. Yang, T. J. Kippenberg, and K. J. Vahala, *Physical Review Letters* **94**, 223902 (2005).
- [52] J. D. Teufel, T. Donner, M. A. Castellanos-Beltran, J. W. Harlow, and K. W. Lehnert, *Nature Nanotechnology* **4**, 820 (2009).
- [53] T. J. Kippenberg, H. Rokhsari, T. Carmon, A. Scherer, and K. J. Vahala, *Physical Review Letters* **95**, 033901 (2005).
- [54] A. Schliesser, P. Del’Haye, N. Nooshi, K. J. Vahala, and T. J. Kippenberg, *Physical Review Letters* **97**, 243905 (2006).
- [55] F. Marquardt, J. P. Chen, A. A. Clerk, and S. M. Girvin, *Physical Review Letters* **99**, 093902 (2007).
- [56] I. Wilson-Rae, N. Nooshi, W. Zwerger, and T. J. Kippenberg, *Physical Review Letters* **99**, 093901 (2007).
- [57] T. J. Kippenberg and K. J. Vahala, *Science* **321**, 1172 (2008), arXiv:0712.1618 .
- [58] O. Arcizet, P.-F. Cohadon, T. Briant, M. Pinard, and A. Heidmann, *Nature* **444**, 71 (2006).
- [59] S. Gigan, H. R. Böhm, M. Paternostro, F. Blaser, G. Langer, J. B. Hertzberg, K. C. Schwab, D. Bäuerle, M. Aspelmeyer, and A. Zeilinger, *Nature* **444**, 67 (2006).
- [60] J. Chan, T. P. M. Alegre, A. H. Safavi-Naeini, J. T. Hill, A. Krause, S. Gröblacher, M. Aspelmeyer, and O. Painter, *Nature* **478**, 89 (2011).
- [61] J. D. Teufel, T. Donner, D. Li, J. W. Harlow, M. S. Allman, K. Cicak, A. J. Sirois, J. D. Whittaker, K. W. Lehnert, and R. W. Simmonds, *Nature* **475**, 359 (2011).
- [62] G. Anetsberger, E. Gavartin, O. Arcizet, Q. P. Unterreithmeier, E. M. Weig, M. L. Gorodetsky, J. P. Kotthaus, and T. J. Kippenberg, *Phys. Rev. A* **82**, 061804 (2010).
- [63] K. W. Murch, K. L. Moore, S. Gupta, and D. M. Stamper-Kurn, *Nature Physics* **4**, 561 (2008).
- [64] T. P. Purdy, R. W. Peterson, and C. A. Regal, *Science* **339**, 801 (2013), arXiv:1209.6334 .

-
- [65] F. Y. Khalili, H. Miao, H. Yang, A. H. Safavi-Naeini, O. Painter, and Y. Chen, *Phys. Rev. A* **86**, 033840 (2012).
- [66] J. Teufel, F. Lecocq, and R. Simmonds, *Physical Review Letters* **116**, 013602 (2016).
- [67] A. H. Safavi-Naeini, J. Chan, J. T. Hill, T. P. M. Alegre, A. Krause, and O. Painter, *Physical Review Letters* **108**, 033602 (2012).
- [68] T. P. Purdy, P.-L. Yu, N. S. Kampel, R. W. Peterson, K. Cicak, R. W. Simmonds, and C. A. Regal, *Physical Review A* **92**, 031802 (2015).
- [69] M. Underwood, D. Mason, D. Lee, H. Xu, L. Jiang, A. B. Shkarin, K. Børkje, S. M. Girvin, and J. G. E. Harris, *Physical Review A* **92**, 061801 (2015).
- [70] A. J. Weinstein, C. U. Lei, E. E. Wollman, J. Suh, A. Metelmann, A. A. Clerk, and K. C. Schwab, *Physical Review X* **4**, 041003 (2014).
- [71] V. Sudhir, D. J. Wilson, R. Schilling, H. Schütz, S. A. Fedorov, A. H. Ghadimi, A. Nunnenkamp, and T. J. Kippenberg, *Physical Review X* **7**, 011001 (2017).
- [72] T. P. Purdy, P.-L. Yu, R. W. Peterson, N. S. Kampel, and C. A. Regal, *Physical Review X* **3**, 031012 (2013).
- [73] A. H. Safavi-Naeini, S. Gröblacher, J. T. Hill, J. Chan, M. Aspelmeyer, and O. Painter, *Nature* **500**, 185 (2013).
- [74] S. Schreppler, N. Spethmann, N. Brahms, T. Botter, M. Barrios, and D. M. Stamper-Kurn, *Science* **344**, 1486 (2014).
- [75] D. J. Wilson, V. Sudhir, N. Piro, R. Schilling, A. Ghadimi, and T. J. Kippenberg, *Nature* **524**, 325 (2015), arXiv:1410.6191 .
- [76] M. Rossi, D. Mason, J. Chen, Y. Tsaturyan, and A. Schliesser, *Nature* **563**, 53 (2018), arXiv:1805.05087 .
- [77] J. B. Hertzberg, T. Rocheleau, T. Ndukum, M. Savva, A. A. Clerk, and K. C. Schwab, *Nature Physics* **6**, 213 (2010).
- [78] J. Suh, A. J. Weinstein, C. U. Lei, E. E. Wollman, S. K. Steinke, P. Meystre, A. A. Clerk, and K. C. Schwab, *Science* **344**, 1262 (2014).
- [79] J. Suh, M. D. Shaw, H. G. LeDuc, A. J. Weinstein, and K. C. Schwab, *Nano Letters* **12**, 6260 (2012).

Bibliography

- [80] J. Suh, A. J. Weinstein, and K. C. Schwab, *Applied Physics Letters* **103**, 052604 (2013).
- [81] A. Kronwald, F. Marquardt, and A. A. Clerk, *Physical Review A* **88**, 063833 (2013), arXiv:1307.5309 .
- [82] E. E. Wollman, C. U. Lei, A. J. Weinstein, J. Suh, A. Kronwald, F. Marquardt, A. A. Clerk, and K. C. Schwab, *Science* **349**, 952 (2015), arXiv:1507.01662 .
- [83] C. Lei, A. Weinstein, J. Suh, E. Wollman, A. Kronwald, F. Marquardt, A. Clerk, and K. Schwab, *Physical Review Letters* **117**, 100801 (2016).
- [84] J.-M. Pirkkalainen, E. Damskägg, M. Brandt, F. Massel, and M. A. Sillanpää, *Physical Review Letters* **115**, 243601 (2015).
- [85] F. Lecocq, J. B. Clark, R. W. Simmonds, J. Aumentado, and J. D. Teufel, *Physical Review X* **5**, 041037 (2015), arXiv:1509.01629 .
- [86] R. W. Peterson, T. P. Purdy, N. S. Kampel, R. W. Andrews, P. L. Yu, K. W. Lehnert, and C. A. Regal, *Physical Review Letters* **116**, 063601 (2016), arXiv:1510.03911 .
- [87] S. P. Vyatchanin and E. A. Zubova, *Physics Letters A* **201**, 269 (1995).
- [88] H. J. Kimble, Y. Levin, A. B. Matsko, K. S. Thorne, and S. P. Vyatchanin, *Physical Review D* **65**, 022002 (2001).
- [89] N. S. Kampel, R. W. Peterson, R. Fischer, P.-L. Yu, K. Cicak, R. W. Simmonds, K. W. Lehnert, and C. A. Regal, *Physical Review X* **7**, 021008 (2017), arXiv:1607.06831 .
- [90] D. Mason, J. Chen, M. Rossi, Y. Tsaturyan, and A. Schliesser, arXiv:1809.10629 [quant-ph] (2018), arXiv: 1809.10629.
- [91] T. P. Purdy, K. E. Grutter, K. Srinivasan, and J. M. Taylor, *Science* **356**, 1265 (2017).
- [92] V. Sudhir, R. Schilling, S. A. Fedorov, H. Schütz, D. J. Wilson, and T. J. Kippenberg, *Phys. Rev. X* **7**, 031055 (2017).
- [93] J. Cripe, N. Aggarwal, R. Lanza, A. Libson, R. Singh, P. Heu, D. Follman, G. D. Cole, N. Mavalvala, and T. Corbitt, *Nature* **568**, 364 (2019).
- [94] L. S. Collaboration, *Nature Photonics* **7**, 613 (2013).
- [95] W. Marshall, C. Simon, R. Penrose, and D. Bouwmeester, *Physical Review Letters* **91**, 130401 (2003).

-
- [96] S. Hong, R. Riedinger, I. Marinković, A. Wallucks, S. G. Hofer, R. A. Norte, M. Aspelmeyer, and S. Gröblacher, *Science* **358**, 203 (2017).
- [97] R. Riedinger, A. Wallucks, I. Marinković, C. Löschnauer, M. Aspelmeyer, S. Hong, and S. Gröblacher, *Nature* **556**, 473 (2018).
- [98] N. R. Bernier, L. D. Tóth, A. Koottandavida, M. A. Ioannou, D. Malz, A. Nunnenkamp, A. K. Feofanov, and T. J. Kippenberg, *Nature Communications* **8**, 604 (2017).
- [99] G. A. Peterson, F. Lecocq, K. Cicak, R. W. Simmonds, J. Aumentado, and J. D. Teufel, *Physical Review X* **7**, 031001 (2017).
- [100] H. Xu, L. Jiang, A. A. Clerk, and J. G. E. Harris, *Nature* **568**, 65 (2019).
- [101] T. A. Palomaki, J. W. Harlow, J. D. Teufel, R. W. Simmonds, and K. W. Lehnert, *Nature* **495**, 210 (2013).
- [102] K. Fang, M. H. Matheny, X. Luan, and O. Painter, *Nature Photonics* **10**, 489 (2016), arXiv:1508.05138 .
- [103] A. J. Keller, P. B. Dieterle, M. Fang, B. Berger, J. M. Fink, and O. Painter, *Applied Physics Letters* **111**, 042603 (2017), arXiv:1703.10195 .
- [104] P. Arrangoiz-Arriola, E. A. Wollack, M. Pechal, J. D. Witmer, J. T. Hill, and A. H. Safavi-Naeini, *Physical Review X* **8**, 031007 (2018), arXiv:1804.03625 .
- [105] C. W. Gardiner and M. J. Collett, *Physical Review A* **31**, 3761 (1985).
- [106] M. Wu, A. C. Hryciw, C. Healey, D. P. Lake, H. Jayakumar, M. R. Freeman, J. P. Davis, and P. E. Barclay, *Physical Review X* **4**, 021052 (2014).
- [107] A. K. Tagantsev, I. V. Sokolov, and E. S. Polzik, *Physical Review A* **97**, 063820 (2018).
- [108] C. H. Metzger and K. Karrai, *Nature* **432**, 1002 (2004).
- [109] S. Weis, R. Rivière, S. Deléglise, E. Gavartin, O. Arcizet, A. Schliesser, and T. J. Kippenberg, *Science* **330**, 1520 (2010).
- [110] A. H. Safavi-Naeini, T. P. Alegre, J. Chan, M. Eichenfield, M. Winger, Q. Lin, J. T. Hill, D. E. Chang, and O. Painter, *Nature* **472**, 69 (2011), arXiv:1012.1934 .
- [111] A. A. Clerk, M. H. Devoret, S. M. Girvin, F. Marquardt, and R. J. Schoelkopf, *Reviews of Modern Physics* **82**, 1155 (2010).

Bibliography

- [112] J. Chan, T. P. Alegre, A. H. Safavi-Naeini, J. T. Hill, A. Krause, S. Gröblacher, M. Aspelmeyer, and O. Painter, *Nature* **478**, 89 (2011), arXiv:1106.3614 .
- [113] C. F. Ockeloen-Korppi, E. Damskägg, J. M. Pirkkalainen, M. Asjad, A. A. Clerk, F. Massel, M. J. Woolley, and M. A. Sillanpää, *Nature* **556**, 478 (2018), arXiv:1711.01640 .
- [114] P. Rabl, C. Genes, K. Hammerer, and M. Aspelmeyer, *Phys. Rev. A* **80**, 063819 (2009).
- [115] M. G. Holland, *Physical Review* **132**, 2461 (1963).
- [116] F. Y. Khalili, H. Miao, H. Yang, A. H. Safavi-Naeini, O. Painter, and Y. Chen, *Physical Review A* **86**, 033840 (2012).
- [117] K. Børkje, *Physical Review A* **94**, 043816 (2016).
- [118] I. Wilson-Rae, N. Nooshi, W. Zwerger, and T. J. Kippenberg, *Physical Review Letters* **99**, 093901 (2007), arXiv:0702113 [cond-mat] .
- [119] F. Marquardt, J. P. Chen, A. A. Clerk, and S. M. Girvin, *Physical Review Letters* **99**, 093902 (2007), arXiv:0701416 [cond-mat] .
- [120] J. B. Clark, F. Lecocq, R. W. Simmonds, J. Aumentado, and J. D. Teufel, *Nature* **541**, 191 (2017), arXiv:1606.08795 .
- [121] I. Shomroni, L. Qiu, D. Malz, A. Nunnenkamp, and T. J. Kippenberg, *Nature Communications* **10**, 2086 (2019).
- [122] L. Qiu, I. Shomroni, M. A. Ioannou, N. Piro, D. Malz, A. Nunnenkamp, and T. J. Kippenberg, *Physical Review A* **100**, 053852 (2019).
- [123] J. F. Poyatos, J. I. Cirac, and P. Zoller, *Physical Review Letters* **77**, 4728 (1996), publisher: American Physical Society.
- [124] A. Kronwald, F. Marquardt, and A. A. Clerk, *Physical Review A* **88**, 063833 (2013).
- [125] E. E. Wollman, C. U. Lei, A. J. Weinstein, J. Suh, A. Kronwald, F. Marquardt, A. A. Clerk, and K. C. Schwab, *Science* **349**, 952 (2015).
- [126] I. Shomroni, A. Youssefi, N. Sauerwein, L. Qiu, P. Seidler, D. Malz, A. Nunnenkamp, and T. J. Kippenberg, *Physical Review X* **9**, 041022 (2019).
- [127] K. W. Murch, K. L. Moore, S. Gupta, and D. M. Stamper-Kurn, *Nature Physics* **4**, 561 (2008).

-
- [128] A. Schliesser, P. Del’Haye, N. Nooshi, K. J. Vahala, and T. J. Kippenberg, *Physical Review Letters* **97**, 243905 (2006), arXiv:0611235 [physics] .
- [129] E. Yablonovitch, *Physical Review Letters* **58**, 2059 (1987).
- [130] S. John, *Physical Review Letters* **58**, 2486 (1987).
- [131] Y. Akahane, T. Asano, B.-S. Song, and S. Noda, *Nature* **425**, 944 (2003).
- [132] K. J. Vahala, *Nature* **424**, 839 (2003).
- [133] E. Gavartin, R. Braive, I. Sagnes, O. Arcizet, A. Beveratos, T. J. Kippenberg, and I. Robert-Philip, *Physical Review Letters* **106**, 203902 (2011), publisher: American Physical Society.
- [134] S. G. Johnson, M. Ibanescu, M. A. Skorobogatiy, O. Weisberg, J. D. Joannopoulos, and Y. Fink, *Physical Review E* **65**, 066611 (2002), publisher: American Physical Society.
- [135] D. K. Biegelsen, *Physical Review Letters* **32**, 1196 (1974), publisher: American Physical Society.
- [136] J. Chan, A. H. Safavi-Naeini, J. T. Hill, S. Meenehan, and O. Painter, *Applied Physics Letters* **101**, 081115 (2012).
- [137] G. S. MacCabe, H. Ren, J. Luo, J. D. Cohen, H. Zhou, A. Sipahigil, M. Mirhosseini, and O. Painter, arXiv:1901.04129 [cond-mat, physics:quant-ph] (2019), arXiv: 1901.04129.
- [138] I. Marinković, A. Wallucks, R. Riedinger, S. Hong, M. Aspelmeyer, and S. Gröblacher, *Phys. Rev. Lett.* **121**, 220404 (2018).
- [139] M. Schmidt, S. Kessler, V. Peano, O. Painter, and F. Marquardt, *Optica* **2**, 635 (2015).
- [140] C. Brendel, V. Peano, O. J. Painter, and F. Marquardt, *Proceedings of the National Academy of Sciences* **114**, 3390 (2017).
- [141] K. C. Balram, M. Davanço, J. Y. Lim, J. D. Song, and K. Srinivasan, *Optica* **1**, 414 (2014), publisher: Optical Society of America.
- [142] M. J. Burek, J. D. Cohen, S. M. Meenehan, N. El-Sawah, C. Chia, T. Ruelle, S. Meesala, J. Rochman, H. A. Atikian, M. Markham, D. J. Twitchen, M. D. Lukin, O. Painter, and M. Lončar, *Optica* **3**, 1404 (2016).
- [143] L. Kipfstuhl, F. Guldner, J. Riedrich-Möller, and C. Becher, *Optics Express* **22**, 12410 (2014).

Bibliography

- [144] D. Navarro-Urrios, J. Gomis-Bresco, S. El-Jallal, M. Oudich, A. Pitanti, N. Capuj, A. Tredicucci, F. Alzina, A. Griol, Y. Pennec, B. Djafari-Rouhani, A. Martínez, and C. M. Sotomayor Torres, *AIP Advances* **4**, 124601 (2014).
- [145] L. Qiu, I. Shomroni, P. Seidler, and T. J. Kippenberg, *Physical Review Letters* **124**, 173601 (2020), publisher: American Physical Society.
- [146] P. E. Barclay, K. Srinivasan, and O. Painter, , 20 (2005).
- [147] R. Riedinger, S. Hong, R. A. Norte, J. A. Slater, J. Shang, A. G. Krause, V. Anant, M. Aspelmeyer, and S. Gröblacher, *Nature* **530**, 313 (2016).
- [148] S. M. Meenehan, J. D. Cohen, S. Gröblacher, J. T. Hill, A. H. Safavi-Naeini, M. Aspelmeyer, and O. Painter, *Physical Review A* **90**, 011803 (2014).
- [149] J. Komma, C. Schwarz, G. Hofmann, D. Heinert, and R. Nawrodt, *Applied Physics Letters* **101**, 041905 (2012), publisher: American Institute of Physics.
- [150] A. D. Kashkanova, A. B. Shkarin, C. D. Brown, N. E. Flowers-Jacobs, L. Childress, S. W. Hoch, L. Hohmann, K. Ott, J. Reichel, and J. G. E. Harris, *Nature Physics* **13**, 74 (2016).
- [151] G. I. Harris, D. L. McAuslan, E. Sheridan, Y. Sachkou, C. Baker, and W. P. Bowen, *Nature Physics* **12**, 788 (2016).
- [152] C. G. Baker, G. I. Harris, D. L. McAuslan, Y. Sachkou, X. He, and W. P. Bowen, *New Journal of Physics* **18**, 123025 (2016).
- [153] D. McAuslan, G. Harris, C. Baker, Y. Sachkou, X. He, E. Sheridan, and W. Bowen, *Physical Review X* **6** (2016), 10.1103/PhysRevX.6.021012.
- [154] A. B. Shkarin, A. D. Kashkanova, C. D. Brown, S. Garcia, K. Ott, J. Reichel, and J. G. E. Harris, *arXiv:1709.02794 [physics, physics:quant-ph]* (2017), arXiv: 1709.02794.
- [155] H. Zhang, X. Zhao, Y. Wang, Q. Huang, and J. Xia, *Optics Express* **25**, 821 (2017).
- [156] A. Salmela, J. Tuoriniemi, and J. Rysti, *Journal of Low Temperature Physics* **162**, 678 (2011).
- [157] X. Sun, X. Zhang, C. Schuck, and H. X. Tang, *Scientific Reports* **3** (2013), 10.1038/s-rep01436.
- [158] L. Childress, M. P. Schmidt, A. D. Kashkanova, C. D. Brown, G. I. Harris, A. Aiello, F. Marquardt, and J. G. E. Harris, *Physical Review A* **96** (2017), 10.1103/PhysRevA.96.063842.

-
- [159] Y. P. Sachkou, C. G. Baker, G. I. Harris, O. R. Stockdale, S. Forstner, M. T. Reeves, X. He, D. L. McAuslan, A. S. Bradley, M. J. Davis, and W. P. Bowen, arXiv:1902.04409 [cond-mat, physics:physics, physics:quant-ph] (2019), arXiv: 1902.04409.
- [160] S. H. Autler and C. H. Townes, *Physical Review* **100**, 703 (1955).
- [161] J. H. Shirley, *Physical Review* **138**, B979 (1965).
- [162] Y.-M. He, H. Wang, C. Wang, M.-C. Chen, X. Ding, J. Qin, Z.-C. Duan, S. Chen, J.-P. Li, R.-Z. Liu, C. Schneider, M. Atatüre, S. Höfling, C.-Y. Lu, and J.-W. Pan, *Nature Physics*, 1 (2019).
- [163] L. W. Clark, N. Jia, N. Schine, C. Baum, A. Georgakopoulos, and J. Simon, *Nature* **571**, 532 (2019).
- [164] J. Cayssol, B. Dóra, F. Simon, and R. Moessner, *physica status solidi (RRL) - Rapid Research Letters* **7**, 101 (2013), arXiv: 1211.5623.
- [165] M. C. Rechtsman, J. M. Zeuner, Y. Plotnik, Y. Lumer, D. Podolsky, F. Dreisow, S. Nolte, M. Segev, and A. Szameit, *Nature* **496**, 196 (2013).
- [166] R. Fleury, A. B. Khanikaev, and A. Alù, *Nature Communications* **7**, 11744 (2016).
- [167] K. Fang, Z. Yu, and S. Fan, *Nature Photonics* **6**, 782 (2012).
- [168] G. Jotzu, M. Messer, R. Desbuquois, M. Lebrat, T. Uehlinger, D. Greif, and T. Esslinger, *Nature* **515**, 237 (2014).
- [169] J. Zhang, P. W. Hess, A. Kyprianidis, P. Becker, A. Lee, J. Smith, G. Pagano, I.-D. Potirniche, A. C. Potter, A. Vishwanath, N. Y. Yao, and C. Monroe, *Nature* **543**, 217 (2017).
- [170] E. Verhagen, S. Deléglise, S. Weis, A. Schliesser, and T. J. Kippenberg, *Nature* **482**, 63 (2012).
- [171] F. Diedrich, J. C. Bergquist, W. M. Itano, and D. J. Wineland, *Physical Review Letters* **62**, 403 (1989).
- [172] P. S. Jessen, C. Gerz, P. D. Lett, W. D. Phillips, S. L. Rolston, R. J. C. Spreeuw, and C. I. Westbrook, *Physical Review Letters* **69**, 49 (1992).
- [173] T. R. Hart, R. L. Aggarwal, and B. Lax, *Physical Review B* **1**, 638 (1970).
- [174] R. J. Nemanich, D. K. Biegelsen, R. A. Street, and L. E. Fennell, *Physical Review B* **29**, 6005 (1984).

Bibliography

- [175] J. B. Cui, K. Amtmann, J. Ristein, and L. Ley, *Journal of Applied Physics* **83**, 7929 (1998).
- [176] A. C. Eckbreth, *Laser diagnostics for combustion temperature and species*, 2nd ed., Combustion science and technology No. 3 (CRC Press, Boca Raton, Fla., 2000).
- [177] A. Ukil, H. Braendle, and P. Krippner, *IEEE Sensors Journal* **12**, 885 (2012).
- [178] A. M. Jayich, J. C. Sankey, K. Børkje, D. Lee, C. Yang, M. Underwood, L. Childress, A. Petrenko, S. M. Girvin, and J. G. E. Harris, *New Journal of Physics* **14**, 115018 (2012).
- [179] T. J. Kippenberg, A. Schliesser, and M. L. Gorodetsky, *New Journal of Physics* **15**, 015019 (2013).
- [180] A. Schliesser, R. Rivière, G. Anetsberger, O. Arcizet, and T. J. Kippenberg, *Nature Physics* **4**, 415 (2008).
- [181] S. M. Meenehan, J. D. Cohen, G. S. MacCabe, F. Marsili, M. D. Shaw, and O. Painter, *Physical Review X* **5**, 041002 (2015).
- [182] F. Lecocq, J. B. Clark, R. W. Simmonds, J. Aumentado, and J. D. Teufel, *Physical Review X* **5**, 041037 (2015).
- [183] W. P. Bowen and G. J. Milburn, *Quantum Optomechanics* (Taylor & Francis, Boca Raton, 2015).
- [184] A. H. Safavi-Naeini, J. Chan, J. T. Hill, S. Gröblacher, H. Miao, Y. Chen, M. Aspelmeyer, and O. Painter, *New Journal of Physics* **15**, 035007 (2013).
- [185] V. S. Il'chenko and M. L. Gorodetskii, *Laser Physics* **2**, 1004 (1992).
- [186] A. E. Fomin, M. L. Gorodetsky, I. S. Grudinin, and V. S. Ilchenko, *Journal of the Optical Society of America B* **22**, 459 (2005).
- [187] H. Rokhsari and K. J. Vahala, *Optics Letters* **30**, 427 (2005).
- [188] V. B. Braginsky, M. L. Gorodetsky, and S. P. Vyatchanin, *Physics Letters A* **271**, 303 (2000).
- [189] C. Gardiner and P. Zoller, *Quantum Noise: A Handbook of Markovian and Non-Markovian Quantum Stochastic Methods with Applications to Quantum Optics*, Springer Series in Synergetics (Springer, 2004).
- [190] D. Malz and A. Nunnenkamp, *Physical Review A* **94**, 023803 (2016).

-
- [191] E. B. Aranas, P. Z. G. Fonseca, P. F. Barker, and T. S. Monteiro, *New Journal of Physics* **18**, 113021 (2016).
- [192] E. B. Aranas, M. J. Akram, D. Malz, and T. S. Monteiro, *Physical Review A* **96**, 063836 (2017).
- [193] Jiang Li, S. Diddams, and K. Vahala, in *2014 IEEE Photonics Conference*, Vol. 22 (IEEE, 2014) pp. 286–287.
- [194] S. De Liberato, N. Lambert, and F. Nori, *Physical Review A - Atomic, Molecular, and Optical Physics* **83** (2011), 10.1103/PhysRevA.83.033809.
- [195] J. Restrepo, J. Gabelli, C. Ciuti, and I. Favero, *Comptes Rendus Physique* **12**, 860 (2011).
- [196] C. H. Metzger and K. Karral, *Nature* **432**, 1002 (2004).
- [197] A. B. Shkarin, A. D. Kashkanova, C. D. Brown, S. Garcia, K. Ott, J. Reichel, and J. G. E. Harris, *Physical Review Letters* **122**, 153601 (2019).
- [198] I. Moaddel Haghighi, N. Malossi, R. Natali, G. Di Giuseppe, and D. Vitali, *Physical Review Applied* **9**, 034031 (2018).
- [199] A. B. Matsko, A. A. Savchenkov, D. Strekalov, V. S. Ilchenko, and L. Maleki, *Physical Review A* **71**, 033804 (2005).
- [200] S. Gupta, K. L. Moore, K. W. Murch, and D. M. Stamper-Kurn, *Physical Review Letters* **99**, 213601 (2007).
- [201] R. Leijssen, G. R. L. Gala, L. Freisem, J. T. Muhonen, and E. Verhagen, *Nature Communications* **8**, ncomms16024 (2017).
- [202] A. Schliesser, *Cavity Optomechanics and Optical Frequency Comb Generation with Silica Whispering-Gallery-Mode Microresonators*, Ph.D. thesis, Ludwig-Maximilians-Universität, München (2009), section 1.5.1.
- [203] J. Suh, A. J. Weinstein, C. U. Lei, E. E. Wollman, S. K. Steinke, P. Meystre, A. A. Clerk, and K. C. Schwab, *Science* **344**, 1262 (2014).
- [204] A. Kronwald, F. Marquardt, and A. A. Clerk, *New Journal of Physics* **16**, 063058 (2014).
- [205] M. J. Woolley and A. A. Clerk, *Physical Review A* **89**, 063805 (2014).
- [206] C. F. Ockeloen-Korppi, E. Damskägg, J.-M. Pirkkalainen, M. Asjad, A. A. Clerk, F. Massel, M. J. Woolley, and M. A. Sillanpää, *Nature* **556**, 478 (2018).

Bibliography

- [207] M. Schmidt, M. Ludwig, and F. Marquardt, *New Journal of Physics* **14**, 125005 (2012).
- [208] A. A. Clerk, M. H. Devoret, S. M. Girvin, F. Marquardt, and R. J. Schoelkopf, *Reviews of Modern Physics* **82**, 1155 (2010), arXiv:0810.4729 .
- [209] A. F. Pace, M. J. Collett, and D. F. Walls, *Physical Review A* **47**, 3173 (1993).
- [210] G. Anetsberger, E. Gavartin, O. Arcizet, Q. P. Unterreithmeier, E. M. Weig, M. L. Gorodetsky, J. P. Kotthaus, and T. J. Kippenberg, *Physical Review A* **82**, 061804 (2010).
- [211] V. B. Braginsky and A. B. Manukin, *JETP* **25**, 653 (1967).
- [212] M. T. Jaekel and S. Reynaud, *EPL (Europhysics Letters)* **13**, 301 (1990).
- [213] M. J. Woolley and A. A. Clerk, *Physical Review A* **87**, 063846 (2013).
- [214] C. Ockeloen-Korppi, E. Damskägg, J.-M. Pirkkalainen, A. Clerk, M. Woolley, and M. Sillanpää, *Physical Review Letters* **117**, 140401 (2016).
- [215] E. S. Polzik and K. Hammerer, *Annalen der Physik* **527**, A15 (2015).
- [216] C. B. Møller, R. A. Thomas, G. Vasilakis, E. Zeuthen, Y. Tsaturyan, M. Balabas, K. Jensen, A. Schliesser, K. Hammerer, and E. S. Polzik, *Nature* **547**, 191 (2017).
- [217] W. P. Bowen and G. J. Milburn, *Quantum optomechanics* (CRC Press, 2016).
- [218] A. H. Safavi-Naeini, J. Chan, J. T. Hill, T. P. M. Alegre, A. Krause, and O. Painter, *Physical Review Letters* **108**, 033602 (2012), arXiv:1108.4680 .
- [219] A. J. Weinstein, C. U. Lei, E. E. Wollman, J. Suh, A. Metelmann, A. A. Clerk, and K. C. Schwab, *Physical Review X* **4**, 041003 (2014), arXiv:1404.3242 .
- [220] T. P. Purdy, P.-L. Yu, N. S. Kampel, R. W. Peterson, K. Cicak, R. W. Simmonds, and C. A. Regal, *Physical Review A* **92**, 031802 (2015), arXiv:arXiv:1406.7247v1 .
- [221] M. Underwood, D. Mason, D. Lee, H. Xu, L. Jiang, A. B. Shkarin, K. Børkje, S. M. Girvin, and J. G. E. Harris, *Physical Review A* **92**, 061801 (2015), arXiv:1406.7254 .
- [222] K. Børkje, *Physical Review A* **94**, 043816 (2016).
- [223] A. Kronwald, F. Marquardt, and A. A. Clerk, *New Journal of Physics* **16**, 063058 (2014).
- [224] V. B. Braginsky and A. B. Manukin, *Measurement of weak forces in physics experiments* (University of Chicago Press, Chicago, 1977).

-
- [225] J. M. Aguirregabiria and L. Bel, *Physical Review A* **36**, 3768 (1987).
- [226] L. Bel, J.-L. Boulanger, and N. Deruelle, *Physical Review A* **37**, 1563 (1988).
- [227] V. B. Braginsky, S. E. Strigin, and S. P. Vyatchanin, *Physics Letters A* **287**, 331 (2001).
- [228] M. Ludwig, B. Kubala, and F. Marquardt, *New Journal of Physics* **10**, 095013 (2008).
- [229] A. Pai, S. V. Dhurandhar, P. Hello, and J.-Y. Vinet, *The European Physical Journal D* **8**, 333 (2000).
- [230] V. B. Braginsky, S. E. Strigin, and S. P. Vyatchanin, *Physics Letters A* **305**, 111 (2002).
- [231] S. W. Schediwy, C. Zhao, L. Ju, and D. G. Blair, *Classical and Quantum Gravity* **21**, S1253 (2004).
- [232] L. Ju, S. Grass, C. Zhao, J. Degallaix, and D. G. Blair, *Journal of Physics: Conference Series* **32**, 282 (2006).
- [233] L. Ju, S. Gras, C. Zhao, J. Degallaix, and D. G. Blair, *Physics Letters A* **354**, 360 (2006).
- [234] L. Ju, C. Zhao, S. Gras, J. Degallaix, D. G. Blair, J. Munch, and D. H. Reitze, *Physics Letters A* **355**, 419 (2006).
- [235] A. G. Gurkovsky, S. E. Strigin, and S. P. Vyatchanin, *Physics Letters A* **362**, 91 (2007).
- [236] A. Dorsel, J. D. McCullen, P. Meystre, E. Vignes, and H. Walther, *Physical Review Letters* **51**, 1550 (1983).
- [237] F. Marquardt, J. G. E. Harris, and S. M. Girvin, *Physical Review Letters* **96**, 103901 (2006).
- [238] A. G. Krause, J. T. Hill, M. Ludwig, A. H. Safavi-Naeini, J. Chan, F. Marquardt, and O. Painter, *Physical Review Letters* **115**, 233601 (2015).
- [239] L. Bakemeier, A. Alvermann, and H. Fehske, *Physical Review Letters* **114**, 013601 (2015).
- [240] L. S. Collaboration, *Physical Review Letters* **114**, 161102 (2015).
- [241] J. Suh, M. D. Shaw, H. G. LeDuc, A. J. Weinstein, and K. C. Schwab, *Nano Letters* **12**, 6260 (2012).
- [242] R. D. Delaney, A. P. Reed, R. W. Andrews, and K. W. Lehnert, *arXiv:1903.02151* (2019).
- [243] M. Eichenfield, J. Chan, R. M. Camacho, K. J. Vahala, and O. Painter, *Nature* **462**, 78 (2009), *arXiv:0906.1236*.

Bibliography

- [244] D. Walls and G. J. Milburn, *Quantum Optics* (Springer Berlin Heidelberg, Berlin, Heidelberg, 2008) chapter 5.
- [245] D. Malz and A. Nunnenkamp, *Physical Review A* **94**, 023803 (2016).
- [246] S. H. Strogatz, *Nonlinear dynamics and chaos: with applications to physics, biology, chemistry, and engineering*, 2nd ed. (Westview Press, a member of the Perseus Books Group, Boulder, CO, 2015) chapter 5.
- [247] J. Miller, M. Evans, L. Barsotti, P. Fritschel, M. MacInnis, R. Mittleman, B. Shapiro, J. Soto, and C. Torrie, *Physics Letters A* **375**, 788 (2011).
- [248] G. I. Harris, U. L. Andersen, J. Knittel, and W. P. Bowen, *Phys. Rev. A* **85**, 061802 (2012).
- [249] L. D. Toth, N. R. Bernier, A. Nunnenkamp, A. K. Feofanov, and T. J. Kippenberg, *Nature Physics* **13**, 787 (2017), arXiv:1602.05180 .
- [250] N. R. Bernier, L. D. Tóth, A. Koottandavida, M. A. Ioannou, D. Malz, A. Nunnenkamp, A. K. Feofanov, and T. J. Kippenberg, *Nature Communications* **8**, 604 (2017).
- [251] C. Fabre, M. Pinard, S. Bourzeix, A. Heidmann, E. Giacobino, and S. Reynaud, *Physical Review A* **49**, 1337 (1994).
- [252] M. J. Woolley and A. A. Clerk, *Physical Review A* **89**, 063805 (2014).
- [253] S. Chu, *Reviews of Modern Physics* **70**, 685 (1998).
- [254] C. N. Cohen-Tannoudji, *Reviews of Modern Physics* **70**, 707 (1998).
- [255] C. E. Wieman, D. E. Pritchard, and D. J. Wineland, *Reviews of Modern Physics* **71**, S253 (1999).
- [256] A. Ashkin, *Physical Review Letters* **40**, 729 (1978).
- [257] D. J. Wineland and W. M. Itano, *Physical Review A* **20**, 1521 (1979), arXiv:arXiv:1011.1669v3 .
- [258] E. S. Shuman, J. F. Barry, and D. Demille, *Nature* **467**, 820 (2010), arXiv:1103.6004 .
- [259] L. Anderegg, B. L. Augenbraun, Y. Bao, S. Burchesky, L. W. Cheuk, W. Ketterle, and J. M. Doyle, *Nature Physics* **14**, 890 (2018), arXiv:1803.04571 .
- [260] C. Ospelkaus, U. Warring, Y. Colombe, K. R. Brown, J. M. Amini, D. Leibfried, and D. J. Wineland, *Nature* **476**, 181 (2011), arXiv:1104.3573 .

-
- [261] C. Monroe and J. Kim, *Science* **339**, 1164 (2013), arXiv:0402594v3 [arXiv:cond-mat] .
- [262] R. Blatt and C. F. Roos, *Nature Physics* **8**, 277 (2012), arXiv:0905.0118 .
- [263] T. Li, S. Kheifets, and M. G. Raizen, *Nature Physics* **7**, 527 (2011), arXiv:1101.1283 .
- [264] LIGO Scientific Collaboration, *New Journal of Physics* **11**, 73032 (2009).
- [265] A. Schliesser, R. Rivière, G. Anetsberger, O. Arcizet, and T. J. Kippenberg, *Nature Physics* **4**, 415 (2008), arXiv:0709.4036 .
- [266] E. Verhagen, S. Deléglise, S. Weis, A. Schliesser, and T. J. Kippenberg, *Nature* **482**, 63 (2012), arXiv:1107.3761 .
- [267] I. Shomroni, L. Qiu, and T. J. Kippenberg, *Physical Review A* **101**, 033812 (2020), publisher: American Physical Society.
- [268] W. H. P. Pernice, C. Schuck, M. Li, and H. X. Tang, *Optics Express* **19**, 3290 (2011).
- [269] L.-A. Wu, H. J. Kimble, J. L. Hall, and H. Wu, *Physical Review Letters* **57**, 2520 (1986), publisher: American Physical Society.
- [270] D. F. Walls, *Nature* **306**, 141 (1983), number: 5939 Publisher: Nature Publishing Group.
- [271] D. Rugar and P. Grütter, *Physical Review Letters* **67**, 699 (1991), publisher: American Physical Society.
- [272] A. Mari and J. Eisert, *Physical Review Letters* **103**, 213603 (2009), publisher: American Physical Society.
- [273] R. Ruskov, K. Schwab, and A. N. Korotkov, *Physical Review B* **71**, 235407 (2005), publisher: American Physical Society.
- [274] A. Szorkovszky, A. C. Doherty, G. I. Harris, and W. P. Bowen, *Physical Review Letters* **107**, 213603 (2011), publisher: American Physical Society.
- [275] A. Szorkovszky, G. A. Brawley, A. C. Doherty, and W. P. Bowen, *Physical Review Letters* **110**, 184301 (2013), publisher: American Physical Society.
- [276] K. Jähne, C. Genes, K. Hammerer, M. Wallquist, E. S. Polzik, and P. Zoller, *Physical Review A* **79**, 063819 (2009), publisher: American Physical Society.
- [277] P. Seidler, *Journal of Vacuum Science & Technology B* **35**, 031209 (2017), publisher: American Vacuum Society.

Curriculum Vitae

Address: PHD3345, EPFL, Lausanne, Switzerland **Email:** yocto.qiu@gmail.com
Phone: (41) 0768236740 **Date of Birth:** 25/10/1987

Education

Swiss Federal Institute of Technology Lausanne (EPFL) Lausanne, Switzerland
 Ph.D. in Photonics April 2014 – April 2020
 Thesis: “**Quantum Measurement of Mechanical Motion close to the Standard Quantum Limit**”
 Adviser: **Professor Tobias Kippenberg**, Laboratory of Photonics and Quantum Measurement (LPQM)

Institute of Physics, Chinese Academy of Sciences (IOP, CAS) Beijing, China
 M.S. in Optics Sept. 2010 – Aug. 2013
 Thesis: “**Quantum states manipulation in hybrid quantum photonic systems**”
 Adviser: **Professor Zhi-Yuan Li**, Laboratory of Optics

Department of Physics, Nanjing University Nanjing, China
 B.S. in Condensed Matter Physics Sept. 2006 – July 2010
 Thesis: “**Magnetic plasmon in coupled nanosandwich structure**”
 Adviser: **Professor Shi-Ning Zhu**, Dielectric Superlattice Laboratory (DSL)

Experience

- ❖ Research Assistant in LPQM, EPFL, Switzerland Nov. 2013 – April 2020
 - **Observation of Floquet dynamics** in quantum optomechanics.
 - **Demonstration of Optical Back-action Evasion Measurement** of the mechanical motion
 - **Discovery of fundamental instability in Optical Backaction Evading Measurement**, demonstrated in both optical and microwave domain.
 - Laser cooling of mechanical motion to *its zero-point energy*.
 - **Dissipation in micro-cavity coherent and incoherent spectroscopy**.
 - **Observation of quantum mechanical squeezing with light**.
- ❖ Research Assistant in Laboratory of Optics in IOP, CAS, China Sept. 2010 – July 2013
 - Theoretical investigation on the quantum state transfer and quantum dynamics in two three-level quantum dots in single and coupled photonic crystal cavities.
 - Single photon generation by pulsed laser in optomechanical system via photon blockade.
- ❖ Summer Research in Lab. of Quantum Optics, Queensland University Nov. 2012 – Feb. 2013
 - Integrated microscale electric field sensor using Cavity Optomechanical System.
- ❖ Research Assistant in DSL, Nanjing University July 2009 – July 2010
 - Investigate the magnetic resonant modes in the coupled nanosandwich structure.

Honors and Awards

- Swiss National Science Foundation Fellowship, EPFL, Switzerland 2016 – 2017
- Nature Nanotechnology Poster Prize 2017
- Marie-Curie ITN Fellowship, EPFL, Switzerland 2014 – 2016
- First Class Research Scholarship, IOP, Chinese Academy of Sciences, China 2010 – 2013
- Summer Research Scholarship, University of Queensland, Australia 2012
- National University Student Innovation Program, Nanjing University, China 2009 – 2010
- Renming Scholarship, Nanjing University, China 2007 – 2009

Publications

- 1 **Liu Qiu**[†], Itay Shomroni[†], Jiahe Pan, Paul Seidler, Tobias Kippenberg, “Quantum squeezing of mechanical motion with light”, In preparation.
- 2 **Liu Qiu**, Itay Shomroni, Paul Seidler, Tobias Kippenberg, “Optical micro-cavity spectroscopy with dissipation”, In preparation.
- 3 Amir Youssefi, Itay Shomroni, Nathan Bernier, Yash J. Joshi, Anton Lukashchuk, **Liu Qiu**, Tobias Kippenberg, “Cryogenic electro-optical interconnect for superconducting circuits”, arXiv:2004.04705 (2020).
- 4 **Liu Qiu**[†], Itay Shomroni[†], Paul Seidler, Tobias Kippenberg, “Laser cooling of a nanomechanical oscillator to its zero-point energy”, **Phys. Rev. Lett.** **124**, 173601 (2020).
- 5 Itay Shomroni, **Liu Qiu**, Tobias Kippenberg, “Optomechanical generation of a mechanical catlike state by phonon subtraction”, **Phys. Rev. A** **101**, 033812 (2020).
- 6 Itay Shomroni[†], Amir Youssefi[†], Nick Sauerwein[†], **Liu Qiu**[†], Daniel Malz, Andreas Nunnenkamp, Paul Seidler, Tobias J. Kippenberg, “Two-Tone Optomechanical Instability and Its Fundamental Implications for Backaction-Evading Measurements”, **Phys. Rev. X** **9**, 041022 (2019).
- 7 Itay Shomroni[†], **Liu Qiu**[†], Daniel Malz, Andreas Nunnenkamp, Tobias J. Kippenberg, “Optical Backaction-Evading Measurement of a Mechanical Oscillator”, **Nature Communications** **10**, 2086 (2019).
- 8 **Liu Qiu**[†], Itay Shomroni[†], Marie Adrienne Ioannou, Daniel Malz, Andreas Nunnenkamp, Tobias Kippenberg, “Floquet dynamics in the quantum measurement of mechanical motion”, **Phys. Rev. A** **100**, 053852 (2019).
- 9 **Liu Qiu**, Lin Gan, Wei Ding, Zhiyuan Li, “Single photon state generation by pulsed laser in optomechanical system via photon blockade effect”, **J. Opt. Soc. Am. B** **30**, 001683(2013).
- 10 **Liu Qiu**, Ke Zhang, Zhiyuan Li, “Spontaneous emission of two quantum dots in a single-mode cavity”, **Chin. Phys. B** **22**, 094207(2013).
- 11 **Liu Qiu**, Shuming Wang, Hui Liu, Tao Li, Shining Zhu, and Xiang Zhang, “Magnetic plasmon in coupled nanosandwich structure”, **J. Opt. Soc. Am. B** **28**, 1655(2011).

Conferences and Colloquiums

Talks:

- 1) March 2020, “Laser cooling of a nanomechanical oscillator to its zero-point energy”, APS March Meeting, Denver, US
- 2) April 2019, “Optical Back-action Evasion measurement of mechanical motion”, Quantum Information and Measurement (QIM) V: Quantum Technologies, Rome, Italy
- 3) Jan. 2019, “Quantum Optomechanics in the Presence of Kerr-type Nonlinearities”, Optomechanical Technology and Hybrid Optomechanical Technology 2019, Saanen, Switzerland
- 4) August 2018, “Motional Sideband Asymmetry in Quantum Optomechanics in the Presence of Kerr-type Nonlinearities”, Swiss Physics Society Annual Conference, Lausanne, Switzerland
- 5) August 2018, “Backaction evasion measurement of mechanical motion in the optical domain” Swiss Physics Society Annual Conference, Lausanne, Switzerland
- 6) July 2018, “Backaction-Evading Measurement of Mechanical Motion in the Optical Domain”, Conference on Optical MEMS and Nanophotonics 2018, Lausanne, Switzerland
- 7) July 2018, “Quantum Motional Sideband Asymmetry in the Presence of Kerr-Type Nonlinearities, Conference on Optical MEMS and Nanophotonics 2018, Lausanne, Switzerland
- 8) March 2018, “Effect of Thermal Nonlinearities on Sideband Asymmetry Measurements in Quantum Optomechanics”, CLEO US, San Jose, US
- 9) Mar. 2018, “Probing sideband asymmetry in mechanical oscillators in the presence of thermal effects”, APS March meeting, Los Angeles, US
- 10) May 2016, “Cryogenic Quantum Cavity Optomechanics with High frequency mechanical oscillators”, cQOM workshop: "From Photonics Research to CMOS-fab", Ghent, Belgium
- 11) Feb. 2016, “Cryogenic Quantum Cavity Optomechanics with High frequency mechanical oscillators”, Diavolezza 2016 CQOM Annual ITN Workshop, Diavolezza, Switzerland
- 12) July 2014, “Optomechanical coupling in 1D phoxonic crystal cavity”, ITN CQOM workshop, Lausanne, Switzerland

Colloquiums:

- 1) Jan. 2019, “Quantum measurement of mechanical motion with light”, Southern University of Science and Technology, Shenzhen, China
- 2) Dec. 2018, “Quantum measurement of mechanical motion with light”, Huazhong University of Science and Technology, Wuhan, China
- 3) Dec. 2018, “Quantum measurement of mechanical motion with light”, Zhejiang University, Zhejiang, China
- 4) Dec. 2018, “Quantum measurement of mechanical motion with light”, Sun Yat-sen University, Guangzhou, China
- 5) Dec. 2018, “Put Mechanics into Quantum Mechanics with Light”, South China University of Technology, Guangzhou, China
- 6) July 2015, “A novel scheme for Cavity Optomechanics of high frequency mechanical oscillator”, IBM Zurich symposium, Rüschlikon, Switzerland

Posters:

- 1) July 2019, “High-fidelity laser cooling to the quantum ground state of a silicon nanomechanical oscillator”, Hybrid Optomechanical Technologies (HOT) 2019, Monte Verita, Switzerland
- 2) June 2019, “High-fidelity laser cooling to the quantum ground state of a silicon nanomechanical oscillator”, 16th International Workshop on Nanomechanical Sensors, Lausanne, Switzerland
- 3) February 2019, “Quantum Measurement of mechanical motion with light”, "Frontiers of Nanomechanical Systems (FNS)", Palm Springs, United States
- 4) Sep. 2017, “Sideband Asymmetry of Mechanical Motion”, “20 Years of Nanophotonics”, Erlangen, Germany
- 5) Feb. 2017, “Ground State Cooling of Optomechanical Crystal close to the ground state”, "Frontiers of Nanomechanical Systems (FNS)" La Thuile, Italy. *Nature Nanotechnology Poster Prize*
- 6) July 2016, “Ground State Cooling of a Mechanical Oscillator”, "OPTO- AND ELECTRO-MECHANICAL TECHNOLOGIES", Ascona, Switzerland
- 7) Dec. 2016, “Laser Cooling of a Mechanical Oscillator in a Buffered Gas ^3He cryostat”, cQOM workshop: "Taking a Research Idea to a Product", Rüschlikon, Switzerland
- 8) Feb. 2015, “Novel Coupling Scheme for Cryogenic Cavity Optomechanics with high frequency mechanical oscillator”, Diavolezza 2015 Annual ITN cQOM Workshop, Diavolezza, Switzerland

Teaching Experience

2014 - 2018 Teaching Assistant in in Mechanics, Electromagnetism and Physical Experiments at EPFL